

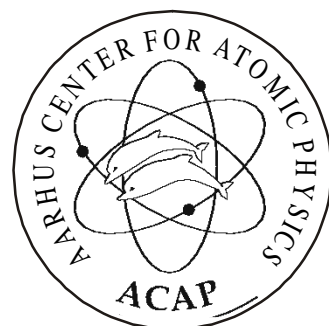
Hydrogen-Related Defects in Proton-Implanted Silicon and Germanium

An Infrared Absorption Spectroscopy Study

Michael Budde

Aarhus Center for Atomic Physics
Institute of Physics and Astronomy
University of Aarhus
Denmark

October 1998



Contents

Preface	I
List of publications	II
I. Introduction	1
II. Introduction to local mode spectroscopy	13
III. Experimental	25
IV. The positive charge state of bond-centre hydrogen in silicon	41
V. The H_2^* defect in germanium and silicon	59
VI. Vacancy-hydrogen complexes in silicon	77
VII. Vacancy-hydrogen complexes in germanium	103
VIII. The hydrogen-saturated self-interstitials in silicon and germanium	119
IX. Summary	147
X. Danish summary	153
XI. Acknowledgements	159

Preface

This thesis is submitted to the Faculty of Natural Sciences, University of Aarhus, Denmark, in partial fulfilment of the requirements for the PhD degree in physics. The work was carried out at the Institute of Physics and Astronomy, University of Aarhus, under the supervision of Brian Bech Nielsen. The experimental work presented in this thesis was performed in the period from August 1994 to June 1998. Included in the PhD study was a visit at the Oak Ridge National Laboratory, Tennessee, USA, from September 1997 to January 1998. The experimental results obtained during that stay are not included in the present thesis. The publications produced during the PhD study are listed on the following pages. The PhD study was financed by a grant from the Danish National Research Foundation through Aarhus Center for Atomic Physics (ACAP).

The objective of the work described in this thesis is to identify hydrogen-related point defects in crystalline silicon and germanium and to study their microstructural properties. The defects are studied by infrared absorption spectroscopy in combination with isochronal annealing, isotope substitution, and uniaxial stress experiments. The microscopic information obtained from such experiments is seldom sufficient to allow unambiguous assignments of the absorption lines to specific defects. However, if complementary information on the defects is available from other experimental techniques or theory, reliable assignments can be made. The experimental studies described in this thesis have benefited significantly from a close collaboration with the theory group of R. Jones at the University of Exeter, UK, and the collaboration has resulted in a number of joint publications. The theoretical results obtained by the Exeter group are used extensively in this thesis, as they are a prerequisite for a proper description of the experimental results. It should be stressed, however, that my contribution to the work presented in the thesis is of experimental character.

The thesis is divided into eleven chapters. Chapter I gives an introduction to the properties of hydrogen in silicon and germanium and motivates the present work. Chapter II describes the basic concepts of local mode spectroscopy and gives an introduction to uniaxial stress experiments. Chapter III is concerned with experimental details of this work, and describes the preparation of samples by ion implantation, the basic concepts of the FTIR (Fourier Transform InfraRed) spectrometer, and gives a technical description of the experimental setup used for the infrared absorption measurements. The chapters IV - VIII are the backbone of the thesis and describe the experimental results obtained. Each of these chapters contains an introduction to the experimental and theoretical studies of the defect(s) described in that chapter. The experimental results are summarised in chapter IX (in English) and chapter X (in Danish). Finally, chapter XI acknowledges the people who have made the completion of this work possible.

List of publications

1. *The H_2^* defect in crystalline germanium.*
M. Budde, B. Bech Nielsen, R. Jones, J. Goss, and S. Öberg, in "Defects in Semiconductors 18", edited by M. Suezawa and H. Katayama-Yoshida, Materials Science Forum (Trans Tech, Aedermannsdorf, 1995), p. 879.
2. *H interacting with intrinsic defects in silicon.*
B. Bech Nielsen, L. Hoffmann, M. Budde, R. Jones, J. Goss, and S. Öberg, in "Defects in Semiconductors 18", edited by M. Suezawa and H. Katayama-Yoshida, Materials Science Forum Vol. (Trans Tech, Aedermannsdorf, 1995), p. 933.
3. *Local modes of the H_2^* dimer in germanium.*
M. Budde, B. Bech Nielsen, R. Jones, J. Goss, and S. Öberg, Phys. Rev. B, **54**, 5485 (1996).
4. *Si-H stretch modes of hydrogen-vacancy defects in silicon.*
B. Bech Nielsen, L. Hoffmann, and M. Budde, Mater. Sci. Eng. B, **36**, 259 (1996).
5. *The hydrogen-saturated self-interstitial in silicon and germanium.*
M. Budde, B. Bech Nielsen, P. Leary, J. Goss, R. Jones, P. R. Briddon, S. Öberg, and S. J. Breuer, in "Defects in Semiconductors 19", edited by G. Davies and M. H. Nazaré, Materials Science Forum (Trans Tech, Aedermannsdorf, 1997), p. 35.
6. *Identification of the hydrogen-saturated self-interstitials in silicon and germanium.*
M. Budde, B. Bech Nielsen, P. Leary, J. Goss, R. Jones, P. R. Briddon, S. Öberg, and S. J. Breuer, Phys. Rev. B, **57**, 4397 (1998).
7. *Vacancy-hydrogen complexes in germanium.*
B. J. Coomer, P. Leary, M. Budde, B. Bech Nielsen, R. Jones, S. Öberg, and P. R. Briddon, to appear in the Proceedings from the E-MRS Spring Meeting, June 1998, Strasbourg, France.

Publications not included in this thesis

8. *Local vibrational modes of weakly bound O-H complexes in Si.*
B. Bech Nielsen, K. Tanderup, M. Budde, K. Bonde Nielsen, J. L. Lindström, R. Jones, S. Öberg, B. Hourahine, and P. R. Briddon, in "Defects in Semiconductors 19", edited by G. Davies and M. H. Nazaré, Materials Science Forum Vol. (Trans Tech, Aedermannsdorf, 1998), p. 391.

I. Introduction

Hydrogen is often characterised as the simplest element in the periodic table. This point of view is correct considering the atomic structure of the elements but does not apply when the chemical properties of the elements are taken into account. Hydrogen has very rich chemical properties and forms more molecular compounds than any other element [1]. For example, the strong covalent bonds of hydrogen with carbon, oxygen, and nitrogen constitute the basis for organic chemistry and, thus, for our existence.

Hydrogen is an important impurity in crystalline semiconductors, and its properties have been studied extensively both experimentally and theoretically for more than two decades. By far the largest amount of work has been concerned with hydrogen in silicon, which reflects the dominance of silicon technology on the market for electronic devices. The properties of hydrogen in semiconductors have been discussed in a number of recent reviews [2-6].

Hydrogen is invariably incorporated into semiconductors during crystal growth or processing steps such as wafer polishing, wet chemical etching, or reactive ion etching [5]. The solubility of hydrogen in semiconductors is low. For example, the solubility of hydrogen in intrinsic silicon is $\sim 10^{15} \text{ cm}^{-3}$ at 1200°C [7] and $\sim 10^6 \text{ cm}^{-3}$ at 300°C [7,8]. However, the effective solubility at moderate temperatures is determined by the concentration of hydrogen traps, e.g. dopants, and exceeds the intrinsic value by several orders of magnitude. Hydrogen is a very fast diffuser in silicon with the diffusivity

$$D_H = (9 \pm 4) \times 10^{-3} \exp\left[-\frac{0.48 \pm 0.06 \text{ eV}}{k_B T}\right] \text{ cm}^2/\text{s} \quad (\text{I.1})$$

in the temperature range $970 - 1200^\circ\text{C}$ [7]. The diffusivity given in Eq. I.1 is only observed at high temperatures or under conditions of low impurity concentrations, where trapping of hydrogen (including self-trapping) is negligible. The effective diffusivity is typically several orders of magnitude smaller than the value given by Eq. I.1.

The diffusion studies which led to Eq. I.1 indicated that hydrogen diffuses as an atomic species in silicon, i.e. as an “isolated” hydrogen atom in an otherwise perfect lattice [7]. According to theory [6], isolated hydrogen in silicon can reside either at the bond-centre (*BC*) site or at (or close to) the tetrahedral interstitial (*T*) site of the silicon lattice (see Fig. I.1). Moreover, theory predicts that isolated hydrogen has both a donor ($0/+$) and an acceptor level ($-/0$) in the band gap [6], and that the acceptor level may be located *below* the donor level [9,10]. The calculations agree that the

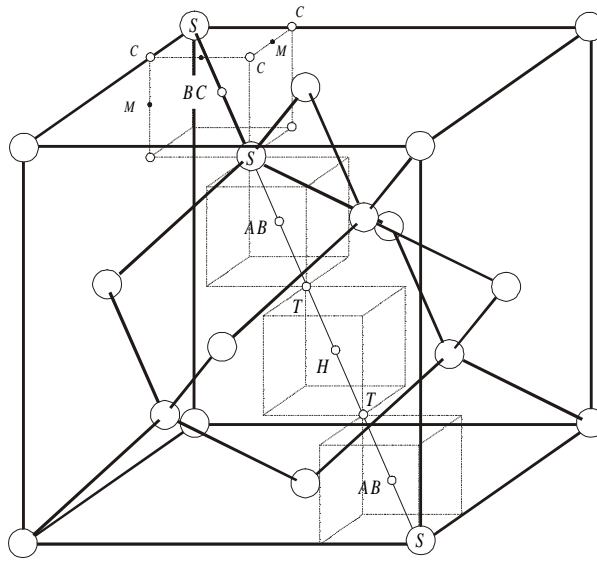


Fig. I.1. High-symmetry sites in a diamond lattice. *S*: substitutional, *T*: tetrahedral, *BC*: bond-centre, *AB*: anti-bonding, *H*: hexagonal, *C*, and *M*.

positive and negative charge state of isolated hydrogen only is stable at the *BC* site and the *T* site, respectively, whereas the neutral charge state may be metastable with energy minima at both lattice sites [6]. The *BC* hydrogen species has been identified experimentally by EPR [11] and the donor level was found 0.16 eV below the edge of the conduction band with DLTS [12]. In contrast, hydrogen at or close to the *T* site has not yet been identified. The incomplete understanding of isolated hydrogen in silicon (and other semiconductors) is unfortunate as it impedes the understanding of important issues such as hydrogen diffusion and hydrogen-impurity reactions.

The small size of the hydrogen atom and its ability to form strong covalent bonds with a number of elements in the periodic table makes hydrogen a very diverse impurity, which interacts with virtually any imperfection in the crystal such as impurities, intrinsic (native) defects, interfaces, and surfaces.

For example, it has been established that isolated hydrogen defects interact with each other and form two types of hydrogen dimers called H_2^T and H_2^* in silicon. The H_2^T defect consists of a hydrogen molecule located at a *T* site and its existence was first proposed in 1983 on the basis of theoretical calculations [13,14]. The existence of H_2^T was confirmed very recently by the observation of an H-H vibrational mode with Raman spectroscopy [15] and infrared absorption spectroscopy [16]. The H_2^* defect is shown in

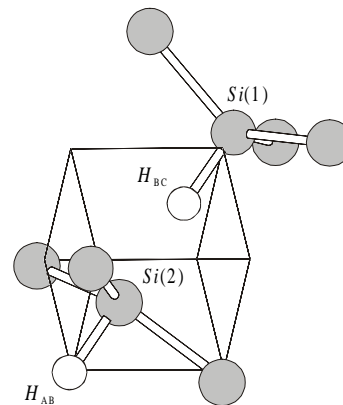


Fig. I.2. Calculated structure of the H_2^* defect in silicon [17].

Fig. I.2, and consists of a hydrogen atom located at a BC site (H_{BC}) bonded to the host atom denoted $Si(1)$ and a hydrogen atom located at an anti-bonding site (H_{AB}), which is bonded to the host atom $Si(2)$. The existence of the H_2^* defect in silicon was first suggested by Chang *et al* [9] on the basis of theoretical calculations and was subsequently confirmed by infrared spectroscopy [17]. As depicted in Fig. I.2, theory predicts that the silicon atom $Si(2)$ relaxes into an almost planar configuration with its three nearest neighbour silicon atoms, which clearly illustrates that a Si-H bond may induce considerable strain in the surrounding silicon lattice. Thus, the atomic configuration of a hydrogen-related point defect is a result of a delicate balance between the energy gained by chemical bonding and the increase in strain energy.

The fact that hydrogen forms strong bonds with silicon suggests that hydrogen may interact with dangling bonds at lattice imperfections. Indeed, it has been established that hydrogen saturates dangling bonds at surfaces [18] and at Si/SiO₂ interfaces [19], which generally removes the electronic levels associated with the dangling bond from the band gap and thus neutralises its electrical activity. Hydrogen-passivation of dangling bonds at Si/SiO₂ interfaces is presently used as a standard processing step in the fabrication of electronic devices [20].

Apart from interacting with existing defects, hydrogen also *induces* defects in crystalline silicon. It has been observed [21] that exposure of silicon to a remote hydrogen plasma leads to the formation of extended planar defects within ~ 100 nm of the surface. The defects, called *platelets*, are aligned with $\{111\}$ or $\{100\}$ crystallographic planes, and each platelet has a diameter of ~ 10 nm and contains ~ 350 hydrogen atoms bonded to silicon [21]. The microscopic structure of the platelets is at present not well understood.

It has also been established that hydrogen interacts with impurities in semiconductors. For example, hydrogen enhances the diffusion of oxygen in silicon at temperatures below 450°C, which e.g. leads to enhanced rates for formation of thermal donors in the presence of hydrogen [22,23]. The microscopic mechanism for hydrogen-enhanced diffusion of oxygen still remains to be explained. The binding of hydrogen at impurities often leads to drastic changes of their electronic properties. For example, hydrogen neutralises shallow acceptors [5,24] and donors [5,21], and the deep levels associated with transition metal impurities and thermal donors [5,25]. The microscopic properties of hydrogen-passivated shallow acceptors and donors in silicon have been studied extensively in the past decade, and the microstructure of these complexes is now well understood [5,26]. On the contrary, the level of understanding of the interaction between hydrogen and deep centres is at a much cruder stage. The electrical activity of hydrogen-passivated shallow and deep levels can be regenerated by annealing at temperatures around 200°C and 400°C,

respectively [5]. This has important technological implications: First, *unintentional* passivation of shallow dopants during device processing can be removed by annealing at relatively low temperatures. Second, the electrical deactivation is too thermally unstable to make hydrogen-passivation of deep levels useful for most practical applications.

The features of hydrogen in semiconductors mentioned above are primarily of fundamental interest. However, in recent years a process has been developed,

which uses hydrogen-induced exfoliation to transfer macroscopic layers of a semiconductor onto a supporting wafer [27]. The process, called Smart-Cut, consists of four steps, as illustrated in Fig. I.3:

1. Implantation with protons of a wafer A through a layer of insulating SiO_2 .
2. Hydrophilic bonding of the implanted face of wafer A to the handle wafer B.
3. Heating of the bonded sandwich structure at $\sim 500^\circ\text{C}$, which causes the implanted wafer A to split at the end-of-range, R_p , of the implanted protons.
4. Polishing of the layer of wafer A attached to the wafer B.

The outcome of the Smart-Cut process is a Silicon-On-Insulator (*SOI*) wafer consisting of the thin layer of wafer A separated from the handle wafer by a thin insulating layer of SiO_2 . The Smart-Cut process may lower the production cost of *SOI* wafers and make such wafers available for mass production [27]. The microscopic processes leading to the splitting of the wafer A are at present not well understood. However, recent studies of the process in silicon indicate that the heat treatment in the third step causes the implanted hydrogen to aggregate into platelets, which evolve into micro-cracks, and ultimately results in large-area splitting [28]. Hence, an improved understanding of the fundamental phenomena that determine the hydrogen-induced exfoliation, in particular the transition from point defects to platelets, may stimulate further refinements of the Smart-Cut process.

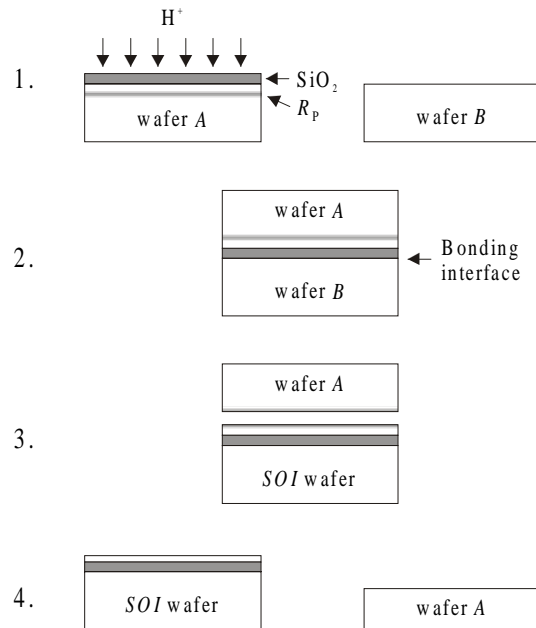
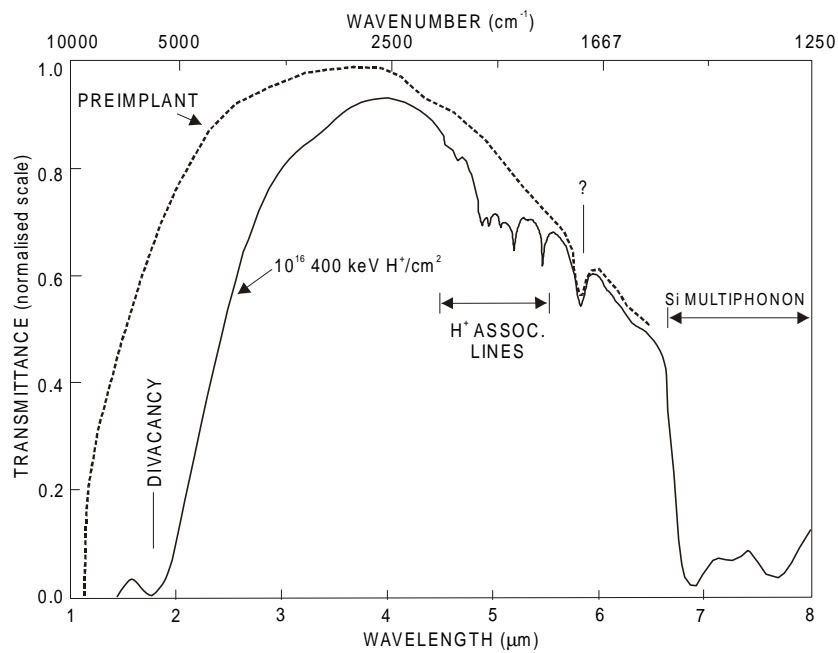


Fig. I.3. Principle of the Smart-Cut process. R_p indicated in the top part of the figure corresponds to the end-of-range of the implanted protons.

a)



b)

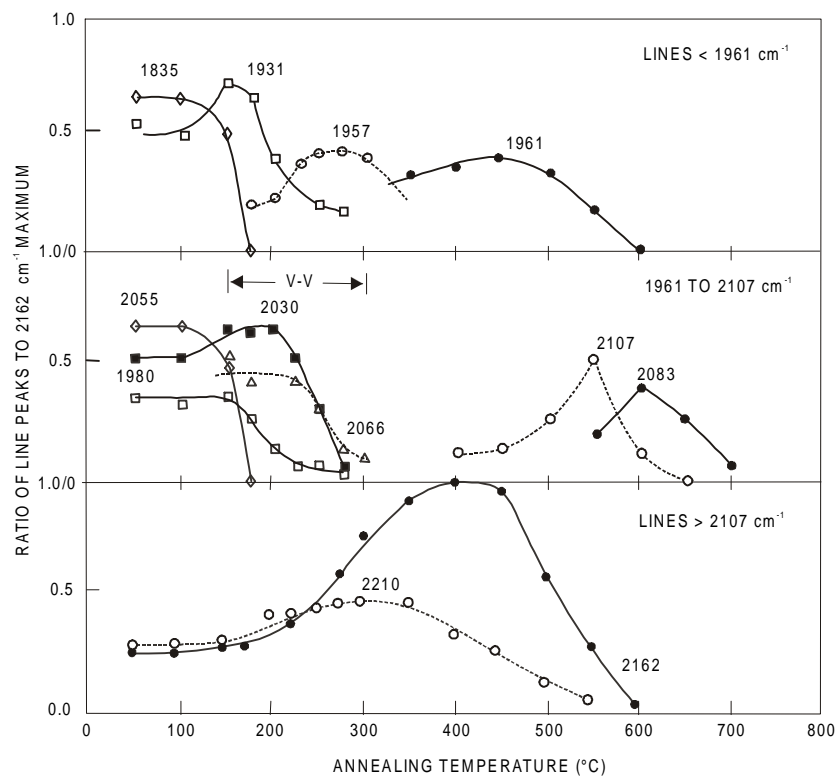


Fig. I.4. a) Transmittance of silicon (multiple internal reflection) before and after implantation of protons at room temperature. b) Isochronal annealing behaviour of the major Si-H bands. The figures are reproduced from Ref. [30]. The line frequencies given in the figure are those observed at room temperature. The lines at 1835, 2055, and 2210 cm^{-1} are observed at 1838, 2062, and 2223 cm^{-1} at ~ 10 K. The lines at 1980 and 2162 cm^{-1} split into two components at {1987, 1990} cm^{-1} and {2162, 2166} cm^{-1} , respectively, when the sample is cooled to ~ 10 K.

Vibrational excitation of Si-H bonds gives rise to absorption of light at distinct frequencies in the infrared part of the spectrum, which are characteristic of the bonding configuration. For instance, molecular SiH₄ has vibrational modes at 2187 and 2191 cm⁻¹ (see footnote 1) which primarily involve stretching of the Si-H bonds, together with modes at 914 and 975 cm⁻¹ associated with angular deformations of the molecule [29]. If deuterium is substituted for hydrogen to form SiD₄, the four vibrational modes shift down in frequency to 1558, 1597, 681, 700 cm⁻¹ [29], i.e. by a factor of $\sim\sqrt{2}$. Such isotopic shifts of infrared absorption lines unambiguously show that the lines originate from hydrogen-related vibrational modes.

In 1975, Stein [30] reported a pioneering infrared absorption study of crystalline silicon implanted with protons at room temperature. After implantation more than ten absorption lines were observed in the range 1800 – 2250 cm⁻¹ (see Fig. I.4.a). The lines shifted down in frequency by a factor of $\sim\sqrt{2}$ when deuterons were implanted instead of protons. Based on the observed isotopic shifts and the proximity of the lines to those of Si-H bonds in molecules, Stein assigned the lines to local vibrational stretch modes of Si-H bonds associated with hydrogen-decorated implantation-induced defects. No assignments to specific defects were made. The thermal stability of the defects giving rise to the absorption lines was studied by performing an isochronal annealing sequence. The annealing behaviour of the distinct absorption lines is shown in Fig. I.4.b, which also serves to list the frequencies of the absorption lines. Since the original work by Stein, a number of additional Si-H absorption lines have been observed in proton-implanted silicon [31,32] or silicon grown in a H₂ ambient and subsequently irradiated with electrons [33,34] or neutrons [35]. At present, more than 30 distinct absorption lines have been observed in the frequency region associated with Si-H stretch modes. In addition, a number of lines have been observed in the region 550 – 900 cm⁻¹, which are ascribed to angular vibrations of Si-H bonds [31,32].

In 1979, Stein [36] reported on the infrared absorption of silicon implanted with protons at ~ 80 K, which was kept at ~ 80 K between the implantation and the absorption measurements. In contrast to the rich spectrum observed after implantation at room temperature, implantation at ~ 80 K gives rise to a single dominant absorption line at 1990 cm⁻¹, as shown in Fig. I.5. The 1990-cm⁻¹ line disappeared upon annealing at ~ 150 K, and based on the annealing behaviour, Stein tentatively assigned the line to hydrogen trapped at a vacancy cluster.

¹ The photon energy associated with an infrared absorption line is in this thesis given in wave number units (cm⁻¹). The photon energy can be converted to eV by use of the relation 1 eV = 8065.48 cm⁻¹.

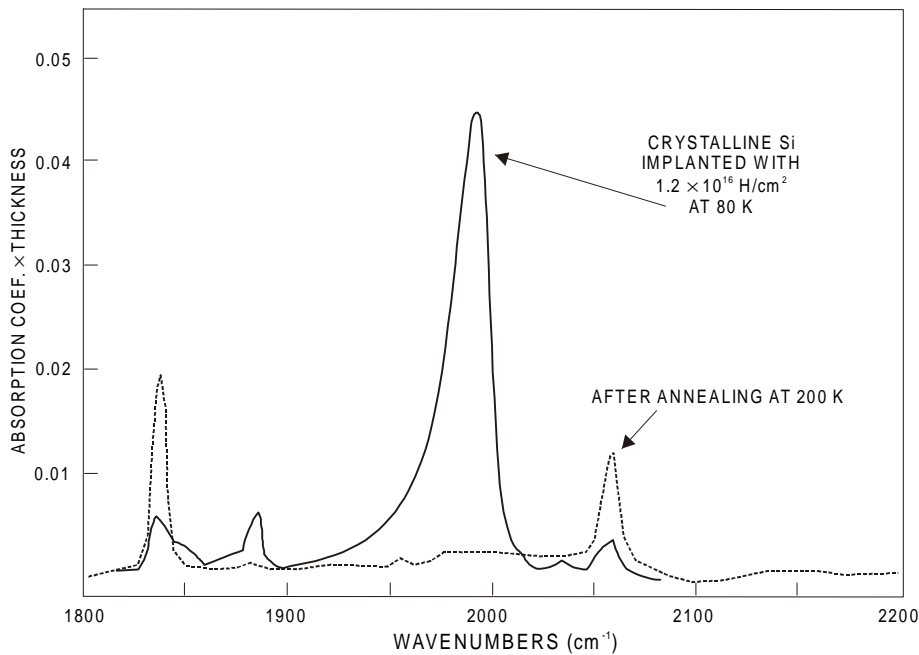


Fig. I.5. Absorption in the Si-H stretch region of silicon implanted with protons at ~ 80 K (solid line), and after annealing at 200 K (dashed line). The figure is reproduced from Ref. [36].

Several attempts have been made to assign the Si-H vibrational modes in silicon to specific hydrogen-related defects [17,37-44]. However, many of the assignments are conflicting and in 1994, when the present PhD project was initiated, only few of the lines had been assigned unambiguously [17]. The apparent lack of understanding of the Si-H vibrational spectrum is unfortunate, as it impedes the usage of infrared absorption spectroscopy as a probe for the microscopic structure of the defects, and as a means for monitoring the thermal evolution of hydrogen-related defects in proton-implanted silicon.

The objective of the work described in this thesis is to identify the defects giving rise to the most prominent infrared absorption lines in proton-implanted crystalline silicon. The identifications are based on the annealing behaviour of the lines, the isotopic shifts induced by full or partial isotope substitution, and on the symmetry of the pertinent defects deduced from uniaxial stress measurements.

In addition, the infrared absorption studies of hydrogen-related point defects are extended to proton-implanted germanium. Much less is known about hydrogen in germanium than in silicon. To my knowledge, the only existing infrared absorption study of hydrogen-related point defects in proton-implanted germanium was reported in 1987 by Tatarkiewicz *et al* [46]. The implantation of protons gave rise to seven absorption lines in the range $1750 - 2100 \text{ cm}^{-1}$, which shifted down in frequency by a factor of $\sim \sqrt{2}$ when deuterons were implanted instead of protons. Tatarkiewicz *et al*

assigned the absorption lines to local vibrational stretch modes of Ge-H bonds but no assignments to specific defects were made.

The chemical properties of silicon and germanium are very similar. Both elements crystallise in the diamond structure and form covalent bonds with hydrogen, which have similar lengths and

strengths (see Table I.1). Consequently, one would expect hydrogen to behave similarly in silicon and germanium; in particular that hydrogen forms the same types of defects in proton-implanted silicon and germanium. As shown in Table I.1, the strength of the Ge-H bond is somewhat smaller than the Si-H bond strength, which suggests that processes involving dissociation of Ge-H bonds occur at lower temperatures than similar processes for Si-H bonds. Only few comparable reports exist on hydrogen in silicon and germanium, but they indicate that hydrogen behaves differently in the two materials. Measurements of the thermal effusion of deuterium from plasma-treated material show that the total amount of deuterium incorporated during plasma treatment increases with increasing temperature for silicon, whereas it decreases in the case of germanium [47]. The passivation of shallow acceptors and donors by hydrogen is almost complete in silicon, whereas, in germanium, acceptors are only partly passivated [2], and there are no reports on successful hydrogen passivation of donors. However, the reduced hydrogen passivation in germanium may simply reflect lower thermal stabilities of hydrogen-dopant complexes, as suggested by the lower bond strength of Ge-H bonds as compared to Si-H bonds. In summary, it remains unclear whether hydrogen has significantly different properties in silicon and germanium.

The motivation for extending the infrared absorption studies to proton-implanted germanium is to identify hydrogen-related defects in this material and to study their microstructure. This might help to clarify whether hydrogen has similar properties in silicon and germanium. In addition, it may serve as a starting point for experimental studies of hydrogen-related defects in $\text{Si}_{1-x}\text{Ge}_x$ alloys.

Table I.1. Strength and length of selected chemical bonds.

Bond	Bond strength (eV)	Bond length (Å)
Si-Si ^a	2.32	2.35
Ge-Ge ^a	1.93	2.45
Si-H ^b	3.92	1.48
Ge-H ^b	3.59	1.53

^a The bond strength is derived from the cohesive energy [45].
^b SiH_4 or GeH_4 molecular compounds [29].

A. References

- [1] F.A. Cotton, G. Wilkinson, and P.L. Gaus, "Basic Inorganic Chemistry", (Wiley, New York, 1987).
- [2] S. J. Pearton, J. W. Corbett, and T. S. Shi, *Appl. Phys. A.*, **43**, 153 (1987).
- [3] "Hydrogen in semiconductors: semiconductors and semimetals", vol. 34, edited by J.I. Pankove and N.M. Johnson (Academic Press, New York, 1991).
- [4] S. M. Myers, M. I. Baskes, H. K. Birnbaum, J. W. Corbett, S. K. Estreicher, E. E. Haller, P. Jena, N. M. Johnson, R. Kirchheim, S. J. Pearton, and M. J. Stavola, *Rev. Mod. Phys.*, **64**, 559 (1992).
- [5] S. J. Pearton, J. W. Corbett, and M. Stavola, in "Hydrogen in crystalline semiconductors" (Springer-Verlag, Berlin, 1992).
- [6] S. K. Estreicher, *Mater. Sci. Eng. Rep.*, **14**, 319 (1995).
- [7] A. Van Weiringen, and N. Warmholz, *Physica*, **22**, 849 (1956).
- [8] T. Ichimiya and A. Furuichi, *Int. J. Appl. Radiat. Isot.* **19**, 573 (1968).
- [9] K. J. Chang and D. J. Chadi, *Phys. Rev. Lett.*, **62**, 937 (1989).
- [10] C. G. Van de Walle, Y. Bar-Yam, and S. T. Pantelides, *Phys. Rev. Lett.*, **60**, 2761 (1988).
- [11] Y. V. Gorelkinskii and N. N. Nevinnyi, *Physica B*, **170**, 155 (1991).
- [12] B. Holm, K. Bonde Nielsen, and B. Bech Nielsen, *Phys. Rev. Lett.*, **66**, 2360 (1991).
- [13] J. W. Corbett, S. N. Sahu, T. S. Shi, and L. C. Snyder, *Physics Letters A*, **93**, 303 (1983).
- [14] A. Mainwood, and A. M. Stoneham, *J. Phys. C*, **17**, 2513 (1984).
- [15] A. W. R. Leitch, V. Alex, and J. Weber, *Phys. Rev. Lett.*, **81**, 421 (1998).
- [16] R. E. Pritchard, M. J. Ashwin, J. H. Tucker, and R. C. Newman, *Phys. Rev. B*, **57**, 15048 (1998).
- [17] J. D. Holbeck, B. Bech Nielsen, R. Jones, P. Sitch, and S. Öberg, *Phys. Rev. Lett.*, **71**, 875 (1993).
- [18] Y. J. Chabal, *Physica B*, **170**, 447 (1991).
- [19] K. L. Brower, *Phys. Rev. B*, **38**, 9657 (1988); K. L. Brower, *Phys. Rev. B*, **42**, 3444 (1990).
- [20] A. Stesman and V. V. Afanas'ev, *Appl. Phys. Lett.*, **72**, 2271 (1998).
- [21] N. M. Johnson, chapter 7 in Ref. [3].
- [22] R. C. Newman and R. Jones, in "Oxygen in silicon: semiconductors and semimetals", vol. 42, edited by F. Shimura (Academic Press, San Diego, 1994).

- [23] S. A. McQuaid, M. J. Binns, C. A. Londros, J. H. Tucker, A. R. Brown, and R. C. Newman, *J. Appl. Phys.*, **77**, 1427 (1995).
- [24] J. I. Pankove, chapter 6 in Ref. [3].
- [25] S.J. Pearton, chapter 5 in Ref. [3].
- [26] M. Stavola and S.J. Pearton, chapter 8 in Ref. [3].
- [27] M. Bruel, B. Aspar, A.-J. Auberton-Hervé, *Jpn. J. Appl. Phys.*, **36**, 1636 (1997).
- [28] Y. J. Chabal and M. K. Weldon, *private communication*
- [29] "Handbook of Chemistry and Physics", 73rd ed. (CRC Press Inc., Boca Raton, 1992).
- [30] H. J. Stein, *J. Electron. Mater.*, **4**, 159 (1975).
- [31] N. N. Gerasimenko, M. Rollé, L. J. Cheng, Y. H. Lee, J. C. Corelli, and J. W. Corbett, *Phys. Stat. Sol. (b)*, **90**, 689 (1978).
- [32] B. N. Mukashev, K. H. Nussupov, and M. F. Tamendarov, *Physics Letters A*, **72**, 381 (1979).
- [33] G. R. Bai, M. W. Qi, L. M. Xie and T. S. Shi, *Solid State Communications*, **56**, 277 (1985).
- [34] T. S. Shi, L. M. Xie, G. R. Bai, and M. W. Qi, *Phys. Stat. Sol. (b)*, **131**, 511 (1985).
- [35] X. T. Meng, Y. C. Chang, and Y. D. Fan, *Phys. Stat. Sol. (a)*, **101**, 619 (1987).
- [36] H. J. Stein, *Phys. Rev. Lett.*, **43**, 1030 (1979).
- [37] T.S. Shi, S. N. Sahu, G. S. Oerhleim, A. Hiraki, and J. W. Corbett, *Phys. Stat. Sol. (a)*, **74**, 329 (1982).
- [38] B. N. Mukashev, K. H. Nussupov, M. F. Tamendarov, and V. V. Frolov, *Physics Letters A*, **87**, 376 (1982).
- [39] T. S. Shi, G. R. Bai, M. W. Qi, and J. K. Zhou, in "Defects in Semiconductors", edited by H. J. von Bardeleben, *Materials Science Forum* Vol. 10-12 (Trans Tech, Aedermannsdorf, 1986), p. 597.
- [40] G. R. Bai, J. K. Zhou, J. M. Chen, T. S. Shi, M. W. Qi, L. M. Xie, *Scienta Sinica (series A)*, **16**, 499 and 630 (1988).
- [41] B. Bech Nielsen, J. Olajos, and H.G. Grimmeiss, *Phys. Rev. B*, **39**, 3330 (1989).
- [42] B. Bech Nielsen, and H. G. Grimmeiss, *Phys. Rev. B*, **40**, 12403 (1989).
- [43] B. N. Mukashev, S. Z. Tokmoldin, and M. F. Tamendarov, in "Proceedings of the International Conference on Defect Control in Semiconductors, Yokohama, Japan, 1989", edited by K. Sumino, (North Holland, Amsterdam, 1990), p. 429.

- [44] L. M. Xie, M. W. Qi, and J. M. Chen, *J. Phys.: Condens. Matter*, **3**, 8519 (1991).
- [45] C. Kittel, "Introduction to Solid State Physics", (Wiley, New York, 1986).
- [46] J. Tatarkiewicz, A. Król, A. Breitschwerdt, and M. Cardona, *Phys. Stat. Sol. (b)*, **140**, 369 (1987).
- [47] M. Stutzmann, J.-B. Chevrier, C. P. Herrero, and A. Breitschwerdt, *Appl. Phys. A*, **53**, 47 (1991).

II. Introduction to local mode spectroscopy

This chapter gives a brief description of the basic properties of local vibrational modes and an introduction to studies of local vibrational modes by infrared absorption spectroscopy.

A. Basics of local vibrational modes

A light impurity in a crystalline host gives rise to vibrational modes corresponding to collective vibrations of the impurity and the surrounding atoms [1]. The modes are characterised by vibrational amplitudes, which fall off very rapidly with the distance from the defect core and are therefore called *local vibrational modes*. The physical description of local vibrational modes closely resembles that of molecular vibrations [2], except that point defects do not have rotational degrees of freedom.

The vibrational motion is for each mode Γ described in terms of a normal coordinate Q_Γ , which specifies the atomic displacements of the atoms associated with the local mode. The normal coordinates have distinct symmetry properties and transform according to one of the symmetry species (irreducible representations) of the point group of the defect [2]. This property is used extensively throughout this thesis, as the symmetry species of a given local mode is used to label the mode.

A local vibrational mode interacts with light by absorption and Raman scattering [2]. In the present context only the absorption process will be discussed. The infrared absorption measurements presented in this thesis were carried out at a sample temperature below 100 K, at which the population of excited states of the hydrogen-related local vibrational modes is negligible. Hence, the initial state in the absorption process is always the total-symmetric vibrational ground state $|A,0\rangle$. The final state is denoted $|\Gamma, \nu\rangle$, where Γ is the symmetry species of the state and ν is the sum of local mode vibrational quantum numbers. The probability of a light-induced transition from the initial state $|A,0\rangle$ to the excited state $|\Gamma, \nu\rangle$ is in the electric dipole approximation proportional to

$$\left| \vec{\epsilon} \cdot \langle A,0 | \vec{d} | \Gamma, \nu \rangle \right|^2, \quad (\text{II.1})$$

where $\vec{\epsilon}$ is the electric polarisation vector of the light and \vec{d} is the electric dipole moment of the defect. The rigorous selection rule for vibrational transitions states that the transition matrix element $\langle A,0 | \vec{d} | \Gamma, \nu \rangle$, and thus the transition probability, is zero unless one of the symmetry species of the dipole moment is equal to the symmetry species Γ of the final state [2]. The symmetry species of the dipole moment are typically given in the character tables of the point groups [2]. An alternative and less mathematical version of this selection rule states that the transition probability is non-zero only if the vibrational mode induces a dipole moment of the defect. In the present

thesis the term ‘‘infrared active’’ is used for local modes, which may have non-zero transition probability according to the rigorous selection rule. For example, inspection of the character table reveals that in the case of a defect with D_{3d} symmetry, only the A_{2u} and E_u modes are infrared active, whereas transitions to A_{1g} , A_{1u} , A_{2g} and E_g states are forbidden [2].

The description of vibrations in terms of normal modes is based on the harmonic approximation, which assumes that the motion of the atoms is determined by a potential given as a quadratic form in the displacement coordinates of the atoms. In this approximation, the energy levels and wavefunctions of each normal mode are those of a harmonic oscillator in the normal coordinate Q_Γ with frequency ω_Γ [2]. In the harmonic approximation only fundamental transitions, i.e. transitions corresponding to the excitation of just one normal mode Γ from the ground state to its first excited state, have non-zero transition probability. The absorption strength associated with the fundamental transition $|A_1, 0\rangle \rightarrow |\Gamma, 1\rangle$ can be expressed as [4]

$$\int_{\text{line } \Gamma} \alpha(\sigma) d\sigma = \frac{g_\Gamma \pi N e^2 \eta_\Gamma^2}{3n c^2 \mu}, \quad (\text{II.2})$$

where $\alpha(l)$ is the absorption coefficient, g_Γ the degeneracy of the mode Γ , N the density of defects, n the refractive index of the host material, c the speed of light in vacuum, and e is the elementary charge. The ratio $e\eta_\Gamma/\sqrt{\mu}$ is the derivative of the dipole moment of the defect with respect to the normal coordinate Q_Γ . An infrared absorption experiment typically allows one to determine the intensity of the absorption line, i.e. the area under the absorption peak. The intensity is related to the integral of the absorption coefficient, as discussed in Sec. III.B.2, and if the degeneracy of the mode and the area density of defects is known, the ratio η_Γ^2/μ can be deduced. This quantity is characteristic for the mode and depends on e.g. the structure and the charge state of the defect.

The ratio η_Γ^2/μ is introduced in the first place because it is a custom in the literature to interpret the absorption strength of the mode in terms of the effective charge η_Γ , which may be regarded as the oscillating charge (in elementary charge units) of a linear dipole with reduced mass μ which gives rise to the measured absorption strength per defect. The reduced mass is generally not known, but may be expressed as [5]

$$\mu^{-1} = M_{\text{imp}}^{-1} + (\chi M_{\text{host}})^{-1}, \quad (\text{II.3})$$

where M_{host} and M_{imp} are the atomic masses of host and impurity atoms, and χ is a parameter which represents the coupling of the vibrating entity to the crystalline host. The χ parameter depends on the structure of the defect but is presumably close to unity for hydrogen-related local modes in silicon and germanium. For example,

$\chi \cong 1.7$ for the stretch mode of the hydrogen-saturated vacancy in silicon [6], and in the case of the Si-H complex in GaAs $\chi \cong 2.7$ [7]. Due to the small mass of hydrogen compared to silicon and germanium, the results obtained by use of Eq. II.3 are quite insensitive to the exact value of χ . In the present thesis, it is assumed that $\chi = 1$.

As mentioned above, the concept of normal modes is based on the harmonic approximation. In practise, the potential determining the atomic motion is not truly harmonic and the presence of anharmonic terms has several important implications. For example, anharmonicity may give rise to weak overtones and combination bands in the infrared absorption spectra, which correspond to, respectively, excitation of a local mode from the ground state by more than one quantum number ($\Delta v_{\Gamma} > 1$) and to the simultaneous excitation of two local modes of the same defect ($\Delta v_{\Gamma} > 0$ and $\Delta v_{\Gamma'} > 0$). Moreover, anharmonicity shifts the energy levels of the local modes away from the equispaced levels $E_{v_{\Gamma}} = \hbar\omega_{\Gamma}(v_{\Gamma} + \frac{1}{2})$ of the harmonic oscillator, and causes the level separation $E_{v_{\Gamma}+1} - E_{v_{\Gamma}}$ to decrease with increasing v_{Γ} .

The frequency and width of an infrared absorption line associated with a local vibrational mode generally depend on the sample temperature at which the measurement is carried out [8,9]. The frequency of a Si-H or Ge-H local mode is typically $\sim 10 \text{ cm}^{-1}$ higher at liquid helium temperature than at room temperature. The frequencies given throughout this thesis are those observed at $\sim 10 \text{ K}$. The width the absorption lines generally decreases with decreasing temperature. Hence, measurements at the lowest possible temperature quite generally result in the best resolution of close lines and the best signal-to-noise ratio of the spectrum. The measurements reported in this thesis were performed at either $\sim 10 \text{ K}$ or $\sim 80 \text{ K}$, where the intrinsic width of the Si-H and Ge-H lines are $\sim 1 \text{ cm}^{-1}$.

B. Correlation of absorption lines

The number of absorption lines associated with a particular defect depends on the number of impurity atoms contained in the defect and the defect symmetry. Hence, it is crucial to defect studies to establish whether different lines in the spectra originate from the same defect. The minimum criterion for assigning lines to the same defect is that the lines are observed with the same relative intensities independent of the history of the sample. In this thesis, the correlation of absorption lines is studied by isochronal annealing, where the sample is heated to various annealing temperatures for a fixed period of time. Between the individual annealing steps the sample is cooled to the relevant measuring temperature and the infrared absorbance spectrum is measured.

C. Isotope substitution

Hydrogen is the only element in the periodic table with isotopes that differ in mass by a factor of two. The large relative difference in mass of the two isotopes makes hydrogen extremely well suited for isotope substitution experiments. In the harmonic approximation, the vibrational mode frequency of a single bond is

$$\omega = \sqrt{\frac{K}{\mu}} \quad , \quad (\text{II.4})$$

where K is the appropriate force constant and μ is the reduced mass of the vibrating entity. When deuterium is substituted for hydrogen, the vibrational frequency shifts according to Eqs. II.3 and II.4, and the ratio of the frequencies is given by

$$\frac{\omega_D}{\omega_H} = \sqrt{\frac{\mu_H}{\mu_D}} \cong \sqrt{\frac{1}{2}} \quad . \quad (\text{II.5})$$

The isotopic shift given in Eq. II.5 is characteristic for a hydrogen-related local vibrational mode, and is used to establish whether infrared absorption lines originate from such modes. In practise, the observed shifts differ slightly from the expression given in Eq. II.5 because of anharmonicity [8].

Information on the number of hydrogen atoms contained in a defect and whether the hydrogen atoms are equivalent or inequivalent can be obtained from partial substitution of hydrogen with deuterium. To illustrate this, let us consider a defect (H_1H_2) with two *inequivalent* hydrogen atoms bonded to silicon, which has two distinct Si-H stretch modes and gives rise to two absorption lines. In a sample containing deuterium instead of hydrogen the defect D_1D_2 exists, and two distinct Si-D stretch modes are observed. If both hydrogen and deuterium is present in the sample, two isotopically mixed defects H_1D_2 and D_1H_2 coexist with the two isotopically “pure” defects. The defects H_1D_2 and D_1H_2 each have one Si-H and one Si-D stretch mode. In total, the four isotopic configurations of the defect have four Si-H and four Si-D stretch modes and, consequently, such a defect can at most give rise to four absorption lines in the Si-H stretch region and four lines in the Si-D stretch region.¹ If we instead consider a defect with two *equivalent* hydrogen atoms (HH) and two distinct Si-H stretch modes, the isotopically mixed defects HD and DH cannot be distinguished. Hence, the Si-H (and Si-D) modes of the HD and DH defects are degenerate, and only three absorption lines are observed in the Si-H stretch region, together with three lines in the Si-D stretch region. According to this example,

¹ The assignment of absorption lines to the same defect is typically based on isochronal annealing studies as described in the previous subsection.

the number of absorption lines in a sample that contains both hydrogen and deuterium depends on whether the hydrogen atoms are equivalent or inequivalent and, consequently, partial isotope substitution may be used to distinguish between the two types of defects.

In practise, some of the modes of the various isotopic configurations of the defect may accidentally be degenerate or the absorption lines may be too weak to be observed. The number of lines observed might therefore be less than the number of modes, and the interpretation of a partial isotope substitution experiment is normally not unambiguous. For example, the observation of four Si-H and four Si-D modes of the same defect in a sample containing both hydrogen and deuterium does exclude that the defect contains a single or two equivalent hydrogen atoms, but it does not rule out that it contains more than two hydrogen atoms.

D. Uniaxial stress

When uniaxial stress is applied to a crystal, the quantum states of the system are perturbed. Since the energies of two different states normally change differently, the frequency corresponding to an optical transition between the two states quite generally shifts as a function of the magnitude of the stress. For a non-cubic defect in silicon or germanium, a number of different orientations of the defect exist. In the absence of stress all orientations are equivalent and, hence, for a given transition a single absorption line is observed. In the presence of uniaxial stress, the frequency shift of the transition depends on the orientation of the defect with respect to the stress-direction. Consequently, the uniaxial stress will cause the single absorption line to split into a specific number of components determined by the symmetry of the defect and the stress direction. In the case of transitions involving degenerate states, additional splittings may occur due to the lifting of this degeneracy by the stress perturbation.

To illustrate the basic concepts of the uniaxial stress perturbation technique, let us consider the stress-response of an absorption line associated with an $A_{1g} \rightarrow A_{2u}$ transition of a defect with D_{3d} symmetry.² This could for example be the fundamental transition of the stretch mode of a hydrogen atom located at the BC site in silicon or germanium. As shown in Fig. II.1, four different orientations of the defect exist, which are characterised by having their primary axis directed along either the $[111]$, $[1\bar{1}\bar{1}]$, $[\bar{1}1\bar{1}]$, or $[\bar{1}\bar{1}1]$ axis of the crystal. The four orientations are indicated with an index b , where $b \in \{1, 2, 3, 4\}$. For uniaxial stress applied along the $[100]$ direction ($\vec{F} // [100]$), all four defect orientations have the same angle between their

² Both the initial and final state is non-degenerate. Hence, the present example only illustrates the reduction in *orientational* degeneracy induced by uniaxial stress.

primary axis and the stress direction. Consequently, they remain equivalent and no splitting of the absorption line occurs. For $\vec{F} // [111]$ the defect $b = 1$ is perturbed differently than the defects $b \in \{2, 3, 4\}$, which in turn are equivalent. Hence, the absorption line splits into two components for [111] stress. Uniaxial stress applied along [110] also splits the absorption line into two components, as the stress divides the defects into two groups $b \in \{1, 4\}$ and $b \in \{2, 3\}$.

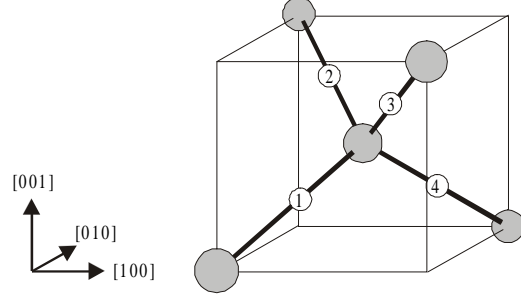


Fig. II.1. Orientations of a centre with D_{3d} symmetry in silicon and germanium.

The qualitative considerations made above are useful for illustrational purposes. However, to fully exploit the potential of the uniaxial stress technique, a quantitative treatment of the stress-induced frequency shift is required. Following Kaplyanskii [10], the frequency shift induced by uniaxial stress along the $[hkl]$ direction can for each of the four defect orientations be expanded to first order in the components $\sigma_{ij}^{[hkl]}$ of the stress tensor:

$$\Delta\omega_b^{[hkl]} = \sum_{i,j=1}^3 \mathcal{C}_{ij}^{(b)} \sigma_{ij}^{[hkl]}. \quad (\text{II.6})$$

The expansion coefficients $\mathcal{C}_{ij}^{(b)}$, $i, j \in \{1, 2, 3\}$, define a symmetric second-rank tensor $\mathcal{C}^{(b)}$ called the *piezo-spectroscopic tensor* [10], and the stress tensor $\sigma^{[hkl]}$ corresponding to a uniaxial stress of magnitude σ applied along the direction $[hkl]$ is given by

$$\sigma^{[hkl]} = \frac{\sigma}{h^2 + k^2 + l^2} \begin{Bmatrix} h^2 & hk & hl \\ hk & k^2 & kl \\ hl & kl & l^2 \end{Bmatrix}. \quad (\text{II.7})$$

The symmetry of the defect imposes certain restrictions on the components of the piezo-spectroscopic tensors. For example, the fact that the defect $b = 1$ is invariant under a 120° rotation about [111] implies that $\mathcal{C}_{11}^{(1)} = \mathcal{C}_{22}^{(1)} = \mathcal{C}_{33}^{(1)}$ and $\mathcal{C}_{12}^{(1)} = \mathcal{C}_{13}^{(1)} = \mathcal{C}_{23}^{(1)}$, and, hence, the stress-response of the defect is determined by only two parameters $\mathcal{C}_1 \equiv \mathcal{C}_{11}^{(1)}$ and $\mathcal{C}_2 \equiv \mathcal{C}_{12}^{(1)}$. The defect orientations $b \in \{2, 3, 4\}$ can be generated from the defect $b = 1$ by 180° rotations about [100], [010], and [001] directions. Consequently, the piezo-spectroscopic tensors $\mathcal{C}^{(2)}$, $\mathcal{C}^{(3)}$, and $\mathcal{C}^{(4)}$ of these defects can be derived from $\mathcal{C}^{(1)}$ by use of the relations.

$$\begin{aligned}
 \mathcal{A}^{(2)} &= C_2^{[100]} \mathcal{A}^{(1)} C_2^{[100]}, \\
 \mathcal{A}^{(3)} &= C_2^{[010]} \mathcal{A}^{(1)} C_2^{[010]}, \\
 \mathcal{A}^{(4)} &= C_2^{[001]} \mathcal{A}^{(1)} C_2^{[001]},
 \end{aligned} \tag{II.8}$$

where $C_2^{[hkl]}$ is the 3×3 matrix representing a 180° rotation about the $[hkl]$ axis. If Eq. II.8 is inserted into Eq. II.6, the following frequency shifts are obtained for the four defect orientations:

$$\begin{aligned}
 \Delta\omega_1^{[hkl]} &= \mathcal{A}_1 \left\{ \sigma_{11}^{[hkl]} + \sigma_{22}^{[hkl]} + \sigma_{33}^{[hkl]} \right\} + 2\mathcal{A}_2 \left\{ \sigma_{12}^{[hkl]} + \sigma_{13}^{[hkl]} + \sigma_{23}^{[hkl]} \right\}, \\
 \Delta\omega_2^{[hkl]} &= \mathcal{A}_1 \left\{ \sigma_{11}^{[hkl]} + \sigma_{22}^{[hkl]} + \sigma_{33}^{[hkl]} \right\} + 2\mathcal{A}_2 \left\{ -\sigma_{12}^{[hkl]} - \sigma_{13}^{[hkl]} + \sigma_{23}^{[hkl]} \right\}, \\
 \Delta\omega_3^{[hkl]} &= \mathcal{A}_1 \left\{ \sigma_{11}^{[hkl]} + \sigma_{22}^{[hkl]} + \sigma_{33}^{[hkl]} \right\} + 2\mathcal{A}_2 \left\{ -\sigma_{12}^{[hkl]} + \sigma_{13}^{[hkl]} - \sigma_{23}^{[hkl]} \right\}, \\
 \Delta\omega_4^{[hkl]} &= \mathcal{A}_1 \left\{ \sigma_{11}^{[hkl]} + \sigma_{22}^{[hkl]} + \sigma_{33}^{[hkl]} \right\} + 2\mathcal{A}_2 \left\{ \sigma_{12}^{[hkl]} - \sigma_{13}^{[hkl]} - \sigma_{23}^{[hkl]} \right\}.
 \end{aligned} \tag{II.9}$$

The splitting-pattern obtained from Eq. II.9 for uniaxial stresses applied along $[100]$, $[111]$, and $[110]$ are given in Table II.1. The absorption line is found not to split for $\vec{F} \parallel [100]$ and to split into two components for $\vec{F} \parallel [111]$ and $[110]$, consistent with the qualitative considerations given above. In addition, Table II.1 shows that the stress-induced frequency shifts for all three stress-directions can be described in terms of the two piezo-spectroscopic parameters \mathcal{A}_1 and \mathcal{A}_2 . The intensity of each of the stress-split components is proportional to

$$\sum_b \left| \vec{\epsilon} \cdot \vec{d}_b \right|^2, \tag{II.10}$$

where $\vec{\epsilon}$ is the electric polarisation vector, \vec{d}_b is a unit vector defining the direction of the dipole moment for the defect orientation b , and the sum extends over those defect orientation, which contribute to the particular stress-split component. The dipole moment associated with an A_{2u} mode of a defect with D_{3d} symmetry is parallel to the

Table II.1. Stress-pattern of an $A_{1g} \rightarrow A_{2u}$ transition of a defect with D_{3d} symmetry for uniaxial stresses applied along $[100]$, $[111]$, and $[110]$. The second column gives the defect orientations (see Fig. II.1) contributing to the individual splitting components. The third column lists the frequency shifts of the components obtained from Eq. II.9. The columns titled I_{\parallel} and I_{\perp} contain the relative intensities calculated from Eq. II.10 for light polarised parallel and perpendicular to the stress direction, whereas the columns $I_{[hkl]}$ give the intensities calculated for light polarised along $[hkl]$.

\vec{F}	b	$\Delta\omega_b^{[hkl]}$	I_{\parallel}	I_{\perp}
$[100]$	1, 2, 3, 4	$\mathcal{A}_1 \sigma$	4/3	4/3
$[111]$	1	$(\mathcal{A}_1 + 2\mathcal{A}_2) \sigma$	1	0
	2, 3, 4	$(\mathcal{A}_1 - 2/3\mathcal{A}_2) \sigma$	1/3	4/3
$[110]$	1, 4	$(\mathcal{A}_1 + \mathcal{A}_2) \sigma$	$I_{[110]}$	$I_{[001]}$
	2, 3	$(\mathcal{A}_1 - \mathcal{A}_2) \sigma$	4/3	2/3
			0	$I_{[\bar{1}\bar{0}]}$
			0	2/3
				4/3

primary axis of the defect. Hence, the relative intensities of the stress-split components can be calculated for a given polarisation $\bar{\mathbf{e}}$ and a given relative population of the four defect orientations. If the defects of interest are formed in the absence of uniaxial stress, they are normally randomly oriented, i.e. the four defect orientations are equally populated. The relative intensities of such a distribution of defects is given in Table II.1 for light polarised parallel and perpendicular to the applied stress.³

The splitting-pattern given in Table II.1 is based on the assumption that the defects are invariant under a 120° rotation about one of the $\langle 111 \rangle$ directions, whereas the basis for the relative intensities is that the dipole moments of the transitions are parallel to $\langle 111 \rangle$ directions. These are not unique features of an $A_{1g} \rightarrow A_{2u}$ transition of a defect with D_{3d} symmetry. In fact, the stress-pattern given in Table II.1 also applies for the excitation of a non-degenerate mode of defects with S_6 , D_3 , C_{3v} , and C_3 symmetry [10], and it is therefore virtually impossible to determine the point group of the defect on the basis of uniaxial stress measurements alone. Instead, uniaxial stress experiments determine the crystallographic system [11] of the defect, as shown in Table II.2. For example, the point groups D_{3d} , S_6 , D_3 , C_{3v} , and C_3 all belong to the trigonal system, and an absorption line which exhibits a stress-pattern consistent with that given in Table II.1 is said to originate from an $A \rightarrow A$ transition of a defect with trigonal symmetry.

Table II.2. Restrictions imposed by symmetry on the components of the second-rank piezo-spectroscopic tensor \mathcal{A} in the basis defined by the $\langle 100 \rangle$ vectors of the cubic lattice [10]. The point groups that have identical symmetry restrictions define the crystallographic systems given in the first column.

System	Point group	Restrictions on tensor components
Cubic	T_d, T	$\mathcal{A}_{11} = \mathcal{A}_{22} = \mathcal{A}_{33}; \mathcal{A}_{12} = \mathcal{A}_{13} = \mathcal{A}_{23} = 0$
Tetragonal	S_4, D_{2d}	$\mathcal{A}_{11} = \mathcal{A}_{22}; \mathcal{A}_{12} = \mathcal{A}_{13} = \mathcal{A}_{23} = 0$
Trigonal	$D_{3d}, S_6, D_3, C_{3v}, C_3$	$\mathcal{A}_{11} = \mathcal{A}_{22} = \mathcal{A}_{33}; \mathcal{A}_{12} = \mathcal{A}_{13} = \mathcal{A}_{23}$
Orthorhombic-I	C_{2v}	$\mathcal{A}_{11} = \mathcal{A}_{22}; \mathcal{A}_{13} = \mathcal{A}_{23} = 0$
Orthorhombic-II	D_2	$\mathcal{A}_{12} = \mathcal{A}_{13} = \mathcal{A}_{23} = 0$
Monoclinic-I ^a	C_2, C_{1h}, C_{2h}	$\mathcal{A}_{11} = \mathcal{A}_{22}; \mathcal{A}_{13} = \mathcal{A}_{23}$
Monoclinic-II ^b	C_2	$\mathcal{A}_{13} = \mathcal{A}_{23} = 0$
Triclinic	C_1, S_2	<i>none</i>

^a C_{1h} : the mirror plane is a $\{110\}$ plane; C_2, C_{2h} : the C_2 axis is parallel to $\langle 110 \rangle$.
^b The C_2 axis is parallel to $\langle 100 \rangle$.

³ The relative intensities of the split-components for $[100]$ and $[111]$ stress are identical for all polarisations perpendicular to the stress direction. For $[110]$ stress, however, the crystal becomes biaxial and the particular direction of polarisation perpendicular to the applied stress has to be specified. Normally, two different stress-patterns for $\vec{F} // [110]$ are considered, namely those with $\bar{\mathbf{e}} // \vec{F}$ and $\bar{\mathbf{e}} // [001]$ and $[1-10]$.

The derivation of the stress-induced frequency shifts and the relative intensities of the splitting components given above can be generalised to excitations of non-degenerate modes of defects with tetragonal [10], orthorhombic [10], monoclinic [10,12,13], and triclinic symmetry [10], and to degenerate modes of defects with cubic [14], tetragonal [15], and trigonal [15] symmetry. The theoretical stress-patterns are summarised in Table II.3.

Table II.3. Stress-pattern of infrared active transitions of point defects in a diamond lattice. The point groups associated with the various crystallographic systems are given in Table II.2. The columns titled $\Delta\omega_{[hkl]}/\sigma$ give the frequency shift per unit stress applied along the direction $[hkl]$. The columns $I_{//}$, I_{\perp} , $I_{[hkl]}$ contain the relative intensities of the stress-split components for light with the electric field polarised parallel to the stress, perpendicular to the stress, and parallel to $[hkl]$, respectively. The intensity at zero stress is normalised to unity.

System	Mode	$\vec{F} // [100]$			$\vec{F} // [111]$			$\vec{F} // [110]$			
		$\Delta\omega_{[100]}/\sigma$	$I_{//}$	I_{\perp}	$\Delta\omega_{[111]}/\sigma$	$I_{//}$	I_{\perp}	$\Delta\omega_{[110]}/\sigma$	$I_{[110]}$	$I_{[001]}$	$I_{[1-10]}$
Cubic Ref. [14]	T	$(C\mathcal{A} - C\mathcal{B})$	0	1	$(C\mathcal{A} - \alpha C\mathcal{E})$	0	1	$(C\mathcal{A} + \frac{1}{2} C\mathcal{B} + \frac{1}{2} C\mathcal{E})$	1	0	0
		$(C\mathcal{A} + 2C\mathcal{B})$	1	0	$(C\mathcal{A} + \beta C\mathcal{E})$	1	0	$(C\mathcal{A} + \frac{1}{2} C\mathcal{B} - \frac{1}{2} C\mathcal{E})$	0	0	1
Tetragonal Refs. [10,15]	B	$C\mathcal{A}_1$	1	0	$\alpha (C\mathcal{A}_1 + 2 C\mathcal{A}_2)$	1	1	$\frac{1}{2} (C\mathcal{A}_1 + C\mathcal{A}_2)$	1	0	1
		$C\mathcal{A}_2$	0	1				$C\mathcal{A}_2$	0	1	0
	E	$C\mathcal{A}_1$	0	$\frac{1}{2}$	$\alpha (C\mathcal{A}_1 + 2 C\mathcal{A}_2 + C\mathcal{E})$	1	$\frac{1}{4}$	$\frac{1}{2} (C\mathcal{A}_1 + C\mathcal{A}_2 + C\mathcal{B})$	0	1	0
		$(C\mathcal{A}_2 + C\mathcal{B})$	0	$\frac{1}{2}$	$\alpha (C\mathcal{A}_1 + 2 C\mathcal{A}_2 - C\mathcal{E})$	0	$\frac{3}{4}$	$\frac{1}{2} (C\mathcal{A}_1 + C\mathcal{A}_2 - C\mathcal{B})$	$\frac{1}{2}$	0	$\frac{1}{2}$
Trigonal Refs. [10,15]	A	$C\mathcal{A}_1$	1	1	$(C\mathcal{A}_1 + 2 C\mathcal{A}_2)$	$\frac{3}{4}$	0	$(C\mathcal{A}_1 + C\mathcal{A}_2)$	1	$\frac{1}{2}$	0
		$(C\mathcal{A}_1 - \beta C\mathcal{A}_2)$			$(C\mathcal{A}_1 - \beta C\mathcal{A}_2)$	$\frac{1}{4}$	1	$(C\mathcal{A}_1 - C\mathcal{A}_2)$	0	$\frac{1}{2}$	1
	E	$(C\mathcal{A}_1 - 2C\mathcal{B})$	1	$\frac{1}{4}$	$(C\mathcal{A}_1 + 2 C\mathcal{A}_2)$	0	δ	$(C\mathcal{A}_1 + C\mathcal{A}_2 - C\mathcal{B} + C\mathcal{E})$	0	0	$\frac{3}{4}$
		$(C\mathcal{A}_1 + 2C\mathcal{B})$	0	$\frac{3}{4}$	$(C\mathcal{A}_1 - \beta C\mathcal{A}_2 - \frac{4}{3} C\mathcal{E})$	1	$\frac{1}{16}$	$(C\mathcal{A}_1 + C\mathcal{A}_2 + C\mathcal{B} - C\mathcal{E})$	$\frac{1}{4}$	$\frac{1}{2}$	0
Orthorhombic-I Ref. [10]	A ₁	$C\mathcal{A}_2$	0	1	$\alpha (C\mathcal{A}_1 + 2 C\mathcal{A}_2 + 2 C\mathcal{A}_3)$	$\frac{1}{2}$	$\frac{1}{2}$	$(C\mathcal{A}_2 + C\mathcal{A}_3)$	0	$\frac{1}{2}$	0
		$C\mathcal{A}_1$	1	0	$\alpha (C\mathcal{A}_1 + 2 C\mathcal{A}_2 - 2 C\mathcal{A}_3)$	$\frac{1}{2}$	$\frac{1}{2}$	$\frac{1}{2} (C\mathcal{A}_1 + C\mathcal{A}_2)$	1	0	1
	B ₁	$C\mathcal{A}_2$	1	$\frac{1}{2}$	$\alpha (C\mathcal{A}_1 + 2 C\mathcal{A}_2 + 2 C\mathcal{A}_3)$	1	$\frac{1}{4}$	$(C\mathcal{A}_2 + C\mathcal{A}_3)$	$\frac{1}{2}$	0	0
		$C\mathcal{A}_1$	0	$\frac{1}{2}$	$\alpha (C\mathcal{A}_1 + 2 C\mathcal{A}_2 - 2 C\mathcal{A}_3)$	0	$\frac{3}{4}$	$\frac{1}{2} (C\mathcal{A}_1 + C\mathcal{A}_2)$	$\frac{1}{2}$	1	$\frac{1}{2}$
							$(C\mathcal{A}_2 - C\mathcal{A}_3)$	0	0	$\frac{1}{2}$	

Table II.3. (Continued) Stress-pattern of infrared active transitions of point defects in a diamond lattice. The point groups associated with the various crystallographic systems are given in Table II.2. The columns titled $\Delta\omega_{[hkl]}/\sigma$ give the frequency shift per unit stress applied along the direction $[hkl]$. The columns $I_{//}$, I_{\perp} , $I_{[hkl]}$ contain the relative intensities of the stress-split components for light with the electric field polarised parallel to the stress, perpendicular to the stress, and parallel to $[hkl]$, respectively. The intensity at zero stress is normalised to unity. s_{φ} and c_{φ} are abbreviations for $\sin[\varphi]$ and $\cos[\varphi]$.

System	Mode	$\vec{F} // [100]$			$\vec{F} // [111]$			$\vec{F} // [110]$			
		$\Delta\omega_{[100]}/\sigma$	$I_{//}$	I_{\perp}	$\Delta\omega_{[111]}/\sigma$	$I_{//}$	I_{\perp}	$\Delta\omega_{[110]}/\sigma$	$I_{[110]}$	$I_{[001]}$	$I_{[1-10]}$
Orthorhombic-II Ref. [10]	B	$c_{\mathcal{A}1}$	0	$\frac{1}{2}$	$\alpha (c_{\mathcal{A}1} + c_{\mathcal{A}2} + c_{\mathcal{A}3})$	1	1	$\frac{1}{2} (c_{\mathcal{A}1} + c_{\mathcal{A}2})$	$\frac{1}{2}$	0	$\frac{1}{2}$
		$c_{\mathcal{A}2}$	1	0				$\frac{1}{2} (c_{\mathcal{A}1} + c_{\mathcal{A}3})$	0	1	0
		$c_{\mathcal{A}3}$	0	$\frac{1}{2}$				$\frac{1}{2} (c_{\mathcal{A}2} + c_{\mathcal{A}3})$	$\frac{1}{2}$	0	$\frac{1}{2}$
Monoclinic-I Ref. [12]	A	$c_{\mathcal{A}1}$	c_{φ}^2	$\frac{1}{2} s_{\varphi}^2$	$\alpha (c_{\mathcal{A}1} + 2c_{\mathcal{A}2} + 2c_{\mathcal{A}3})$	$\frac{1}{2} c_{\varphi}^2$	$\frac{1}{4} (2 + s_{\varphi}^2)$	$\frac{1}{2} (c_{\mathcal{A}1} + c_{\mathcal{A}2} + 2c_{\mathcal{A}4})$	$\frac{1}{4} (1 + c_{\varphi}^2 + \sqrt{2} s_{2\varphi})$	$\frac{1}{2} s_{\varphi}^2$	$\frac{1}{4} (1 + c_{\varphi}^2 - \sqrt{2} s_{2\varphi})$
		$c_{\mathcal{A}2}$	s_{φ}^2	$\frac{1}{2} (1 + c_{\varphi}^2)$	$\alpha (c_{\mathcal{A}1} + 2c_{\mathcal{A}2} - 2c_{\mathcal{A}3} + 4c_{\mathcal{A}4})$	$\frac{1}{4} (1 + s_{\varphi}^2 + \sqrt{2} s_{2\varphi})$	$\chi (1 + c_{\varphi}^2 - \sqrt{2} s_{2\varphi})$	$\frac{1}{2} (c_{\mathcal{A}2} - c_{\mathcal{A}3})$	$\frac{1}{2} s_{\varphi}^2$	$\frac{1}{2} c_{\varphi}^2$	0
					$\alpha (c_{\mathcal{A}1} + 2c_{\mathcal{A}2} - 2c_{\mathcal{A}3} - 4c_{\mathcal{A}4})$	$\frac{1}{4} (1 + s_{\varphi}^2 - \sqrt{2} s_{2\varphi})$	$\chi (1 + c_{\varphi}^2 + \sqrt{2} s_{2\varphi})$	$\frac{1}{2} (c_{\mathcal{A}1} + c_{\mathcal{A}2} - 2c_{\mathcal{A}4})$	$\frac{1}{4} (1 + c_{\varphi}^2 - \sqrt{2} s_{2\varphi})$	$\frac{1}{2} s_{\varphi}^2$	$\frac{1}{4} (1 + c_{\varphi}^2 + \sqrt{2} s_{2\varphi})$
Monoclinic-II Refs. [10,13]	A	$c_{\mathcal{A}1}$	1	0	$\alpha (c_{\mathcal{A}1} + c_{\mathcal{A}2} + c_{\mathcal{A}3} + 2c_{\mathcal{A}4})$	$\frac{1}{2}$	$\frac{1}{2}$	$\frac{1}{2} (c_{\mathcal{A}2} + c_{\mathcal{A}3} + 2c_{\mathcal{A}4})$	0	$\frac{1}{2}$	0
		$c_{\mathcal{A}2}$	0	$\frac{1}{2}$	$\alpha (c_{\mathcal{A}1} + c_{\mathcal{A}2} + c_{\mathcal{A}3} - 2c_{\mathcal{A}4})$	$\frac{1}{2}$	$\frac{1}{2}$	$\frac{1}{2} (c_{\mathcal{A}2} + c_{\mathcal{A}3} - 2c_{\mathcal{A}4})$	0	$\frac{1}{2}$	0
		$c_{\mathcal{A}3}$	0	$\frac{1}{2}$				$\frac{1}{2} (c_{\mathcal{A}1} + c_{\mathcal{A}2})$	$\frac{1}{2}$	0	$\frac{1}{2}$
	B	$c_{\mathcal{A}1}$	0	$\frac{1}{2}$	$\alpha (c_{\mathcal{A}1} + c_{\mathcal{A}2} + c_{\mathcal{A}3} + 2c_{\mathcal{A}4})$	$\frac{1}{2} (1 + s_{2\varphi})$	$\frac{1}{4} (2 - s_{2\varphi})$	$\frac{1}{2} (c_{\mathcal{A}2} + c_{\mathcal{A}3} + 2c_{\mathcal{A}4})$	$\frac{1}{4} (1 + s_{2\varphi})$	0	$\frac{1}{4} (1 - s_{2\varphi})$
		$c_{\mathcal{A}2}$	s_{φ}^2	$\frac{1}{2} c_{\varphi}^2$	$\alpha (c_{\mathcal{A}1} + c_{\mathcal{A}2} + c_{\mathcal{A}3} - 2c_{\mathcal{A}4})$	$\frac{1}{2} (1 - s_{2\varphi})$	$\frac{1}{4} (2 + s_{2\varphi})$	$\frac{1}{2} (c_{\mathcal{A}2} + c_{\mathcal{A}3} - 2c_{\mathcal{A}4})$	$\frac{1}{4} (1 - s_{2\varphi})$	0	$\frac{1}{4} (1 + s_{2\varphi})$
		$c_{\mathcal{A}3}$	c_{φ}^2	$\frac{1}{2} s_{\varphi}^2$				$\frac{1}{2} (c_{\mathcal{A}1} + c_{\mathcal{A}2})$	$\frac{1}{2} s_{\varphi}^2$	c_{φ}^2	$\frac{1}{2} s_{\varphi}^2$
							$\frac{1}{2} (c_{\mathcal{A}1} + c_{\mathcal{A}3})$	$\frac{1}{2} c_{\varphi}^2$	s_{φ}^2	$\frac{1}{2} c_{\varphi}^2$	

Monoclinic-I: C_{1h} point group: φ is the angle between the dipole moment and the $\langle 100 \rangle$ axis in the $\{110\}$ symmetry plane. C_2 and C_{2h} : φ is the angle between the dipole moment and the $\langle 100 \rangle$ axis in the $\{110\}$ plane perpendicular to the C_2 axis.

Monoclinic-II: φ is the angle between the dipole moment and a $\langle 100 \rangle$ axis in the $\{100\}$ plane normal to the C_2 axis.

E. References

- [1] A. S. Barker Jr., A. J. Sievers, *Reviews of Modern Physics Suppl. No. 2*, 47, S1 (1975).
- [2] E. B. Wilson Jr., J. C. Decius, and P. C. Cross, "Molecular vibrations", (Dover Publications, New York, 1955).
- [3] R. C. Newman, "Infra-red studies of crystal defect", (Taylor and Francis, London, 1973).
- [4] B. Clerjaud and D. Côte, *J. Phys.: Condens. Matter*, **4**, 9919 (1992).
- [5] R. S. Leigh and R. C. Newman, *Semicond. Sci. Technol.*, **3**, 84 (1988).
- [6] *Master thesis* of J. Holbech, Institute of Physics and Astronomy, University of Aarhus (April, 1993). (in danish)
- [7] A. N. Walck and W. B. Fowler, *Phys. Rev. B*, **51**, 13146 (1995).
- [8] R. Darwich, B. Pajot, B. Rose, D. Robein, B. Theys, R. Rahbi, C. Porte, and F. Gendron, *Phys. Rev. B*, **48**, 17776 (1993).
- [9] M. D. McCluskey, E. E. Haller, J. Walker, and N. M. Johnson, *Phys. Rev. B*, **52**, 16 (1995).
- [10] A. A. Kaplyanskii, *Opt. Spectrosk.* **16**, 329 (1964) [*Opt. Spectrosc. (USSR)* 16, 602 (1964)].
- [11] J. F. Nye, "Physical Properties of Crystals", (Oxford University Press, 1985).
- [12] B. Bech Nielsen, and H. G. Grimmeiss, *Phys. Rev. B*, **40**, 12403 (1989).
- [13] M. Budde, B. Bech Nielsen, P. Leary, J. Goss, R. Jones, P. R. Briddon, S. Öberg, and S. J. Breuer, *Phys. Rev. B*, **57**, 4397 (1998).
- [14] A. A. Kaplyanskii, *Opt. Spectrosk* **16**, 557 (1964) [*Opt. Spectrosc. (USSR)* **16**, 1031 (1964)].
- [15] A. E. Hughes, and W. A. Runciman; *Proc. Phys. Soc. London*, **90**, 827 (1967).

III. Experimental

This chapter describes experimental details regarding the preparation of samples and the subsequent infrared absorption measurements. The samples were prepared by implantation of protons and/or deuterons at multiple energies. The chapter therefore gives a brief introduction to ion implantation in general and to multiple-energy implantations. The spectroscopic measurements were carried out with a Fourier-Transform InfraRed (FTIR) spectrometer equipped with a cryostat for measurements at cryogenic temperatures. The present chapter describes the basic principles and technical details of the FTIR spectrometer. In addition, the cryostats and the setup for uniaxial stress measurements are described.

A. Sample preparation

1. Pre-implantation preparations

The samples used in the experimental studies were cut from high-resistivity single crystals of silicon and germanium grown by the floating-zone method. The silicon samples were *n*-type with a resistivity of $\sim 1000 \Omega \text{ cm}$ corresponding to a phosphorous concentration less than 10^{13} cm^{-3} . The (quoted) concentration of carbon and oxygen was less than 3×10^{16} and $1 \times 10^{16} \text{ cm}^{-3}$, respectively. The germanium samples were cut from an ultra-pure germanium single crystal with (quoted) concentrations of impurities less than $1 \times 10^{16} \text{ cm}^{-3}$.

Two different types of samples were prepared of each material. The samples used for isochronal annealing and isotope substitution studies were cut as rectangular disks and measured $\sim 10 \times 10 \times 2 \text{ mm}^3$. The uniaxial stress samples were shaped as rectangular parallelepipeds with dimensions $\sim 10 \times 2 \times 2 \text{ mm}^3$ and were cut with the long edges parallel to $\langle 100 \rangle$, $\langle 110 \rangle$, or $\langle 111 \rangle$ directions. It is crucial to uniaxial experiments that the long edges of the sample are accurately aligned with the desired crystal axis and that the two end surfaces are parallel to each other and perpendicular to the long edges of the sample. The samples were aligned with the desired crystal axis by x-ray diffraction, within an estimated error of $\pm 1^\circ$. The end surfaces of the samples were made parallel by use of a specially designed jig, which allowed the sample to be rotated exactly 180° without remounting.

After cutting, the two $10 \times 10\text{-mm}^2$ surfaces of the standard samples and two parallel $10 \times 2\text{-mm}^2$ surfaces of the uniaxial stress samples were mechanically and electrically polished in order to optimise the transmission of infrared light through the sample. After polishing, the dimensions of the stress samples were measured with a micrometer.

2. Multiple-energy ion implantation

Ion implantation is a convenient method for incorporating hydrogen and deuterium into silicon and germanium, and has several advantages as compared to other hydrogenation methods such as plasma treatment or incorporation of hydrogen during growth. First, the number of ions introduced by ion implantation can easily be controlled. Second, the implantation can be carried out at cryogenic temperatures, which makes it possible to study defects that are unstable at room temperature. Third, it is possible to design and prepare particular profiles of implants by implantation at multiple energies. Fourth, ion implantation inevitably leads to the formation of intrinsic defects in the same region of the sample as the implanted ions. This is advantageous if one wants to study the interactions between the implanted ions and intrinsic defects.

Protons or deuterons moving through a silicon (germanium) crystal transfer energy to the crystal by scattering processes with electrons and nuclei. At energies above ~ 24 (67) keV the stopping is determined by the interaction with electrons, whereas nuclear stopping gradually becomes important at lower energies and dominates below ~ 1.2 (3.4) keV [1]. This implies that the range of MeV protons or deuterons implanted into silicon and germanium essentially is determined by the electronic stopping. Moreover, scattering processes with the host nuclei are most probable close to the end-of-range of the ions where the ion energy is small. Hence, displacements of host atoms caused by such processes are most likely to occur close to the end-of-range and the damage and implant profiles nearly coincide. The stopping of an ion consists of a series of scattering events. The number of scattering events required to stop the ion is subject to statistical fluctuations [2], which causes the profile resulting from a mono-energetic implantation to exhibit a certain energy-dependent width.

The spatial distribution of implanted ions and displaced host atoms can be simulated with the Monte-Carlo simulation program *TRIM* developed by Ziegler⁴ during the last decade [3]. In the present work, *TRIM* has been used extensively to simulate implantation profiles of protons and deuterons implanted into silicon and germanium. The simulations show that the hydrogen and deuterium profiles nearly are Gaussian for implantation energies above 500 keV. The energy-dependence of the projected range and Full Width at Half Maximum (FWHM) of protons implanted into silicon is shown in Fig. III.1. The profile of displaced host atoms generally consists of a peak which coincides with the hydrogen or deuterium profile and a tail extending to the surface of the sample. The average number of displaced host atoms per incoming

⁴ *TRIM* is part of the program package *SRIM* (Stopping and Ranges of Ions in Matter) that can be downloaded free of charge from <http://www.research.ibm.com/ionbeams/>

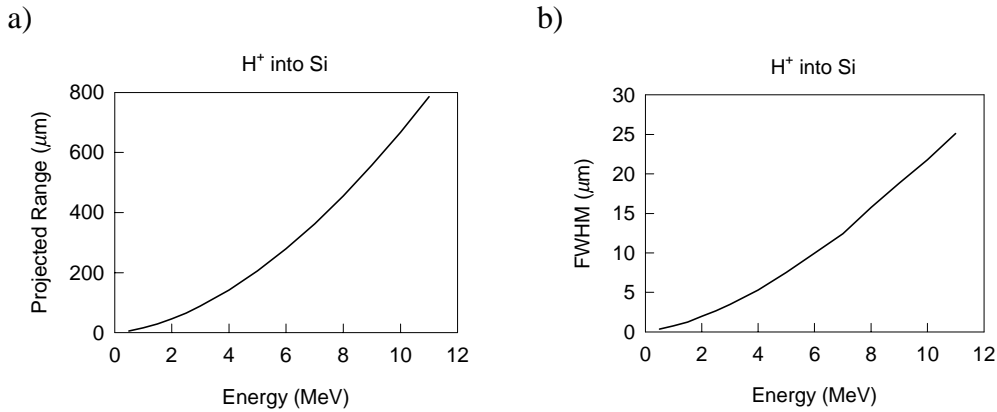


Fig. III.1. (a) Range and (b) Full Width at Half Maximum of the profiles resulting from implantation of protons into silicon at various energies. The data shown are obtained by fitting a Gaussian profile to the profile simulated with the *TRIM* program.

ion increases with increasing implantation energy. For example, *TRIM* predicts that a proton with an energy of 10 keV, 1 MeV, or 10 MeV implanted into silicon on average displaces respectively 11, 29, or 94 silicon atoms, and that the production rate of defects in germanium is approximately 30 % larger than in silicon. Moreover, deuteron implantation creates about twice as many defects as proton implantation in both materials. It is important to note, however, that *TRIM* does not include diffusion of vacancies and self-interstitials and thus neglects recombination and agglomeration of defects. The actual number of implantation-induced defects are therefore less than the *TRIM* estimates stated above, particularly if the implantation temperature is larger than the temperature at which the defects start to migrate. The recombination and agglomeration of implantation-induced defects has been confirmed experimentally. For example, channeling measurements have shown that the number of host atoms displaced by implantation of 10-keV deuterons into silicon at 30 K is consistent with the result of *TRIM* simulations, and that more than 95% of the damage disappears upon annealing below RT [4]. Infrared absorption measurements have revealed that implantation of 9-MeV protons into silicon at RT creates about 1/3 divacancy per proton [5]. Hence, the concentration of intrinsic defect induced by proton- or deuteron-implantation is expected to be one or two orders of magnitude in excess of the concentration of implants at very low temperature and of the same order of magnitude as the hydrogen or deuterium concentration after annealing at RT.

Experimental studies of point defects require fairly low concentrations of defects in order to reduce the effect of interactions between defects. The maximum concentration depends on the degree of localisation of the physical quantity being studied and hence on the experimental technique used. In the case of infrared absorption spectroscopy on hydrogen-related local modes in proton implanted silicon,

the practical maximum concentration is ~ 0.2 at. %. Implantation of higher concentrations results in a broad absorption feature in the Si-H stretch range rather than an increase in the intensity of the sharp absorption lines of hydrogen-related point defects [6]. Infrared absorption studies typically require area densities (doses) of hydrogen of $\sim 5 \times 10^{16} \text{ cm}^{-2}$. If these two requirements are to be obtained by implantation at a single energy, the FWHM of the hydrogen profile needs to be greater than $\sim 5 \mu\text{m}$. According to Fig. III.1.b, this implies that the proton energy be greater than 4 MeV, which requires access to a high-energy accelerator.

A useful alternative to single-energy implantation is to implant the sample with ions at a series of different energies. This generally results in a wider profile than a single-energy implantation (at a similar energy) and hence in a reduction in both the concentration of hydrogen and damage at the same implanted dose. In addition, implantation profiles can be prepared which are uniform in a depth range determined by the minimum and maximum energy of the implantation sequence, which makes it possible to study defects at well-defined concentrations of the implanted species. The infrared absorption experiments described in this thesis were carried out on silicon and germanium samples implanted with protons and/or deuterons at 50 - 100 different energies in the range $\sim 1 - 3$ MeV or $5.3 - 11.2$ MeV. The resulting hydrogen profiles were nearly uniform of a range of ~ 50 and $\sim 500 \mu\text{m}$, respectively. The dose at each energy required to yield uniform concentration profiles of hydrogen and deuterium was determined by *TRIM* simulations.

3. Experimental details on ion implantation

The experimental studies presented in chapter V - IIX were carried out with similar sets of samples. The samples were implanted with protons and/or deuterons at the "5-MV" Van de Graaf accelerator at the Institute of Physics and Astronomy, University of Aarhus. The implantations were carried out with the samples mounted on a copper block inside a vacuum chamber, attached to a beam-line of the accelerator. The copper block was connected to a closed-cycle cryocooler, which made it possible to cool the samples to ~ 30 K during implantation. Each sample was implanted into one of the polished surfaces at 50 - 100 different energies in the range $680 - 2500$ keV for protons and $840 - 3000$ keV for deuterons. The dose at each energy was chosen to yield a uniform profile of implants of 0.02 or 0.05 at.% ranging from ~ 10 to $\sim 50 \mu\text{m}$ below the surface of the sample. In order to obtain a homogeneous lateral distribution of implants, the beam was swept horizontally and vertically. The beam current was measured with a beam cup located ~ 1 m behind the slits and ~ 2 m in front of the sample. At each energy, the current averaged over a period of 1 min. was measured and used to determine the implantation time needed to

yield the planned dose. The variations in the current were less than 10%, which gives an estimate of the uncertainty in the implanted dose. The background pressure during implantation was less than 1×10^{-6} torr. The silicon samples were implanted at either ~ 30 K, ~ 100 K, or room temperature (RT), whereas the implantations into germanium were performed at ~ 30 K. The samples were stored at RT after implantation. Samples were implanted with either protons (Si:H or Ge:H), deuterons (Si:D or Ge:D), or overlapping profiles of protons and deuterons (Si:HD or Ge:HD). After implantation, the samples were cleaned with acetone and lightly etched in HF to remove surface defects. The details on the implantation conditions of the individual samples are summarised in Table III.1.

The studies described in chapter IV were carried out on silicon samples with implanted hydrogen concentrations of 0.0002 - 0.001 at. %, i.e. 20 – 100 times less than the samples described above. The hydrogen concentration was reduced by lowering the total implanted dose to $(0.5 - 1) \times 10^{16}$ cm⁻² and by increasing the implantation energy to 5.3 - 11.2 MeV. These implantations were carried out at the Tandem accelerator at the Institute of Physics and Astronomy, University of Aarhus. The samples were implanted with protons and/or deuterons at ~ 50 different energies and the dose at each energy was adjusted to result in a nearly uniform profile of

Table III.1. Implantation conditions of the samples studied in the present thesis. The fifth column denoted “Meas. type” indicates the type of infrared absorption studies the samples were used for: *a/i* = annealing/isotope substitution and *u* = uniaxial stress.

Chapter	Sample	Ion	Conc. (at. %)	Meas. type	Energy (MeV)		T_{imp} (K)	R_p (μm)	
					min	max		min	max
IV	Si:H ^a	H	0.00017	<i>a/i</i>	5.3	11.2	~ 20	0	600
	Si:D ^a	D	0.00067	<i>a/i</i>	6.7	11.5	~ 20	0	300
	Si:HD ^a	H	0.00067	<i>a/i</i>	5.3	8.5	~ 20	0	300
		D	0.00067		6.7	11.5		0	300
VI, VIII	Si:H	H	0.02	<i>a/i</i>	0.68	2.50	~ 100	8	60
	Si:H	H	0.02	<i>a/i</i>	0.68	2.50	~ 300	8	60
	Si:D	D	0.02	<i>a/i</i>	0.84	3.00	~ 300	8	60
	Si:HD	H	0.02	<i>a/i</i>	0.68	2.50	~ 300	8	60
		D	0.02		0.84	3.00		8	60
	Si:H	H	0.02	<i>u</i>	0.68	2.50	~ 30	8	60
V, VII, VIII	Ge:H	H	0.05	<i>a/i</i>	0.68	2.48	~ 30	11	43
	Ge:D	D	0.05	<i>a/i</i>	0.88	3.00	~ 30	11	43
	Ge:HD ^b	H	0.05	<i>a/i</i>	0.68	2.48	~ 30	11	43
		D	0.05		0.88	3.00		11	43
	Ge:H	H	0.05	<i>u</i>	0.68	2.48	~ 30	11	43

^a The ions were implanted through a 200 μm thick aluminium window.

^b The Ge:HD sample was stored at room temperature between the H⁺ and D⁺ implantation.

implants from the surface and $\sim 500 \mu\text{m}$ into the bulk (for details on the implantation conditions, see Table III.1). At each energy, the ion current was measured before the implantation in a beam cup with a 2-mm acceptance hole, and the implantation time was then calculated to yield the desired dose. The current typically fluctuated by $\sim 20\%$, which gives a measure of the uncertainty of the implanted dose. The implantations were carried out at $\sim 20 \text{ K}$ with the samples mounted in a cryostat designed for optical measurements. The cryostat is described in more detail in Sec. III.B.4. In order to obtain a homogeneous lateral distribution of implants, the implantations were carried out with a defocused beam.

B. Spectroscopic measurements

The spectroscopic measurements described in this thesis were performed with a Fourier Transform InfraRed (FTIR) spectrometer. The following sections give a description of the basic principles and technical details of the spectrometer.

1. Basic concepts of the FTIR spectrometer

The goal of infrared absorption spectroscopy is to measure the attenuation in intensity as a function of frequency caused by the penetration of infrared light through a particular specimen. This can be accomplished with an FTIR spectrometer, which basically consists of three components: a broadband light source, a Michelson interferometer, and a detector (see sketch in Fig. III.2). In addition, a computer for data acquisition and processing is connected to the spectrometer.

The Michelson interferometer provides a means of measuring the intensity of infrared light as function of frequency. The interferometer consists of a beamsplitter, a fixed mirror, and a movable mirror (see Fig. III.2). Infrared light from the broadband source is directed into the interferometer and impinges on the beamsplitter, which splits the incoming beam into two separate beams with approximately the same intensity. One of the beams is reflected off the beamsplitter and is directed onto the fixed mirror, whereas the second beam is transmitted through the beamsplitter and propagates towards the movable mirror. At the two mirrors the beams are reflected and propagate back towards the beamsplitter where they are split once more. After the second beam splitting, approximately

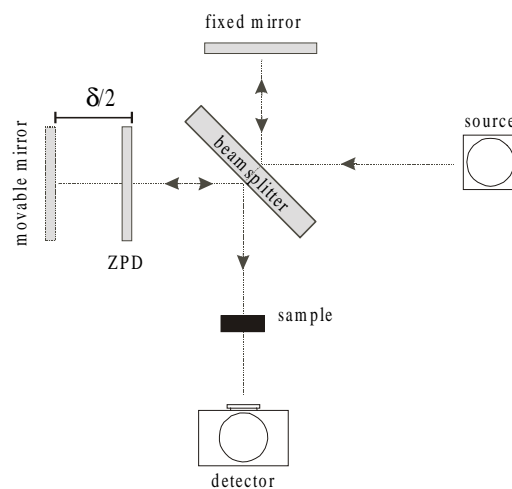


Fig. III.2. Sketch of an FTIR spectrometer.

one half of each beam is directed towards the sample and detector, whereas the other halves propagate in the direction of the source where they are lost. The two beams propagating towards the detector first pass through the sample, where light is absorbed because of electronic or vibrational excitations. The beams then impinge on the detector, where the intensity integrated over all frequencies is measured.

The description given above describes the propagation of light in the Michelson interferometer but does not explain how spectral information can be obtained from the integral intensity measurement. The remainder of this section gives a brief description of the basic theory of Fourier transform spectroscopy. The description is based on the introduction to the subject by Bell [7], to which the reader is referred for further details.

Let us consider an idealised spectrometer with a beamsplitter that splits the beam into pairs of electromagnetic waves moving towards the detector, which have equal electric field amplitudes $E_0(\sigma)$ for a given wave number σ . The optical path length from the source to the detector of the wave reflected at the movable and fixed mirror is denoted respectively z_1 and z_2 . The electric field at the detector is the sum of the electric fields of the two separate waves:

$$E(\sigma) = E_0(\sigma) \left\{ e^{i[\omega t - 2\pi\sigma z_1]} + e^{i[\omega t - 2\pi\sigma z_2]} \right\}. \quad (\text{III.1})$$

The contribution to the light intensity at the detector from waves with a particular wave number σ is (in CGS units) given by

$$B(\sigma, z) = \frac{c}{8\pi} |E(\sigma)|^2 = \frac{c}{4\pi} E_0^2(\sigma) \{1 + \cos[2\pi\sigma z]\}, \quad (\text{III.2})$$

where $z \equiv z_1 - z_2$ is the difference in optical path length of the two waves. Eq. III.2 shows that the intensity from waves with wave number σ oscillates about the value $cE_0^2(\sigma)/4\pi$ as a function z with the period of oscillation $\sigma^{-1} = \lambda$. Moreover, it is evident from Eq. III.2 that all wave numbers contribute with their maximum intensity only at $z = 0$, i.e. at zero path difference. Hence, the detector measures the maximum intensity at this position of the movable mirror. The output from the detector at a given position, z , of the movable mirror is proportional to the intensity given in Eq. III.2 integrated over all wave numbers:

$$I(z) = C \int_0^\infty B(\sigma, z) d\sigma = \frac{I(0)}{2} + C \int_0^\infty \frac{c}{4\pi} E_0^2(\sigma) \cos[2\pi\sigma z] d\sigma, \quad (\text{III.3})$$

where C is a constant, which depends on the design of the detector. According to Eq. III.3, the measurable quantity $[I(z) - I(0)/2]$, also denoted the *interferogram*, is given by the cosine Fourier transform of the square of the electric field amplitude. This implies that the light intensity vs. wave number, i.e. the spectrum, can be

obtained by calculating the inverse cosine Fourier transform of the interferogram:

$$B(\sigma) = \frac{c}{8\pi} E_0^2(\sigma) = \frac{2}{C} \int_0^{\infty} [I(z) - I(0)/2] \cos[2\pi\sigma z] dz \quad . \quad (\text{III.4})$$

In practise it is impossible to measure the interferogram from zero to infinite optical path difference as required by Eq. III.4, and the interferogram is therefore truncated at some maximum path difference z_{\max} . The truncation of the interferogram has important implications on the spectra obtained. First, it can be shown [7] that the spectral resolution $\delta\sigma$ approximately is given by z_{\max}^{-1} .⁵ Second, the signal-to-noise ratio is approximately proportional to $\sqrt{\delta\sigma}$ in absorbance spectroscopy [8], and an improvement of the spectral resolution thus has a prize in terms of a decrease in the signal-to-noise ratio. Third, the truncation of the interferogram distorts the shape of narrow peaks in the spectra [7]. The distortions can be attenuated by smoothing (“apodising”) the cut-off of the interferogram at z_{\max} , which is done by multiplying the interferogram with an appropriate apodisation function. The apodisation of the interferogram generally leads to a modest decrease in the spectral resolution. In the infrared absorption experiments described in this thesis, the Happ-Genzel apodisation function

$$f_{\text{Happ-Genzel}}(z) = 0.54 + 0.46 \cos\left[\frac{\pi}{2} \frac{z}{z_{\max}}\right] \quad (\text{III.5})$$

was used.

In practise the interferogram is sampled at equidistant positions of the movable mirror rather than measured at all possible values of z . The movable mirror is scanned with constant speed with z varying from $-z_{\min}$ to z_{\max} , where $0 < z_{\min} \ll z_{\max}$. The position of the mirror is monitored by a second Michelson interferometer with the same fixed and movable mirrors but with a monochromatic source consisting of a He-Ne laser and a separate detector. The duration of one scan depends on the mirror velocity and the travelled distance of the mirror. The measurements described in this thesis were carried out with a spectral resolution of $\sim 1 \text{ cm}^{-1}$ and a mirror velocity of 1.58 cm/s , which corresponds to a scanning time of less than one second. The short duration of one scan makes it possible to perform a large number of scans (e.g. hundreds or thousands) within a reasonable period of time and then use the average interferogram to calculate the spectrum. The signal-to-noise ratio is proportional to the square root of the number of scans [7], and averaging of interferograms thus results in a great improvement of the signal-to-noise ratio.

⁵ The expression $\delta\sigma = 1/z_{\max}$ is used as a definition of the spectral resolution in the remainder of this thesis.

2. Absorbance measurements with an FTIR spectrometer

The introduction to the FTIR spectrometer given in the previous section was only concerned with the basic principles and did not take into account the effect of positioning a sample in the infrared beam.

By generalisation of the derivation of the previous section, it can be shown that the spectrum obtained by Fourier transformation of the interferogram measured with a sample positioned in the infrared beam between the beamsplitter and the detector (see Fig. III.2) is given by

$$B_s(\sigma) = |t_0 + t_1 + t_2 + \dots|^2 B(\sigma) , \quad (\text{III.6})$$

where t_m is the amplitude transmission coefficient of light which has experienced $2m$ internal reflections inside the sample. The transmission coefficients are

$$t_0 = a(1-r^2) \quad , \quad t_1 = t_0 a^2 r^2 \quad , \quad t_2 = t_0 a^4 r^4 \quad , \quad \dots \quad (\text{III.7})$$

where

$$a = e^{-\alpha(\sigma)l/2} e^{i2\pi\sigma nl} \quad \text{and} \quad r \cong \frac{1-n}{1+n} \quad (\text{III.8})$$

for light with normal incidence on a sample with refractive index n , absorption coefficient $\alpha(\sigma)$ and thickness l [7,9]. Neglecting absorption, the norm of the transmission coefficients $|t_0|$, $|t_1|$, and $|t_2|$ are 0.70, 0.21, and 0.060 in silicon and 0.64, 0.23, and 0.080 in germanium, and $|t_m|$ thus decreases rapidly with increasing m .

All spectra shown in this thesis are given in absorbance units, which are defined as

$$Abs(\sigma) = -\log_{10} \frac{B_s(\sigma)}{B(\sigma)} = -\log_{10} |t_0 + t_1 + t_2 + \dots|^2 , \quad (\text{III.9})$$

where $B_s(\sigma)$ is the single-beam sample spectrum and $B(\sigma)$ is the background spectrum measured with the same spectrometer setup but without a sample. If Eqs. III.7 and III.8 are inserted into Eq. III.9, and t_m terms with $m > 1$ are omitted, the absorbance is given by

$$Abs(\sigma) = -2 \log_{10}(1-r^2) + \alpha(\sigma)l \times \log_{10} e - \log_{10} \left\{ 1 + r^4 e^{-2\alpha(\sigma)l} + 2 r^2 e^{-\alpha(\sigma)l} \cos[4\pi\sigma nl] \right\} . \quad (\text{III.10})$$

The first term in Eq. III.10 is due to the reflection of light when the light enters the sample and is essentially constant in the region $500 - 2500 \text{ cm}^{-1}$ of interest in this thesis. The second term is proportional to the absorption coefficient of the sample and reflects the electronic and vibrational transition induced by the infrared light. The third term is due to absorption of light that is internally reflected once at both surfaces

of the sample and to the interference between light that is internally reflected once at both surfaces with light transmitted without internal reflection.

For an absorbance peak with a FWHM of $\sim 1 \text{ cm}^{-1}$, the contribution to the absorbance of internally reflected light is about 14% in silicon and 18% in germanium, when $\alpha(\sigma)l$ is in the range 0.01 – 0.99. This contribution therefore has to be taken into account if one intends to convert the intensity

$$I_{\Gamma} \equiv \int_{\text{peak } \Gamma} Abs(\sigma) d\sigma \quad (\text{III.11})$$

of an absorbance peak into an effective charge by use of Eqs. II.2 and III.9.

The interference of internally reflected light with light transmitted without internal reflection gives rise to a small replica of the main interferogram displaced by $2nl$ from zero path difference, where l is the thickness and n the refractive index of the sample. The replica induces deleterious oscillations in the spectrum with a period $\Delta\sigma = (2nl)^{-1}$. Fortunately, the oscillations can be removed by choosing $z_{\text{max}} < 2nl$, which for a silicon (germanium) sample with a thickness of 2 mm corresponds to a spectral resolution of $\delta\sigma_{\text{max}} = 0.7$ (0.6) cm^{-1} , which is comparable to the intrinsic width ($\sim 1 \text{ cm}^{-1}$) of the absorption lines of Si-H and Ge-H modes in proton-implanted silicon and germanium.

3. Technical description of the FTIR spectrometer

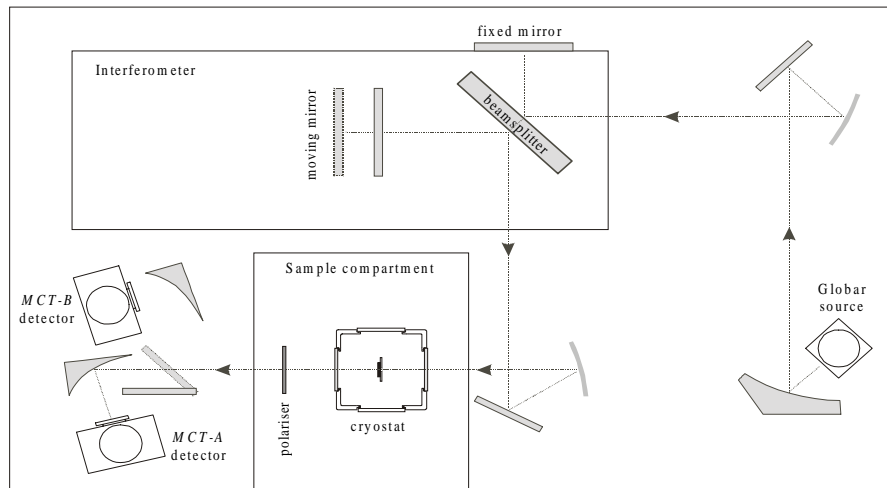


Fig. III.3. Sketch of the Nicolet System-800 FTIR spectrometer. The individual components are described in the text.

The infrared absorption measurements described in the present thesis were carried out with a Nicolet System-800 FTIR spectrometer (see Fig. III.3). The spectrometer is equipped with a Globar™ broadband source that emits light in the frequency range 50 - 8000 cm^{-1} and a beamsplitter consisting of a thin germanium film on a

transparent KBr substrate which works in the range $350 - 7000 \text{ cm}^{-1}$. The detector is of the type *MCT-A* produced by Nicolet Analytical Instruments. It is based on a photoconductor made of the ternary compound semiconductor $\text{Hg}_{1-x}\text{Cd}_x\text{Te}$ and operates at liquid nitrogen temperature. The detector is highly sensitive in the range $\sim 600 - 7400 \text{ cm}^{-1}$. The spectrometer was purged off atmospheric air by a steady flow of dried air in order to reduce the absorption by H_2O and CO_2 .

4. Technical description of cryostats and stress-rig

Two different cryostats were used for the spectroscopic measurements. All the uniaxial stress measurements and some of the isochronal annealing and isotope substitution studies were performed with a Leybold VSK 4-300 flow-cryostat sketched in Fig. III.4. The cryostat is constructed with two separate concentric volumes. The wall separating the two volumes is cooled by liquid nitrogen or helium flowing through channels in the wall, and the temperature of the wall can be measured with a thermistor. In order to reduce the transfer of heat from the surroundings to the central cold parts of the cryostat, the outer volume is evacuated to a pressure of $\sim 10^{-6}$ torr by a turbo-molecular pump, and a thermal radiation shield is placed between the inner and outer wall. The outermost wall of the cryostat is equipped with two 4-mm thick CsI windows, which provide optical access in the frequency range $300 - 33000 \text{ cm}^{-1}$ to the sample mounted in the innermost volume. The axis defined by the centres of the two windows is henceforth called the optical axis of the cryostat.

Two different configurations of the flow cryostat are used. In one of the configurations, the inner wall is equipped with two windows and the inner volume is then filled with an ultra-pure helium gas, which provides a good thermal contact between the cold inner wall and the sample. With this setup the sample can be cooled

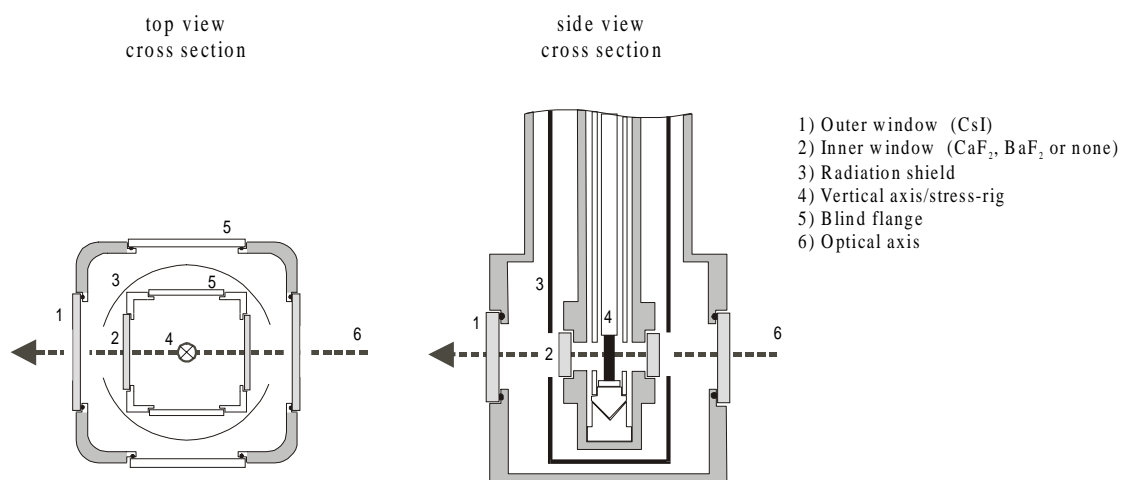


Fig. III.4. Sketch of the Leybold VSK 4-300 flow cryostat.

to ~ 80 K (~ 10 K) with liquid nitrogen (helium), and the minimum temperature of the sample is obtained after cooling for ~ 1 hour. Due to the direct contact between the windows and the cold inner wall, it is necessary to use windows made of a material with a thermal expansion coefficient similar to that of the inner wall, in order to prevent leaks from being formed during cool-down. The experiments presented in this thesis were carried out with inner windows made of CaF_2 or BaF_2 , which are transparent above ~ 725 cm^{-1} .

In the second configuration of the flow cryostat no inner windows are used. This implies that the inner and outer volumes of the cryostat are connected, and both volumes of the cryostat are evacuated. In the absence of inner windows, the sample is in thermal contact with the cold inner wall through the sample holder and a thermal connector, as shown in Fig. III.4 and Fig. III.5. The minimum temperature with this configuration is ~ 100 K when the cryostat is cooled with liquid nitrogen. The cool-down times range from ~ 1 hour with a sample holder designed for standard transmission measurements to several hours with the stress-rig for uniaxial stress measurements mounted in the cryostat. The configuration with inner windows and a contact gas is, with respect to cooling efficiency and rate, clearly superior to the setup without inner windows. However, the use of the latter is justified by the setup being technically more simple and by the fact that the absence of CaF_2 and BaF_2 windows extends the spectral range down to the low-frequency cut-off of the detector at ~ 600 cm^{-1} .

The uniaxial stress measurements were carried out with a home-built stress-rig mounted in the flow-cryostat. The stress-rig, sketched in Fig. III.5, consists of a vertical stainless steel tube which fits into the flow cryostat. The bottom end of the tube is terminated with a copper screw with a flat top and conical bottom part. The uniaxial stress samples is positioned inside the tube on a thin brass disk, which is glued to the top of the copper screw (see Fig. III.5). The long edges of the sample are parallel to the vertical axis of the tube (and cryostat) and the centre of the sample is at the same height as the optical axis. Optical access to the sample is provided by two holes drilled in the tube at the height of the optical axis. The holes are fitted with slits, which prevent light from being transmitted through the cryostat without penetrating the sample. When the sample is positioned, a push-rod of stainless steel is lowered into the tube until it makes contact with the top of the sample. Then, the top part of the stress-rig, consisting of a pneumatic cylinder, a Hottinger-Baldwin Messtechnik (HBM) UA9 force transducer and an extension to the push-rod, is mounted on the bottom-part of the stress-rig. The pneumatic cylinder can apply a static compressive force on the push-rod and sample, and the magnitude of the force can be read-off on a HBM MVD2405A amplifier connected to the force transducer. The maximum force is 5000 N, which for a sample with a $2 \times 2 \text{ mm}^2$ cross section corresponds to a uniaxial stress of 1.25 GPa. The uniaxial stress measurements are carried out with a Specac-

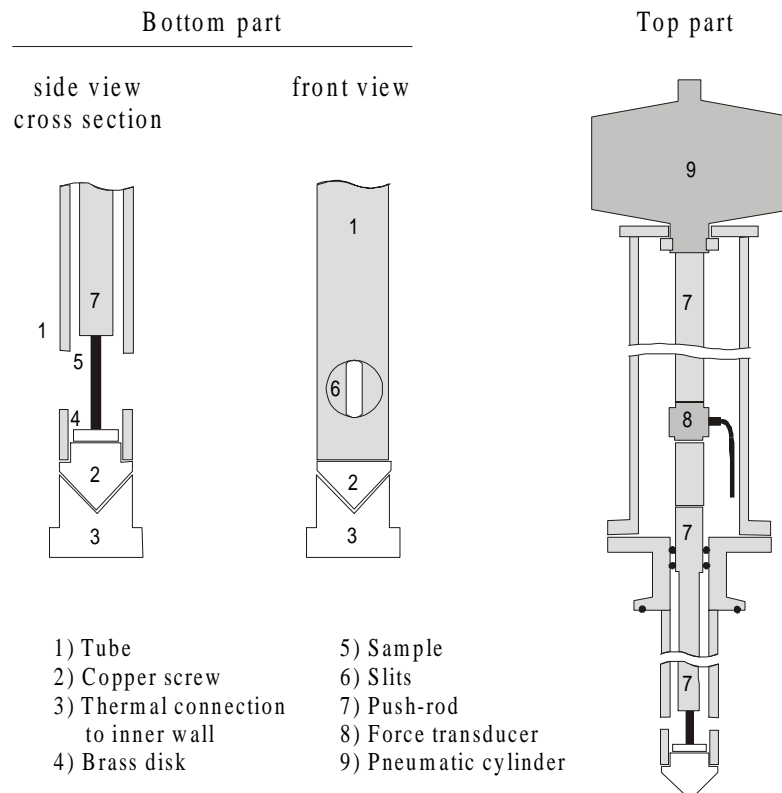


Fig. III.5. Sketch of the stress-rig used for the uniaxial stress measurements.

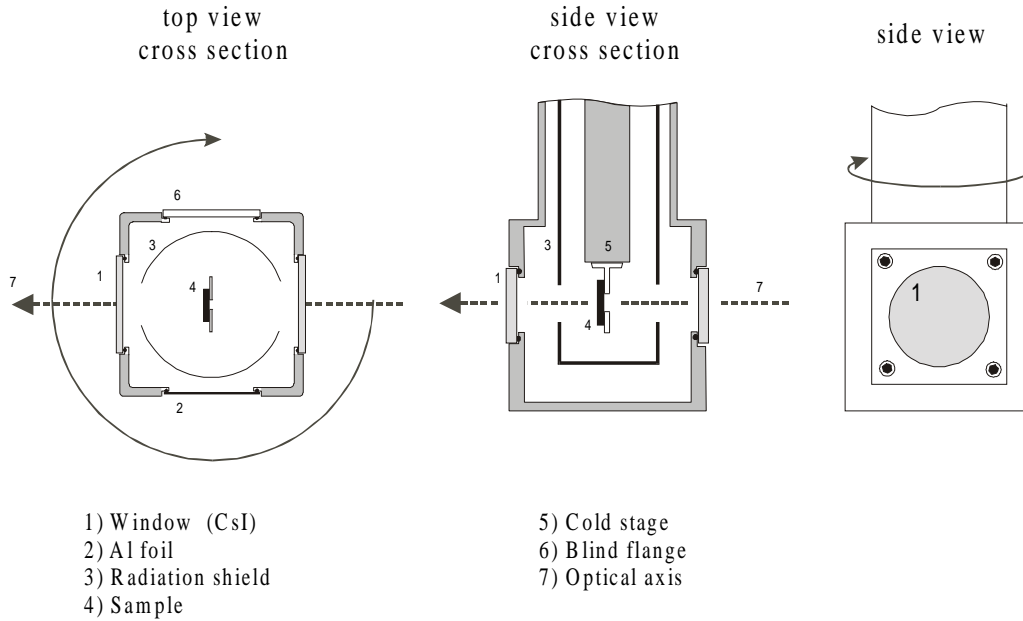


Fig. III.6. Sketch of the APD DE 204 SL closed-cycle cryostat.

Graseby IGP 225 grid-polariser placed in the infrared light beam between the cryostat and the detector (see Fig. III.3). The polariser can be rotated about the optical axis, and the infrared absorption can thus be measured separately with light polarised parallel ($\vec{\epsilon} // \vec{F}$) and perpendicular ($\vec{\epsilon} \perp \vec{F}$) to the applied force.

Most isochronal annealing and isotope substitution studies were performed with an APD DE 204 SL closed-cycle cryostat purchased from APD Cryogenics Inc. The cryostat, sketched in Fig. III.6, is based on a closed-cycle cryocooler with a cooling capacity of 6.75 W at 20 K, which is capable of cooling the sample to the minimum temperature of 9 ± 1 K in 45 minutes. In order to reduce the transfer of heat from the outer wall of the cryostat to the sample and the cold stage, the cryostat is evacuated to a pressure of $\sim 10^{-6}$ torr with a turbo-molecular pump and the cold stage and the sample is surrounded by a thermal radiation shield. The temperature of the cold stage can be measured with a calibrated Lakeshore DT-470-SD silicon-diode temperature sensor. The temperature sensor is embedded in the cold stage ~ 3 cm from the sample and gives a good measure of the sample temperature. The temperature sensor is connected to a Lakeshore Model 330 temperature controller, which also controls a resistive heater wound around the cold stage of the cryostat. The sample is mounted on a sample holder with a circular aperture (diameter = 3.0 mm) attached to the bottom of the cold stage. The outer wall is equipped with two 4-mm thick CsI windows, which allows infrared light to be transmitted through the cryostat and sample. In addition, the outer wall has a 0.2-mm thick aluminium window mounted at right angles to the optical axis, which is used for low-temperature implantation of protons and deuterons into a sample mounted on the sample holder. The outer wall

can be rotated about the vertical axis without breaking the vacuum. This makes it possible to implant a sample through the aluminium window, rotate the outer wall by 90° , and then measure the infrared absorption without heating the sample between the implantation and the spectroscopic measurement. Extensive use of this feature was made in the experimental studies of isolated hydrogen defects in silicon described in chapter IV.

C. References

- [1] H. E. Schiøtt, *Rad. Eff.*, **6**, 107 (1970).
- [2] F. Besenbacher, J. U. Andersen, and E. Bonderup, *Nucl. Instr. Meth.*, **168**, 1 (1980).
- [3] J. F. Ziegler, J. P. Biersack and U. Littmark, *The stopping and ranges of ions in solids*, (Pergamon Press, New York, 1985).
- [4] B. Bech Nielsen and J. U. Andersen, *Phys. Rev. B*, **35**, 2732 (1987).
- [5] J. Tatarkiewicz, *Phys. Stat. Sol. (a)*, **63**, 423 (1980).
- [6] B. N. Mukashev, M. F. Tamendarov, S. Z. Tokmoldin, and V. V. Frolov, *Phys. Stat. Sol. (a)*, **91**, 509 (1985).
- [7] R. J. Bell, "Introductory Fourier Transform Spectroscopy" (Academic Press, New York, 1972).
- [8] "FT-IR Theory" (Nicolet Analytical Instruments, 1986).
- [9] G. R. Fowles, "Introduction to modern optics" (Dover Publications Inc, New York, 1975).

IV. The positive charge state of bond-centre hydrogen in silicon

A. Introduction

According to the introduction given in chapter I, the infrared absorption spectrum of crystalline silicon implanted with protons at ~80 K, and measured *in-situ*¹ without annealing of the sample, is much less complex than the spectrum observed after implantation at room temperature (see Fig. I.4 and Fig. I.5). The spectrum observed by Stein [1] after implantation at ~80 K is dominated by an intense absorption line at 1990 cm⁻¹, whereas the spectrum observed after annealing at room temperature contains more than ten distinct absorption lines in the Si-H stretch region 1800 - 2250 cm⁻¹. The 1990-cm⁻¹ line disappeared upon annealing at ~150 K and exhibited significant annealing even at 80 K when the implanted surface was illuminated with band-gap light. Based on the similarity in annealing behaviour of the 1990-cm⁻¹ line and the neutral monovacancy, Stein tentatively ascribed the 1990-cm⁻¹ line to hydrogen bound in a vacancy cluster [1].

The present chapter describes *in-situ* infrared absorption studies of the 1990-cm⁻¹ line and provides an unambiguous assignment of the line to the positive charge state of isolated hydrogen located at the bond-centre (*BC*) site. In particular, it is shown that implantation of protons into silicon below 20 K gives rise to a single, very intense absorption line at 1998 cm⁻¹, when the spectrum is measured at 9 K. The 1998-cm⁻¹ line shifts down in frequency with increasing measuring temperature and coincides with the 1990-cm⁻¹ line observed by Stein at ~80 K, which shows that the two lines are identical. Isochronal annealing studies of the 1998-cm⁻¹ line carried out with the sample illuminated with band-gap light and in the dark reveal that the annealing behaviour of the 1998-cm⁻¹ line is in very good agreement with that reported previously for the AA9 EPR signal [2], which originates from the neutral charge state of isolated hydrogen located at the *BC* site (H_{BC}^0) [3]. However, the AA9 signal is observed only during illumination with band-gap light, whereas the 1998-cm⁻¹ line is observed without band-gap illumination and decreases in intensity when the sample is illuminated. Based on these observations the 1998-cm⁻¹ line is assigned to the positive charge state of bond-centre hydrogen (H_{BC}^+) in silicon.

Isolated hydrogen centres in silicon have been studied with a variety of experimental techniques, including EPR, DLTS, channeling, infrared spectroscopy,

¹ In this thesis, the term *in-situ* designates a type of experiment in which the sample is both prepared (e.g. by ion implantation) and studied at cryogenic temperature without heating the sample between the preparation and the experimental investigation.

and μ SR. Sec. IV.A.1 gives a survey of the experimental studies carried out to date with special emphasis on the microscopic structure of the centres. Isolated hydrogen in silicon has also been subject to a large number of theoretical studies in the past two decades. The results of the theoretical studies are briefly discussed in Sec. IV.A.2.

1. Survey of experimental studies of isolated hydrogen in silicon

Until the late eighties, structure-sensitive techniques, such as EPR, had failed to detect and identify isolated hydrogen centres in silicon. The only experimental information on the structure of these centres available at that time was therefore obtained from μ SR. μ SR is a spectroscopic technique, which measures the spin-precession of muons implanted into a specimen, e.g. silicon, placed in a magnetic field. The technique provides structural information on muon-centres similar to that obtainable from EPR. The μ SR studies will not be discussed in detail in this context. Instead, the reader is referred to some of the reviews on the subject [4,5,6]. The relevance of μ SR studies to isolated hydrogen defects stems from the fact that the muon (μ^+) can be regarded as a light ($M_\mu = M_H/9$) radioactive ($\tau = 2.2 \mu\text{s}$) pseudoisotope of hydrogen. Within the adiabatic approximation, the potential energy surface of the muon is identical to that of hydrogen and, consequently, the structures of muon- and hydrogen-related centres are believed to be essentially the same. On the other hand, the small mass of the muon as compared to the proton implies that the dynamics of the two types of centres is very different.

The first complete μ SR spectrum in silicon was reported by Brewer *et al* in 1973 [7]. Three distinct muon states were observed; a diamagnetic state (μ^+) and two paramagnetic states denoted normal muonium (Mu) and anomalous muonium (Mu^*), respectively. Normal muonium has an atomic-like, isotropic hyperfine interaction between the spin of the muon and the unpaired electron, and was ascribed to muonium ($\mu^+ e^-$) fast diffusing between T sites or between sites of lower symmetry. Anomalous muonium has an anisotropic hyperfine tensor with trigonal symmetry and a very small contact density of the unpaired electron at the muon. The origin of Mu^* was heavily debated in the following decade [4,5]. The first step toward the correct assignment of Mu^* was made by Symons in 1984 [8], who proposed that Mu^* (in diamond) corresponds to muonium located at a BC site. The next step was taken in 1988, where μ LCR experiments by Kiefl *et al* [9] showed that Mu^* has two equivalent silicon neighbours and six equivalent next-nearest neighbours, which confirmed that Mu^* indeed originates from a muon located at a BC site. The identification of the sites associated with the two muonium states has changed the nomenclature somewhat. Normal (anomalous) muonium is now denoted Mu_T^0 (Mu_{BC}^0) in the literature. The new nomenclature is used in the remainder of this thesis.

The first observation of a hydrogen-related defect in silicon by EPR was reported in 1987 by Gorelkinskii *et al*, who observed a signal, called AA9, by *in-situ* EPR studies of silicon implanted with protons at 80 K [10]. The AA9 signal originated from a spin- $\frac{1}{2}$ centre with trigonal symmetry and was only observed during illumination with band-gap light. The signal exhibited a proton hyperfine splitting and additional splittings were observed due to hyperfine interactions with ^{29}Si nuclei at two equivalent sites. The AA9 signal disappeared upon annealing at ~ 180 K. Gorelkinskii *et al* originally ascribed the AA9 signal to an interstitial silicon atom at a BC site with one of its dangling bonds saturated by a hydrogen atom. However, after the identification of anomalous muonium as muonium at the BC site [9], the AA9 EPR data were reinterpreted [3,5,11]. Both the AA9 centre and Mu_{BC}^0 have trigonal symmetry, two equivalent silicon nearest neighbours, and a very small electron density at the site of the proton or muon. In addition, the proton hyperfine interaction of the AA9 centre is very similar to the muon hyperfine interaction of Mu_{BC}^0 , when the difference in magnetic moment of the proton and the muon is taken into account [3]. Based on these observations the AA9 signal was assigned to the proton counterpart of Mu_{BC}^0 in silicon, i.e. to H_{BC}^0 .

This assignment is consistent with channeling measurements of the lattice location of deuterons in silicon reported by Bech Nielsen in 1988 [12]. The deuterons were implanted into silicon at ~ 30 K, and the subsequent channeling measurements were performed *in-situ* at ~ 30 K. The channeling measurements revealed that 80 ± 3 % of the deuterons occupied near-BC sites at 30 K, while 20 ± 3 % were located near T sites. An annealing stage was observed at ~ 140 K, after which the deuterons were distributed with 67 ± 3 % located near BC sites and 33 ± 3 % near T sites.

In 1984, Irscher *et al* reported *in-situ* DLTS and C-V studies of the electronic levels produced by implantation of protons into silicon at liquid nitrogen temperature [13]. The implantation of protons gave rise to a hydrogen-related donor level, called $E3'$, at $E_c - E_t \sim 0.2$ eV. The area density of $E3'$ centres nearly equalled the dose of protons implanted, which led Irscher *et al* to conclude that the $E3'$ centre contains a single hydrogen atom. The $E3'$ level disappeared upon annealing at ~ 120 K in *n*-type and at ~ 250 K in *p*-type silicon. The formation of approximately one $E3'$ centre per implanted proton and the dominance of the 1990-cm^{-1} line in the infrared spectrum observed by Stein [1] led Irscher *et al* to suggest that the two signals are related.

The $E3'$ level was reinvestigated by Holm *et al* in 1991 by DLTS and C-V measurements on p^+n and Schottky diodes implanted with protons at ~ 45 K [14]. The ionisation enthalpy of the level was found to be $E_c - E_t = 0.16 \pm 0.01$ eV. At zero bias, the $E3'$ level annealed at ~ 100 K, whereas it annealed at ~ 210 K under reverse bias. After annealing the $E3'$ level could be retrieved by cooling below the annealing

temperature followed by injection of holes under forward bias, which indicates that the DLTS-invisible centre formed by annealing is the true ground state, and that the centre giving rise to the $E3'$ donor level is metastable. The $E3'$ centre was lost irreversibly upon annealing above ~ 250 K. C-V measurements suggested that the $E3'$ centre is neutral at zero bias and positively charged under reverse bias, and that the DLTS-invisible state is negatively charged. Based on qualitative similarities between the $E3'$ signal and theoretical predictions for isolated hydrogen, $E3'$ was assigned to the donor level (0/+) of H_{BC} and the DLTS-invisible centre to H_T^- .

The correlation of the $E3'$ level and the AA9 EPR signal was studied in more detail by Bech Nielsen *et al* in 1994 [2]. Silicon was implanted with protons at multiple energies at ~ 10 K, and during illumination with band-gap light the AA9 signal was observed. The dependence of the AA9 intensity on measuring temperature was found to be consistent with the unpaired electron of the AA9 centre (H_{BC}^0) being thermally emitted from the $E3'$ donor level at ~ 80 K. In addition, it was shown that the AA9 signal disappeared upon annealing at ~ 100 K if the sample was illuminated with band-gap light during annealing. The annealing during illumination was consistent with the first-order process observed for the zero bias anneal of $E3'$, provided that thermal ionisation of the level was taken into account. Finally, it was shown that the annealing of AA9 in the dark was in good agreement with that observed for $E3'$ under reverse bias conditions. The measurements confirmed that the $E3'$ level and the AA9 signal originate from the same centre, which is hydrogen located at a BC site.

In 1996, Gorelkinskii *et al* reported an indirect study of the diamagnetic centre, which converts into H_{BC}^0 during illumination [15]. Silicon was implanted with protons at 80 K, and after the implantation the AA9 EPR signal was observed during illumination. The sample was then subjected to a uniaxial stress along a $\langle 110 \rangle$ direction at 170 K in the dark. After cooling to 80 K under stress, the stress was removed, and the AA9 spectrum was measured. Before the stress treatment, the AA9 signal was consistent with a random orientational distribution of H_{BC}^0 centres, whereas the AA9 signal observed after the stress treatment exhibited a significant alignment of the H_{BC}^0 centres. The defect alignment was induced in the dark, where the defect is diamagnetic. Hence, the uniaxial stress study shows that the diamagnetic centre has less than cubic symmetry. Moreover, the observation that the defect alignment is preserved during formation of H_{BC}^0 by illumination strongly suggests that no site change is involved in the formation of H_{BC}^0 from the diamagnetic centre. As pointed out by Gorelkinskii, these observations strongly suggest that the diamagnetic hydrogen species is H_{BC}^+ and confirm the assignments of the $E3'$ level and the AA9 signal to hydrogen at a BC site.

According to μ SR [4,5,6] and theory (see Sec. IV.A.2), hydrogen can exist at or close to the T site of the silicon crystal in a neutral and/or negative charge state. None of these hydrogen species have at present been detected with structure-sensitive techniques and, hence, no structural information on the centres exists. Nevertheless, strong evidence for the existence for a negatively charged hydrogen species (H^-) has been reported. In 1990, Tavendale *et al* [16] and Zhu *et al* [17] independently studied the drift of hydrogen released by thermal dissociation of donor-hydrogen complexes in the depletion region of Schottky diodes. The hydrogen was found to drift in the direction opposite to the electric field in the depletion region, showing that it was negatively charged.

In 1992, Johnson *et al* [18] reported fast capacitance transient studies of H^- released from phosphorous-hydrogen complexes by a hole-pulse. The measurements indicated that H^- is stable when the Fermi level is positioned 0.3 eV above mid-gap. In the light of the identification of the $E_{3'}$ level at $E_c - E_t = 0.16 \pm 0.01$ eV as the (0/+) donor level of isolated hydrogen [2,14], the results of Johnson *et al* imply that the (-/0) acceptor level of isolated hydrogen is located at least 0.2 eV below the donor level [18]. Hence, the fast capacitance transient measurements suggested that isolated hydrogen in silicon is a “negative- U ” impurity.

Johnson *et al* reported a more detailed study of the location of the acceptor level of isolated hydrogen in 1994 [19]. The rates of the reactions $H^+ + 2e^- \leftrightarrow H^-$ were determined by fast capacitance transient measurements, and with the assumption that the measured reaction rates are representative for the $H^0 + e^- \leftrightarrow H^-$ reactions, the acceptor level was found to be located essentially at mid-gap (the location of the acceptor level was subsequently corrected to ~ 0.05 eV below mid-gap [20]). The validity of the basic assumption of the analysis, and hence the correctness of the acceptor level position obtained, has subsequently been disputed [21].

2. Survey of theoretical studies of isolated hydrogen in silicon

The properties of isolated hydrogen in silicon have been studied extensively at various levels of theory in the past two decades. A review of the theoretical studies was recently given by Estreicher [22]. The theoretical studies can largely be divided into two periods. Before 1986, the calculations were carried out with no or minor relaxation of the silicon atoms surrounding the hydrogen atom. Around 1986 it was realised that the relaxation is an essential feature of the interaction between the hydrogen atom and the lattice and, thus, that calculations without lattice relaxations do not provide the true picture of the interaction.

The present survey starts in 1984, where Symons [8] proposed that anomalous muonium in diamond corresponds to muonium located at a *BC* site. This proposition triggered a series of theoretical studies in silicon, which included the relaxed *BC* site. To my knowledge, the first report on such a study was published in 1986 by Estle *et al* [23]. Approximate *ab initio* Hartree-Fock calculations were carried out on a hydrogen-terminated cluster containing 20 silicon atoms and with a muon was added either at the *T*, *H* or *BC* site (see Fig. I.1). Without relaxation of the silicon atoms neighbouring the muon, the total energy was lowest at the *T* site. For the *BC* configuration it was found that relaxation of the two nearest-neighbour silicon atoms away from the *BC* site resulted in a large decrease in the total energy of the cluster. The global energy minimum was obtained at a symmetric relaxation corresponding to an increase in Si-Si bond length of ~35%. With this configuration the *BC* site was lower in energy than the *T* site by 0.9 eV. The work by Estle *et al* was, to my knowledge, the first to clearly demonstrate the importance of lattice relaxations in the theoretical modelling of hydrogen defects in silicon.

In the period from 1987 to 1991, more than ten theoretical studies of isolated hydrogen in silicon were reported [24-34]. The individual studies will not be discussed in detail here. Instead, the predictions of the theoretical studies are compared and discussed. Table IV.1 shows the stable sites of isolated hydrogen in silicon in the positive, neutral, and negative charge state predicted by theory.

The theoretical studies agree that isolated hydrogen in silicon can exist in either a positive, neutral, or negative charge state. In the positive charge state only the BC site is stable (H_{BC}^+), whereas the negative charge state only is stable in the open part of the lattice at either the AB or the T site (both denoted H_T^-). The neutral charge state may be metastable with a global energy minimum at the BC site (H_{BC}^0) and a secondary minimum in the open part of the lattice (e.g. the T or AB site, both denoted H_T^0). There is no agreement on the depth of the secondary minimum.

All the calculations agree that the wavefunction of the unpaired electron of H_{BC}^0 can be described as an antibonding combination of atomic orbitals of the two nearest neighbour silicon atoms. Such a wavefunction has a node at the BC site, consistent

Table IV.1. The stable sites of isolated hydrogen in silicon in the positive, neutral, and negative charge state predicted by theory. Only calculations where the relaxed BC site was considered are included. The table is, apart from few modifications, taken from Ref. [22].

First author	H^0		H^+	H^-
	Stable	Metastable (ΔE)		
Estle [23] ^a	BC	T (0.3)		
Estreicher [24], Chu [32] ^b	BC	T (0.3)	BC	
Deák [25,26,33] ^c	BC	AB (0.9)	BC	AB
Van de Walle [27,29] ^d	BC	none	BC	T
DeLeo [28] ^e	BC	^e	BC	
Chang [30] ^f	T	BC (0.25)	BC	T
Briddon [31], Jones [34] ^g	BC	AB (0.1)	BC	T

ΔE is the energy difference (in eV) between the stable and the metastable configuration. The calculated relaxation of the two silicon atoms neighbouring H at the BC site is always around 35-40%. Notice that the references are enumerated according to the date of publication.

^a Approximate *ab initio* Hartree-Fock (PRRDO) on a hydrogen-terminated Si_{20} -cluster. Only nearest neighbours are relaxed.

^b *Ab initio* Hartree-Fock and PRRDO on hydrogen-terminated clusters containing from 2 to 44 Si atoms. The $BC \rightarrow T$ barrier is < 0.89 eV. The prediction for H_{BC}^+ is from Ref. [32].

^c Semi-empirical MINDO/3 on 32-atom supercells. The H_{AB}^- prediction is from Ref. [33], in which the authors find that H_{BC}^0 is stable in a narrow range of Fermi level positions.

^d LDF (*ab initio*) on 32-atom supercells. The atoms are fully relaxed for all positions of H, H_{BC}^+ has lowest energy in intrinsic and p -type silicon and H_T^- is energetically favoured in n -type material.

^e Semi-empirical MNDO on small clusters (Si_5H_{13} and Si_8H_{19}) containing no high-symmetry sites other than BC . H_{BC}^0 is found to have two degenerate minima along the bond axis, just off and on either side of BC .

^f LDF (*ab initio*) on 8- and 18-atom supercells. H_{BC}^+ is stable in intrinsic and p -type silicon, whereas H_T^- has lowest energy in n -type material.

^g LDF (*ab initio*) on $Si_{51}H_{52}$ cluster.

Table IV.2. Calculated vibrational frequencies (cm^{-1}) for isolated hydrogen in silicon.

First author	H^0		H^+	H^-
	BC	AB	BC	AB
Estreicher [24] ^a				
Deák [26]	784	2223		
Deák [35,36]	977	2179	1950	2036
DeLeo [28] ^b	800			
Van de Walle [29]	1945		2210	
Briddon [31], Jones [34] ^c	1768		2203	

^a The energy surface for displacement of H along the bond-axis was found to be U-shaped rather than parabolic. The curvature for displacements along the bond was ~20% smaller than for displacements perpendicular to it. Estimated frequency: $\omega_{\text{Si-H}}/3$, where $\omega_{\text{Si-H}}$ is a typical Si-H stretch frequency.

^b The minimum-energy configuration was found slightly displaced from the BC site along the bond-axis and the energy surface was extremely anharmonic. The quoted frequency was found by solving the one-dimensional vibrational problem exactly.

^c The frequencies presented in Ref. [34] are identical to those in Ref. [31].

with the very small contact density observed at the site of the proton and muon for the AA9 signal [10] and Mu_{BC}^0 [9].

Three of the studies also considered the relative stability of the different charge states as a function of the Fermi level position [29,30,33]. They all agree that H_{BC}^+ is stable in material with the Fermi level located below the centre of the band-gap, and that H_T^- is favoured when the Fermi level is close to the conduction band. With respect to the intermediate region of Fermi levels no consensus has been reached. Van de Walle *et al* [29] and Chang *et al* [30] found that the neutral charge state is metastable for all Fermi level positions, i.e. that hydrogen is a “negative-U” impurity. On the contrary, Deák *et al* found that H_{BC}^0 is stable in a narrow range of Fermi level positions close to mid-gap [33]. Although H_{BC}^0 may be metastable, all the calculations (apart from Ref. [28]) agree that both H_{BC}^+ and H_{BC}^0 correspond to minima in the total energy surface. The position of the (0/+) level of H_{BC} could not be calculated accurately at the levels of theory used.

The vibrational properties of isolated hydrogen have been considered in several theoretical studies [24,26,28,29,31,35,36]. The calculated stretch frequencies are summarised in Table IV.2. The frequencies of the two charge states of hydrogen at the BC site have been calculated both with *ab initio* [29,31] and semi-empirical theory [26,28,35,36]. In the particular case of H_{BC}^0 , the theoretical predictions can clearly be divided into two groups. Semi-empirical calculations obtain very small stretch frequencies ($\sim 900 \text{ cm}^{-1}$), whereas *ab initio* calculations based on density functional theory predict that the stretch frequency is in the region typical for covalent Si-H bonds. For H_{BC}^+ the *ab initio* and semi-empirical calculations agree that the stretch

frequency is located in the Si-H stretch region. The stretch frequency of the neutral and negative charge state of isolated hydrogen in the open part of the lattice has only been calculated with semi-empirical theory [26,35,36]. For both charge states the stretch frequencies are predicted to be located in the Si-H stretch region (see Table IV.2).

B. Experimental

The silicon samples used in the present studies were cut from high-resistivity single crystals and polished, as described in Sec. III.A. The samples for annealing and isotope substitution measurements were mounted in the closed-cycle cryostat described in Sec. II.B.4. The outer wall of the cryostat was rotated so that the plane of the aluminium window was parallel to the polished surface of the sample. Then the cryostat was mounted in a vacuum chamber attached to a beam-line of the Tandem accelerator, the cryostat was cooled to 9 K, and protons and/or deuterons were implanted through the aluminium window and into the sample. The temperature measured ~ 3 cm from the sample did not exceed 20 K during the implantation process. Protons (deuterons) were implanted at 61 (30) different energies in the range 5.3 - 11.2 MeV (6.7 - 11.5 MeV) to a total dose of $5 \times 10^{15} \text{ cm}^{-2}$ or $1 \times 10^{16} \text{ cm}^{-2}$ (see details in Table III.1), with the dose at each energy adjusted to ensure a nearly uniform distribution of implants from the surface and 0.6 mm (0.3 mm) into the sample. One sample (Si:HD) was coimplanted with overlapping profiles of protons and deuterons to a dose of $1 \times 10^{16} \text{ cm}^{-2}$ of each species. The implantation of protons was carried out at the same energies and with the same doses as the samples used for the EPR measurements on the AA9 centre reported in Ref. [2].

After the implantation, the cryostat was moved to the infrared spectrometer and the outer wall of the cryostat was rotated by 90° , which allowed the infrared light to propagate through the CsI windows and the sample. The sample temperature did not exceed 20 K during the transfer process. The infrared absorption of the implanted sample was measured with the FTIR spectrometer described in Sec. III.A.3 at a sample temperature of 9 K, unless stated otherwise. The spectral resolution was 0.7 cm^{-1} . Some of the absorption measurements were performed with a low-pass filter with a cut-off frequency of 4000 cm^{-1} placed in the infrared beam between the source and the cryostat.

One of the proton-implanted samples was used for absorption measurements in combination with illumination of the sample with band-gap light from a *cw*-Nd:YAG laser ($\lambda = 1.06 \mu\text{m}$). The laser beam was guided into the sample compartment of the spectrometer by an optical fiber. The output-end of the fiber was placed between the cryostat and the detector, offset by ~ 1 cm from the optical axis of the

spectrometer/cryostat, and with the laser beam directed through the CsI window of the cryostat and onto the sample. The light intensity at the sample was measured to be 0.3 W/cm^2 with a Gentec TPM-310B powermeter.

C. Results

1. Infrared absorbance and isotope substitution

The infrared absorbance spectrum of proton-implanted silicon measured *in-situ* after implantation at $\sim 20 \text{ K}$ is shown in Fig. IV.1. The spectrum consists of a single very intense absorption line at 1998 cm^{-1} . Also shown in Fig. IV.1 is the spectrum measured with the same sample after annealing at 260 K . In contrast to the “as implanted” spectrum, this spectrum contains more than ten absorption lines in the Si-H stretch region, which are ~ 80 times less intense than the 1998-cm^{-1} line. When deuterons are implanted instead of protons, the 1998-cm^{-1} line is not observed. Instead, a very intense line appears at 1449 cm^{-1} (see Fig. IV.2), which disappears upon annealing at the same temperature as the 1998-cm^{-1} line. The lines at 1449 cm^{-1} in Si:D and 1998 cm^{-1} in Si:H are ascribed to the same defect containing deuterium and hydrogen, respectively. The ratio of the two frequencies is $\sim \sqrt{2}$, which shows that the 1998-cm^{-1} line originates from a hydrogen-related local vibrational mode. The large intensity of the 1998-cm^{-1} line and the low concentration of impurities in the sample practically exclude that the hydrogen atom is bonded to other elements than silicon and the 1998-cm^{-1} line is therefore ascribed to a Si-H stretch mode. When protons and deuterons are implanted with overlapping profiles, no additional lines are

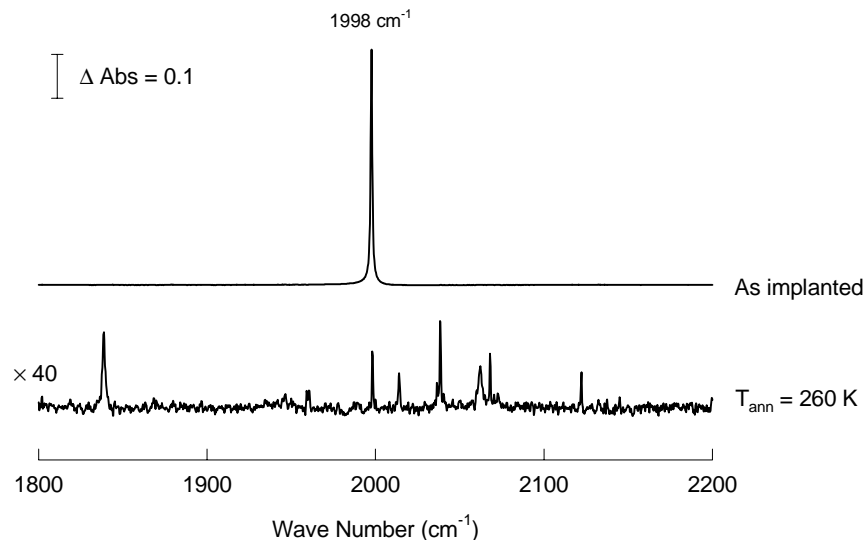


Fig. IV.1. Absorbance spectrum of silicon implanted with protons below 20 K and measured without annealing (top spectrum), and after annealing at 260 K (bottom spectrum). Notice that the bottom spectrum is multiplied by a factor of 40.

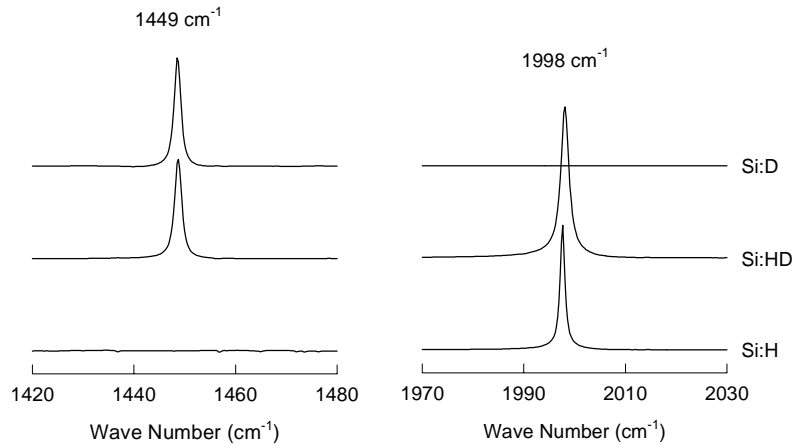


Fig. IV.2. Absorbance in the Si-D and Si-H stretch-regions of silicon implanted with protons (Si:H), deuterons (Si:D), and both protons and deuterons with overlapping profiles (Si:HD). The Si:H and Si:D sample was implanted with a dose of $5 \times 10^{15} \text{ cm}^{-2}$ and $1 \times 10^{16} \text{ cm}^{-2}$, respectively. The Si:HD sample was implanted with a dose of $1 \times 10^{16} \text{ cm}^{-2}$ of each isotope.

observed as compared to samples implanted with a single isotope (see Fig. IV.2). This shows that the 1998-cm^{-1} centre contains a single hydrogen atom.

2. Isochronal annealing

The annealing behaviour of the 1998-cm^{-1} line was studied in two isochronal annealing series. In one of the studies, the sample was illuminated with band-gap light from the Nd:YAG laser during annealing, whereas the second annealing sequence was carried out in the dark. In both cases, the steps in annealing temperature were 20 K and the annealing time 15 minutes.

Fig. IV.3 shows the normalised intensity of the 1998-cm^{-1} line as a function of annealing temperature. Two distinct annealing stages are observed both with and without illumination. When the annealing is carried out in the dark, the first stage is observed at ~ 100 K, at which the intensity of the 1998-cm^{-1} decreases by $\sim 20\%$. The second stage takes place at ~ 200 K, where the 1998-cm^{-1} line disappears. When the sample is illuminated with band-gap light during annealing, the first stage starts at ~ 60 K, and leads to a reduction in the line intensity of 20% at 100 K, where the second stage takes over and brings the intensity down to zero at 160 K. Further discussion of the first annealing stage is postponed to Sec. IV.D.

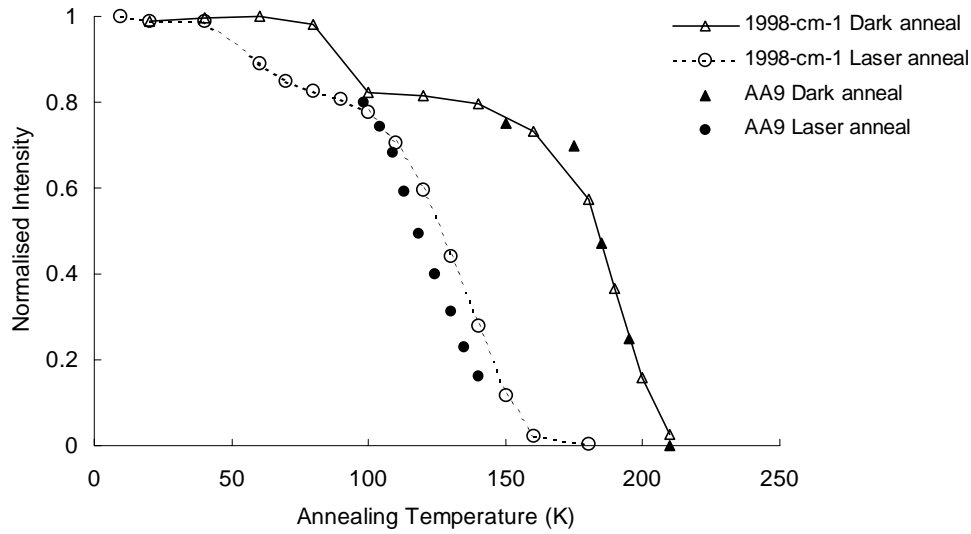


Fig. IV.3. Normalised intensity of the 1998-cm^{-1} line vs. annealing temperature (open symbols). The triangles and circles correspond to annealing in the dark and during illumination, respectively. The filled symbols show the annealing behaviour of the AA9 centre [2].

Fig. IV.3 also compares the annealing behaviour of the 1998-cm^{-1} line with that of the AA9 EPR signal [2]. The comparison is justified by the fact that the samples used in the two studies were implanted at the same energies and with the same doses. In addition, the intensity of the band-gap light used for illumination and the annealing time was approximately the same in the two studies. It is evident from Fig. IV.3 that the second annealing stage of the 1998-cm^{-1} line is in very good agreement with the annealing of the AA9 signal, both with and without illumination. This strongly suggests that the 1998-cm^{-1} line originates from the diamagnetic centre which converts into H_{BC}^0 during illumination with band-gap light.

3. Infrared absorption with and without band-gap light

In order to study the effect of band-gap light on the intensity of the 1998-cm^{-1} line, the absorbance spectrum of the Si:H sample was measured, while the sample was illuminated with band-gap light from the Nd:YAG laser. As shown in Fig. IV.4, the intensity of the 1998-cm^{-1} line is reduced by 20% when the sample is illuminated with laser light during the absorption measurement. When the laser is turned off, the intensity of the 1998-cm^{-1} line returns to its

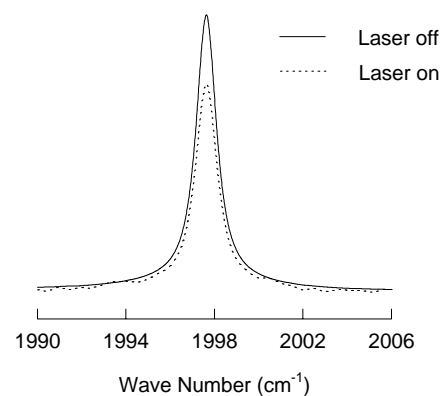


Fig. IV.4. Absorbance profile of the 1998-cm^{-1} line measured without (solid line) and with (dotted line) laser illumination.

original value, which shows that the reduction in intensity is reversible. Moreover, the absorbance spectrum was measured with a low-pass filter placed in the infrared beam between the source and the sample, which prevented light from the source with frequencies above 4000 cm^{-1} from reaching the sample. The intensity of the 1998-cm^{-1} line increased with $\sim 10\%$ when the low-pass filter was placed in the infrared beam. The observation of the 1998-cm^{-1} line without band-gap light and the reversible decrease in intensity during illumination strongly suggests that illumination with band-gap light causes a fraction of the 1998-cm^{-1} centres to convert into H_{BC}^0 observed by EPR [2].

D. Discussion

The isochronal annealing and infrared absorption measurements with and without band-gap light presented in Sec. IV.C show that the 1998-cm^{-1} line originates from the diamagnetic centres that partly converts into H_{BC}^0 in the presence of band-gap light. As described in Sec. IV.A.1, the uniaxial stress study by Gorelkinskii *et al* [15] showed that the stress-induced defect alignment is preserved by conversion of the diamagnetic centre to H_{BC}^0 by illumination. This shows that no reorientation is involved in the conversion and strongly suggests that the diamagnetic centre is H_{BC}^+ . Based on these observations, the 1998-cm^{-1} line is assigned to the stretch mode of H_{BC}^+ in silicon.

Two decades ago, Stein performed the first *in-situ* infrared absorption experiment on proton-implanted silicon [1]. Protons with energies of 50 and 100 keV were implanted at 80 K to a dose of $6 \times 10^{15}\text{ cm}^{-2}$ at each energy. Then, the infrared absorption spectrum was measured at 80 K. As shown in Fig. I.5, the spectrum obtained by Stein is dominated by a peak at 1990 cm^{-1} with a FWHM of 20 cm^{-1} . The absorbance spectrum of the present work contains a single line at 1998 cm^{-1} , which shifts down in frequency and broadens when the measuring temperature is increased from 9 K. As shown in Fig. IV.5, the absorption profile of the 1998-cm^{-1} line is very similar to that of the 1990-cm^{-1} line at 100 K. At this temperature both lines are centred at 1990 cm^{-1} and have similar asymmetric line

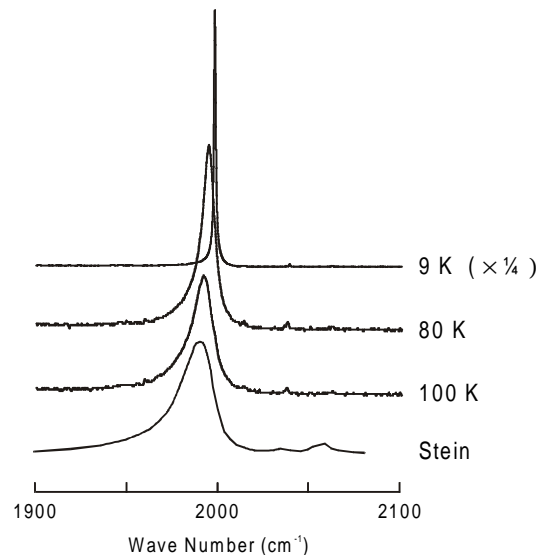


Fig. IV.5. Comparison of the 1990-cm^{-1} line observed by Stein [1] and the 1998-cm^{-1} line measured at 9, 80, and 100 K. The absorbance scale of Stein's spectrum is arbitrary.

shapes. The width of the 1998-cm⁻¹ line is 15 cm⁻¹ at 100 K, which is somewhat less than the 20 cm⁻¹ of the line observed by Stein. The peak concentration of hydrogen in Stein's sample was ~0.6 at. %, whereas the samples studied in the present work have a uniform hydrogen concentration of ~0.00017 at. %. Hence, the larger width of the line observed by Stein may be explained by inhomogeneous broadening caused by the much larger concentration of hydrogen and damage in Stein's sample. The striking similarities between the 1990-cm⁻¹ line observed by Stein and the 1998-cm⁻¹ line of this work with respect to frequency, absorption profile, production, and annealing show that the two lines are identical. Moreover, the observation that the 1998-cm⁻¹ line coincides with the 1990-cm⁻¹ line at a measuring temperature of ~100 K indicates that Stein's measurements were performed at a somewhat higher temperature than the 80 K stated in Ref. [1].

As shown in Fig. IV.1, the intensity of the 1998-cm⁻¹ line is extremely large compared to the total intensity of its annealing products. This suggests that the 1998-cm⁻¹ mode either has an unusually large effective charge or that the majority of H_{BC}^+ centres convert into infrared-inactive defects upon annealing. The effective charge of the 1998-cm⁻¹ mode can be estimated from the intensity of the 1998-cm⁻¹ line by assuming that all the implanted protons form H_{BC}^+ centres and thus contribute to the intensity of the absorption line. As discussed in Sec. III.B.2, the intensity of an absorption line consists of contributions from light having experienced an even number of internal reflections in the sample. If it is assumed that the transmission coefficients t_m are given by Eqs. III.7 and III.8 and the absorbance by Eq. III.9, the contribution from directly transmitted light ($m = 0$) to the intensity of the 1998-cm⁻¹ line can be estimated to be ~87%. The intensity of the 1998-cm⁻¹ line measured *without* low-pass filter is $I_{1998} = 1.0 \pm 0.2$ cm⁻¹, where the error bar reflects the uncertainty in the implanted dose. Correcting for internally reflected light and the ~10% reduction in intensity of the 1998-cm⁻¹ line caused by band-gap light from the source, the absorption strength of the 1998-cm⁻¹ mode is

$$\int_{1998\text{-cm}^{-1}\text{ line}} l\alpha(\sigma)d\sigma \times \log_{10}e = 1.0 \pm 0.2 \text{ cm}^{-1} . \quad (\text{IV.1})$$

Insertion of Eq. IV.1, $g_{\Gamma} = 1$ (non-degenerate mode), $Nl = D = 5 \times 10^{15}$ cm⁻², and $\mu = M_{\text{H}}$ (see footnote 2) into Eq. II.2 gives the estimate $\eta_{1998} = 3.0 \pm 0.3$. The effective charge of the 1998-cm⁻¹ mode is about six times larger than the mean effective charge $\langle \eta \rangle = 0.5$ of the Si-H stretch modes observed after annealing at 260 K, but is comparable to those of the Si-H stretch mode of the acceptor-hydrogen complexes

² Due to the large difference in the mass of hydrogen and silicon, the error introduced by neglecting the co-vibration of the silicon atoms is negligible.

B-H and Al-H in silicon [37]. The large effective charge of the 1998-cm⁻¹ mode supports the assignment of the line at 1998 cm⁻¹ to the charged H_{BC}^+ defect.

As shown in Fig. IV.3, the primary annealing stage observed at ~100 K in the dark and at ~60 K during illumination reduces the intensity of the 1998-cm⁻¹ line by ~20 %. Instead, three new lines appear at 1872, 1879, and 2038 cm⁻¹. The 2038-cm⁻¹ line has recently been identified as the Si-H stretch mode of the monovacancy binding a single hydrogen (VH) [38]. Thus, the formation of the 2038-cm⁻¹ line shows that monovacancies are involved in the primary annealing stage. Because of the damage induced by implantation, the Fermi level is believed to be located deep in the upper half of the band-gap. This suggests that the monovacancies either are in the negative (V^-) or double negative (V^{--}) charge state [39]. V^- starts to migrate at ~80 K [39], whereas the temperature for the on-set of V^- migration, to my knowledge, is unknown [39]. The formation of VH in the primary annealing stage is consistent with that the monovacancies are in the V^- charge state, and are trapped at the H_{BC}^+ centres after the on-set of V^- migration at ~80 K. Additional support to this interpretation is given by the uniaxial stress studies performed by Gorelkinskii *et al* [15], which showed that the jump-rate of H_{BC}^+ in the dark at 100 K is about one jump per 65 years. Hence, the H_{BC}^+ centres are practically immobile at the conditions of the first annealing stage. The downshift in temperature of the primary annealing stage induced by band-gap illumination might be explained by photo-induced diffusion of monovacancies [40]. The 1872- and 1879-cm⁻¹ lines formed in the primary annealing stage have not been reported previously. The lines originate from distinct complexes, which disappear after annealing at ~160 K. The similar stretch frequency and annealing behaviour of the two lines indicate that they originate from structurally very similar centres. The formation of the centres in the same annealing stage as VH suggests that they may be vacancy-related.

The final point to be addressed in this discussion is the annealing of the 1998-cm⁻¹ line at ~200 K in the dark. According to Gorelkinskii *et al*, the activation energy for annealing of the AA9 signal in the dark is $E_A = 0.48 \pm 0.04$ eV [11] and the activation energy for reorientation of H_{BC}^+ is $E_A = 0.43 \pm 0.02$ eV [15]. The good agreement between these activation energies indicates that the rate-limiting step for annealing of H_{BC}^+ in the dark is the thermally activated jump between BC sites. Hence, the annealing of the 1998-cm⁻¹ line at ~200 K in the dark may be ascribed to the on-set of H_{BC}^+ migration, which leads to trapping of the hydrogen by implantation-induced defects or by other hydrogen atoms. This interpretation is supported by the observation of the absorption lines at {1838, 2062}, 2068, and 2121 cm⁻¹ after annealing at 260 K (see Fig. IV.1), which originate from the H_2^* defect [41], the divacancy binding one hydrogen atom [38], and the monovacancy binding two

hydrogen atoms,³ respectively. In addition, thermal migration of self-interstitials may play a role in the annealing of the 1998-cm⁻¹ line at ~200 K in the dark. *In-situ* channeling measurements have indicated that the self-interstitials in silicon start to migrate at ~190 K [42] and, hence, they may be trapped by H_{BC}^+ .

E. Conclusion

Implantation of protons into silicon below 20 K gives rise to a single and very intense infrared absorption line at 1998 cm⁻¹. The line originates from a Si-H stretch mode of a centre that contains a single hydrogen atom and has an unusually large effective charge of $\eta_{1998} = 3.0 \pm 0.3$. Isochronal annealing experiments with the sample illuminated with band-gap light and in the dark reveal that the 1998-cm⁻¹ line anneals at two distinct annealing stages. The primary stage is observed at ~100 K in the dark and at ~60 K during illumination, and reduces the intensity of the 1998-cm⁻¹ line by ~20 %. The secondary annealing stage is observed at ~200 K in the dark and at ~160 K during illumination, and is in excellent agreement with that of the AA9 EPR signal under similar conditions. The intensity of the 1998-cm⁻¹ line is reduced by ~20% during illumination, which is ascribed to partial conversion of the 1998-cm⁻¹ centres to H_{BC}^0 . Based on the annealing behaviour and the photo-induced conversion to H_{BC}^0 , the 1998-cm⁻¹ line is ascribed to H_{BC}^+ in silicon. The primary annealing stage of the 1998-cm⁻¹ line is ascribed to the trapping of monovacancies at H_{BC}^+ , whereas the secondary annealing stage is ascribed to the on-set of H_{BC}^+ migration. The 1998-cm⁻¹ line shifts down in frequency and broadens with increasing measuring temperature. At 100 K the line coincides with the 1990-cm⁻¹ line observed previously by Stein, which shows that the two lines are identical. Hence, the long-standing problem of assigning the 1990-cm⁻¹ line to a specific defect is solved.

F. References

- [1] H. J. Stein, Phys. Rev. Lett., **43**, 1030 (1979).
- [2] B. Bech Nielsen, K. Bonde Nielsen, and J. R. Byberg, in "Defects in Semiconductors 17", edited by H. Heinrich and W. Jantsch, Materials Science Forum Vol. 143-147 (Trans Tech, Aedermannsdorf, 1994), p. 909.
- [3] R.B. Gel'fand, V.A. Gordeev, Y.V. Gorelkinskii, R.F. Konopleva, S.A. Kuten, A.V. Mudryi, N.N. Nevinnyi, Y.V. Obukhov, V.I. Rapoport, A.G. Ylyashin, and V.G. Firsov, Fiz. Tverd. Tela, **31**, 176 (1989) [Sov. Phys. Solid State, **31**,

³ The assignment of the 2121-cm⁻¹ line to the monovacancy binding two hydrogen atoms is discussed in detail in chapter VI.

- 1376 (1990)], and V.A. Gordeev, R.F. Konopleva, V.G. Firsov, Y.V. Obukkov, Y.V. Gorelkinskii, N.N. Nevinnyi, *Hyp. Int.*, **60**, 717 (1990).
- [4] B. D. Patterson, *Rev. Mod. Phys.*, **60**, 69 (1988).
- [5] R. F. Kiefl and T. L. Estle in "Hydrogen in Semiconductors: semiconductors and semimetals", vol. 34, edited by J.I. Pankove and N.M. Johnson (Academic Press, New York, 1991).
- [6] R. L. Lichti, to appear in "Hydrogen in Semiconductors II: semiconductors and semimetals", edited by N. Nickel (Academic Press).
- [7] J. H. Brewer, K. M. Crowe, F. N. Gyax, R. F. Johnson, B. D. Patterson, D. G. Fleming, and A. Schenk, *Phys. Rev. Lett.*, **31**, 143 (1973).
- [8] M. C. R. Symons, *Hyp. Int.*, **17-19**, 771 (1984).
- [9] R. F. Kiefl, M. Celio, T. L. Estle, S. R. Kreitzman, G. M. Luke, T. M. Riseman, and E. J. Ansaldo, *Phys. Rev. Lett.*, **60**, 224 (1988).
- [10] Y. V. Gorelkinskii, and N. N. Nevinnyi, *Pis'ma Zh. Tekh. Fiz.*, **13**, 105 (1987) (*Sov. Tech. Phys. Lett.*, **13**, 45, (1987)).
- [11] Y. V. Gorelkinskii, and N. N. Nevinnyi, *Physica B*, **170**, 155 (1991).
- [12] B. Bech Nielsen, *Phys. Rev. B*, **37**, 6353 (1988).
- [13] K. Irmscher, K. Klose, and K. Maass, *J. Phys. C*, **17**, 6317 (1984).
- [14] B. Holm, K. Bonde Nielsen, and B. Bech Nielsen, *Phys. Rev. Lett.*, **66**, 2360 (1991).
- [15] Y. V. Gorelkinskii, and N. N. Nevinnyi, *Mater. Sci. Eng. B.*, **36**, 133 (1996).
- [16] A. J. Tavendale, S. J. Pearton, and A. A. Williams, *Appl. Phys. Lett.*, **56**, 949 (1990).
- [17] J. Zhu, N. M. Johnson, and C. Herring, *Phys. Rev. B*, **41**, 12354 (1990).
- [18] N. M. Johnson and C. Herring, *Phys. Rev. B*, **46**, 15554 (1992).
- [19] N. M. Johnson, C. Herring, and C. G. Van de Walle, *Phys. Rev. Lett.*, **73**, 130 (1994).
- [20] N. M. Johnson, C. Herring, and C. G. Van de Walle, *Phys. Rev. Lett.*, **74**, 1889 (1995).
- [21] Comment to Ref. [19]: C. H. Seager, R. A. Anderson, and S. K. Estreicher, *Phys. Rev. Lett.*, **74**, 4565 (1995); Reply: N. M. Johnson, C. Herring, and C. G. Van de Walle, *Phys. Rev. Lett.*, **74**, 4566 (1995).
- [22] S. K. Estreicher, *Mat. Sci. Eng.*, **R14**, 319 (1995).
- [23] T. L. Estle, S. K. Estreicher, and D. S. Marynick, *Hyp. Int.*, **32**, 637 (1986).
- [24] S. K. Estreicher, *Phys. Rev. B*, **36**, 9122 (1987).
- [25] P. Deák, L. C. Snyder, J. L. Lindström, J. W. Corbett, S. J. Corbett, and A. J. Tavendale, *Physics Letters A*, **126**, 427 (1988).
- [26] P. Deák, L. C. Snyder, and J. W. Corbett, *Phys. Rev. B*, **37**, 6887 (1988).

- [27] C. G. Van de Walle, Y. Bar-Yam, and S. T. Pantelides, *Phys. Rev. Lett.*, **60**, 2761 (1988).
- [28] G. G. DeLeo, M. J. Dorogi, and W. B. Fowler, *Phys. Rev. B*, **38**, 7520 (1988).
- [29] G. Van de Walle, P. J. H. Denteneer, Y. Bar-Yam, and S. T. Pantelides, *Phys. Rev. B*, **39**, 10791 (1989).
- [30] K. J. Chang, and D. J. Chadi, *Phys. Rev. B*, **40**, 11644 (1989).
- [31] P. R. Briddon, and R. Jones, *Hyp. Int.*, **64**, 593 (1990).
- [32] C. H. Chu, and S. K. Estreicher, *Phys. Rev. B*, **42**, 9486 (1990).
- [33] P. Deák, L. C. Snyder, and J. W. Corbett, *Phys. Rev. B*, **43**, 4545 (1991).
- [34] R. Jones, *Physica B*, **170**, 181 (1991).
- [35] P. Deák, M. Heinrich, L.C. Snyder, and J. W. Corbett, *Mater. Sci. Eng. B*, **4**, 57 (1989).
- [36] P. Deák, L.C. Snyder, M. Heinrich, C. R. Ortiz, and J. W. Corbett, *Physica B*, **170**, 253 (1991).
- [37] B. Clerjoud, and D. Côte, *J. Phys.: Condens. Matter.*, **4**, 9919 (1992).
- [38] P. Stallinga, P. Johannesen, S. Herstrøm, K. Bonde Nielsen, B. Bech Nielsen, and J. R. Byberg, *Phys. Rev. B*, **58**, 3842 (1998).
- [39] G. D. Watkins, in “Materials Science and Technology”, edited by W. Schröter (VCH, Weinheim, 1991), vol 4.
- [40] G. D. Watkins, in “Deep Centers in Semiconductors”, edited by S. T. Pantelides (Gordon and Breach Science Publishers, New York, 1986), p. 147.
- [41] J. D. Holbeck, B. Bech Nielsen, R. Jones, P. Sitch, and S. Öberg, *Phys. Rev. Lett.*, **71**, 875 (1993).
- [42] B. Bech Nielsen and J. U. Andersen, *Phys. Rev. B*, **35**, 2732 (1987).

V. The H_2^* dimer in germanium and silicon

A. Introduction

The present chapter describes the identification of the H_2^* dimer in crystalline germanium by local mode spectroscopy. The interest in hydrogen dimers in silicon was triggered in 1983 by two independent suggestions by Corbett *et al* [1] and Mainwood *et al* [2] that molecule formation might explain the large discrepancy in the diffusivity of hydrogen measured with samples containing different concentrations of hydrogen [3]. The suggestions were based on semi-empirical theoretical calculations, which predicted that the gain in energy by formation of a hydrogen molecule at the T site (H_2^T) from two H_T^0 atoms was 0.8 eV [1] and 1 eV [2] per hydrogen atom.¹ The barrier for diffusion of the H_2^T molecule was found to be significantly larger than for the atomic H_T^0 species [2].

Ab initio calculations on hydrogen dimers in *diamond* by Briddon *et al* [4] in 1988 revealed that the configuration shown Fig. V.1, with one hydrogen atom (H_{BC}) located close to a BC site and a second hydrogen atom (H_{AB}) located at the AB site along the same $\langle 111 \rangle$ axis, is lower in energy by 3.3 eV than H_2^T in diamond. In this configuration the H_{BC} atom is strongly bonded to the host atom denoted $X(1)$ in Fig. V.1, whereas H_{AB} forms a strong bond with $X(2)$, which relaxes away from the substitutional site along $\langle 111 \rangle$ into the plane spanned by the three nearest-neighbour host atoms.

The first theoretical study of this hydrogen dimer in silicon was reported by Chang *et al* in 1989 [5]. The *ab initio* calculations predicted that the hydrogen dimer is favoured energetically over two H_{BC}^0 centres by 0.6 eV but that it is less stable than H_2^T by 0.2 eV. Chang *et al* denoted the dimer H_2^* , which has become the generally accepted name of the complex. Since then, the relative stability of the H_2^* and H_2^T dimers in silicon has been studied with semi-empirical theory by Deák *et al* [6] and *ab initio* theory by Jones *et al* [7], Van de Walle [8], and Estreicher *et al* [9]. The calculations agree that the two hydrogen dimers essentially are equally stable. According to the semi-empirical calculations, the H_2^* defect is energetically favoured by ~ 0.2 eV [6], whereas the *ab initio* calculations agree that H_2^T is more stable than H_2^* by ~ 0.1 eV [7-9]. Van de Walle also compared the binding energy of the H_2^* and H_2^T defects with those calculated for a number of other hydrogen-related defects in silicon within the same calculational scheme [8]. The comparison revealed that the hydrogen dimers are more stable than

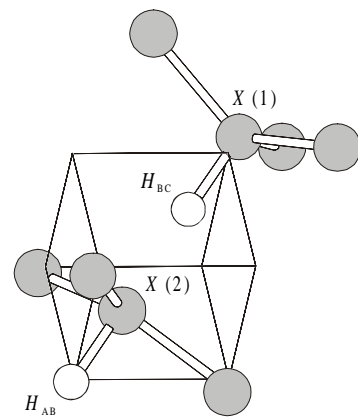


Fig. V.1. The H_2^* defect in a diamond-type lattice.

¹ All the calculated energies quoted in this section are normalised to the energy *per hydrogen atom*.

isolated hydrogen at the BC site by ~ 0.9 eV, whereas they are less stable than the dopant-hydrogen complexes and vacancy-hydrogen complexes by respectively ~ 0.3 eV and ~ 1.8 eV.

The *ab initio* theoretical study by Estreicher *et al* reported in Ref. [9] is a comparative study of the relative stability of the H_{BC}^0 , H_T^0 , H_2^T , and H_2^* defects in diamond, silicon, germanium, and α -tin. The defect structures were energy-optimised by the approximate Hartree-Fock method called PRRDO, and the energies of the configurations were then re-calculated with *ab initio* Hartree-Fock theory. The calculations predicted that the stability of H_2^* decreases significantly relative to H_2^T on passing from diamond to silicon, germanium, and α -tin, with the two dimers being equally stable in silicon. This trend reflects that the stability of H_2^T increases with increasing lattice parameter due to the increase in open volume surrounding the T site, whereas the stability of H_2^* essentially is independent of the lattice parameter of the host crystal. The independence of H_2^* -stability on the lattice parameter is a result of two competing effects: i) the strength of bond between the host atom and hydrogen decreases on passing down group IV of the periodic table and ii) the elastic energy stored in the strain field of the H_2^* decreases from diamond to silicon, germanium, and α -tin. Based on the calculations, the Estreicher *et al* proposed that the equilibrium fraction of dimers present as H_2^* in germanium is less than in silicon.

The H_2^* defect in silicon was identified experimentally by Holbech *et al* in 1993 [11] by a combination of infrared spectroscopy and *ab initio* calculations. Four absorption lines at 817, 1599, 1838, and 2062 cm^{-1} were assigned to the H_2^* defect. The quartet of lines was observed after implantation of protons into silicon at room temperature and disappeared after annealing at ~ 470 K. The 1838- and 2062- cm^{-1} lines were first observed in the pioneering infrared absorption study by Stein [12] (see Fig. I.4), and subsequent uniaxial stress measurements by Bech Nielsen *et al* revealed that both lines originate from $A \rightarrow A$ transitions of trigonal centres [13]. Studies of the annealing behaviour and dose-dependence of the 1838- and 2062- cm^{-1} lines by Mukashev *et al* [14] suggested that they originate from the same defect, which also gives rise to the lines at 817 and 1599 cm^{-1} . Holbech *et al* [11] showed that the 817- cm^{-1} line corresponds to an $A \rightarrow E$ transition if a centre with trigonal symmetry, and a detailed isotope substitution study revealed that the four lines originate from a centre containing two weakly coupled inequivalent hydrogen atoms. The observed isotopic shifts induced by partial isotope substitution were in excellent agreement with those calculated for the H_2^* defect with *ab initio* theory, which strongly supported the assignment of the 817-, 1599-, 1838-, and 2062- cm^{-1} lines to H_2^* in silicon.

In the present chapter it is shown that the H_2^* defect is a prominent defect in proton-implanted germanium. The defect is identified with infrared spectroscopy in combination with isochronal annealing, isotope substitution and uniaxial stress. Absorption lines at 1774 and 1989 cm^{-1} are assigned to stretch vibrations of H_{AB} and H_{BC} (see Fig. V.1) and lines at 765 and 1499 cm^{-1} are ascribed to the fundamental and second-harmonic transition of the bend mode of H_{AB} . The frequencies of the stretch modes and their intensity ratios are discussed in terms of a simple

model based on two coupled Morse-potential oscillators. The model frequencies are in excellent agreement and the intensity ratios in fair agreement with those observed. In conjunction with the experimental studies, *ab initio* calculations on the H_2^* in germanium were performed by R. Jones and J. Goss from the University of Exeter, UK, and by S. Öberg from the University of Luleå, Sweden. The calculations confirm that H_2^* represents a local minimum in the total energy, as suggested by Estreicher *et al* [9]. Moreover, the vibrational frequencies and isotopic shifts of the defect are calculated, and strongly support our assignments. The experimental and theoretical results have been published in Refs. [15,16].

B. Experimental

Samples of high-resistivity, ultra-pure germanium were cut and polished as described in Sec. III.A.1. Then the samples were implanted with protons and/or deuterons at 73 different energies in the range 680 - 2480 keV for protons and 880 - 3000 keV for deuterons. The dose implanted at each energy was adjusted to result in a uniform hydrogen (or deuterium) concentration of 0.05 at. % ($2.2 \times 10^{19} \text{ cm}^{-3}$) from 11 to 43 μm below the surface of the sample. A sample was coimplanted with protons and deuterons with overlapping profiles. The implantations were carried out at a sample temperature of ~ 30 K and after implantation the samples were stored at room temperature.

The infrared absorption measurements were performed with the FTIR spectrometer described in Sec. III.B.3. The spectrometer was set up with a Globar source, a Ge/KBr beamsplitter, and an *MCT-A* detector. The annealing and isotope substitution studies were carried out with the sample mounted in the closed-cycle cryostat described in Sec. III.B.4 at a sample temperature of 9 ± 1 K and with a spectral resolution of 0.5 cm^{-1} . With this setup the infrared absorption could be measured in the range $\sim 600 - 6000 \text{ cm}^{-1}$. The uniaxial stress studies were performed with the stress-rig placed in the flow-cryostat (see Sec. III.B.4). The flow-cryostat was equipped with BaF_2 windows mounted on the inner wall of the cryostat. The inner volume of the cryostat was filled with a helium gas, which provided a good thermal contact between the sample and the cooled inner wall. With this setup the infrared absorption could be measured in the range $\sim 725 - 6000 \text{ cm}^{-1}$. The uniaxial stress measurements were carried out at a sample temperature of ~ 80 K with a resolution of 0.8 cm^{-1} . The measurements were performed with a polariser placed in the infrared beam between the sample and the detector, which made it possible to measure the absorption of light polarised parallel and perpendicular to the applied force separately.

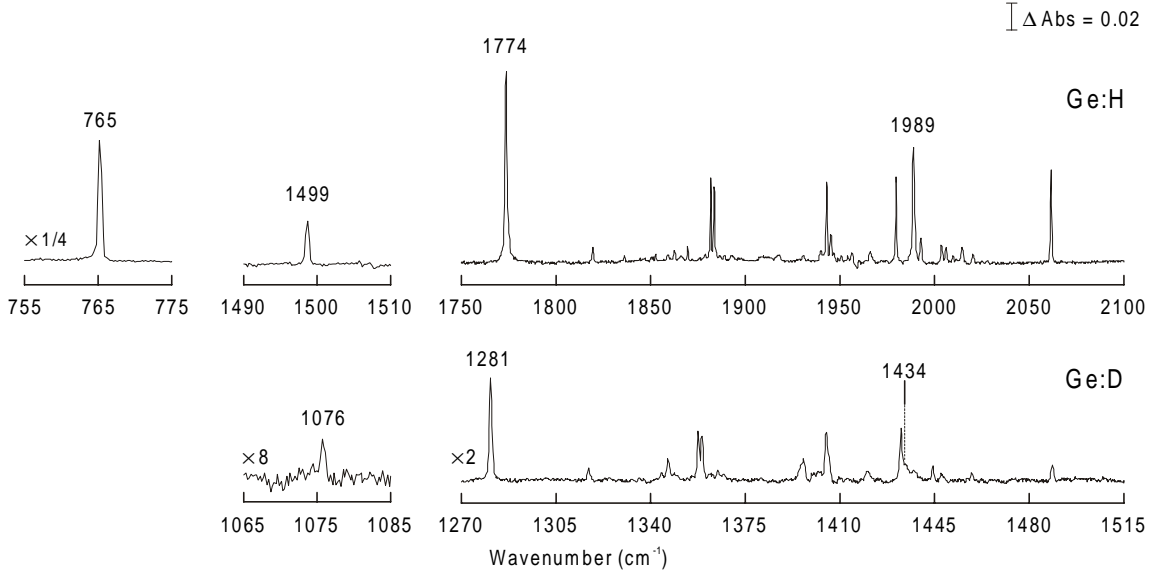


Fig. V.2. Absorbance spectra measured at 9 K on proton- (or deuterium-) implanted germanium samples after annealing at room temperature.

C. Experimental results

The absorbance spectra measured after implantation are shown in Fig. V.2. The implantation of protons gives rise to a series of sharp absorption lines in the range from 1750 to 2100 cm^{-1} . A similar set of lines is observed after deuterium implantation, but all the frequencies are shifted downwards with a factor of 1.39, i.e. very close to $\sqrt{2}$. This establishes that these lines represent local vibrational modes of hydrogen coupled to a heavy element that almost certainly is germanium. The spectra are broadly similar to, but much sharper than, those reported by Tatarikiewicz *et al* [17]. In addition, sharp lines are observed at 765 and 1499 cm^{-1} in proton-implanted samples. The 1499- cm^{-1} line shifts down to 1076 cm^{-1} when protons are substituted by deuterium and, therefore, also represents a local mode of hydrogen. No deuterium analogue to the 765- cm^{-1} line is observed. However, this line broadens and shifts to lower frequencies when the measuring temperature is raised to room temperature. Such behaviour is typical for a local vibrational mode. If the same scaling as above is applied, the deuterium line is expected at about 550 cm^{-1} , which is below the detection limit at $\sim 600 \text{ cm}^{-1}$ with our setup.

In molecular GeH_4 , the bend-mode frequencies are 819 and 931 cm^{-1} whereas the stretch-mode frequencies are 2106 and 2114 cm^{-1} [18]. The absorption lines from 1750 to 2100 cm^{-1} are, therefore, assigned to Ge-H stretch modes and the line at 765 cm^{-1} to a Ge-H bend mode. The 1499- cm^{-1} line is weak and its frequency is slightly less than two times 765 cm^{-1} . This suggests that the 1499- cm^{-1} line reflects the second-harmonic transition of the 765- cm^{-1} mode.

The Ge-H lines at 765, 1499, 1774 and 1989 cm^{-1} and the corresponding Ge-D lines at ~ 550 (unobserved), 1076, 1281 and 1434 cm^{-1} are of particular interest for this work and we shall focus on them in the following. To investigate whether these lines originate from the same centre, an isochronal annealing study was carried out. The absorbance spectrum was measured at 9 K after each 30-min anneal at various temperatures, starting from 298 K and increasing up to 458 K in steps of 20 K. The 765-, 1499-, 1774-, and 1989- cm^{-1} lines have identical annealing behaviour and disappear together around 418 K, as can be seen from Fig. V.3. This indicates that the same defect gives rise to the four lines. Also, the Ge-D lines at 1076, 1281 and 1434 cm^{-1} anneal at this temperature, showing that they originate from the same type of defect. The 1434- cm^{-1} line is broad and superimposed on a sharper line at 1433 cm^{-1} . The 1433- cm^{-1} line anneals at a somewhat lower temperature than the 1434- cm^{-1} line and their intensity ratio depends on the implantation temperature. Therefore, the two lines are not related to the same defect.²

Spectra measured on samples coimplanted with protons and deuterons are shown in Fig. V.4.

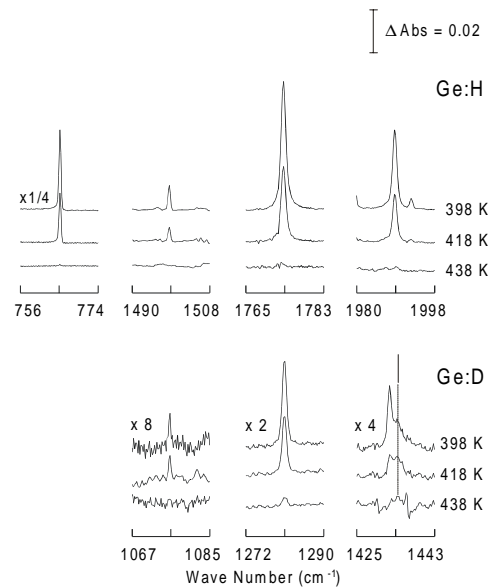


Fig. V.3. Annealing behaviour of the Ge-H (and Ge-D) related lines at 765, 1499 (1076), 1774 (1281) and 1989 (1434) cm^{-1} .

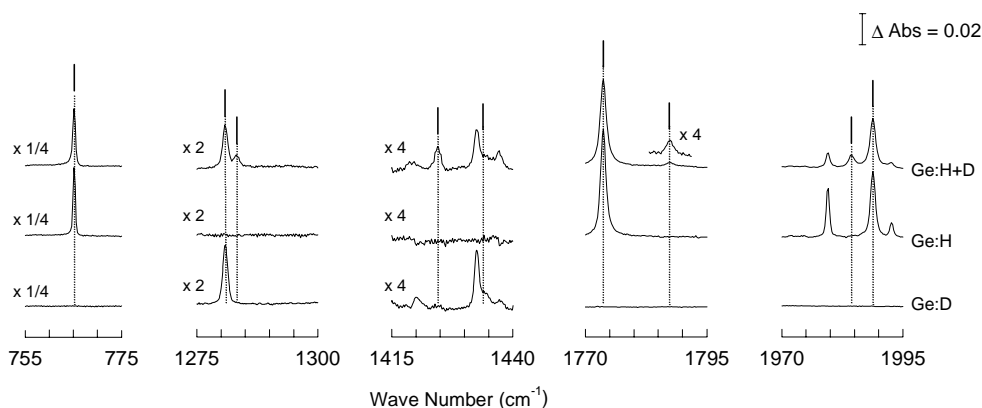


Fig. V.4. Details of absorbance spectra measured on germanium samples coimplanted with protons and deuterons.

² In chapter VII it is shown that the 1433- cm^{-1} line originates from the monovacancy containing two deuterium atoms.

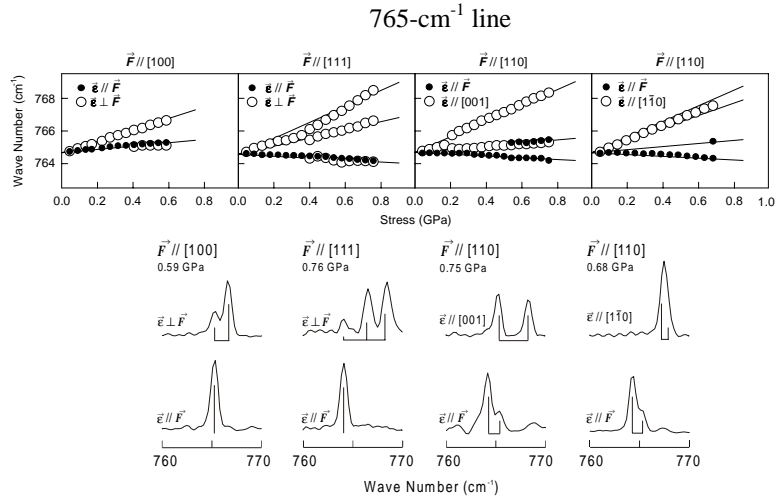
Two new Ge-H lines at 1787 and 1985 cm^{-1} and two new Ge-D lines at 1283 and 1425 cm^{-1} with annealing behaviour identical to the original four Ge-H and three Ge-D lines are observed. Other new lines, e.g. a Ge-D line at 1437 cm^{-1} , appear but their annealing characteristics differ from that of the original lines. Thus coimplantation leads to four new stretch modes related to the Ge-H lines at 765, 1499, 1774 and 1989 cm^{-1} . This establishes that the defect that gives rise to these lines contains two weakly coupled *inequivalent* hydrogen atoms each bonded to the lattice. Such a defect should have two Ge-H stretch modes, in agreement with our observations. Likewise, when the two hydrogen atoms are substituted by deuterium, two Ge-D stretch modes should be observed. However, when one hydrogen atom is substituted by deuterium, two different configurations exist, as the two hydrogen atoms are inequivalent. Each configuration gives rise to two stretch modes, one Ge-H and one Ge-D, which accounts for the appearance of four new lines in samples coimplanted with both isotopes. No new distinct bend mode around 765 cm^{-1} is detected showing that only one hydrogen atom participates in this motion.

The effects of uniaxial stress on the 765-, 1774-, and 1989- cm^{-1} lines are shown in Fig. V.5. The 1774- and 1989- cm^{-1} lines do not split under [100] stress, but split into two components for [111] stress, suggesting they represent excitations of one-dimensional modes of a trigonal defect (see Table II.3). A detailed analysis of the shifts and splittings of the lines, including the effect of polarisation, confirms this symmetry and the piezo-optical parameters, \mathcal{C}_{b1} and \mathcal{C}_{b2} , are given in Table V.1. The best fit to the experimental points with the parameters in Table V.1 is shown by the solid lines in Fig. V.5 and, as can be seen, the agreement is good. The relative intensities of the stress-split lines for various directions of polarisation are also consistent with trigonal symmetry (see Table II.3). The 765- cm^{-1} line splits into two under [100] stress, which is consistent with a trigonal defect only if it represents excitation of an *E* mode. The stress-pattern expected for such a transition is given in Table II.3 and the best fit to the data points are shown by the solid lines in Fig. V.5. The agreement is excellent and the relative intensities of the stress-split components are also in accordance with this assignment (see Table II.3). On this basis, it is concluded that the 1774- and 1989- cm^{-1} lines represent *A* modes and the 765- cm^{-1} line an *E* mode of a trigonal defect.

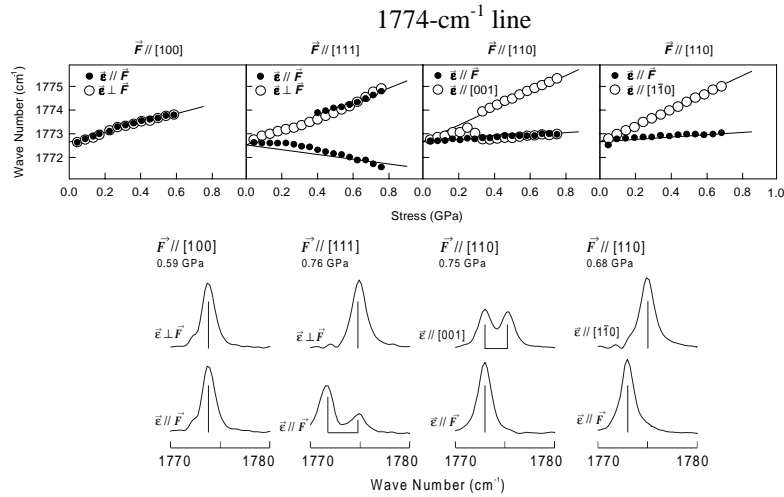
Table V.1. "Best-fit" piezo-spectroscopic parameters (in $\text{cm}^{-1}/\text{GPa}$) for the 765-, 1774-, and 1989- cm^{-1} lines. The 765- cm^{-1} line is fitted to an $A \rightarrow E$ transition and the 1774-, and 1989- cm^{-1} lines to $A \rightarrow A$ transitions of a trigonal centre.

	765 cm^{-1}	1774 cm^{-1}	1989 cm^{-1}
\mathcal{C}_{b1}	2.3 ± 0.5	2.0 ± 0.4	4.7 ± 1.1
\mathcal{C}_{b2}	0.1 ± 0.2	-1.50 ± 0.15	4.1 ± 0.5
\mathcal{C}	0.6 ± 0.2		
\mathcal{E}	2.1 ± 0.2		

a)



b)



c)

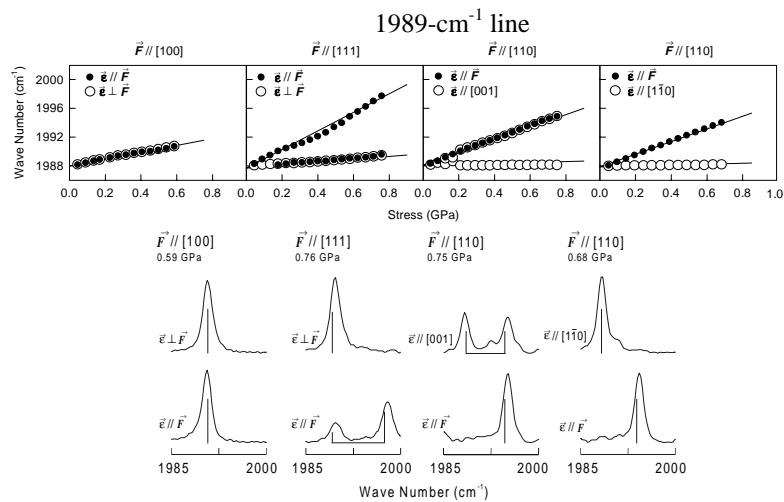


Fig. V.5. The observed stress-induced splittings (top) and absorbance profiles (bottom) of the lines at a) 765, b) 1774, and c) 1989 cm⁻¹. The filled (open) symbols of the top figures of each section correspond to measurements with the electric field \vec{E} of the light polarised parallel (perpendicular) to the applied force \vec{F} . The vertical lines shown in the bottom figures of a), b), and c) show the peak positions and relative intensities from our analysis.

D. Discussion

The experimental findings show that the 765-, 1499-, 1774-, and 1989- cm^{-1} lines originate from a pair of weakly coupled inequivalent hydrogen atoms each bonded to the lattice. As the symmetry of the defect is trigonal and the Ge-H stretch modes are one-dimensional, the defect must have two Ge-H bonds lying on the same [111] axis. The two hydrogen atoms must be close to one another since, otherwise, it would have been impossible to resolve the vibrational coupling between the two atoms. Furthermore, the Ge-H bond lengths are expected to be slightly larger than the 1.52 Å found in GeH_4 as stretch frequencies decrease rapidly with increasing bond lengths. The simplest structure that is consistent with these properties is the H_2^* defect. Structures which involve vacancies or interstitial germanium atom(s) are not likely candidates. It is impossible to construct a realistic vacancy-type defect with two different Ge-H bonds on the same [111] axis and with the hydrogen atoms close together. A vacancy containing one interior and one exterior bonded hydrogen, with C_{3v} symmetry, is not considered to be a credible model. To maintain a reasonable H-H distance, the two hydrogen atoms would be bonded to the same germanium atom, which thereby would become overcoordinated. Moreover, the VH_2 defect in silicon is known to possess C_{2v} symmetry³ and both hydrogen atoms lie interior to the vacancy. A trigonal structure with interstitial germanium atom(s) is bound to possess dangling bonds. Such a defect will probably be energetically unfavourable and will be unstable since it may reduce the number of dangling bonds via interaction with the lattice. On this basis, we assign the 765-, 1499-, 1774-, and 1989- cm^{-1} lines to H_2^* in germanium.

The assignment is also consistent with the local modes of H_2^* in silicon [11]. In Table V.2, the stretch frequencies for H_2^* in silicon and germanium are compared. The ratios of the Ge-H and Si-H stretch frequencies have an average value of 0.9648, very close to the average ratio 0.9639 found from the stretch modes of GeH_4 and SiH_4 . It is evident that the Ge-H modes at 1774 and 1989 cm^{-1} and the Si-H modes at 1838 and 2062 cm^{-1} must originate from equivalent defects. This establishes a link between our assignments in silicon and germanium.

If the effective charges of the Ge-H stretch modes are assumed to be ~ 0.3 (see Sec. V.F), then the fraction of implanted hydrogen atoms ending up in H_2^* complexes may be estimated to be

Table V.2. Observed Ge-H and Si-H stretch frequencies (cm^{-1}) of the H_2^* defect in germanium and silicon [11]. The frequency ratios between similar Ge-H and Si-H modes are given and compared with corresponding values from GeH_4 and SiH_4 ($X = \text{Ge}$ or Si).

Config.	Ge:H	Si:H	Ratio
H_2^*	1988.8	2061.5	0.9647
	1773.8	1838.3	0.9649
XH_4	2106.0	2187.0	0.9630
	2113.6	2190.6	0.9648

³ Experimental studies of the VH_2 defect in silicon and germanium are presented in chapter VI and VII.

$\sim 20\%$. This suggests that H_2^* is a prominent defect in proton-implanted germanium. The intensities of the H_2^* modes are very similar in proton-implanted germanium and silicon crystals with the same hydrogen concentration. Thus, our measurements do not support that H_2^* is less stable in germanium than in silicon [9] but no definite conclusions should be made at this stage. It is crucial to realise that implantation is a non-equilibrium process and different hydrogen-related centres are not necessarily formed in accordance with their relative stabilities.

E. Simple model of the H_2^* defect

In order to demonstrate that our assignments are quantitatively consistent with the observed Ge-H and Si-H stretch frequencies and with their isotope shifts, a simple model will be introduced below. In the harmonic approximation, the relation between the Ge-H and Ge-D (or Si-H and Si-D) stretch frequencies of H_2^* is

$$\frac{\omega_H}{\omega_D} = \sqrt{\frac{\mu_D}{\mu_H}}, \quad (\text{V.1})$$

where $\mu_{H/D}$ is the effective mass of the hydrogen/deuterium atom, which we calculate from the formula

$$\frac{1}{\mu_{H/D}} = \frac{1}{m_{H/D}} + \frac{1}{\chi M}, \quad (\text{V.2})$$

where $m_{H/D}$ is the mass of the relevant isotope, M is the mass of the host atom (germanium or silicon) bonded to the hydrogen, and χ is a factor which accounts for the coupling to the lattice [19]. Since it is expected that $\chi \approx 1$, the ratio ω_H/ω_D should be about 1.404 for Ge-H and 1.390 for Si-H modes. However, the experimental ratios for the H_2^* modes are smaller, 1.385 and 1.387 in germanium, 1.372 and 1.375 in silicon. This indicates that anharmonic effects are important to obtain a satisfactory description.

The Morse potential includes anharmonic effects and is known to represent the bonding of diatomic molecules quite accurately [20]. Also, for H_2^* we expect that the vibrational properties are largely determined by the Ge-H (or Si-H) bonds. Consequently, we assume that the effective bonding of the hydrogen atoms to the host atoms are well described by such potentials. Since the two hydrogen are coupled, an additional term is needed.

With a harmonic coupling term, the model Hamiltonian is

$$\hat{H} = -\frac{\hbar^2}{2\mu_1} \frac{\partial^2}{\partial r_1^2} - \frac{\hbar^2}{2\mu_2} \frac{\partial^2}{\partial r_2^2} + D_1 [\exp(-a_1 r_1) - 1]^2 + D_2 [\exp(-a_2 r_2) - 1]^2 + f_{12} r_1 r_2, \quad (\text{V.3})$$

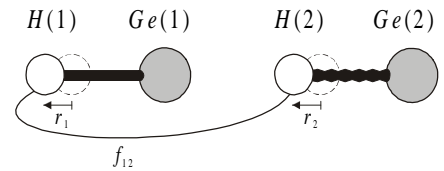


Fig. V.6. Sketch of two coupled Ge-H oscillators. r_1 and r_2 are the bond extensions, and f_{12} is the harmonic coupling constant.

where μ_1 and μ_2 are the effective masses calculated from Eq. V.2 with $\chi = 1$, and r_1 and r_2 are the displacement coordinates corresponding to bond stretching (see Fig. V.6). The potential energy is assumed to be independent of the isotopic configuration, which implies that the parameters a_1 , D_1 , a_2 , D_2 , and f_{12} in Eq. V.3 are the same for all configurations: H_1H_2 , H_1D_2 , D_1H_2 , and D_1D_2 .

The Schrödinger equation with the Hamiltonian in Eq. V.3 has no simple analytical solution, and further approximations have been made to make the calculations tractable. There are two obvious possibilities. Either the coupling term $f_{12}r_1r_2$ is treated as a first order perturbation using the known eigenfunctions of the Morse potential [20] as basis functions, or the Morse potentials are expanded to fourth order and then the cubic and quartic terms are treated as perturbations⁴ to a system of two coupled harmonic oscillators. Both approaches have been investigated, and the calculated frequencies have been fitted to the observed values. Our analysis shows that it is immaterial whether the harmonic coupling or the anharmonicity is treated perturbatively.⁵ In the following, the anharmonic terms will be treated as perturbations, since this is most convenient. Thus the following expression for the zero-order Hamiltonian is obtained:

$$\hat{H} = -\frac{\hbar^2}{2\mu_1} \frac{\partial^2}{\partial r_1^2} - \frac{\hbar^2}{2\mu_2} \frac{\partial^2}{\partial r_2^2} + D_1 a_1^2 r_1^2 + D_2 a_2^2 r_2^2 + f_{12} r_1 r_2 . \quad (\text{V.4})$$

The harmonic frequencies ω_1 and ω_2 may be found from the secular equation [21]

$$|\mathbf{GF} - \omega_i^2 \mathbf{I}| = 0 , \quad (\text{V.5})$$

where \mathbf{I} is the identity matrix, and

$$\mathbf{G} = \begin{pmatrix} \mu_1^{-1} & 0 \\ 0 & \mu_2^{-1} \end{pmatrix} , \quad \mathbf{F} = \begin{pmatrix} 2D_1 a_1^2 & f_{12} \\ f_{12} & 2D_2 a_2^2 \end{pmatrix} . \quad (\text{V.6})$$

The perturbations which represent the cubic and quartic contributions to the potential energy in Eq. V.3 are

$$U_3 = -D_1 a_1^3 r_1^3 - D_2 a_2^3 r_2^3 , \quad (\text{V.7})$$

$$U_4 = \frac{7}{12} D_1 a_1^4 r_1^4 + \frac{7}{12} D_2 a_2^4 r_2^4 . \quad (\text{V.8})$$

⁴ The third order terms contribute only to second order whereas the fourth order terms contribute to first order.

⁵ This is due to a remarkable property of the Morse potential. If the Morse potential is expanded to fourth order and the cubic and quartic terms are treated by, respectively, second-order and first-order perturbation theory, the energies of the ground state and the fundamental state are equal to the near-exact energies given by Morse [20].

The energies of the fundamental transitions are calculated for H_1H_2 , H_1D_2 , D_1H_2 and D_1D_2 , and the optimum choice of parameters a_1 , D_1 , a_2 , D_2 , and f_{12} is determined by minimising the sum of the squares of the deviations between the calculated and observed frequencies. The “best-fit” parameters for germanium and silicon are given in Table V.3, and the observed and calculated frequencies are compared in the same table. As can be seen, the model reproduces the observed stretch frequencies within 3 cm^{-1} . This corresponds to a relative maximum deviation of 2×10^{-3} , which we consider to be remarkably good.

To investigate whether the intensities of the modes also are consistent with our assignments, a few additional assumptions are made. It is assumed that the dipole moment of the defect is the sum of dipole moments of each Ge-H (or Si-H) bond and that these bond moments are parallel to the bonds. If the bonds are aligned, and it is sufficient to expand the dipole moment d to first order in r_1 and r_2 , we obtain

$$\begin{aligned} d &\approx d \Big|_{(r_1, r_2)=(0,0)} + \frac{\partial d}{\partial r_1} \Big|_{(r_1, r_2)=(0,0)} r_1 + \frac{\partial d}{\partial r_2} \Big|_{(r_1, r_2)=(0,0)} r_2, \\ &\equiv d^0 + \eta_1 e r_1 + \eta_2 e r_2 \end{aligned} \quad (\text{V.9})$$

where η_1 and η_2 are the effective charges of the individual Ge-H (or Si-H) bonds, e is the elementary charge, and d^0 is the permanent dipole moment. The relation between the displacements coordinates r_1 , r_2 and the normal coordinates Q_1 , Q_2 is

$$\begin{pmatrix} r_1 \\ r_2 \end{pmatrix} = \mathbf{L} \begin{pmatrix} Q_1 \\ Q_2 \end{pmatrix}, \quad (\text{V.10})$$

where \mathbf{L} is the 2×2 matrix with column vectors \vec{L}_1 and \vec{L}_2 given by [21]

$$\mathbf{G} \mathbf{F} \vec{L}_i = \omega_i^2 \vec{L}_i \quad \wedge \quad \vec{L}_i \mathbf{F} \vec{L}_j = \omega_i^2 \delta_{ij}, \quad i, j \in \{1, 2\}. \quad (\text{V.11})$$

When Eqs. V.9 and V.10 are combined, d may be expressed in terms of normal coordinates as

Table V.3. Calculated model frequencies (cm^{-1}) compared with those observed for H_2^* in germanium and silicon [11]. The bold characters identify the isotope and the site which are most active for a specific mode. The model frequencies are calculated using the “best-fit” parameters a_1 , D_1 , a_2 , D_2 , and f_{12} given in the lower part of the table.

Isotope config.	Germanium		Silicon	
	Model	Observed	Model	Observed
H_1H_2	1990.7	1988.8	2062.7	2061.5
$H_1\mathbf{H}_2$	1775.5	1773.8	1838.8	1838.3
H_1D_2	1985.7	1984.5	2057.3	2058.1
$H_1\mathbf{D}_2$	1282.6	1283.3	1342.3	1342.0
D_1H_2	1422.6	1424.6	1488.8	1488.5
$D_1\mathbf{H}_2$	1786.9	1787.4	1851.3	1851.5
D_1D_2	1431.6	1434.4	1498.8	1499.7
$D_1\mathbf{D}_2$	1279.5	1280.9	1338.9	1339.6
a_1 (\AA^{-1})		1.3779		1.4144
D_1 (eV)		4.0504		4.0490
a_2 (\AA^{-1})		1.4348		1.4719
D_2 (eV)		3.0598		3.0632
f_{12} (eV/ \AA^2)		-0.5504		-0.5935

$$d = d^0 + \lambda_1 Q_1 + \lambda_2 Q_2 , \quad (\text{V.12})$$

where

$$\lambda_i = \eta_1 e L_{1i} + \eta_2 e L_{2i} . \quad (\text{V.13})$$

Finally, if local field corrections are neglected, the intensity I_i of the absorption line associated with the fundamental transitions of the i th (non-degenerate) mode can now be calculated from the formula⁶ (see Eq. II.2)

$$I_i \equiv \int_{\text{peak } i} Abs(\sigma) d\sigma \approx \log_{10} e \times \int_{\text{peak } i} l \alpha(\sigma) d\sigma = \log_{10} e \frac{\pi D}{3n c^2} \lambda_i^2 , \quad (\text{V.14})$$

where $Abs(\sigma)$ is the absorbance, $\alpha(\sigma)$ is the absorption coefficient, l is the thickness of the implantation profile, D is the number of centres per area, n is the refractive index, and c the speed of light. It may be noted that although η_1 and η_2 are independent of the particular isotopic configuration, the intensity depends on the configuration through the mass-dependence of λ_i .

With the parameters a_1 , D_1 , a_2 , D_2 , and f_{12} kept fixed at the values in Table V.3, the ratio I_1/I_2 depends, for a given isotope configuration, only on the ratio η_1/η_2 . From comparison with the experimental intensity ratios, the value of η_1/η_2 is found to be 1.1 ± 0.1 in both germanium and silicon. The calculated values of I_1/I_2 with $\eta_1/\eta_2 = 1.1$ are compared with those observed in Table V.4. The calculated ratios reproduce the observed trend and quantitatively the two sets of values agree within 20%. This agreement is considered satisfactory taking into account the experimental uncertainties on I_1/I_2 ($\sim 15\%$) and keeping in mind the approximations made.

Table V.4. The observed intensity ratios I_1/I_2 in germanium and silicon are compared with those calculated with $\eta_1/\eta_2 = 1.1$.

Isotope config.	Germanium		Silicon	
	I_1/I_2 (obs)	I_1/I_2 (calc)	I_1/I_2 (obs)	I_1/I_2 (calc)
H_1H_2	0.53	0.54	0.53	0.50
H_1D_2	1.81	1.91	2.08	1.76
D_1H_2	1.05	0.82	0.64	0.81
D_1D_2	0.44	0.54	0.51	0.50

F. *Ab initio* calculations on H_2^* in germanium

The simple model gives insight into the basic physics of the local modes of H_2^* but it suffers from shortcomings. It is impossible to decide whether H_{AB} or H_{BC} is responsible for the 1989-cm⁻¹ (or 1774-cm⁻¹) line and no information about the assignment of the line at 765 cm⁻¹ is obtained.

⁶ In this formula the contribution to the intensity from internally reflected light (see Sec. III.B.2) is neglected. Since the absorption lines studied in this chapter have similar intensities, the error on the effective charges introduced by this approximation is essentially the same for all the lines. Consequently, the error on ratios of effective charges obtained from measured intensity ratios by use of Eq. V.14 is negligible.

Finally, the detailed structure of the defect, including Ge-H bond lengths together with the relaxed positions of the germanium atoms, cannot be determined experimentally.

In order to address such issues R. Jones, J. Goss, and S. Öberg have performed *ab initio* calculations of the structure and the local vibrational mode frequencies of H_2^* in germanium. The calculations are based on local density functional theory and are similar to those performed on the same defect in silicon [11]. The crystal was represented by an 88-atom trigonal cluster, $Ge_{44}H_{44}$, centred on the middle of a Ge-Ge bond. Two hydrogen atoms were placed interior to the cluster with one, H_{BC} , at the central BC site, and the other, H_{AB} , at an AB site to one of the two central germanium atoms (see Fig. V.1). All 88 cluster atoms were allowed to relax to minimise the total energy. Further details of the method have been described elsewhere [22,23].

The energy minimisation resulted in the configuration shown in Fig. V.7, in which H_{BC} forms a 1.524 Å long bond with $Ge(1)$. The $H_{BC}-Ge(1)-Ge$ angle is 104° , which is close to the 109.47° found in the perfect lattice, indicating that the $Ge(1)-H_{BC}$ bonding is sp^3 -like. H_{AB} is bonded to the other central germanium atom $Ge(2)$ with a bond length of 1.603 Å and the angle $H_{AB}-Ge(2)-Ge$ is 90° . Hence, the bonding of the $Ge(2)-H_{AB}$ is largely p -like, and weaker than that of $Ge(1)-H_{BC}$. This suggests that the lower stretch frequency at 1774 cm^{-1} is to be identified with the $Ge(2)-H_{AB}$ stretch mode, whereas the 1989-cm^{-1} line reflects the $Ge(1)-H_{BC}$ stretch. This corresponds exactly to the previous assignments made for H_2^* in silicon [11]. The separation of H_{BC} and H_{AB} is 3.80 Å and the defect has no electronic levels in the gap. These findings are similar to those of Estreicher *et al* [9].

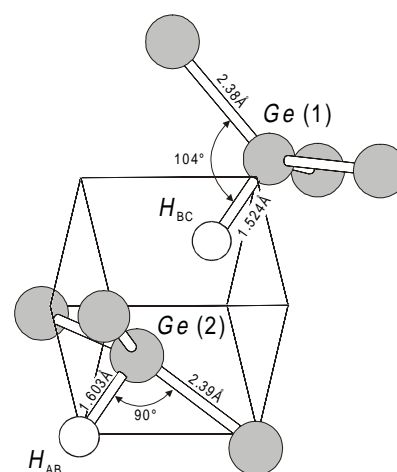


Fig. V.7. The structure of H_2^* in germanium according to *ab initio* theory.

The local mode frequencies of the H_2^* defect were calculated (see Table V.5). There are two bend modes (two-dimensional) with calculated frequencies at 503 and 851 cm^{-1} . The 851-cm^{-1} mode is mainly associated with the vibration of H_{AB} and deviates by 86 cm^{-1} from the Ge-H bend mode observed at 765 cm^{-1} . This deviation is within the limits of the method, and we assign the 765-cm^{-1} line to the $Ge(2)-H_{AB}$ bend mode. The $Ge(1)-H_{BC}$ bend mode is calculated to lie at 503 cm^{-1} , which is below the detection limit of the spectrometer, explaining why it is not observed.

For the $H_{BC}H_{AB}$ configuration, the Ge-H stretch mode with the highest frequency involves mostly H_{BC} , and that with the lowest corresponds mainly to the vibration of H_{AB} . The calculated H_{BC} mode is within 107 cm^{-1} of that observed while the H_{AB} mode is 174 cm^{-1} too high. These deviations decrease to 57 and 104 cm^{-1} , respectively, when $H_{BC}H_{AB}$ is substituted by $D_{BC}D_{AB}$, which indicates that anharmonicity contributes to the error. Some anharmonicity is included in

Table V.5. *Ab initio* local-mode frequencies (cm^{-1}) of H_2^* in germanium. The bold characters identify the isotope and the site which are most active for a specific mode. The frequencies corresponding to the calculated structure and to 3% lengthened bonds are given, together with the calculated effective charges η of the modes. For the (two-dimensional) bend modes, the degeneracy is included in the stated values.

Isotope config.	stretch modes			bend modes		
	ω_{calc}	ω_{calc} 3% lengthened	η	ω_{calc}	ω_{calc} 3% lengthened	η
$H_{\text{BC}}H_{\text{AB}}$	2095.9	1846.8	0.23	503	615	0.17
$H_{\text{BC}}H_{\text{AB}}$	1948.4	1710.1	0.38	851	919	0.27
$H_{\text{BC}}D_{\text{AB}}$	2092.6	1838.5		503	613	
$H_{\text{BC}}D_{\text{AB}}$	1387.3	1220.7		603	653	
$D_{\text{BC}}H_{\text{AB}}$	1487.5	1304.6		367	440	
$D_{\text{BC}}H_{\text{AB}}$	1953.1	1722.0		851	919	
$D_{\text{BC}}D_{\text{AB}}$	1491.1	1313.8		366	397	
$D_{\text{BC}}D_{\text{AB}}$	1385.2	1215.3		603	651	

the calculated frequencies, as they are based on calculations of the energy of the cluster at finite displacements of the atoms. However, a more likely source of error is the overbinding caused by density functional theory leading to Ge-H lengths which are too short. If the Ge-H bonds are expanded by 3 % ($\sim 0.05 \text{ \AA}$), the $H_{\text{BC}}H_{\text{AB}}$ modes become 1847 and 1710 cm^{-1} , which now lie below those observed (see Table V.5). The important conclusion is then that small changes to the calculated geometry give modes which straddle the experimental results. This gives us confidence in assigning the observed modes to the H_2^* defect.

The calculations also account for the observed isotope shifts. The calculated H_{BC} mode at 1847 cm^{-1} is displaced downwards by 8.3 cm^{-1} when H_{AB} is substituted by D_{AB} compared with the experimental value of 4.3 cm^{-1} . The calculated H_{AB} mode at 1710 cm^{-1} is displaced upwards by 11.9 cm^{-1} when H_{BC} is substituted by D_{BC} compared with the observed value of 13.6 cm^{-1} . These isotope shifts are determined by the coupling parameter f_{12} . The *ab initio* (quasi-harmonic) value is -0.35 eV/\AA^2 , which is in fair agreement with the -0.55 eV/\AA^2 derived from the simple model discussed in the Sec. V.E. Finally, the calculated H_{AB} bend mode does not shift when H_{BC} is substituted with D_{BC} , in agreement with our experimental findings for the 765-cm^{-1} mode.

The effective charges of the normal modes have also been calculated, and are given in Table V.5. Since the intensity of a given mode is proportional to the square of its effective charge, the relative intensities of the modes $Ge-H_{\text{BC}}$ (stretch), $Ge-H_{\text{AB}}$ (stretch), $Ge-H_{\text{AB}}$ (bend), $Ge-H_{\text{BC}}$ (bend) should be $1.0 : 2.7 : 1.4 : 0.5$ which differ somewhat from those observed $1.0 : 1.7 : 1.9 : \text{UD}$ (undetected).

Anharmonic effects were investigated by calculating the energy necessary to distort H_{BC} (or H_{AB}) with H_{AB}

Table V.6. *Ab initio* stretch frequencies ω of H_2^* calculated from the fits to Morse potentials. The Morse parameters a and D are also given.

	Mode	
	H_{BC}	H_{AB}
$\omega (\text{cm}^{-1})$	2061.2	1960.9
$a (\text{\AA}^{-1})$	1.585	1.481
$D (\text{eV})$	3.320	3.402

(or H_{BC}) fixed at its equilibrium site. These energies were then fitted to a Morse potential, $V(r) = D[\exp(-ar) - 1]^2$, and the frequencies of the oscillators were calculated using the near-exact analytical result of Morse [20]. The mass taken is that given by Eq. V.2, with $\chi = 1$. The calculated Ge-H stretch frequencies are given in Table V.6 together with the values of the Morse parameters D and a . The effect of the full anharmonic calculation is to lower the frequency of the 2096-cm⁻¹ mode to 2061 cm⁻¹, and to increase that of the 1948-cm⁻¹ mode to 1961 cm⁻¹. This does not imply that the anharmonic effects are negligible. The anharmonic corrections to the frequencies⁷ are 75 cm⁻¹ for the 2061-cm⁻¹ mode and 59 cm⁻¹ for the 1961-cm⁻¹ mode. Apparently, the quasi-harmonic frequencies account for a substantial part of the anharmonicity. The Morse parameters in Table V.6 may be directly compared with those obtained by our simple model in Table V.3. The two sets of parameters deviate by less than 18 %.

G. Conclusion

Infrared absorption lines at 765, 1499, 1774, and 1989 cm⁻¹ in proton-implanted germanium originate from a trigonal defect containing of a pair of weakly coupled inequivalent hydrogen atoms. These lines are assigned to local vibrational modes of the H_2^* defect. A simple vibrational model is presented which accounts for the observed Ge-H (Si-H) stretch frequencies in germanium (silicon) within 3 cm⁻¹. The calculated intensity ratios of the stretch modes deviate at most by 20% from the observed values. *Ab initio* local density functional cluster calculations confirm that H_2^* is stable in germanium. The calculations yield local-mode frequencies in fair agreement with those observed. The *ab-initio* intensities, however, deviate somewhat from the experimental values. It is concluded that the 765- and 1774-cm⁻¹ lines reflect bend and stretch modes of H_{AB} , whereas the 1989-cm⁻¹ line is due to a stretch mode which mainly involves H_{BC} . The line at 1499 cm⁻¹ is ascribed to the second-harmonic transition of the 765-cm⁻¹ mode. The similarity in the formation efficiencies for H_2^* defects by low temperature proton implantation in silicon and germanium suggests that hydrogen has the same chemistry in germanium and silicon.

⁷ The anharmonic correction ω_{anharm} is calculated by $\omega_{\text{anharm}} = \omega_{\text{harm}} - \omega$, where $\omega_{\text{harm}}^2 = 2Da^2/\mu_{\text{H}}$, and ω is given in Table V.6.

H. References

- [1] J. W. Corbett, S. N. Sahu, T. S. Shi, and L. C. Snyder, *Physics Letters A*, **93**, 303 (1983); T.S. Shi, S.N. Sahu, J.W. Corbett, and L.C. Snyder, *Scientica Sinica*, **27**, 98 (1984).
- [2] A. Mainwood, and A. M. Stoneham, *J. Phys. C*, **17**, 2513 (1984).
- [3] S. J. Pearton, J. W. Corbett, and M. Stavola, in "Hydrogen in crystalline semiconductors" (Springer-Verlag, Berlin, 1992).
- [4] P. Briddon, R. Jones, and G.M.S. Lister, *J. Phys. C*, **21**, L1027 (1988).
- [5] K.J. Chang and D.J. Chadi, *Phys. Rev. Lett.* **62**, 937 (1989); K. J. Chang, and D. J. Chadi, *Phys. Rev. B*, **40**, 11644 (1989).
- [6] P. Deák and L.C. Snyder; *Radiat. Eff. and Defects in Solids* **111&112**, 77 (1989).
- [7] R. Jones, *Physica B*, **170**, 181 (1991).
- [8] C. G. Van de Walle, *Phys. Rev. B*, **49**, 4579 (1994).
- [9] S.K. Estreicher, M.A. Roberson, and Dj.M. Maric, *Phys. Rev. B* **50**, 17018 (1994); Dj. M. Maric, M. A. Roberson, and S. K. Estreicher, in "Defects in Semiconductors 17", edited by H. Heinrich and W. Jantsch, *Materials Science Forum Vol. 143-147* (Trans Tech, Aedermannsdorf, 1994) p. 1245.
- [10] P. Deák, M. Heinrich, L.C. Snyder, and J. W. Corbett, *Mater. Sci. Eng. B*, **4**, 57 (1989); P. Deák, L.C. Snyder, M. Heinrich, C. R. Ortiz, and J. W. Corbett, *Physica B*, **170**, 253 (1991).
- [11] J.D. Holbeck, B. Bech Nielsen, R. Jones, P. Sitch, and S. Öberg, *Phys. Rev. Lett.* **71**, 875 (1993).
- [12] H. J. Stein, *J. Electron. Mater.*, **4**, 159 (1975).
- [13] B. Bech Nielsen, and H. G. Grimmeiss, *Phys. Rev. B*, **40**, 12403 (1989).
- [14] B.N. Mukashev, S.Z. Tokmoldin, and M.F. Tamendarov, in "Proceedings of the International Conference on the Science and Technology of Defect Control in Semiconductors, Yokahama, Japan, 1989", edited by K. Sumino, (North-Holland, Amsterdam, 1990), p. 429.
- [15] M. Budde, B. Bech Nielsen, R. Jones, J. Goss, and S. Öberg, *Phys. Rev. B*, **54**, 5485 (1996).
- [16] M. Budde, B. Bech Nielsen, R. Jones, J. Goss, and S. Öberg, in "Defects in Semiconductors 18", edited by M. Suezawa and H. Katayama-Yoshida, *Materials Science Forum Vol. 196-201* (Trans Tech, Aedermannsdorf, 1995), p. 879.
- [17] J. Tatarkiewicz, A. Król, A. Breitschwerdt, and M. Cardona, *Phys. Stat. Sol. B*, **140**, 369 (1987).
- [18] *American Institute of Physics Handbook* (Third Edition, Edited by D.W.E. Gray, McGraw-Hill Book Company, New York, 1972) p. 7-189.

- [19] R. S. Leigh and R. C. Newman, *Semicond. Sci. Technol.*, **3**, 84 (1988).
- [20] P.M. Morse, *Phys. Rev.*, **34**, 57 (1929).
- [21] See e.g., E. B. Wilson, J.C. Decius, and P.C. Cross; *Molecular Vibrations* (Dover Publications Inc, New York, 1980).
- [22] R. Jones *Philos. Trans. R. Soc. London* , Ser. A, **341**, 351 (1992).
- [23] F. Berg Rasmussen, R. Jones, and S. Öberg, *Phys. Rev. B*, **50**, 4378 (1994).
- [24] R. Jones and S. Öberg, *Phys. Rev. B*, **44**, 3673 (1991).

VI. Vacancy-hydrogen complexes in silicon

A. Introduction

In chapter IV it was shown that essentially all protons implanted into silicon at cryogenic temperature form *isolated hydrogen* centres, i.e. centres formed by the interaction of a hydrogen atom with an otherwise perfect lattice. The *isolated hydrogen* centres disappear upon annealing at ~ 200 K and, instead, a number of distinct hydrogen-related centres are formed. The following three chapters of this thesis are concerned with the identification of some of the prominent lines observed in the infrared absorption spectra, when the basic hydrogen centres disappear at ~ 200 K and upon annealing at higher temperatures. In particular, it will be shown that most of these lines are associated with hydrogen saturating dangling bonds of implantation-induced defects like monovacancies, divacancies and interstitial silicon atoms (self-interstitials).

As shown by the existence of stable molecular compounds, such as silane (SiH_4) and disilane (Si_2H_6) [1], hydrogen forms strong bonds with silicon. Moreover, it has been established that hydrogen saturates dangling bonds at silicon surfaces [2] and Si/SiO₂ interfaces [3]. Based on these observations, one might also expect hydrogen to interact with dangling bonds in vacancy-type defects and to form vacancy-hydrogen complexes in silicon.

As mentioned in the introduction to this thesis, implantation of protons into virtually any semiconductor followed by a heat treatment may cause the implanted wafer to split at the end-of-range of the implanted protons. This is used in the Smart-Cut process [4], which may revolutionise the production of e.g. silicon-on-insulator (SOI) structures. The microscopic processes leading to the layer splitting are at present not well understood. It has recently been proposed that one of the fundamental steps of the splitting process is the agglomeration of hydrogen-saturated vacancies, which leads to the formation of platelet-like structures that again evolve into micro-cracks and layer splitting [5]. Consequently, an improved understanding of the properties of vacancy-hydrogen complexes in semiconductors may stimulate the development and refinement of the promising Smart-Cut process.

In this chapter infrared absorption studies of vacancy-hydrogen complexes in silicon are presented. The infrared absorption measurements are combined with annealing, isotope substitution, and uniaxial stress measurements. The annealing and isotope substitution experiments were carried out by L. Hoffmann as part of her Master project [6]. The results are nevertheless included as an integral part of the present chapter, as they are a requisite for a proper description of the results. Parts of the

present work has been published elsewhere [7,8]. Before the results are described, an introduction is given to the experimental and theoretical studies of vacancy-hydrogen complexes in silicon carried out to date. In the remainder of this thesis, vacancy-hydrogen complexes are denoted V_mH_n , where m (n) is the number of vacancies (hydrogen atoms) contained. In case of the monovacancy ($m = 1$) the m -index is dropped.

1. Survey of theoretical studies of vacancy-hydrogen complexes in silicon

The VH_n complexes in silicon (with $n = 1, 2, 3, 4$) have been studied theoretically at various levels of theory during the last two decades. The first study, based on Extended Hückel theory, was reported by Singh *et al* in 1977. The calculations showed that it is energetically favourable for hydrogen to saturate a dangling bond inside a vacancy rather than to reside as an “isolated” entity at a T site. Moreover, they showed that the vacancy at most can bind four hydrogen atoms and that the Si-H bonds point towards the centre of the vacancy. The vibrational stretch frequencies were also calculated and exhibited a steady increase with increasing n for the VH_n complexes. Singh *et al* ascribed this frequency increase to a repulsive interaction between the hydrogen atoms.

Since the original work by Singh *et al* [9], theoretical studies of the VH_n complexes have been extended to more advanced levels of theory. For instance, semi-empirical calculations have been reported by Deák *et al* [10] and Xu [11], *ab initio* calculations by Van de Walle *et al* [12,13], Roberson *et al* [14], and Jones *et al* [7], and a molecular-dynamics study by Park *et al* [15]. The more advanced calculations generally confirm the predictions made by Singh *et al* [9]. The theoretical studies agree that the atomic configurations of the VH_n complexes are similar to those illustrated in Fig. VI.1 [7,10-15].

VH is formed by saturation of one of the dangling bonds of the vacancy by a hydrogen atom. The resulting structure is unstable against a Jahn-Teller distortion,

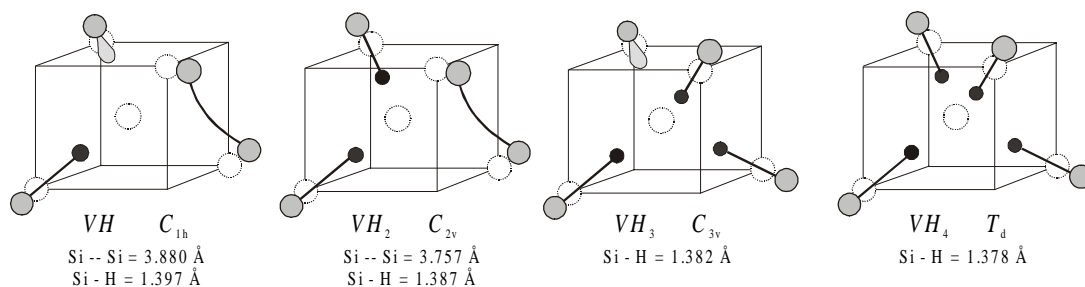


Fig. VI.1. Structure of the VH_n complexes in silicon calculated by Roberson *et al* [14]. The black and grey spheres are hydrogen and silicon atoms, respectively, whereas the white spheres are substitutional sites of the diamond lattice. The symmetry and internuclear distances (in Å) are indicated.

which lowers the symmetry to C_{1h} (monoclinic-I) by formation of an extended bond between two of the remaining dangling bonds. According to the theoretical study of the electronic structure of the VH_n complexes by Xu [11], VH in its neutral charge state is paramagnetic and thus detectable with EPR. The electronic structure of the complex is predicted [11] to be very similar to that of the vacancy-phosphorous pair, also called the E centre [16]. The Si-H bond of VH gives rise to one stretch mode with A' symmetry.

VH_2 has C_{2v} (orthorhombic-I) symmetry, and consists of two hydrogen atoms each saturating a dangling bond of the vacancy. The electronic structure of the complex is predicted to be very similar to that of the vacancy-oxygen pair (A centre). The ground state of the neutral complex is diamagnetic, and VH_2 is predicted to possess an excited spin-triplet state, which might be amenable to observation by magnetic resonance experiments [11]. VH_2 has two Si-H stretch modes with A_1 and a B_1 symmetry, respectively.¹

VH_3 has C_{3v} (trigonal) symmetry, and is, according to the calculations by Xu [11], paramagnetic in its neutral charge state. The complex has a non-degenerate A_1 and a two-fold degenerate E stretch mode.

VH_4 has all four dangling bonds of the vacancy saturated by hydrogen, which renders the complex electrically inactive. The complex has T_d (cubic) symmetry, and gives rise to a three-fold degenerate T_2 and a non-degenerate A_1 stretch mode. Apart from the A_1 mode of VH_4 , all stretch modes of the VH_n complexes are infrared active.

The binding energy per hydrogen atom² has been calculated for the VH_n complexes with semi-empirical [10] and *ab initio* [13,14] theory. The calculations agree that the average binding energy per hydrogen atom decreases with increasing n due to the repulsion between the hydrogen atoms. Moreover, calculations of binding energies for various hydrogen-related defects, including the dimers H_2^T and H_2^* discussed in chapter V, predict that the VH_n complexes in silicon have the largest average binding energies of all the hydrogen-related defects investigated [10,12,14].

¹ The asymmetric mode of VH_2 can either be denoted B_1 or B_2 depending on whether the σ_v or σ'_v mirror plane of the C_{2v} point group is chosen as the {110} plane containing the two Si-H bonds [17].

² The binding energy per hydrogen atom of the VH_n complex is defined as [10]

$$E_{\text{bind}} = - [E(VH_n) - E(V) - n E(H)] / n ,$$

where $E(VH_n)$ and $E(V)$ is the total energy of the cluster or supercell containing, respectively, a VH_n complex and a vacancy, and $E(H)$ is the energy of a hydrogen atom outside the cluster.

Table VI.1. Calculated symmetry and stretch frequencies (cm^{-1}) of the vacancy-hydrogen complexes in silicon. The last column gives the stretch frequencies of the VH , VH_3 , and VH_4 defects observed experimentally as described in Sec. VI.A.2.

	Point group	Mode	Deák [10] ^a	Park [15] ^b	Jones [7] ^c	Experiment
VH_4	T_d	A_1	2364	~ 2334	2404	2223
		T_2	2347		2319	
VH_3	C_{3v}	A_1	2360	~ 2301	2283	2185
		E	2348		2209	2155
VH_2	C_{2v}	A_1	2331	~ 2268	2316	
		B_1	2327		2267	
VH	C_{1h}	A'	2305	~ 2168	2293	2038

^a Semi-empirical theory on Si_{31}H_n supercells.

^b Molecular-dynamics simulation with Si_{63}H_n supercells.

^c *Ab initio* LDF cluster theory on tetrahedral $\text{Si}_{34}\text{H}_{36+n}$ cluster.

The stretch frequencies of the VH_n complexes have been calculated by Deák *et al* [10], Jones *et al* [7], and Park *et al* [15]. The calculated frequencies are given in Table VI.1, together with the frequencies of the VH , VH_3 , and VH_4 defects determined experimentally, as discussed in the following sections. The calculations by Deák *et al* [10] and Jones *et al* [7] predict that, for each of the three complexes VH_2 , VH_3 , and VH_4 , the symmetric A_1 mode has a higher vibrational frequency than the asymmetric B_1 , E , and T_2 mode. Moreover, the frequencies calculated for the VH_n series exhibit an increasing trend with increasing n , which reflects a decrease in Si-H bond length caused by the increase in hydrogen-hydrogen repulsion. A comparison of the calculated frequencies with those observed for VH , VH_3 , and VH_4 confirms the increasing trend but also shows that the calculated frequencies are too large by 5 - 10 %.

Table VI.2. Calculated stretch frequencies (cm^{-1}) of the isotopically mixed VH , VH_2 , VH_3^+ , and VH_4 complexes in silicon [7]. Columns 3 - 6 contain the frequencies of the Si-H modes and columns 6 - 10 the frequencies of the Si-D modes. All the modes are infrared active except the A_1 mode of VH_4 and VD_4 .

	Point group	Si-H				Si-D			
		Mode	Freq.	Mode	Freq.	Mode	Freq.	Mode	Freq.
VH_4	T_d	A_1	2404.2	T_2	2319.3				
VH_3D	C_{3v}	A_1	2384.3	E	2319.3	A_1	1676.7		
VH_2D_2	C_{2v}	A_1	2363.6	B_1	2319.2	A_1	1690.4	B_2	1663.6
VHD_3	C_{3v}	A_1	2341.9			A_1	1705.1	E	1663.6
VD_4	T_d					A_1	1721.0	T_2	1663.5
VH_3^+	C_{3v}	A_1	2318.0	E	2255.6				
VH_2D^+	C_{1h}	A'	2298.1	A''	2255.5	A'	1632.3		
VHD_2^+	C_{1h}	A'	2277.2			A'	1646.1	A''	1618.9
VD_3^+	C_{3v}					A_1	1661.1	E	1618.6
VH_2	C_{2v}	A_1	2315.6	B_1	2266.5				
VHD	C_{1h}	A'	2291.6			A'	1641.4		
VD_2	C_{2v}					A_1	1658.4	B_1	1625.2
VH	C_{1h}	A'	2247.6						
VD	C_{1h}					A'	1612.6		

Jones *et al* [7] calculated the stretch frequencies of the isotopically mixed VH_iD_j complexes derived from VH , VH_2 , VH_3^+ , and VH_4 in silicon (see Table VI.2). According to the table, partial isotope substitution has the following effect on the stretch frequencies of the VH_n complexes: Substitution of a hydrogen atom with a deuterium atom, which converts the complex VH_iD_j into $VH_{i-1}D_{j+1}$, lowers the degeneracy of the asymmetric mode, whereas the frequency of the mode essentially is unaffected. The symmetric (A) mode shifts down in frequency by $\sim 20 \text{ cm}^{-1}$ by such substitution of isotopes.

2. Survey of experimental studies of vacancy-hydrogen complexes in silicon

a. Infrared absorption studies

The first infrared absorption study of hydrogen in crystalline silicon was reported by Stein in 1975 [18]. The study showed that implantation of protons into silicon gives rise to more than ten absorption lines in the region $1800 - 2250 \text{ cm}^{-1}$ (see Fig. I.4), which were ascribed to Si-H stretch modes associated with hydrogen-decorated implantation-produced defects. Of particular interest to the work presented in this chapter is the observation of intense absorption lines at 2166 and 2223 cm^{-1} .³

³ Stein measured the infrared absorption at room temperature, where the two lines are observed at 2162 and 2210 cm^{-1} , respectively. The frequencies quoted in this thesis are those observed at $\sim 10 \text{ K}$.

As shown in Fig. I.4.b, the 2223-cm⁻¹ line attained its maximum intensity after annealing at ~600 K and disappeared after annealing at ~800 K [18]. The 2166-cm⁻¹ line increased significantly in intensity upon annealing at ~550 K, had maximum intensity at ~700 K, and disappeared after annealing at ~900 K [18]. None of the absorption lines were assigned to specific defects.

In 1985, Shi *et al* reported on the effect of isotope substitution on the 2223-cm⁻¹ line [19,23]. Measurements on silicon grown in a mixed H₂ and D₂ ambient revealed four new Si-H lines and four new Si-D lines, which were ascribed to the isotopically mixed configurations of the 2223-cm⁻¹ centre. Based on the splitting of the 2223-cm⁻¹ line into five lines upon partial isotope substitution, Shi *et al* ascribed the 2223-cm⁻¹ line to a T_2 mode of a centre with T_d symmetry containing four equivalent hydrogen atoms. VH_4 and a SiH_4 molecule located at the T site were proposed as the most likely candidates to the 2223-cm⁻¹ line [19]. In conjunction with the isotope substitution studies of the 2223-cm⁻¹ line [20,23], Bai *et al* [21] calculated the relative intensities of the Si-H and Si-D stretch-modes of VH_iD_j and interstitial SiH_iD_j complexes, with $i + j = 4$, using a combination of empirical valence-force and semi-empirical theory. The authors concluded that only the assignment of the 2223-cm⁻¹ line to VH_4 was consistent with both the observed isotopic shifts *and* the relative intensities of the absorption lines observed in samples containing both hydrogen and deuterium. A uniaxial stress study of the 2223-cm⁻¹ line was reported by Bech Nielsen *et al* in 1989 [24], which showed that the 2223-cm⁻¹ line reflects an $A \rightarrow T$ transition of a centre with cubic symmetry. Hence, the uniaxial stress measurements confirmed the interpretation of the isotope substitution experiments by Shi *et al* [19,23]. Bech Nielsen *et al* assigned the 2223-cm⁻¹ line to VH_4 or SiH_4 at the T site (i - SiH_4).

At present, there seems to be consensus that the 2223-cm⁻¹ line originates from VH_4 rather than i - SiH_4 . This conception is based on several observations: First, theory predicts that VH_4 is strongly bound, whereas no theoretical studies have found that i - SiH_4 is a low-energy configuration. Second, isotope substitution experiments [19,23] have shown that the infrared inactive A_1 mode has higher frequency than the T_2 mode observed at 2223 cm⁻¹. This ordering is opposite to that observed for molecular SiH_4 [1] but is in agreement with the theoretical predictions for VH_4 (see Table VI.1). Third, the isotopic shifts of VH_4 calculated by Jones *et al* [7] (see Table VI.2) are in good agreement with those observed for the 2223-cm⁻¹ line [7,19,23]. Fourth, the fact that the 2223-cm⁻¹ line has the highest frequency of all Si-H stretch modes is in full accordance with the increase in frequency of the VH_n complexes with increasing n predicted by theory (see Table VI.1).

The 2166-cm⁻¹ line was reinvestigated by Bech Nielsen *et al* [25] in 1989 and Mukashev *et al* in 1990 [26]. Bech Nielsen *et al* studied the response of the line on

uniaxial stress, and showed that it originates from an $A \rightarrow E$ transition of a trigonal centre. The 2166-cm^{-1} line was tentatively ascribed to VH_3 , V_2H_6 , or $i\text{-SiH}_3$ [25]. Mukashev *et al* studied the annealing behaviour of the line, and concluded that it originates from the same defect as three weaker lines at 2162, 2188, and 2191 cm^{-1} . Based on the trigonal symmetry of the 2166-cm^{-1} line, the formation of the 2166-cm^{-1} centre,⁴ and the observation of four Si-H stretch modes associated with the same centre, Mukashev *et al* assigned the 2162-, 2166-, 2188-, and 2191-cm^{-1} lines to V_2H_6 in silicon [26]. *Ab initio* theory predicts that the hydrogen-saturated divacancy V_2H_6 has D_{3d} (trigonal) symmetry [27]. This implies that the six Si-H bond stretches of the complex give rise to four stretch modes with A_{1g} , A_{2u} , E_g , and E_u symmetry, respectively [28]. However, according to the rigorous selection rule for vibrational transitions stated in Sec. II.A, only the A_{2u} and E_u modes of V_2H_6 are infrared active and, consequently, the assignment of the four absorption lines at 2162, 2166, 2188, and 2191 cm^{-1} to V_2H_6 is incompatible with the vibrational properties of this complex.

Xie *et al* reported on the effect of neutron irradiation on the infrared absorption of silicon grown in a H_2 ambient in 1991 [29]. After irradiation, absorption lines were observed at 817, 1839, 1987, 1990, 2062, 2068, and 2072 cm^{-1} . Based on the results of isotope substitution, annealing, and an expected increase in vibrational frequency with the number of hydrogen atoms inside the vacancy, Xie *et al* assigned the lines at 1839, {1987, 1990}, {2068, 2072}, and 2223 cm^{-1} to, respectively, VH , VH_2 , VH_3 , and VH_4 . A similar assignment of the 1839-, 1987-, and 1990-cm^{-1} lines was made independently by Meng [30]. The assignment of the 1839-cm^{-1} line to VH is inconsistent with recent infrared studies by Holbech *et al* [31], which identified the lines at 817, 1839, and 2062 cm^{-1} as local modes of the H_2^* defect, as discussed in chapter V. In addition, it will be shown in chapter VIII that the 1987- and 1990-cm^{-1} lines originate from a centre with C_2 (monoclinic-II) symmetry and *not* C_{2v} (orthorhombic-I) symmetry as predicted theoretically for VH_2 . Hence, the assignments by Xie *et al* [29] and Meng [30] of the infrared absorption lines at 1839, {1987, 1990} to VH and VH_2 are incorrect.

b. Magnetic resonance studies

The first experimental study of vacancy-hydrogen complexes in silicon with a magnetic resonance technique was reported by Chen *et al* in 1990 [32]. Silicon single crystals (Czochralski-grown) were exposed to a hydrogen or deuterium plasma and

⁴ A centre giving rise to more than one stretch mode is designated by the frequency of the most intense infrared absorption line. For example, the centre which according to Mukashev *et al* gives rise to the absorption lines at 2162, 2166, 2188, and 2191 cm^{-1} is denoted the “ 2166-cm^{-1} centre”.

subsequently irradiated with 2-MeV electrons at room temperature. The samples were studied with ODMR, and a signal originating from a spin-triplet ($S = 1$) state with C_{2v} (orthorhombic-I) symmetry was observed. Moreover, a poorly resolved hyperfine structure was observed, which was ascribed to the hyperfine interaction with two protons or deuterons. Based on these observations, the authors ascribed the ODMR spectrum to an excited $S = 1$ state of VH_2 in silicon. This interpretation was recently challenged by Stallinga *et al* [33], who pointed out that the spin-Hamiltonian parameters obtained by Chen *et al* coincide with those of the excited $S = 1$ state of the A centre. More work is apparently required before an unambiguous assignment of the ODMR spectrum to a specific defect can be made. For example, a correlative study of the ODMR spectrum in Float-zone and Czochralski silicon, which differ in oxygen concentration by about two orders of magnitude, might help to identify the spectrum.

Bech Nielsen *et al* [34] recently reported the identification of VH in proton-implanted silicon by EPR. An EPR signal from a paramagnetic spin- $1/2$ centre with monoclinic-I symmetry was observed at ~ 45 K. Spectra recorded with proton- and deuteron-implanted samples unambiguously showed that the centre is hydrogen-related. The centre was shown to reorient above ~ 85 K, which caused the monoclinic-I signal to convert into a trigonal signal. The values of the spin-Hamiltonian parameters and the activation energy for reorientation closely resemble those of the E centre in silicon [16]. Based on the observed symmetry, spin-Hamiltonian parameters, proton hyperfine interaction, and the thermally activated reorientation, Bech Nielsen *et al* ascribed the EPR spectrum to VH .

Two additional EPR signals, designated SI_a and SI_b , were observed in the same samples as the VH signal described above [35]. The SI_a and SI_b signals correspond to distinct centres with (nearly trigonal) monoclinic-I symmetry and both exhibited a strong, trigonal hyperfine interaction with a single ^{29}Si nucleus. Only the SI_a signal exhibited a proton hyperfine interaction. Hence, the evidence for the presence of

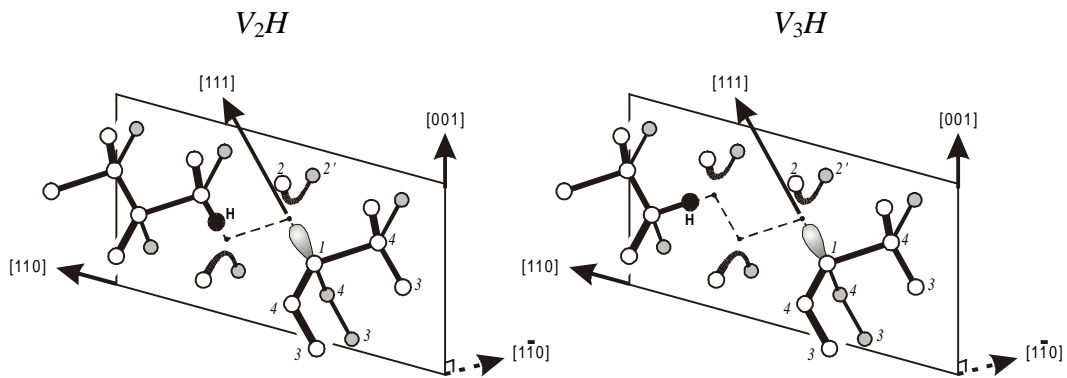


Fig. VI.2. Sketches of the V_2H and V_3H centres, to which the SI_a and SI_b are attributed. The figure is taken from [35].

hydrogen in SI_b is, from an EPR point of view, circumstantial. The authors assigned the SI_a signal to V_2H , and SI_b was tentatively assigned to V_3H or V_4H (see Fig. VI.2).

In order to search for infrared absorption lines correlated with the VH , SI_a , and SI_b EPR signals, correlative isochronal annealing studies were carried out with EPR and infrared spectroscopy on practically identical samples [35]. These studies showed that the VH EPR signal is correlated with an absorption line at 2038 cm^{-1} , and that both signals disappear upon annealing at $\sim 470\text{ K}$. Moreover, it was found that both the SI_a , and SI_b EPR signals anneal out at $\sim 530\text{ K}$, and are correlated with absorption lines at 2068 and 2073 cm^{-1} .⁵ It was not possible to determine which EPR signal corresponds to which absorption line. Nevertheless, the 2068-cm^{-1} line was ascribed to SI_a (V_2H) and the 2073-cm^{-1} line to SI_b (V_3H or V_4H), based on the expectation that the stretch-frequency of the Si-H bond increases with increasing size of the vacancy cluster, as indicated by the upward shift in frequency from 2038 cm^{-1} for VH to $\sim 2070\text{ cm}^{-1}$ for V_nH with $n > 1$.

Finally, VH_3 was recently identified with EPR [36] in samples similar to those of the two previous studies. The EPR signal had a trigonal g-tensor with tensor components characteristic for an electron in a dangling bond orbital of a vacancy-type defect. Moreover, the signal exhibited strong hyperfine interactions with three equivalent hydrogen atoms, in addition to a strong trigonal hyperfine interaction with a single ^{29}Si nucleus. Based on these findings, the EPR signal was assigned to VH_3 in silicon (see Fig. VI.1). Correlative isochronal annealing studies with EPR and infrared spectroscopy revealed that the EPR signal ascribed to VH_3 anneal at $\sim 490\text{ K}$ and is correlated with absorption lines at 2155 and 2185 cm^{-1} .

In summary, VH , V_2H , and VH_3 have been identified with EPR and the Si-H stretch modes of the complexes have been identified at 2038 , 2068 , 2155 , and 2185 cm^{-1} . In addition, there is consensus that the 2223-cm^{-1} line originates from VH_4 , and the absorption line at 2073 cm^{-1} has been assigned to V_3H or V_4H .

3. Introduction to the present work

The present chapter describes infrared absorption measurements on vacancy-hydrogen complexes in proton-implanted silicon. It is shown that absorption lines at 2121 and 2145 cm^{-1} originate from the same centre, which contains two equivalent hydrogen atoms and has orthorhombic-I (C_{2v}) symmetry. The two lines are ascribed to

⁵ The lines at 2068 and 2073 cm^{-1} were ascribed to VH_3 by Xie *et al* [29], as discussed in the previous section. That assignment was partly based on that the 2073-cm^{-1} line was observed to be twice as intense as the 2068-cm^{-1} line, indicating that the former reflects a two-fold degenerate mode and the latter a non-degenerate mode. In the spectra reported in Ref. [35] the 2068-cm^{-1} is more intense than the 2073-cm^{-1} line. This demonstrates that the two lines do not originate from the same centre.

the VH_2 defect. In addition, it is shown that the 2166-cm^{-1} line discussed in Sec. VI.A.2.a originates from the same centre as the 2191 cm^{-1} line, in agreement with the results of Mukashev *et al* [26]. However in contrast to Mukashev *et al* [26], it is demonstrated that the lines 2162 and 2188 cm^{-1} originate from different centres than the 2166- and 2191-cm^{-1} lines. Moreover, it is shown that the 2166-cm^{-1} centre contains more than two hydrogen atoms and has trigonal symmetry, with the 2166- and 2191-cm^{-1} lines reflecting the excitation of a two-fold degenerate E mode and a non-degenerate A mode, respectively. The 2166- and 2191-cm^{-1} lines are ascribed to the V_2H_6 defect.

B. Experimental

Samples of high-resistivity silicon were prepared for implantation as described in Sec. III.A.1. The samples were implanted with protons or deuterons at 50-100 different energies in the range 680 - 2500 keV for protons and 880 - 3000 keV for deuterons. The dose implanted at each energy was adjusted to result in a uniform hydrogen (or deuterium) concentration of 0.02 or 0.05 at. % from 8 to 60 μm below the surface of the sample. The implantation of protons (deuterons) was performed at a sample temperature of $\sim 100\text{ K}$ ($\sim 300\text{ K}$). A sample was coimplanted with protons and deuterons at $\sim 300\text{ K}$ with overlapping profiles, resulting in a concentration of each isotope of 0.05 at. %. Details on the implantation conditions are summarised in Table III.1.

The infrared absorption measurements were performed with the FTIR spectrometer described in Sec. III.B.3. The spectrometer was set up with a Globar source, a Ge-on-KBr beamsplitter and an *MCT-A* detector. The annealing and isotope substitution studies were carried out with the sample mounted in the flow cryostat described in Sec. III.B.3 at a sample temperature of 77 K with a resolution of 0.6 cm^{-1} .

The uniaxial stress studies were performed with the stress-rig described in Sec. III.B.3 placed in the flow-cryostat. The infrared absorption measurements with uniaxial stress were carried out at a sample temperature of $\sim 80\text{ K}$ with a resolution of 0.8 cm^{-1} . During the measurements a polariser was placed between the sample and the detector, which made it possible to measure the absorption of light polarised parallel and perpendicular to the applied force separately.

C. Results

Fig. VI.3 shows the absorbance spectra of silicon implanted with protons at $\sim 100\text{ K}$ and subsequently annealed at room temperature (bottom) and 623 K (top). The spectrum measured after annealing at room temperature contains more than 10 absorption lines in the range $1800 - 2250\text{ cm}^{-1}$. For instance, the lines at $\{1838, 2062\}$, 2038 , 2068 , 2072 , and 2223 cm^{-1} previously assigned to H_2^* [31], VH

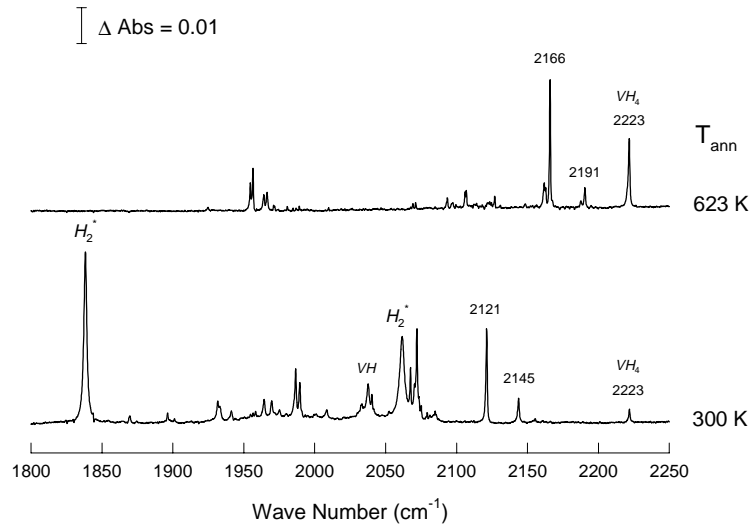


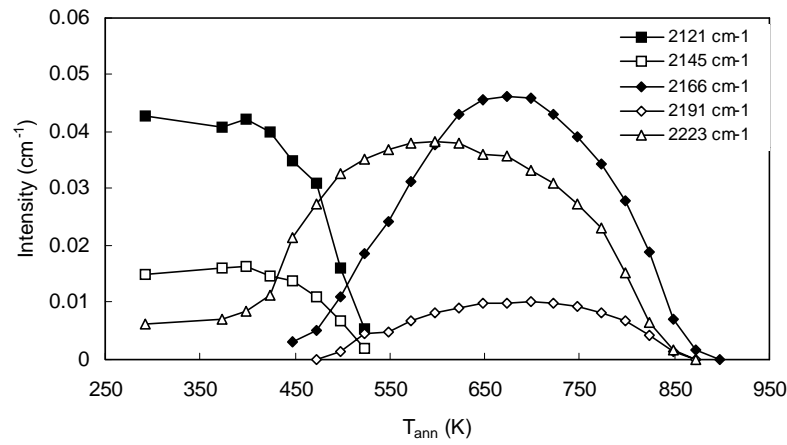
Fig. VI.3. Infrared absorbance of silicon implanted with protons at ~ 100 K and annealed at room temperature (bottom) and 623 K (top).

[34], V_2H [33], V_3H [33], and VH_4 [21] are observed. In addition, two prominent lines are observed at 2121 and 2145 cm^{-1} , which have not yet been identified. The spectrum measured after annealing at 623 K is dominated by the line at 2166 cm^{-1} , which was shown to originate from an $A \rightarrow E$ transition of a trigonal centre [25]. Also observed in this spectrum is the rather weak line at 2191 cm^{-1} . In this chapter, the lines at 2121 , 2145 , 2166 , and 2191 cm^{-1} are studied in detail.

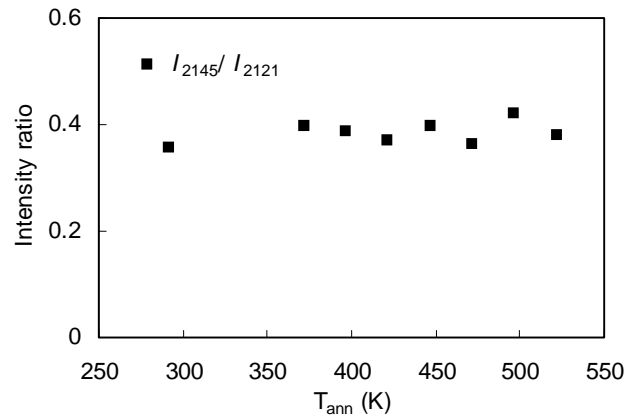
1. Isochronal annealing

The samples were annealed for 30 minutes at temperatures ranging from room temperature to 898 K in steps of 25 K. Between each annealing step, the absorbance of the samples was measured at 77 K. The intensities of the lines at 2121 , 2145 , 2166 , 2191 , and 2223 cm^{-1} are plotted as a function of annealing temperature in Fig. VI.4.a. The 2121 - and 2145 - cm^{-1} lines disappear upon annealing at ~ 485 K. Fig. VI.4.b shows the intensity ratio I_{2145}/I_{2121} as a function of annealing temperature. The relative intensities of the 2121 -, and 2145 - cm^{-1} lines are independent of annealing temperature, which strongly suggests that the two lines originate from the same defect. The 2166 - and 2191 - cm^{-1} lines are formed at ~ 560 K, attain maximum intensity at ~ 670 K, and disappear upon annealing at ~ 800 K. According to Fig. VI.4.c, the intensity ratio of the two lines is independent of the thermal history of the sample. Hence, the lines at 2166 and 2191 cm^{-1} are ascribed to the same centre. Fig. VI.4.c also depicts the intensity ratios I_{2162}/I_{2166} and I_{2188}/I_{2191} as a function of annealing temperature. Both ratios clearly increase above ~ 800 K, which excludes that the 2162 - and 2188 - cm^{-1} lines originate from the 2166 - cm^{-1} centre.

a)



b)



c)

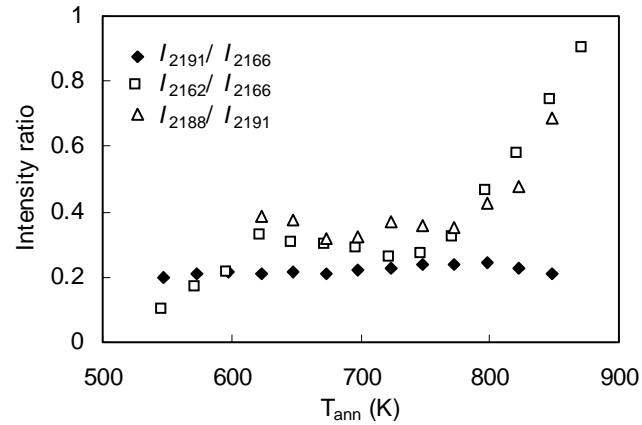


Fig. VI.4. a) Intensity (smoothed) of the lines at 2121, 2145, 2166, 2191, and 2223 cm^{-1} as a function of annealing temperature. b) Intensity ratio I_{2145}/I_{2121} vs. annealing temperature. c) Intensity ratios I_{2191}/I_{2166} , I_{2162}/I_{2166} , and I_{2188}/I_{2191} vs. annealing temperature.

2. Isotope substitution

When deuterons are implanted instead of protons, the absorption lines observed in the region $1800 - 2250 \text{ cm}^{-1}$ in the Si:H sample shift down in frequency to $1300 - 1640 \text{ cm}^{-1}$. In particular, two lines are observed at 1547 and 1564 cm^{-1} after implantation at room temperature, as shown in Fig. VI.5.a. The 1547 - and 1564-cm^{-1} lines in Si:D have the same annealing behaviour and relative intensities as the lines at 2121 and 2145 cm^{-1} in Si:H, suggesting that they originate from the deuterium counterpart of the same centre. When the Si:D sample is annealed, two lines appear at 1576 and 1594 cm^{-1} (see Fig. VI.5.b). The 1576 - and 1594-cm^{-1} lines exhibit the same annealing behaviour as the 2166 - and 2191-cm^{-1} lines in Si:H, and we therefore ascribe them to Si-D stretch modes of the 2166-cm^{-1} centre. The isotopic shift of the 2121 -, 2145 -, 2166 -, and 2191-cm^{-1} lines by approximately a factor $\sqrt{2}$ unambiguously identifies the lines as due to hydrogen-related stretch modes.

Implantation of protons and deuterons with spatially overlapping profiles gives rise to additional absorption lines as compared to the Si:H and Si:D samples implanted

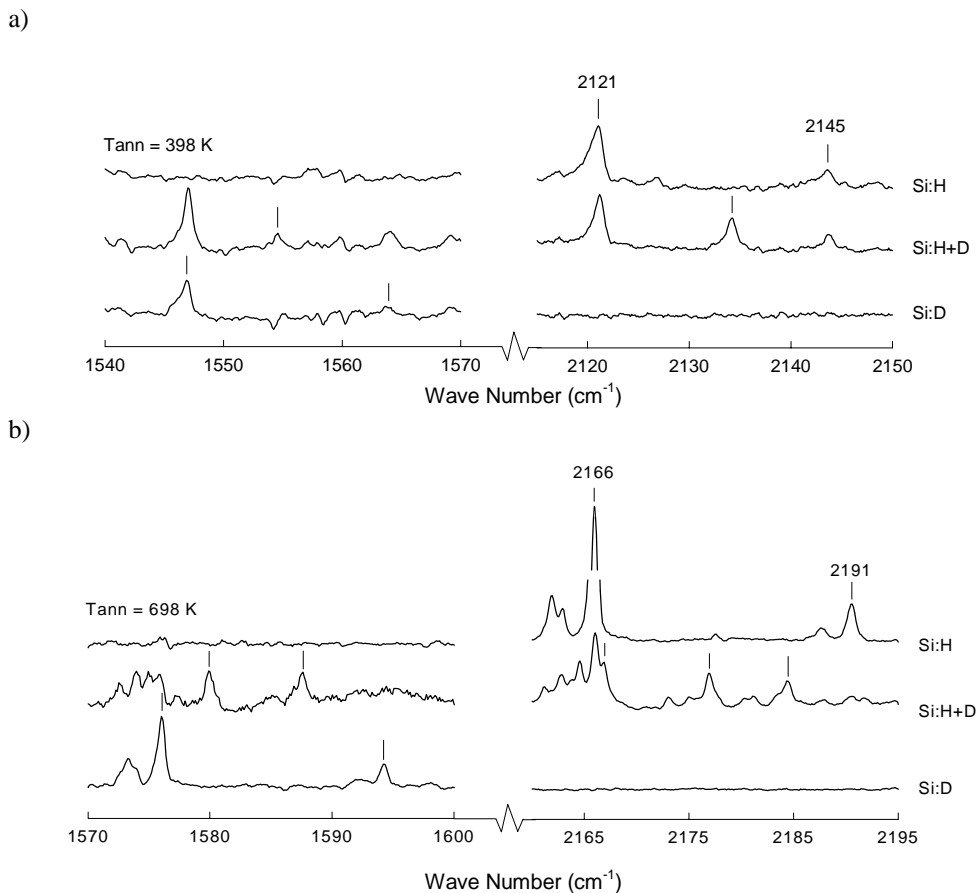


Fig. VI.5. Isotopic shifts of a) the 2121 - and 2145-cm^{-1} lines and b) the 2166 - and 2191-cm^{-1} lines. The middle spectrum (Si:H+D) is measured on the sample implanted with protons and deuterons in overlapping profiles. The lines indicated by vertical markers have the same annealing behaviour as the two lines observed with the Si:H sample.

with only one of the isotopes. The particular lines at 1555 and 2134 cm^{-1} indicated in Fig. VI.5.a exhibit the same annealing behaviour as the lines at 1547 and 1564 cm^{-1} in Si:D and at 2121 and 2145 cm^{-1} in Si:H, and we therefore ascribe them to vibrational modes of the isotopically mixed configurations of the 2121- cm^{-1} centre. The observation of one Si-H and Si-D mode in addition to the two modes present in the Si:H and Si:D samples suggests that the centre contains two equivalent hydrogen atoms. As shown in Fig. VI.5.b, several new absorption lines are observed in the Si:H+D sample in the vicinity of the 2166- and 2191- cm^{-1} lines in Si:H and the 1576- and 1594- cm^{-1} lines in Si:D. The lines at 1580, 1588, 2167, 2177, and 2184 cm^{-1} indicated in Fig. VI.5.b are formed and disappear at the same temperature as the 2166- and 2191- cm^{-1} lines in Si:H. Consequently, we ascribe them to isotopically mixed variants of the 2166- cm^{-1} centre. The observation of three new Si-H stretch modes in the Si:H+D sample, which are correlated with the 2166- and 2191- cm^{-1} lines in Si:H, shows that the 2166- cm^{-1} centre contains at least three hydrogen atoms.

3. Uniaxial stress

a. The 2121- and 2145- cm^{-1} lines

The shifts and splittings of the 2121- and 2145- cm^{-1} lines induced by uniaxial stresses along [100], [111], and [110] directions are shown in Fig. VI.6. Both lines split into two components for all three stress directions. According to Table II.3, this excludes that the lines are associated with excitations of non-degenerate modes of centres with tetragonal, trigonal, and orthorhombic-II symmetry. It can also be excluded that the lines originate from three-fold degenerate modes of a tetrahedral centre because two components are observed with $\vec{F} // [111]$ and $\vec{\epsilon} \perp \vec{F}$. Qualitatively, the observation of two components for all three stress directions is consistent with the splittings expected for an $A_1 \rightarrow E$ transition of a centre with tetragonal or trigonal symmetry. However, a detailed quantitative analysis shows that the slopes of the experimental linear frequency shifts are incompatible with those expected theoretically. The solid straight lines in Fig. VI.6 show the results of a least-squares fit of the theoretical frequency shifts of a centre with orthorhombic-I symmetry to the experimental points. As shown in the figure, all the observed stress-split components are accounted for theoretically and the agreement between the experimental and theoretical frequency shifts is good for both the 2121-

Table VI.3. Piezo-spectroscopic parameters (in $\text{cm}^{-1}/\text{GPa}$) of the lines at 2121 and 2145 cm^{-1} . The parameters were obtained by a least-squares fit of the theoretical frequency shifts of an orthorhombic-I centre to the experimental data.

	2121- cm^{-1}	2145- cm^{-1}
\mathcal{A}_1	-2.6 ± 1.0	-2.2 ± 1.3
\mathcal{A}_2	3.6 ± 0.8	4.6 ± 1.0
\mathcal{A}_3	4.8 ± 0.6	5.4 ± 0.6

however, that the relative intensities of the stress-split components given in Table II.3 are derived with the assumption that the defects are distributed evenly among the equivalent orientations of the centre at zero stress. The validity of this assumption can be tested by measuring the infrared absorption at zero stress and for different polarisations ($\vec{\epsilon}$) of the infrared light, as an even distribution of defects gives intensities of the absorption lines which are independent of the polarisation. Fig. VI.7 shows the 2121- and 2145- cm^{-1} lines measured with $\vec{\epsilon} // \langle 110 \rangle$ and $\vec{\epsilon} // \langle 100 \rangle$. The intensity of the 2121- cm^{-1} line is clearly larger with $\vec{\epsilon} // \langle 110 \rangle$ than with $\vec{\epsilon} // \langle 100 \rangle$, whereas the opposite is the case for the 2145- cm^{-1} line. Hence, we conclude that centre giving rise to the 2121- and 2145- cm^{-1} lines are not evenly distributed and that the relative intensities of the stress-split components given in Table II.3 do not apply for these lines.

The fact that Table II.3 cannot be used in the analysis of the relative intensities of the 2121- and 2145- cm^{-1} lines does not preclude a determination of the symmetry species of the two modes. According to the theoretical stress-pattern of an orthorhombic-I centre given in the table, some of the components are predicted to have zero intensity for a given polarisation of the infrared light. This is only possible if the induced dipole moment associated with all the distinct orientations of the

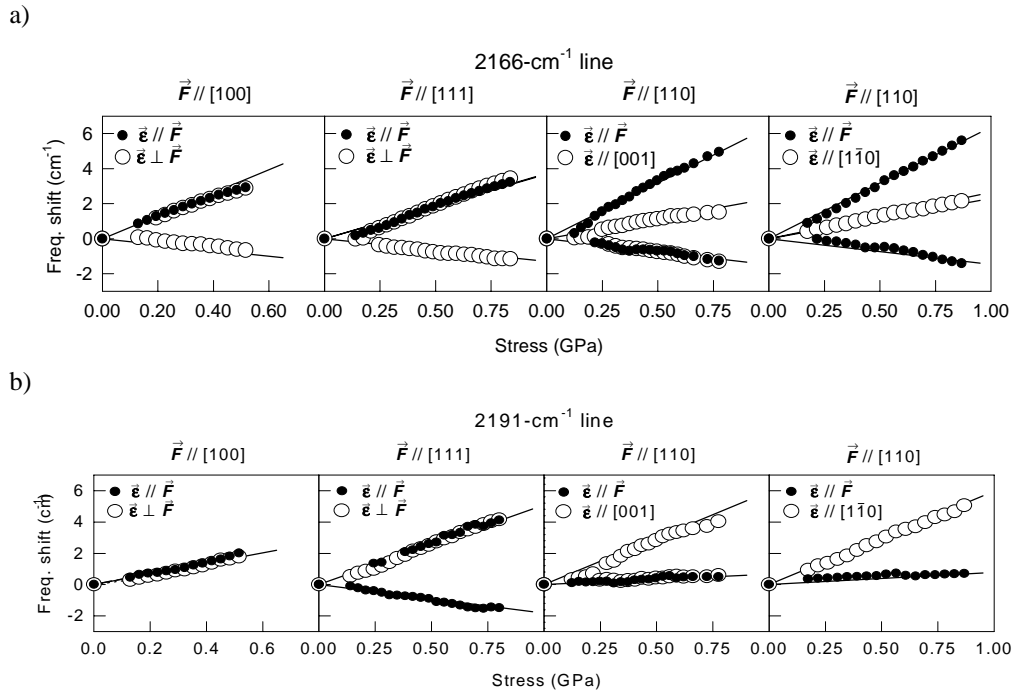


Fig. VI.8. Frequency shifts of a) the 2166- cm^{-1} line and b) the 2191- cm^{-1} line as function of the magnitude of applied uniaxial stresses along [100], [111] and [110] directions. The filled (open) symbols represent the line positions measured with light polarised parallel (perpendicular) to the applied stress. The solid lines are the best-fit frequency shifts for a) an $A \rightarrow E$ and b) an $A \rightarrow A$ transitions of a centre with trigonal symmetry.

centre involved in this component are perpendicular to the polarisation vector of the light. The dipole moments associated with these defect orientations remain perpendicular to the polarisation vector also when the centres are not randomly oriented. Therefore, the components predicted to have zero intensity with a random distribution of centres remain infrared inactive for non-random distributions. With this in mind, a comparison of the experimental stress-pattern depicted in Fig. VI.6 with the theoretical predictions given in Table II.3 imply that the 2121-cm^{-1} line reflects an $A_1 \rightarrow B_1$ transition and the 2145-cm^{-1} line an $A_1 \rightarrow A_1$ transition of an orthorhombic-I centre. The observed asymmetry in the population of the various orientations of the centres persists after annealing at 493 K for 30 minutes, where the 2121-cm^{-1} centre disappears. This shows that the centre does not reorient even at its annealing temperature.

b. The 2166- and 2191-cm^{-1} lines

The effect of uniaxial stress on the absorption line at 2166 cm^{-1} has been studied previously by Bech Nielsen *et al* [25], as discussed in Sec. VI.A.2.a. In the present work, those measurements have been reproduced and new uniaxial stress studies of the line at 2191-cm^{-1} have been performed. The observed splittings and frequency shifts of the 2166- and 2191-cm^{-1} lines induced by uniaxial stress along the major crystal axes are shown in Fig. VI.8. Bech Nielsen *et al* [25] concluded that the 2166-cm^{-1} line originates from an $A \rightarrow E$ transition of a trigonal centre. The straight lines in Fig. VI.8.a correspond to the best fit of the theoretical stress-pattern of such a transition to the experimental data. The fit of the theoretical model to the experimental data is very good, and all splitting components are accounted for. Also, the relative intensities of the stress-split components (not shown) are consistent with the assignment of the 2166-cm^{-1} line to a trigonal $A \rightarrow E$ transition. The best-fit parameters defining the straight lines in Fig. VI.8 are given in Table VI.4 together with the parameters obtained by Bech Nielsen *et al*. The parameters of the 2166-cm^{-1} line obtained previously [25] and in the present work agree within the experimental error bars. Hence, our uniaxial stress study confirms the assignment of the 2166-cm^{-1} to an $A \rightarrow E$ transition of a trigonal centre by Bech Nielsen *et al* [25].

Table VI.4. Piezo-spectroscopic parameters (in $\text{cm}^{-1}/\text{GPa}$) of the lines at 2166 and 2191 cm^{-1} . The parameters were obtained by least-squares fit of the theoretical frequency shifts of $A \rightarrow E$ and $A \rightarrow A$ transitions of a trigonal centre to the experimental data.

	2166-cm^{-1}		2191-cm^{-1}
	This work	Ref. [25]	This work
\mathcal{A}_1	2.8 ± 1.0	2.02 ± 0.13	3.8 ± 0.7
\mathcal{A}_2	-2.0 ± 0.3	-1.96 ± 0.08	-2.9 ± 0.3
\mathcal{B}	-2.4 ± 0.6	-1.60 ± 0.05	
\mathcal{E}	0 ± 0.4	0.29 ± 0.09	

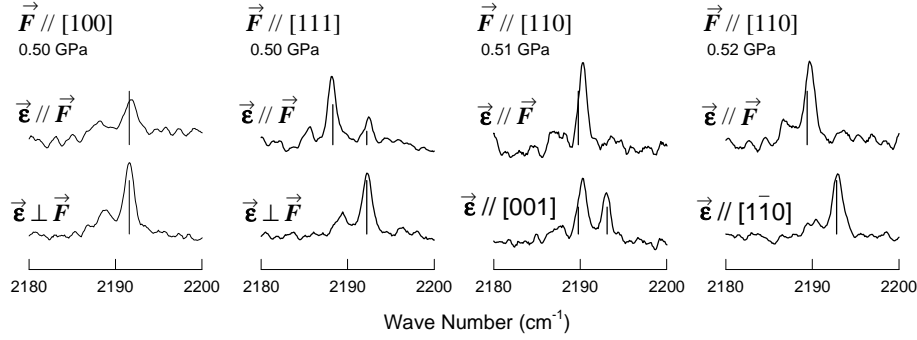


Fig. VI.9. Absorbance profiles measured at with uniaxial stress along [100], [111], and [110] and light polarised parallel and perpendicular to the applied stress. The sticks shown in the plots indicate the best-fit positions obtained with the parameters given in Table VI.4 and the theoretical relative intensities for an $A \rightarrow A$ transition of a trigonal centre.

The 2191-cm^{-1} line does not split under [100] stress and splits into two components when uniaxial stress is applied along [111]. According to Table II.3, this strongly suggests that the line reflects an $A \rightarrow A$ transition of a trigonal centre. The straight lines depicted in Fig. VI.6.b are the result of a least-squares fit of the theoretical frequency shifts of such a transition to the experimental line positions. The agreement between the observed and theoretical splittings is very good. The intensity of the 2191-cm^{-1} line at zero stress does not depend on the direction along which the light is polarised, which suggests that the centres associated with these lines are randomly oriented. The assignment of the 2191-cm^{-1} line to an $A \rightarrow A$ transition of a trigonal centre can thus be studied in more detail by comparison of the experimental and theoretical relative intensities of the stress-split components. The absorbance profiles measured with uniaxial stresses along [100], [111], and [110] directions and with light polarised parallel and perpendicular to the direction of the stress are shown in Fig. VI.9. The best-fit line positions obtained with the parameters given in Table VI.4 and the theoretical relative intensities for an $A \rightarrow A$ transition of a trigonal centre are indicated by vertical sticks in Fig. VI.9. The theoretical positions and intensities of the stress-split components are in very good agreement with the experimental profiles. Based on the results of the uniaxial stress measurements the 2191-cm^{-1} line is assigned to an $A \rightarrow A$ transition of a trigonal centre.

D. Discussion

1. The 2121- and 2145-cm⁻¹ lines

In the previous section it was shown that the absorption lines at 2121 and 2145 cm⁻¹ in proton-implanted silicon originate from the same centre, which contains two equivalent hydrogen atoms and has orthorhombic-I (C_{2v}) symmetry. The strong absorption of the 2121- and 2145-cm⁻¹ lines indicates that the centre is very abundant at room temperature in the proton-implanted crystals. The concentrations of other impurities, such as oxygen and carbon, in the samples are three orders of magnitude less than the implanted hydrogen concentration. This practically excludes that other impurities than hydrogen are involved in the complex and suggests that the centre that gives rise to the lines at 2121 and 2145 cm⁻¹ consists of two hydrogen atoms interacting either with the perfect lattice or intrinsic defects.

The simplest complex which has orthorhombic-I symmetry and contains two equivalent hydrogen atoms consists of two hydrogen atoms located at neighbouring bond-centre sites (see Fig. VI.10.a). However, at least two points argue against that the lines at 2121 and 2145 cm⁻¹ originate from this complex. First, no theoretical calculations have predicted that this complex is stable. Second, the H_2^* defect discussed in chapter V can readily be formed from the complex shown in Fig. VI.10.a by moving one of the hydrogen atoms from its BC site to the AB site adjacent to the central silicon atom. The barrier for this replacement is presumably close to the migration barrier for isolated H_{BC} , which indicates that the replacement should take place at ~200 K. This is incompatible with the fact that the 2121- and 2145-cm⁻¹ lines are stable up to ~485 K. We, therefore, consider it very unlikely that the complex shown in Fig. VI.10.a gives rise to the 2121- and 2145-cm⁻¹ lines.

Implantation of protons into silicon is known to create vacancies and interstitial silicon atoms (self-interstitials). The self-interstitial has not been observed directly, but on the basis of theoretical calculations it is believed that the stable configuration is

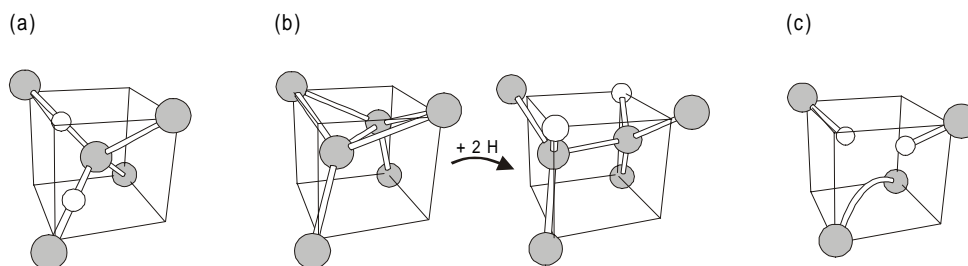


Fig. VI.10. Three centres consisting of two equivalent hydrogen atoms interacting with an otherwise perfect lattice or an intrinsic defect. a) Two hydrogen atoms at neighbouring BC sites, b) the self-interstitial and the effect of hydrogenation, and c) the vacancy binding two hydrogen atoms (VH_2). The grey spheres represent silicon and the white spheres hydrogen atoms.

a $\langle 110 \rangle$ -split, where two silicon atoms share a substitutional site and are split symmetrically along a $\langle 110 \rangle$ direction as shown in Fig. VI.10.b (see e.g. Ref. [37] and references therein). *Ab initio* calculations predict that the self-interstitial can bind two hydrogen atoms [38,37] but the addition of hydrogen causes the two central silicon atoms to distort to the configuration with monoclinic-II (C_2) symmetry shown in Fig. VI.10.b. We therefore conclude that the lines at 2121 and 2145 cm^{-1} do not originate from the complex consisting of two hydrogen atoms bonded to the self-interstitial.

As discussed in the Sec. VI.A.1, theory predicts that hydrogen can saturate the dangling bonds inside the monovacancy or vacancy clusters. In particular, theoretical studies of the atomic and electronic structure and the vibrational properties of the VH_2 defect in silicon have been carried out, as summarised in Sec. VI.A.1. In short, the theoretical studies predict that the VH_2 centre has orthorhombic-I (C_{2v}) symmetry and gives rise to two Si-H stretch modes with frequencies between that of VH at 2038 cm^{-1} and those of VH_3 at 2155 and 2185 cm^{-1} . The predicted splitting of the two stretch modes of VH_2 vary from 4 to 49 cm^{-1} but the theoretical methods employed agree that the A_1 mode has higher frequency than the B_1 mode (see Table VI.1). Jones *et al* [7] have calculated the isotopic shifts of VH_2 and found that VHD gives rise to a Si-H and a Si-D stretch mode located at the mean frequency of the A_1 and B_1 modes of, respectively, VH_2 and VD_2 (see Table VI.2). All these theoretical predictions for the VH_2 complex are consistent with those of the centre giving rise to the 2121- and 2145- cm^{-1} lines.

The observation of the absorption lines at 2068 and 2073 cm^{-1} , which have been assigned to V_2H and V_3H [33], show that vacancy clusters also are present in the sample. However, the experimental results indicate that the 2121- and 2145- cm^{-1} lines are not associated with two hydrogen atoms bonded in a multi-vacancy. The divacancy without any reconstruction has D_{3d} (trigonal) symmetry. This point group does not have C_{2v} as a subgroup and it is therefore impossible to form V_2H_n complexes with C_{2v} symmetry as observed for the 2121- and 2145- cm^{-1} lines. The trivacancy with the two dangling bonds of the central vacancy saturated by hydrogen does have the required C_{2v} symmetry. However, the formation of this complicated species is presumably much less probable than the formation of VH_2 . Therefore, we consider VH_2 as the best candidate to the origin of the 2121- and 2145- cm^{-1} lines.

The assignment of the lines at 2121 and 2145 cm^{-1} to VH_2 is also in accordance with the annealing behaviour of the two lines. Fig. VI.4.a shows that the 2121 and 2145 cm^{-1} lines disappear upon annealing at ~ 485 K, whereas the 2223- cm^{-1} line (assigned to VH_4) increases significantly in intensity around this temperature. This suggests that the loss of VH_2 is due to a conversion of this centre into VH_4 by capture

of hydrogen atoms. It should be noted that e.g. the H_2^* defect anneals at ~ 440 K, which provides a source of hydrogen at this temperature. This hydrogen-capture scenario can also explain an apparent inconsistency between theory and the assignment of the 2121- and 2145- cm^{-1} lines to VH_2 and the 2223- cm^{-1} line to VH_4 . As discussed in Sec. VI.A.1, theory predicts that the binding energy per hydrogen atom for the VH_n complexes decreases with increasing n and, hence, one would expect VH_2 to *dissociate* at higher temperature than VH_4 , in conflict with the observed annealing behaviour. Within the hydrogen-capture scenario this inconsistency does not exist, as the disappearance of VH_2 is due to conversion and not dissociation.

2. The 2166- and 2191- cm^{-1} lines

In Sec. VI.C it was shown that the lines at 2166 and 2191 cm^{-1} appear with the same relative intensities independent of annealing temperature, and that the 2166- cm^{-1} line corresponds to an E mode and the 2191- cm^{-1} line to an A mode of a trigonal centre. This establishes that the 2166- and 2191- cm^{-1} lines originate from the same trigonal defect. The assignment of both an infrared active A and E Si-H stretch modes to the same trigonal centre suggests that the centre contains three or six hydrogen atoms bonded to silicon. This is also qualitatively consistent with the results of partial substitution.

The trigonal symmetry and the presence of three or six hydrogen atoms limits the reasonable candidates to the 2166- cm^{-1} centre to VH_3 , V_2H_6 , and $i\text{-SiH}_3$ centred on a $\langle 111 \rangle$ axis near the T site, as pointed out by Bech Nielsen *et al* [25]. The centres are sketched in Fig. VI.11.

The first complex to be discussed is $i\text{-SiH}_3$ shown in Fig. VI.11.a. The centre has trigonal (C_{3v}) symmetry and two infrared active stretch modes with E and A_1

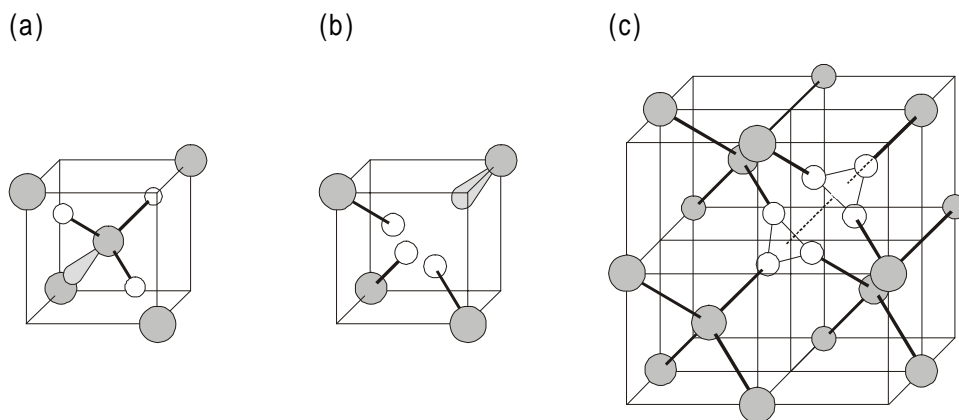


Fig. VI.11. Reasonable candidates to the origin of the 2166- and 2191- cm^{-1} lines. a) An interstitial SiH_3 unit near the T site, b) VH_3 , and c) V_2H_6 . The grey (white) spheres represent silicon (hydrogen) atoms.

symmetry. Infrared studies of trihydride ($-SiH_3$) units in molecular disilane (Si_2H_6) have shown that the frequency of the E mode is 2167 cm^{-1} , whereas the frequency of the A_1 mode is 2153 cm^{-1} [39]. These frequencies are close to those observed in the present work but the ordering of the modes is reversed. This indicates that the sign of the bond-bond interaction which leads to the mode splitting is different for disilane and the centre giving rise to the 2166- and 2191-cm^{-1} lines. In a trihydride unit the three Si-H bonds point away from the common silicon atom, and according to the ordering of the molecular trihydride frequencies, this results in a decrease in the bond-bond interaction when the three bonds are elongated symmetrically. The reverse ordering observed for the 2166- and 2191-cm^{-1} modes show that the bond-bond interaction for this centre increases when the Si-H bonds are elongated symmetrically. This indicates that the Si-H bonds point towards the same centre and thus that the two modes do not originate from a trihydride unit. The 2166- and 2191-cm^{-1} lines disappear upon annealing at $\sim 800\text{ K}$ and are among the most stable hydrogen-related complexes in silicon. On the contrary, semi-empirical calculations by Deák *et al* [10] found that the interstitial SiH_3 unit is unstable as compared to an isolated self-interstitial and three isolated hydrogen atoms. Based on these points, we consider it unlikely that the 2166- and 2191-cm^{-1} lines originate from $i-SiH_3$.

Another likely candidate to the 2166-cm^{-1} centre is the vacancy with three dangling bonds saturated by hydrogen atoms (VH_3) sketched in Fig. VI.11.b. This centre is predicted by theory to have trigonal (C_{3v}) symmetry and to have an E and an A_1 stretch mode located between the stretch mode of VH (2038 cm^{-1}) and the T_2 mode of VH_4 (2223 cm^{-1}). The predicted splitting of the two modes is 12 cm^{-1} [10] and 74 cm^{-1} [7] for VH_3 (see Table VI.1), and the A_1 mode is in both cases predicted to have higher frequency than the E mode. All these predictions are consistent with the observations made for the 2166- and 2191-cm^{-1} lines. In particular, it should be noted that the ordering of the modes is correct as opposed to the trihydride units discussed above. Based on the agreement between experiment and theory we ascribed the lines at 2166 and 2191 cm^{-1} to VH_3 in two conference proceedings [7,8].

Since then, EPR experiments have been performed, which have added substantially to the understanding of vacancy-hydrogen complexes in silicon. For instance, the VH_3 centre was recently identified with EPR in proton-implanted silicon [36]. Annealing studies showed that VH_3 disappears upon annealing at $\sim 500\text{ K}$, i.e. at about the same temperature as the 2166- and 2191-cm^{-1} lines are formed. This shows that the lines at 2166 and 2191 cm^{-1} do not originate from VH_3 .

The third and last reasonable candidate to the origin of the 2166- and 2191-cm^{-1} lines is the hydrogen-saturated divacancy (V_2H_6) sketched in Fig. VI.11.c. V_2H_6 has D_{3d} (trigonal) symmetry and four Si-H stretch modes with A_{1g} , E_g , A_{2u} , and E_u

symmetry. Only the A_{2u} , and E_u modes are infrared active, and V_2H_6 is thus expected to give rise to only two infrared absorption lines in the Si-H stretch region. The theoretical stress-patterns of the $A_{1g} \rightarrow A_{2u}$ and $A_{1g} \rightarrow E_u$ transitions are identical to those of the $A \rightarrow A$ and $A \rightarrow E$ transitions used in the analysis of the uniaxial stress experiments on the 2166-, and 2191- cm^{-1} lines [40]. Thus, the stress-patterns observed for these two lines are consistent with the assignment of the line at 2166 cm^{-1} to an $A_{1g} \rightarrow E_u$ transition and the 2191- cm^{-1} line to an $A_{1g} \rightarrow A_{2u}$ transition of the V_2H_6 centre. Detailed theoretical studies of the vibrational modes of V_2H_6 in silicon have, to my knowledge, not yet been reported, and we must therefore be content with a qualitative description. The V_2H_6 centre can qualitatively be considered as two VH_3 units joined along a common $\langle 111 \rangle$ axis. For V_2H_6 in a rigid lattice with Si-H (Si-Si) bond lengths of 1.48 Å (2.35 Å), the distance between hydrogen atoms in the same vacancy is 1.43 Å, whereas the smallest distance from one of the hydrogen atoms to a hydrogen atom in the opposite vacancy is 4.90 Å. This indicates that the interaction between Si-H bonds in adjacent vacancies is much smaller than the interaction between two Si-H bonds located within the same vacancy and, hence, that the vibrational modes of V_2H_6 resemble those of two weakly coupled VH_3 units. This simple picture is consistent with VH_3 having stretch modes at 2155 and 2185 cm^{-1} [36] and V_2H_6 at 2166- and 2191- cm^{-1} . Moreover, theory predicts that the binding energy per hydrogen atom decreases for the VH_n complexes with increasing n due to the increase in repulsion between the hydrogen atoms. This suggests that the binding energy per hydrogen atom is larger for V_2H_6 than for VH_4 , in agreement with the larger thermal stability of the 2166- and 2191- cm^{-1} lines as compared to the 2223- cm^{-1} line (see Fig. VI.4.a).

In summary, the results of the infrared absorption studies of the 2166- and 2191- cm^{-1} lines in proton-implanted silicon strongly suggest that the two lines correspond to stretch modes of VH_3 or two VH_3 units in the V_2H_6 complex. Based on the thermal stability of the 2166- and 2191- cm^{-1} lines and the assignment of absorption lines at 2155 and 2185 cm^{-1} to VH_3 , we ascribe the 2166- and 2191- cm^{-1} lines to V_2H_6 in silicon.

E. Conclusion

The present chapter has presented infrared absorption studies of prominent absorption lines at 2121, 2145, 2166, and 2191 cm^{-1} in proton-implanted silicon. The 2121- and 2145- cm^{-1} lines are observed after proton implantation at room temperature and in samples implanted at cryogenic temperatures and stored at room temperature. The two lines disappear upon annealing at ~ 485 K. The two lines originate from Si-H stretch modes of a centre containing two equivalent hydrogen atoms. Uniaxial stress

measurements reveal that the 2121- and 2145-cm⁻¹ lines correspond to $A_1 \rightarrow B_1$ and an $A_1 \rightarrow A_1$ transition, respectively, of a centre with orthorhombic-I symmetry. The symmetry, the ordering of the stretch modes, and the isotopic shifts are consistent with theoretical predictions for the VH_2 complex on silicon. Based on these observations we assign the 2121- and 2145-cm⁻¹ lines to VH_2 . The disappearance of the two lines upon annealing at ~500 K is attributed to capture of hydrogen atoms by the centre rather than thermal dissociation of the Si-H bonds. The absorption lines at 2166 and 2191 cm⁻¹ are formed upon annealing at ~560 K and disappear after annealing at ~800 K. The lines originate from Si-H stretch modes of a centre containing more than two hydrogen atoms. The 2166- and 2191-cm⁻¹ lines correspond to the excitation of, respectively, a two-fold degenerate and a non-degenerate mode of a trigonal centre. The 2166- and 2191-cm⁻¹ lines are assigned to V_2H_6 .

F. Acknowledgements

I would like to thank L. Hoffmann for carrying out the annealing and isotope substitution measurements presented in this chapter.

G. References

- [1] "Handbook of Chemistry and Physics", 73rd ed. (CRC Press Inc, Boca Raton, 1992).
- [2] Y. J. Chabal, *Physical B*, **170**, 447 (1991).
- [3] K. L. Brower, *Phys. Rev. B*, **38**, 9657 (1988); K. L. Brower, *Phys. Rev. B*, **42**, 3444 (1990).
- [4] M. Bruel, *Electron. Lett.* **31**, 1201 (1995).
- [5] F. A. Reboledo, M. Ferconi, and S. T. Pantelides, submitted to *Phys. Rev. Lett.*
- [6] *Master thesis* of L. Hoffmann, Institute of Physics and Astronomy, University of Aarhus (April, 1995).
- [7] B. Bech Nielsen, L. Hoffmann, M. Budde, R. Jones, J. Goss, S. Öberg, in "Defects in Semiconductors 18", edited by M. Suezawa and H. Katayama-Yoshida, *Materials Science Forum Vol. 196-201* (Trans Tech, Aedermannsdorf, 1995), 933 (1995).
- [8] B. Bech Nielsen, L. Hoffmann, and M. Budde, *Mater. Sci. Eng. B*, **36**, 259 (1996).
- [9] V. A. Singh, C. Weigel, J. W. Corbett, and L. M. Roth, *Phys. Stat. Sol. (b)*, **81**, 637 (1977); V. A. Singh, J. W. Corbett, C. Weigel, and L. M. Roth, *Physics Letters A*, **65**, 261 (1978).

- [10] P. Deák, M. Heinrich, L.C. Snyder, and J. W. Corbett, *Mater. Sci. Eng. B*, **4**, 57 (1989).
- [11] H. Xu, *Phys. Rev. B*, **46**, 1403 (1992).
- [12] C. G. Van de Walle, *Phys. Rev. B*, **49**, 4579 (1994).
- [13] C. G. Van de Walle, and R. A. Street, *Phys. Rev. B*, **49**, 14766 (1994).
- [14] M. A. Roberson and S. K. Estreicher, *Phys. Rev. B*, **49**, 17040 (1994).
- [15] Y. K. Park, S. K. Estreicher, C. W. Myles, and P. A. Fedders, *Phys. Rev. B*, **52**, 1718 (1995).
- [16] G. D. Watkins and J. W. Corbett, *Phys. Rev.*, **134**, A1359 (1964).
- [17] P. W. Atkins, M. S. Child, and C. S. G. Phillips, "Tables for Group Theory", (Oxford University Press, New York, 1970).
- [18] H. J. Stein, *J. Electron. Mater.*, **4**, 159 (1975).
- [19] T. S. Shi, L. M. Xie, G. R. Bai, and M. W. Qi, *Phys. Stat. Sol. (b)*, **131**, 511 (1985).
- [20] T. S. Shi, G. R. Bai, M. W. Qi, and J. K. Zhou, in "Defects in Semiconductors", edited by H. J. von Bardeleben, *Materials Science Forum* Vol. 10-12 (Trans Tech, Aedermannsdorf, 1986), 597 (1986).
- [21] G. R. Bai, J. K. Zhou, J. M. Chen, T. S. Shi, M. W. Qi, L. M. Xie, *Scientia Sinica (series A)*, **16**, 499 and 630 (1988).
- [22] X. T. Meng, Y. C. Chang, and Y. D. Fan, *Phys. Stat. Sol. (a)*, **101**, 619 (1987).
- [23] G. R. Bai, M. W. Qi, L. M. Xie and T. S. Shi, *Solid State Communications*, **56**, 277 (1985).
- [24] B. Bech Nielsen, J. Olajos, and H.G. Grimmeiss, *Phys. Rev. B*, **39**, 3330 (1989).
- [25] B. Bech Nielsen, and H. G. Grimmeiss, *Phys. Rev. B*, **40**, 12403 (1989).
- [26] B.N. Mukashev, S.Z. Tokmoldin, and M.F. Tamendarov, in "Proceedings of the International Conference on the Science and Technology of Defect Control in Semiconductors, Yokohama, Japan, 1989", edited by K. Sumino, (North-Holland, Amsterdam, 1990), p. 429.
- [27] A. Resende and R. Jones, *private communication*.
- [28] E. B. Wilson Jr., J. C. Decius, and P. C. Cross, "Molecular vibrations", (Dover Publications, New York, 1955).
- [29] L. M. Xie, M. W. Qi, and J. M. Chen, *J. Phys.: Condens. Matter*, **3**, 8519 (1991).
- [30] X. T. Meng, *Physica B*, **170**, 249 (1991).
- [31] J. D. Holbeck, B. Bech Nielsen, R. Jones, P. Sitch, and S. Öberg, *Phys. Rev. Lett.*, **71**, 875 (1993).

- [32] W. M. Chen, O. O. Awadelkarim, B. Monemar, J. L. Lindström, and G. S. Oehrlein, *Phys. Rev. Lett.*, **64**, 3042 (1990).
- [33] Comment to Ref. [32]: P. Stallinga, and B. Bech Nielsen, *Phys. Rev. Lett.*, **80**, 422 (1998); Reply: W. M. Chen, O. O. Awadelkarim, B. Monemar, J. L. Lindström, and G. S. Oehrlein, *Phys. Rev. Lett.*, **80**, 423 (1998).
- [34] B. Bech Nielsen, P. Johannesen, P. Stallinga, K. Bonde Nielsen, and J. R. Byberg, *Phys. Rev. Lett.*, **79**, 1507 (1997).
- [35] P. Stallinga, P. Johannesen, S. Herstrøm, K. Bonde Nielsen, B. Bech Nielsen, and J. R. Byberg, *Phys. Rev. B*, **58**, 3842 (1998).
- [36] *Master thesis* of S. Herstrøm, Institute of Physics and Astronomy, University of Aarhus (June, 1998). *To be published*.
- [37] C. G. Van de Walle and J. Neugebauer, *Phys. Rev. B*, **52**, R14320 (1995).
- [38] M. Budde, B. Bech Nielsen, P. Leary, J. Goss, R. Jones, P. R. Briddon, S. Öberg, and S. J. Breuer, *Phys. Rev. B*, **57**, 4397 (1998).
- [39] M. Cardona, *Phys. Stat. Sol. (b)*, **118**, 463 (1983).
- [40] A. E. Hughes and W. A. Runciman, *Proc. Phys. Soc.*, **90**, 827 (1967).

VII. Vacancy-hydrogen complexes in germanium

A. Introduction

In the preceding chapter it was shown that hydrogen interacts with the dangling bonds of vacancies and vacancy clusters in silicon, which results in the formation of a variety of vacancy-hydrogen complexes in proton-implanted silicon. Hydrogen forms covalent bonds with germanium of nearly the same strength as Si-H bonds (see Table I.1). This suggests that hydrogen interacts with vacancy-type defects in germanium, and that vacancy-hydrogen complexes are formed in proton-implanted germanium.

The infrared absorption of proton-implanted germanium was first studied by Tatarikiewicz *et al* [1] in 1987. Seven absorption lines were observed in the range 1750 – 2100 cm^{-1} , and the isotopic shifts of the lines revealed that they originate from Ge-H stretch modes. No assignments to specific hydrogen-related defects were made.

The present chapter describes annealing, isotope substitution and uniaxial stress studies of two absorption lines at 2014.9 and 2061.5 cm^{-1} observed by Tatarikiewicz *et al* [1]. In addition, three new lines at 1979.5, 1992.6, and 2024.8 cm^{-1} are studied in detail. It is shown that the 1979.5- and 1992.6- cm^{-1} lines originate from the same centre, which contains two equivalent hydrogen atoms and has orthorhombic-I symmetry. The two lines are assigned to VH_2 in germanium. The 2061.5- cm^{-1} line is shown to originate from an $A \rightarrow T$ transition of a centre with cubic symmetry containing four equivalent hydrogen atoms, and the line is assigned to VH_4 in germanium. Finally, it is shown that the 2014.9- and 2024.8- cm^{-1} lines originate from the same centre. The 2014.9- and 2024.8- cm^{-1} lines correspond to, respectively, $A \rightarrow E$ and $A \rightarrow A$ transitions of a centre with trigonal symmetry. The two lines are assigned to V_2H_6 in germanium.

In conjunction with the present work, theoretical studies of vacancy-hydrogen complexes in germanium were carried out by B. J. Coomer *et al*, University of Exeter, UK [2]. The calculations were based on *ab initio* local-density-functional theory on molecular clusters containing 70 germanium atoms and saturated with hydrogen atoms at the surface. The calculations predict that the vacancy in germanium can bind up to four hydrogen atoms and that the atomic configurations of the VH_n complexes, apart from an appropriate scaling of bond lengths, are very similar to those of the pertinent centres in silicon. The V_2H_6 complex in germanium was also studied theoretically, and was found to have D_{3d} symmetry. The vibrational stretch frequencies of the VH_n complexes were calculated and exhibited an increasing trend with increasing n , as in silicon.

To my knowledge, only a single experimental study of vacancy-hydrogen complexes in germanium has been reported. In 1977, Haller *et al* reported on experimental studies of an acceptor level at $E_v + 0.080$ eV [3], which was ascribed to V_2H in germanium. The association of the level with V_2H was inferred from the following observations: 1) The level can only and always be observed in dislocation-free high-purity germanium grown in a hydrogen ambient, which shows that hydrogen is involved in the centre. 2) The level is formed during cool-down after growth, where vacancies and vacancy clusters are abundant in the sample. No microstructural information on the centre is available [4].

B. Experimental

The samples used in the studies of vacancy-hydrogen complexes in proton-implanted germanium described in the present chapter were identical to those used for the studies of the H_2^* defect described in chapter V. In short, ultra-pure, high-resistivity germanium samples were implanted with protons and/or deuterons at multiple energies at ~ 30 K. The dose at each energy was adjusted to result in a homogenous profile of implants from 11 – 44 μm below the surface of the sample. The resulting local concentration of hydrogen and/or deuterium was 0.05 at. %. After implantation the samples were stored at room temperature. Samples were implanted with either protons (Ge:H), deuterons (Ge:D), or protons and deuterons with spatially overlapping profiles (Ge:H+D).

The infrared absorption measurements were carried with the same setup as the studies of the H_2^* defect described in chapter V. The annealing and isotope substitution measurements were performed at 9 ± 1 K with a spectral resolution of 0.5 cm^{-1} , whereas the uniaxial stress measurements were carried out at 77 K with 0.8-cm^{-1} resolution. The reader is referred to chapter III for a detailed description of sample preparation and the experimental setup.

C. Results

Implantation of protons into germanium at ~ 30 K followed by annealing at room temperature gives rise to a series of absorption lines in the range $1750 - 2100$ cm^{-1} , which according to the discussion in Sec. V.C reflect excitations of Ge-H stretch modes. In this chapter, the lines observed at 1979.5, 1992.6, and 2061.5 cm^{-1} after annealing at 300 K (see Fig. VII.1) are studied in detail, together with the two lines observed at 2014.9 and 2024.8 cm^{-1} after annealing at 530 K.

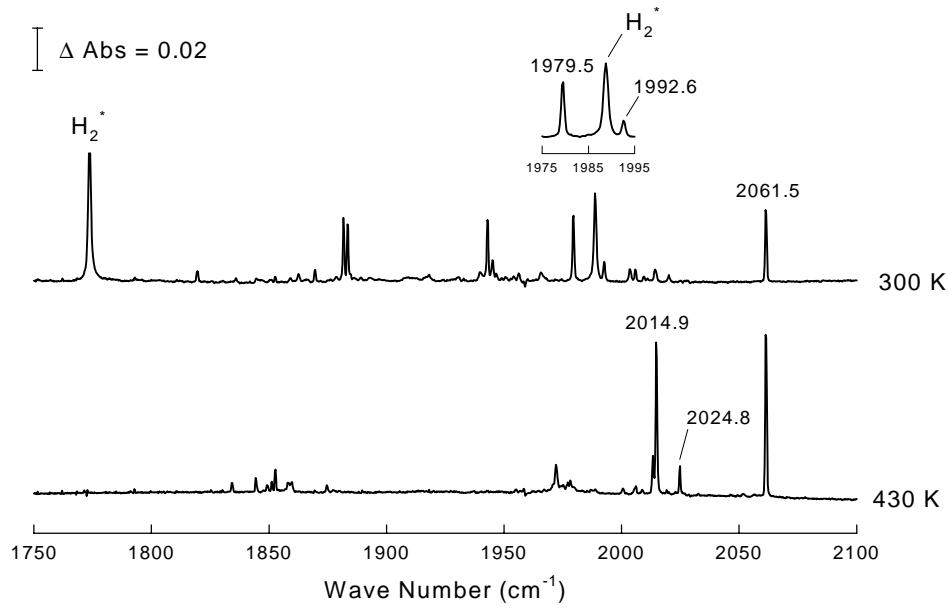


Fig. VII.1. Absorbance spectra of germanium implanted with protons at ~ 30 K and annealed at 300 K and 530 K. The lines indicated by their line positions are studied in the present chapter. The inset shows the spectrum (300 K anneal) in the vicinity of the 1979.5 and 1992.6 cm^{-1} lines. Between these two lines, the 1989- cm^{-1} line of the H_2^* defect is observed.

1. Isochronal annealing

An isochronal annealing study was carried out in order to search for correlated absorption lines in the spectra, and to explore the formation and thermal stability of the pertinent centres. The samples were annealed for 30 minutes at various temperatures, starting from room temperature and ranging up to 693 K. Between each annealing step, the absorbance spectra was measured at 9 K. The effect of annealing on the infrared absorbance of the proton-implanted germanium sample is shown in Fig. VII.2. In the temperature range from 398 to 458 K, a major change to the spectra takes place. For example, the lines at 1979.5 and 1992.6 cm^{-1} and the lines associated

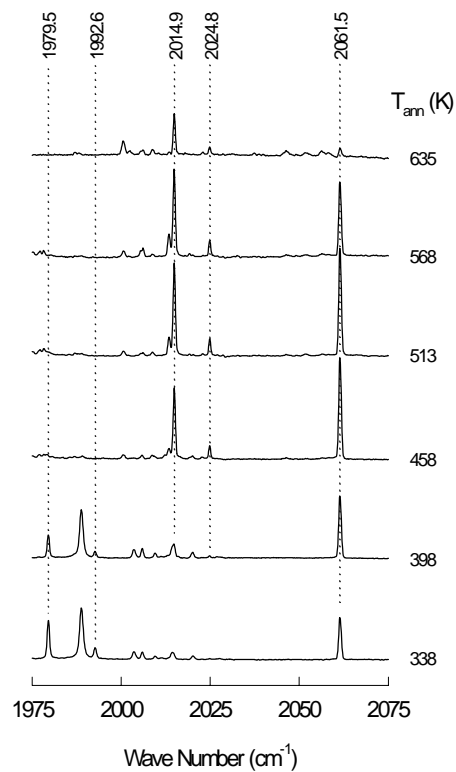


Fig. VII.2. Annealing behaviour of the absorption lines studied in the present chapter.

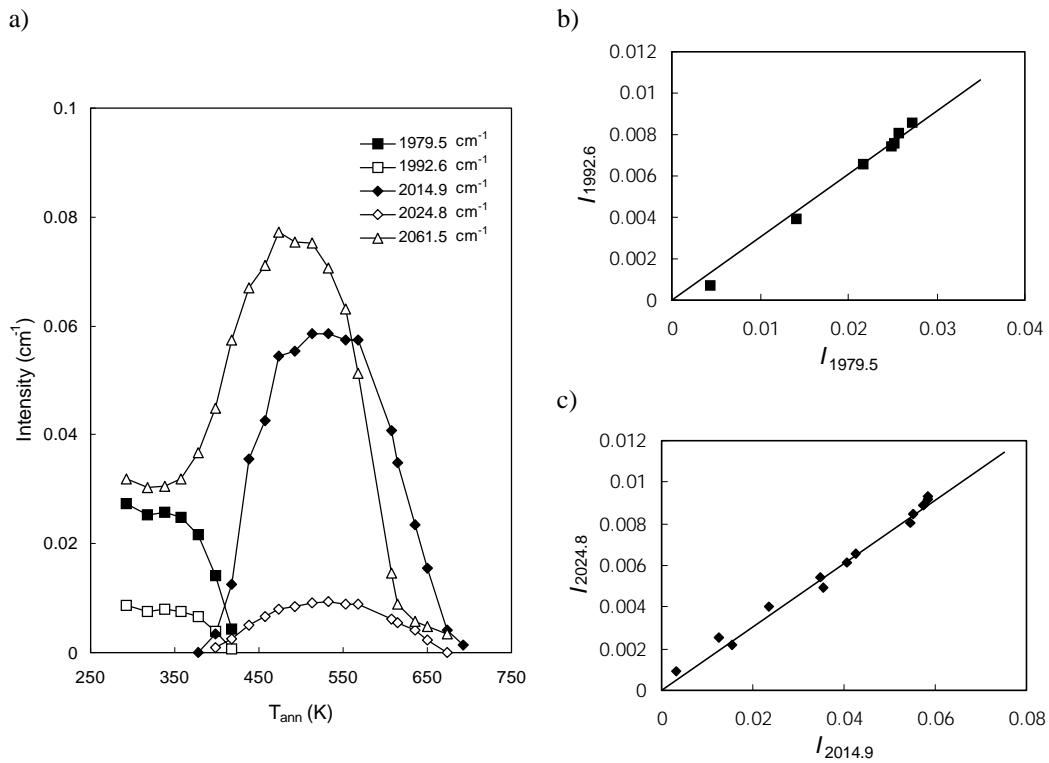


Fig. VII.3. a) Intensity vs. annealing temperature of the lines at 1979.5, 1992.6, 2014.9, 2024.8, and 2061.5 cm⁻¹, b) $I_{1992.6}$ vs. $I_{1979.5}$, and c) $I_{2024.8}$ vs. $I_{2014.9}$. The straight lines shown in b) and c) are the best fits to the data assuming that the two intensities of each plot are proportional.

with the H_2^* defect disappear, whereas the 2014.9- and 2024.8-cm⁻¹ lines appear. The 2061.5-cm⁻¹ line is already present after annealing at room temperature but increases in intensity by a factor of two at this stage. According to Fig. VII.2, the 2061.5-cm⁻¹ line disappears upon annealing between 568 and 635 K, whereas annealing at 635 K reduces the intensity of the lines at 2014.9- and 2024.8-cm⁻¹ by ~60 %. A quantitative account of the intensities of the five lines as a function of annealing temperature is given in Fig. VII.3.a.

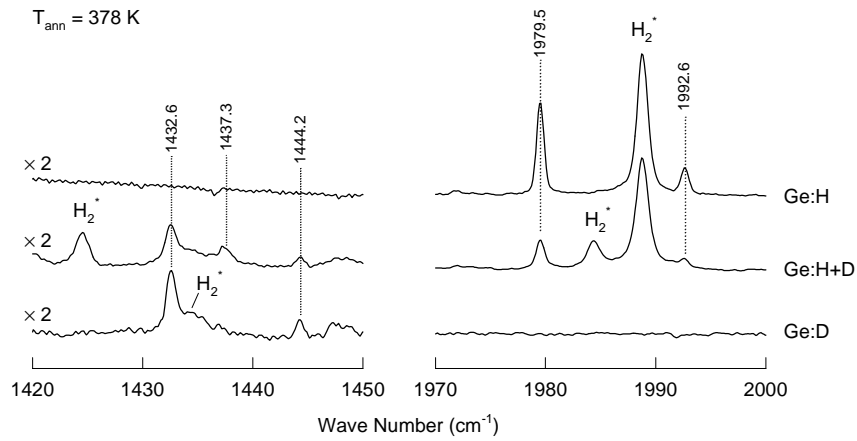
Fig. VII.3.b. shows the intensity of the 1992.6-cm⁻¹ line plotted as a function of the intensity of the 1979.5-cm⁻¹ line for each of the annealing steps shown in Fig. VII.3.a. The intensities of the two lines are proportional, which strongly suggests that they originate from the same centre. The same conclusion can be drawn for the 2014.9- and 2024.8-cm⁻¹ lines on the basis of Fig. VII.3.c. No other absorption lines in the spectra exhibit the same annealing behaviour as these two pairs of lines. The annealing behaviour of the 2061.5-cm⁻¹ line is different from any other line in the Ge:H spectra and, hence, we conclude that the pertinent centre only has one infrared active hydrogen-related stretch mode.

2. Isotope substitution

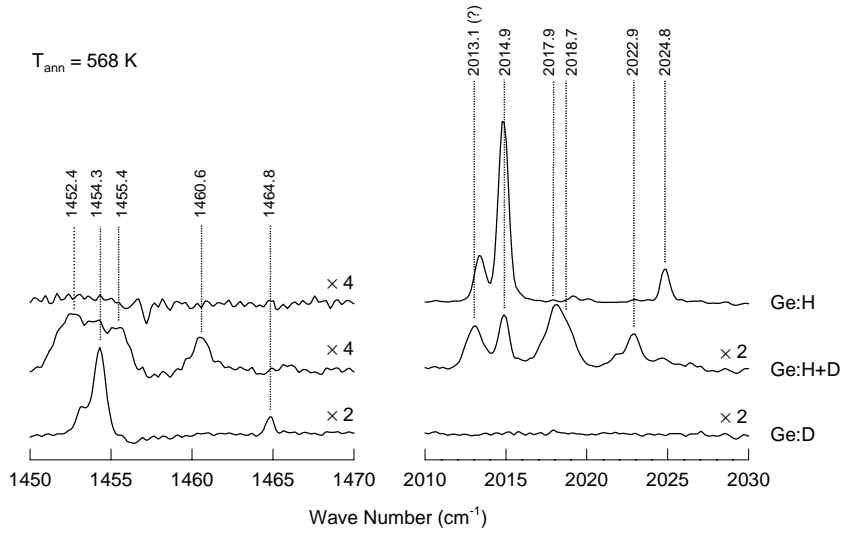
When deuterons are implanted instead of protons, no absorption lines are observed in the range from 1750 to 2100 cm^{-1} . Instead, a manifold of lines is observed in the range from 1270 to 1515 cm^{-1} , i.e. shifted down in frequency by a factor $\sim\sqrt{2}$ (see Fig. V.2), as expected for hydrogen-related local vibrational modes. In particular, two lines are observed at 1432.6 and 1444.2 cm^{-1} in Ge:D, which have the same annealing behaviour and relative intensities as the lines at 1979.5 and 1992.6 cm^{-1} in Ge:H (see Fig. VII.4.a). The two Ge-D lines are ascribed to the deuterium counterparts of the 1979.5- and 1992.6- cm^{-1} lines in Ge-H. In the Ge:H+D sample an additional line is observed at 1437.3 cm^{-1} , close to the mean frequency of the two lines observed in Ge:D. The new line anneals at the same temperature as the four lines observed in samples implanted with a single isotope and is therefore ascribed to an isotopically mixed version of the 1979.5- cm^{-1} centre. The observation of a single new Ge-D line in the Ge:H+D sample suggests that the centre contains two equivalent hydrogen atoms. If this interpretation is correct, an additional Ge-H line should appear close to the mean frequency of the 1979.5- and 1992.6- cm^{-1} lines. Unfortunately, the H_2^* defect gives rise to two intense lines in the same frequency region, as shown in Fig. VII.4.a, which prohibits the detection of the (relatively weak) Ge-H line of the isotopically mixed complex.

After annealing above ~ 440 K a pair of lines appear at 1454.3 and 1464.8 cm^{-1} in Ge:D (see Fig. VII.4.b). The annealing behaviour of the two lines is identical to that of the 2014.9- and 2024.8- cm^{-1} lines in Ge:H, and the two Ge-D lines have the same relative intensities as the two Ge-H lines. Hence, the 1454.3- and 1464.8- cm^{-1} lines originate from the deuterium analogue to the 2014.9- cm^{-1} centre. The infrared absorbance of the Ge:H+D sample annealed at 568 K is shown in Fig. VII.4.b. In the Ge-D region a rather broad absorption profile is observed, which can be decomposed into the 1454.3- cm^{-1} line observed in the Ge:D sample and two new lines at 1452.4 and 1455.4 cm^{-1} . An additional line is observed at 1460.6 cm^{-1} and, thus, a total of three new Ge-D lines is observed in the Ge:H+D sample in the vicinity of the 1454.3- and 1464.8- cm^{-1} lines of Ge:D. In the Ge-H region of Fig. VII.4.b, three new absorption lines are observed at 2013.1, ~ 2018 , and 2022.9 cm^{-1} . Unlike the 2014.9- and 2024.8- cm^{-1} lines in Ge:H, the peak at ~ 2018 cm^{-1} is asymmetric and has FWHM of 1.8 cm^{-1} , which indicates that the line is a superposition of two (or more) unresolved lines. If it is assumed that the peak at ~ 2018 cm^{-1} consists of two lines with the same FWHM and shape as the lines at 2014.9 and 2024.8 cm^{-1} in Ge:H, then the peak at ~ 2018 cm^{-1} can be decomposed into two lines centred at 2017.9 and 2018.7 cm^{-1} . Hence, four Ge-H lines are observed in Ge:H+D sample, in addition to the 2014.9- and 2024.8- cm^{-1} lines observed in Ge:H.

a)



b)



c)

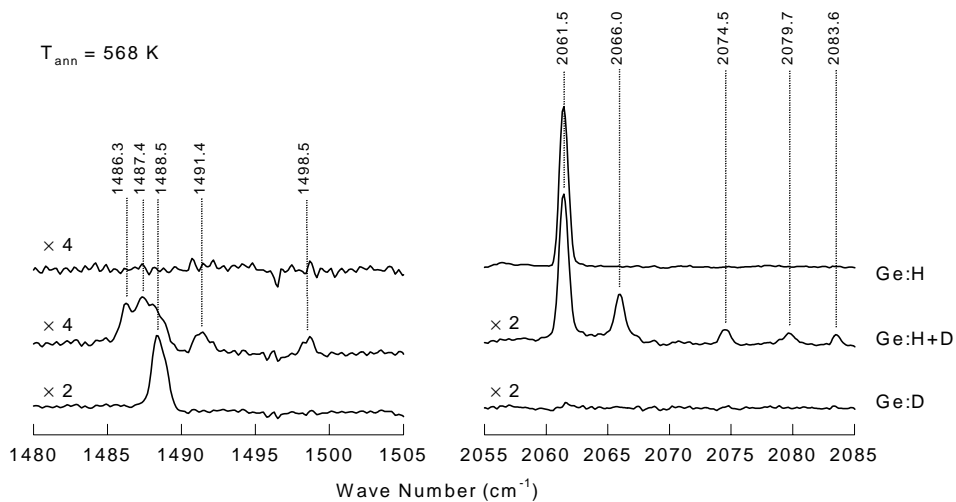


Fig. VII.4. Comparison of absorbance spectra of Ge:H, Ge:H+D and Ge:D samples in the vicinity of a) the 1979.5- and 1992.6- cm^{-1} lines, b) the 2014.9- and 2024.8- cm^{-1} lines, and c) the 2061.5- cm^{-1} line and their deuterium counterparts. The absorption lines indicated by dotted vertical lines in each graph exhibit identical annealing behaviours.

All three Ge-D and four Ge-H lines anneal out at the same temperature as the lines at 2014.9 and 2024.8 cm^{-1} in Ge:H and at 1454.3 and 1464.8 cm^{-1} in Ge:D, suggesting that they originate from isotopically mixed configurations of the 2014.9- cm^{-1} centre in Ge:H.⁶ The observation that partial isotope substitution leads to the formation of at least three additional Ge-H lines and Ge-D lines, shows that the 2014.9- cm^{-1} centre contains more than two hydrogen atoms.

When deuterons are implanted instead of protons, the line at 2061.5 cm^{-1} shifts down in frequency to 1488.5 cm^{-1} as depicted in Fig. VII.4.c. This confirms the assignment of the 2061.5- cm^{-1} line to a Ge-H stretch mode. Implantation of protons and deuterons with overlapping profiles results in the formation of four additional Ge-H lines at 2066.0, 2074.5, 2079.7, and 2083.6 cm^{-1} and four Ge-D lines at 1486.3, 1487.4, 1491.4, and 1498.5 cm^{-1} , as indicated in Fig. VII.4.c. These eight lines have the same annealing behaviour as the 2061.5 cm^{-1} line in Ge:H and the 1488.5 cm^{-1} line in Ge:D. The observation of only a single stretch mode of this centre in samples implanted with either protons or deuterons and the rich spectrum in the samples implanted with both isotopes strongly suggests that the 2061.5- cm^{-1} line (or 1488.5- cm^{-1} line) reflects an $A \rightarrow T$ transition of a cubic centre containing four equivalent hydrogen (or deuterium) atoms.

3. Uniaxial stress

a. The 1979.5- cm^{-1} line

Uniaxial stress experiments were carried out in order to determine the symmetry and type of transitions associated with the absorption lines. Fig. VII.5 shows the shifts and splittings of the 1979.5- cm^{-1} line observed with uniaxial stress applied along the

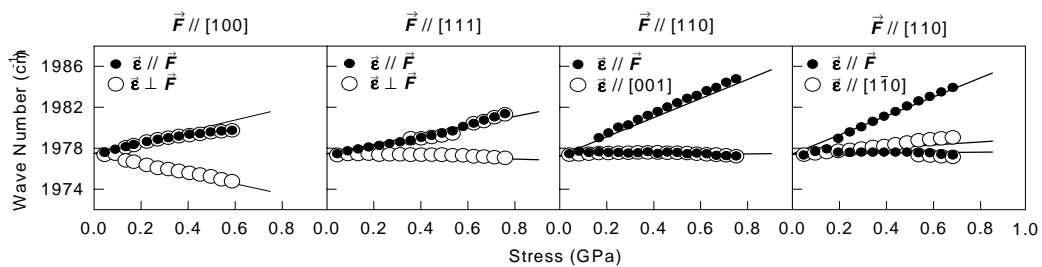


Fig. VII.5. Splittings and shifts of the 1979.5- cm^{-1} line induced by uniaxial stress along [100], [111], and [110] directions. The straight lines are defined by the parameters given in Table VII.1 and represent the best fit of the theoretical splittings of an orthorhombic-I centre to the experimental data.

⁶ It cannot be excluded that the Ge-H line at 2013.1 cm^{-1} is associated with the rather weak line observed at 2013.4 cm^{-1} in Ge:H (see Fig. VII.4.b).

major crystal axes. The splitting-pattern of the 1979.5-cm^{-1} line is qualitatively very similar to that observed for the line at 2121 cm^{-1} in proton-implanted silicon (see Fig. VI.6.a), which was assigned to an $A_1 \rightarrow B_1$ transition of an orthorhombic-I centre.⁷ Also quantitatively, the stress-induced splittings and shifts of the 1979.5-cm^{-1} line are consistent with the assignment of the line to such a transition, as evidenced by the very good agreement between the experimental points and the straight lines shown in Fig. VII.5. Unfortunately, the

stress-response of the 1992.6-cm^{-1} line cannot be studied at 77 K, where the uniaxial stress measurements were carried out, because the line is buried under the intense 1989-cm^{-1} line of the H_2^* defect, as shown in Fig. VII.6. This figure also shows the absorbance profiles measured with light polarised along two perpendicular $\langle 110 \rangle$ directions, which both are in the plane of the implanted $\{100\}$ surface. It is evident from the figure that the intensity of the 1979.5-cm^{-1} line measured with the two different polarisations differs by $\sim 50\%$, whereas the intensity of the H_2^* line at 1989 cm^{-1} is independent of polarisation. This shows that the 1979.5-cm^{-1} line does not reflect an even orientational distribution of centres and, hence, that the relative intensities of the stress-split components will deviate from those given in Table II.3.

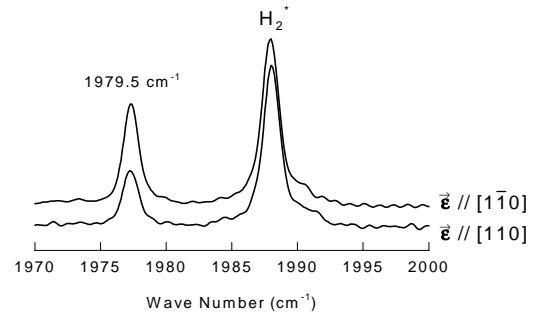


Fig. VII.6. Infrared absorbance in the vicinity of the 1979.5- and 1992.6-cm^{-1} lines in Ge:H measured at 77 K. The infrared light penetrated the sample normal to the implanted (001) face of the crystal, and the infrared absorbance profiles measured with light polarised along two perpendicular $\langle 110 \rangle$ directions are shown.

Table VII.1. Piezo-spectroscopic parameters (in $\text{cm}^{-1}/\text{GPa}$) of the 1979.5- , 2014.9- , 2024.8- , and 2061.5-cm^{-1} lines. The parameters were obtained by least-square fits of the theoretical stress-induced frequency shifts of an $A_1 \rightarrow B_1$ transition of an orthorhombic-I centre (1979.5-cm^{-1}), an $A \rightarrow E$ transition of a trigonal centre (2014.9-cm^{-1}), an $A \rightarrow A$ transition of a trigonal centre (2024.8-cm^{-1}), and $A \rightarrow T$ transition of a cubic centre (2061.5-cm^{-1}) to the experimental data.

	1979.5-cm^{-1}	2014.9-cm^{-1}	2024.8-cm^{-1}	2061.5-cm^{-1}
\mathcal{A}_1	-5.0 ± 2.0	\mathcal{A}_1 2.5 ± 0.7	\mathcal{A}_1 3.4 ± 0.7	\mathcal{A}_1 4.1 ± 0.6
\mathcal{A}_2	5.4 ± 1.6	\mathcal{A}_2 -1.9 ± 0.3	\mathcal{A}_2 -2.3 ± 0.3	\mathcal{B} 1.3 ± 0.4
\mathcal{A}_3	3.9 ± 1.0	\mathcal{C} -1.8 ± 0.3		\mathcal{C} 5.0 ± 0.7
		\mathcal{D} -0.2 ± 0.3		

⁷ The arguments on which this statement is based were presented in section VI.C.3.a and will not be repeated here.

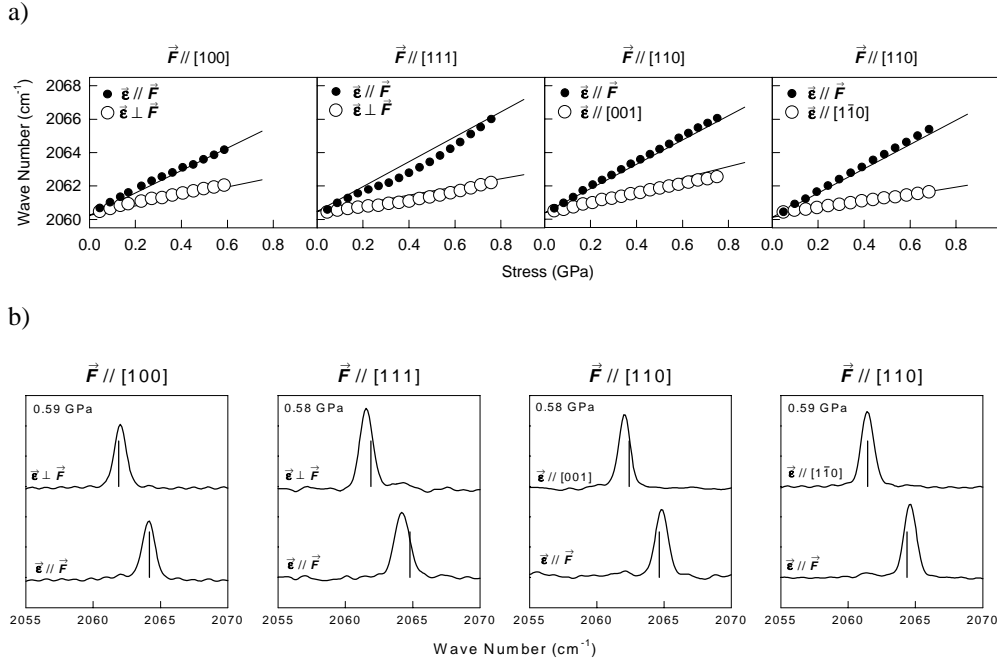


Fig. VII.7. a) Stress-induced shifts of the 2061.5-cm^{-1} line in Ge:H. The straight lines represent the best-fit shifts of an $A \rightarrow T$ transition of a cubic centre. b) Absorbance profiles in the vicinity of the 2061.5-cm^{-1} line measured with uniaxial stresses of ~ 0.6 GPa along the major crystal axes and light polarised parallel and perpendicular to the applied force. The positions of the vertical sticks are the best-fit theoretical positions indicated by the straight lines in a) and the height of the sticks represent the relative intensities of the stress-split components expected theoretically for an $A \rightarrow T$ transition of a cubic centre. The best-fit piezo-spectroscopic parameters of the 2061.5-cm^{-1} line are given in Table VII.1.

b. The 2061.5-cm^{-1} line

As shown in Fig. VII.7.a, the 2061.5-cm^{-1} line splits in two components when uniaxial stresses are applied along either of the [100], [111], and [110] directions. Only one stress-split component is observed with each polarisation of the light for all three stress-directions (see Fig. VII.7.b). According to Table II.3, this is only consistent with the 2061.5-cm^{-1} line originating from an $A \rightarrow T$ transition of centre with cubic symmetry. A detailed analysis of the stress-induced frequency shifts and the relative intensities of the stress-split components confirms this assignment. The straight lines shown in Fig. VII.7.a correspond to the best-fit theoretical shifts obtained from the experimental data for an $A \rightarrow T$ transition of a cubic centre. The agreement between the best-fit frequency shifts and the experimental points is very good. As shown in Fig. VII.7.b, the relative intensities of the stress-split components are also consistent with the assignment of the 2061.5-cm^{-1} line to such a transition. Hence, we conclude that the 2061.5-cm^{-1} line reflects an $A \rightarrow T$ transition of a cubic centre.

c. The 2014.9- and 2024.8-cm⁻¹ lines

Finally, the effect of uniaxial stress on the 2014.9- and 2024.8-cm⁻¹ lines was studied. In order to maximise the intensities of the two lines, the samples were annealed at 518 K before the uniaxial stress measurements were carried out. Only results obtained with $\vec{F} // [100]$, $\vec{F} // [111]$, and $\vec{F} // [110]$ and $\vec{\epsilon} // [110]/[001]$ are presented, as the measurements on the samples with $\vec{F} // [110]$ and $\vec{\epsilon} // [110]/[1\bar{1}0]$ failed. The lack of measurements with $\vec{F} // [110]$ and $\vec{\epsilon} // [1\bar{1}0]$ has no influence on the final conclusions.

The splitting-pattern of the 2014.9-cm⁻¹ line induced by uniaxial stresses along [100], [111], and [110] is shown in Fig. VII.8.a. The splitting-pattern is qualitatively very similar to that of the 2166-cm⁻¹ line in Si:H shown in Fig. VI.8.a, which was assigned to an $A \rightarrow E$ transition of a trigonal centre. This suggests that also the 2014.9-cm⁻¹ line in Ge:H reflects such a transition. A quantitative analysis confirms this proposition, as evidenced the very good agreement between the experimental points and the straight lines shown in Fig. VI.8.a. Also the relative intensities of the stress-split components are in agreement with the theoretical stress-pattern given in

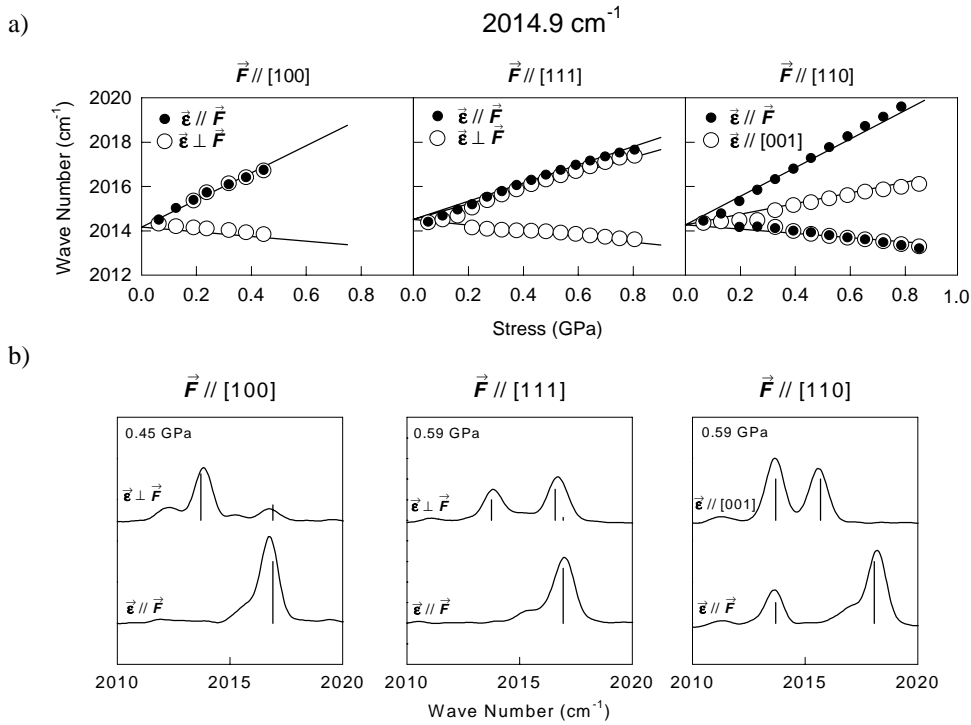


Fig. VII.8. a) Stress-induced shifts of the 2014.9-cm⁻¹ line in Ge:H annealed at 518 K. The straight lines represent the best-fit shifts of an $A \rightarrow E$ transition of a trigonal centre. b) Absorbance profiles in the vicinity of the 2014.9-cm⁻¹ line measured with a uniaxial stress of 0.45 or 0.59 GPa along the major crystal axes and light polarised parallel and perpendicular to the applied force. The positions of the vertical sticks are the best-fit theoretical positions indicated by the straight lines in a) and the height of the sticks represent the relative intensities of the stress-split components expected theoretically for an $A \rightarrow E$ transition of a trigonal centre. The best-fit piezo-spectroscopic parameters of the 2014.9-cm⁻¹ line are given in Table VII.1.

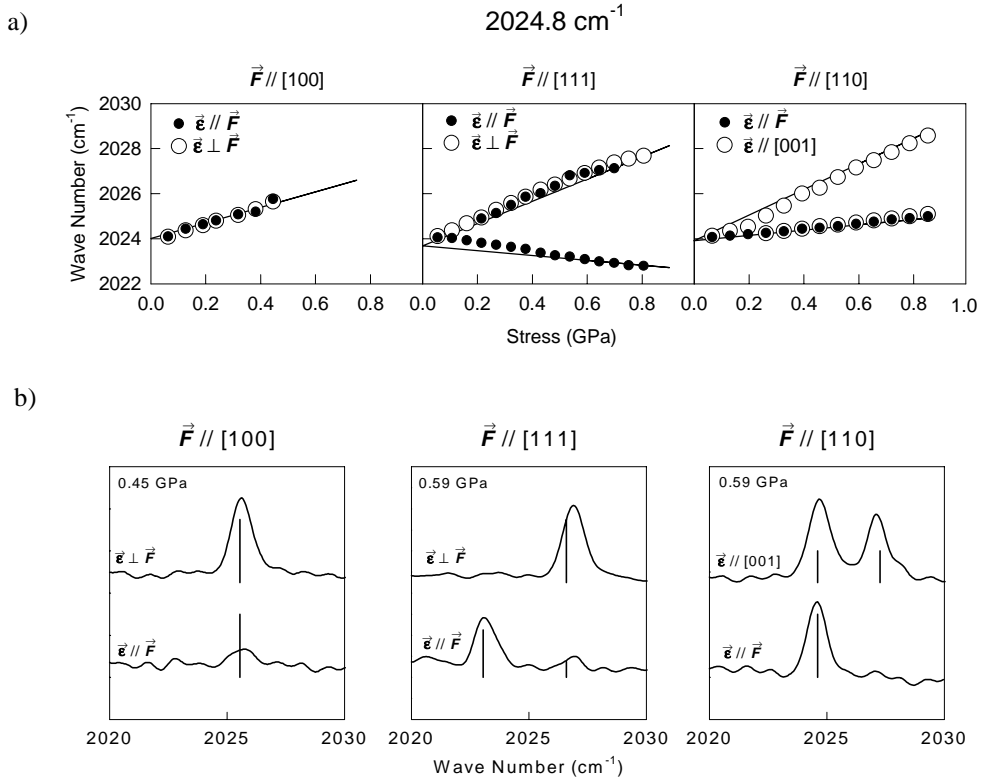


Fig. VII.9. a) Stress-induced shifts of the 2024.8-cm⁻¹ line in Ge:H annealed at 518 K. The straight lines represent the best-fit shifts of an $A \rightarrow A$ transition of a trigonal centre. b) Absorbance profiles in the vicinity of the 2024.8-cm⁻¹ line measured with a uniaxial stress of 0.45 or 0.59 GPa along the major crystal axes and light polarised parallel and perpendicular to the applied force. The positions of the vertical sticks are the best-fit theoretical positions indicated by the straight lines in a) and the height of the sticks represent the relative intensities of the stress-split components expected theoretically for an $A \rightarrow A$ transition of a trigonal centre. The best-fit piezo-spectroscopic parameters of the 2024.8-cm⁻¹ line are given in Table VII.1.

Table II.3 for such a transition (see Fig. VII.8.b). Hence, the 2014.9-cm⁻¹ line is assigned to an $A \rightarrow E$ transition of trigonal centre.

The response of the 2024.8-cm⁻¹ line on uniaxial stresses applied parallel along the major axes is shown in Fig. VII.9.a. The observed splitting-pattern closely resembles that of the 2191-cm⁻¹ line in Si:H (see Fig. VI.8.b), which in Sec. VI.C.3.b was assigned to an $A \rightarrow A$ transition of trigonal centre. The stress-induced splittings and frequency shifts of the 2024.8-cm⁻¹ line are also quantitatively in very good agreement with the theoretical stress splittings of an $A \rightarrow A$ transition of trigonal centre, as evidenced by the very good agreement between the experimental points and the solid lines in Fig. VII.9.a. The observed relative intensities of the stress-split components are only in fair agreement with those given theoretically in Table II.3 for such a transition (see Fig. VII.9.b). According to this table, the sum of the intensities of the stress-split components is independent of the magnitude of the applied stress and of the polarisation of the infrared light. This is obviously not the case for the 2024.8-cm⁻¹

line for e.g. a uniaxial stress of 0.45 GPa applied along [100], as shown in Fig. VII.9.b. In this case, the intensity measured with $\vec{\epsilon} \perp \vec{F}$ is clearly larger than the intensity measured with $\vec{\epsilon} // \vec{F}$, whereas the lines measured with the two distinct polarisations have equal intensity at zero stress (not shown). The reason for the discrepancies between the experimental intensities and the theoretical intensities given in Table II.3 is not known. However, it can be ruled out that it is caused by stress-induced alignment of the defects during the absorption measurements, as the effect is observed for [100] stress, where all orientations of the trigonal centre are perturbed equally. Based on the very good agreement between the observed and theoretical stress-induced frequency shifts, and despite the discrepancies with respect to the relative intensities of the components mentioned above, we conclude that the 2024.8-cm⁻¹ line originates from an $A \rightarrow A$ transition of a trigonal centre.

D. Discussion

1. The 1979.5- and 1992.6-cm⁻¹ lines

The similarities between the 1979.5- and 1992.6-cm⁻¹ lines in Ge:H and the 2121- and 2145-cm⁻¹ lines in Si:H are striking. First, both sets of lines are observed in proton-implanted material after annealing at room temperature. Second, both lines originate from centres with orthorhombic-I symmetry that contain two equivalent hydrogen atoms. Third, the low-frequency line of each set corresponds to an $A_1 \rightarrow B_1$ transition. Fourth, both sets of lines disappear upon annealing at relatively low temperatures (~ 400 K in Ge:H and at ~ 470 K in Si:H). Fifth and finally, proton implantation does not result in an even orientational distribution of the centres in any of the two materials. These profound similarities show that the two sets of lines originate from the same defect in the two materials. Based on the discussion in Sec. VI.D.1, the 2121- and 2145-cm⁻¹ lines were assigned to VH_2 in silicon, and the 1979.5- and 1992.6-cm⁻¹ lines are therefore assigned to VH_2 in germanium.

Some differences between VH_2 in silicon and germanium also exist. As mentioned above, VH_2 disappear after annealing at ~ 400 K in germanium and at ~ 470 K in silicon. This differences in annealing temperature is somewhat larger than for the H_2^* defect, which anneals at ~ 420 K and ~ 435 K, respectively, in the same germanium and silicon sample. As discussed in Sec. VI.D.1, the correlated disappearance of VH_2 and formation of VH_4 indicates that VH_2 converts into VH_4 by capture of two hydrogen atoms. This implies that the difference in annealing temperature of VH_2 in germanium and silicon is determined by the availability of hydrogen in the crystal, i.e. by the amount of hydrogen liberated by dissociation of defects like H_2^* and IH_2 .⁸

⁸ The IH_2 defect is discussed in detail in chapter VIII.

Hence, the annealing temperature of VH_2 in the two materials does not give any information on the thermal stability of the VH_2 defect. Implantation of protons into a $\{110\}$ surface results in a significant orientational alignment of the VH_2 defects in silicon, whereas the VH_2 defects formed by implantation into a $\{100\}$ surface appear to be randomly oriented. On the contrary, an alignment VH_2 centres is formed by implantation into a $\{100\}$ germanium surface, whereas no significant alignment of defects is observed with germanium samples implanted into a $\{110\}$ surface. The reason for this peculiar difference in the formation of VH_2 defects in silicon and germanium is at present not understood.

2. The 2014.9- and 2024.8-cm⁻¹ lines

The experimental results on the lines at 2014.9 and 2024.8 cm⁻¹ in proton-implanted germanium presented section VII.C show that the two lines originate from the same centre. The centre contains at least three hydrogen atoms, and has trigonal symmetry. The 2014.9-cm⁻¹ line originates from an $A \rightarrow E$ transition, whereas the line at 2024.8-cm⁻¹ line is due to an $A \rightarrow A$ transition. The two lines are formed upon annealing at ~440 K and disappear after annealing at ~620 K. Apart from a downshift in both the temperature of formation and disappearance, these characteristics of the lines at 2014.9 and 2024.8 cm⁻¹ in Ge:H are essentially identical to those of the 2166- and 2191-cm⁻¹ lines in Si:H. This shows that the lines at 2014.9 and 2024.8 cm⁻¹ in Ge:H originate from the same defect as the 2166- and 2191-cm⁻¹ lines in Si:H, which were ascribed to the hydrogen-saturated divacancy V_2H_6 .

V_2H_6 is formed by annealing at ~440 K (~560 K) and disappears at ~620 K (~800 K) in germanium (silicon). Analogous to the discussion of VH_2 formation in the preceding subsection, the formation of V_2H_6 appears to be controlled by the dissociation of other hydrogen-related centres, and does therefore not reflect an inherent property of the V_2H_6 defect itself. V_2H_6 does not possess any dangling bonds and, thus, the defect cannot bind strongly additional hydrogen atoms. This suggests that the annealing of V_2H_6 in germanium at ~620 K and in silicon at ~800 K is caused by thermal dissociation of the complex. If it is assumed that the dissociation proceeds by a first-order process, the activation energy for dissociation of the complex is proportional to its annealing temperature.⁹ The annealing temperature can then be used as a qualitative measure of the activation energy for dissociation. Assuming that the proportionality constant is the same for V_2H_6 in germanium and silicon,¹⁰ the

⁹ The annealing temperature is here defined as the temperature at which the intensity of a given line is reduced from its maximum value by 50%.

¹⁰ The proportionality constant is given by $-k_B \ln(\ln(2)/(\nu t))$, where ν is an attempt frequency, t is the annealing time, and k_B is the Boltzmann constant.

observed annealing temperatures imply that the activation energy for dissociation of V_2H_6 in silicon is $\sim 30\%$ larger than in germanium. This relative difference in activation energy is in qualitative agreement with the relative difference of $\sim 20\%$ in bond strength of Si-H and Ge-H bonds in molecular silane and germane (see Table I.1).

3. The 2061.5- cm^{-1} line

In Sec. VI.C it was argued that the line at 2061.5 cm^{-1} is due to the excitation of a Ge-H stretch mode of a centre with only one infrared active stretch mode. The uniaxial stress experiments revealed that the 2061.5- cm^{-1} line reflects an $A \rightarrow T$ transition of a centre with cubic symmetry, which according to the results of partial isotope substitution, contains at least four equivalent hydrogen atoms. The 2061.5- cm^{-1} line was observed in the sample stored at room temperature but increased in intensity upon annealing. The maximum intensity was obtained upon annealing at ~ 470 K, and the line disappeared after annealing at ~ 590 K. Apart from a downshift in both the temperature of formation and disappearance, all these characteristics are essentially identical to those of the 2223- cm^{-1} line in proton-implanted silicon. This shows that the 2061.5- cm^{-1} line in Ge:H and the 2223- cm^{-1} line in Si:H originate from the same defect in the two materials. According to the discussion in Sec. VI.A.2, the 2223- cm^{-1} line originates from VH_4 complex in silicon. Hence, we assign the 2061.5- cm^{-1} line to the $A_1 \rightarrow T_2$ transition of VH_4 in germanium.

VH_4 in germanium and silicon anneals at ~ 590 K and ~ 770 K, respectively. Assuming that the annealing of VH_4 is caused by a first-order dissociation process, the annealing temperatures imply that the activation energy for dissociation of VH_4 is $\sim 30\%$ larger in silicon than in germanium. This relative difference in activation energy is equal to that of V_2H_6 and in qualitative agreement with the relative difference in Si-H and Ge-H bond strengths, as discussed above.

E. Conclusion

Implantation of protons into germanium at ~ 30 K followed by annealing at room temperature gives rise to more than ten absorption lines in the range 1750 – 2100 cm^{-1} . In particular, a pair of lines originating from Ge-H stretch modes of the same centre is observed at 1979.5 and 1992.6 cm^{-1} . The lines disappear upon annealing at ~ 400 K. Uniaxial stress measurements show that the 1979.5- cm^{-1} line originates from an $A_1 \rightarrow B_1$ transition of a centre with orthorhombic-I symmetry. The effect of uniaxial stress on the 1992.6- cm^{-1} line could not be studied because the line overlaps with the intense 1989- cm^{-1} line of the H_2^* defect.

The spectrum measured on the sample stored at room temperature also reveals a prominent absorption line at 2061.5 cm^{-1} . The 2061.5- cm^{-1} line increases in intensity

upon annealing at ~ 410 K, has maximum intensity at ~ 470 K, and disappears after annealing at ~ 590 K. The line is not correlated with other lines in spectra. Isotope substitution experiments identify the 2061.5-cm^{-1} line as due to a Ge-H stretch mode, and strongly suggest that it originates from an $A_1 \rightarrow T_2$ transition of a centre with T_d symmetry containing four equivalent hydrogen atoms. The assignment of the line to such a transition is confirmed by uniaxial stress measurements.

Two prominent absorption lines appear at 2014.9 and 2024.8 cm^{-1} , when the Ge:H sample is annealed at ~ 440 K. The lines have identical annealing behaviour and are therefore ascribed to the same defect. The maximum intensity of the lines is observed in the range $500 - 600$ K, and they disappear after annealing at ~ 620 K. Uniaxial stress measurements show that the 2014.9- and 2024.8-cm^{-1} lines originate from, respectively, an $A \rightarrow E$ and an $A \rightarrow A$ transition of a centre with trigonal symmetry.

Apart from a downshift in annealing temperature and vibrational frequency, the properties of the lines at $\{1979.5, 1992.6\}$, $\{2014.9, 2024.8\}$, and 2061.5 cm^{-1} in Ge:H are essentially identical to those of the lines at $\{2121, 2145\}$, $\{2166, 2191\}$, and 2223 cm^{-1} in Si:H. The three sets of lines are therefore assigned to the same defect in the two materials, which are VH_2 , V_2H_6 , and VH_4 . The disappearance of VH_2 and the formation of V_2H_6 and VH_4 in Ge:H upon annealing at ~ 400 K is ascribed the capture of hydrogen released by dissociation of other hydrogen-related defects. Interpretation of the annealing of VH_4 and V_2H_6 in Ge:H and Si:H in terms of thermal dissociation of the complexes by a first-order process, indicate that the activation energy for dissociation of VH_4 and V_2H_6 is $\sim 30\%$ larger in silicon than in germanium, which is in qualitative agreement with the strength of the Si-H bond being $\sim 20\%$ larger than the strength of the Ge-H bond.

F. References

- [1] J. Tatarkiewicz, A. Król, A. Breitschwerdt, and M. Cardona, *Phys. Stat. Sol.* (b), **140**, 369 (1987).
- [2] B. J. Coomer, P. Leary, M. Budde, B. Bech Nielsen, R. Jones, S. Öberg, and P. R. Briddon, to appear in the Proceedings from the E-MRS Spring Meeting, June 1998, Strasbourg, France.
- [3] E. E. Haller, G. S. Hubbard, W. L. Hansen, and A. Seeger, *Inst. Phys. Conf. Ser.*, **31**, 309 (1977).
- [4] E. E. Haller in "Hydrogen in semiconductors: semiconductors and semimetals", vol. 34, edited by J.I. Pankove and N.M. Johnson (Academic Press, New York, 1991).

VIII. The hydrogen-saturated self-interstitials in silicon and germanium

A. Introduction

The preceding two chapters described infrared absorption studies of complexes formed by the interaction of hydrogen with vacancies created during implantation of protons into silicon and germanium. Apart from vacancies, ion implantation also creates an equal amount of interstitial host atoms (self-interstitials). The present chapter, which is the last experimental chapter of this thesis, describes the identification of a complex formed by the interaction of hydrogen with the self-interstitial in silicon and germanium, namely the hydrogen-saturated self-interstitial IH_2 .¹

The vacancy in silicon has been studied in great detail [1], and it is one of the best-characterised point defects in any crystalline material. In contrast, the self-interstitial in silicon has never been observed directly. Instead, interstitial impurities such as boron, carbon, aluminium or gallium are observed after irradiation [1]. It is believed that the self-interstitials are mobile during the irradiation process, and that interstitial impurities are created by a kick-out mechanism [1]. Thus, our present knowledge about the self-interstitial is based on studies of the products of such reactions and on theoretical calculations [2-6].

A major objective in defect studies is to determine the microstructure of the defects, which is essential for a detailed understanding of their properties. Theoretical calculations [2-6] suggest that the minimum-energy configuration of the self-interstitial in the neutral charge state is a $\langle 110 \rangle$ -split, in which two silicon atoms share a lattice site as shown in Fig. VIII.1.a. Unfortunately, it may be impossible to check the theoretical predictions experimentally due to the high mobility and reactivity of the self-interstitial. Therefore, the best way to obtain microstructural information may be to study reaction products that are stable and closely resemble

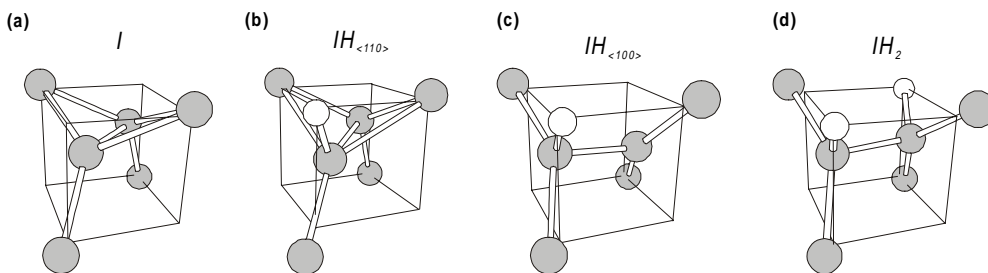


Fig. VIII.1. Calculated structure of the IH_n defects, $n \in \{0, 1, 2\}$, in silicon. a) I , b) $IH_{\langle 110 \rangle}$, c) $IH_{\langle 100 \rangle}$, and d) IH_2 . The shaded spheres are silicon or germanium, whereas the white spheres are hydrogen. The structures are the results of ab initio calculations performed in conjunction with the experimental studies presented in this chapter [7].

¹ The complex consisting of n hydrogen atoms bound to the self-interstitial I is designated IH_n .

the self-interstitial. Two obvious candidates of such products are the self-interstitial binding one or two hydrogen atoms. These complexes are expected to exist, since hydrogen interacts strongly with dangling bonds, as discussed in chapter VI. The addition of hydrogen may immobilise the self-interstitial and, thus, the complexes may be stable even at room temperature. The length of the molecular Si-H bond ($\sim 1.48 \text{ \AA}$) is considerably shorter than that of the Si-Si bond ($\sim 2.35 \text{ \AA}$), which suggests that Si-H bonds may be formed in the open parts of the lattice without introduction of substantial strain. Consequently, the rearrangement of the self-interstitial introduced by trapping of hydrogen could be moderate.

In proton-implanted silicon a series of absorption lines that correspond to Si-H stretch modes are observed in the frequency range $1800 - 2250 \text{ cm}^{-1}$ together with lines associated with Si-H bend modes in the range $700 - 850 \text{ cm}^{-1}$. Of particular interest to this chapter is the line at 1980 cm^{-1} (at room temperature), first observed by Stein in 1975 [11] (see Fig. I.4). Since then, this line has also been observed in hydrogen-doped silicon irradiated with electrons [12], neutrons [13], and γ -rays [14]. Shi *et al* showed that the line splits into a doublet at 1987 and 1989 cm^{-1} when the sample temperature is reduced to 10 K [12]. The two lines have the same production and annealing behaviours, which indicates that they originate from the same defect [12,13]. These observations led Xie *et al* [13] to assign the 1987 - and 1989-cm^{-1} lines to VH_2 , as discussed in Sec. VI.2.a. This assignment, however, disagrees with the assignment of the lines at 2121 and 2145 cm^{-1} to VH_2 in chapter VI. Thus, the origin of the 1987 - and 1989-cm^{-1} lines remains unclear.

In this chapter, four Si-H modes observed at $743.1, 748.0, 1986.5,$ and 1989.4 cm^{-1} in Si:H and four similar Ge-H modes observed at $700.3, 705.5, 1881.8,$ and 1883.5 cm^{-1} in Ge:H are studied in detail. Annealing studies show that the four modes in each material originate from the same defect, which contains two equivalent hydrogen atoms. Uniaxial stress measurements show that the defect has monoclinic-II symmetry, and the orientations of the two Si-H and Ge-H bonds are determined. Based on the experimental evidence, the four Si-H and Ge-H modes are assigned to IH_2 in silicon and germanium. The experimental results are compared with the results of *ab initio* calculations on IH_2 in silicon and germanium. All calculated properties are in close agreement with those observed. This provides strong support to our assignments.

The first theoretical study of IH_n complexes in silicon was reported by Deák *et al* in 1989 [8]. The calculations were based on semi-empirical theory. A hydrogen atom was added to different configurations of the isolated self-interstitial, including an interstitial silicon atom at a puckered BC site, an interstitial silicon atom at the T site, and a $\langle 100 \rangle$ -split interstitial, where two silicon atoms share a lattice site, and are split in a $\langle 100 \rangle$ direction. Then the configurations were relaxed until the total energy was minimised, which resulted in the structure shown in Fig. VIII.1.c, henceforth denoted $IH_{\langle 100 \rangle}$. The central silicon atom, which is not bonded to hydrogen, is only three-fold coordinated and, thus, a second hydrogen atom may be added to the complex to form

the IH_2 defect shown in Fig. VIII.1.d. The binding energy per hydrogen atom² calculated for $IH_{\langle 100 \rangle}$ and IH_2 is given in Table VIII.1. The vibrational stretch frequencies of the IH_n complexes were also calculated and are given in Table VIII.2. New values for the

Table VIII.1. Binding energy per hydrogen atom (in eV) calculated for the IH_n complexes with $n \in \{1,2\}$.

Author	Deák [8]	Deák [9]	Van de Walle [6]
$IH_{\langle 100 \rangle}$	0.78	1.35	
$IH_{\langle 110 \rangle}$			2.60
IH_2	0.88	1.24	2.61

calculated binding energies and vibrational frequencies were reported by Deák *et al* in 1991 [9]. In the revised study, the same calculational method was employed as in the original work [8] but, nevertheless, the calculated values differed significantly from those of the original work. No explanation is given for the change in the calculated values.

The first *ab initio* theoretical calculations on the IH_n complexes in silicon were reported by Van de Walle *et al* in 1995 [6]. The IH complex in silicon was studied by adding a single hydrogen atom to various configurations of the isolated self-interstitial, including $\langle 110 \rangle$ and $\langle 100 \rangle$ split-interstitials, and an interstitial silicon atom located at the T site. Then, the configurations were relaxed until a minimum in the total energy was obtained. The $IH_{\langle 110 \rangle}$ complex shown in Fig. VIII.1.b was found to have the lowest total energy. In addition, Van de Walle *et al* found that the $IH_{\langle 110 \rangle}$ complex is electrically active with a (+/0) donor level located ~ 0.4 eV above the top of the valence band and a (0/-) acceptor level located ~ 0.1 eV above the donor level. The atomic structure of the complex was largely insensitive to the charge state. The calculated binding energy per hydrogen atom was 2 - 3 times larger than the value predicted by Deák *et al* (see Table VIII.1), and falls between those calculated for the H_2^* defect (1.84 eV) and VH (3.76 eV) with the same theoretical approach [10]. The stretch frequency of $IH_{\langle 110 \rangle}$ was estimated by a frozen-phonon approach, where all the silicon atoms (including the atom to which hydrogen is bonded) were kept fixed (see Table VIII.2). When two hydrogen atoms were added to the self-interstitial, the IH_2 configuration shown in Fig. VIII.1.d had the lowest total energy, in agreement with the findings of Deák *et al* [8,9]. The IH_2 complex has monoclinic-II (C_2) symmetry, and the Si-H bonds are nearly aligned with $\langle 110 \rangle$ directions. The IH_2 complex was

Table VIII.2. Calculated vibrational stretch frequencies (in cm^{-1}) of the IH_n complexes in silicon.

	Point group	Mode	Deák [8]	Deák [9]	Van de Walle [6]	Leary [7]
$IH_{\langle 100 \rangle}$	C_{1h}	A'	2217	2197		2166.9
$IH_{\langle 110 \rangle}$	C_{1h}	A'			1870	2190.8
		A	2207	2213		2144.7
		B	2165	2210		2142.9

² The binding energy per hydrogen atom is defined in footnote 2, chapter VI.

predicted to be electrically inactive. The calculated binding energy per hydrogen atom was 2.61 eV, i.e. essentially the same as for $IH_{\langle 110 \rangle}$.

In conjunction with the infrared absorption studies reported in the present chapter, P. Leary, J. Goss, R. Jones, P. R. Briddon, S. Öberg, and S. J. Breuer, from or associated with the theory group at the University of Exeter, UK, performed *ab initio* calculations on I , IH , and IH_2 in silicon and germanium. These calculations were carried out with special emphasis on the vibrational properties of the complexes. The stretch frequencies calculated for the IH_n complexes in silicon are compared with those obtained by Deák *et al* and Van de Walle *et al* in Table VIII.2. A more thorough presentation of the theoretical results is postponed to the end of this chapter. The theoretical work was reported together with the experimental studies in a recent publication [7].

B. Experimental

The samples used in the present studies of the IH_n defects in silicon and germanium were identical to those used in the studies of the vacancy-hydrogen complexes in silicon and germanium described in chapter VI and VII. In short, the samples were implanted with protons and/or deuterons in overlapping profiles to result in a local concentration of hydrogen or deuterium of 0.02 or 0.05 at. %. The implantations into silicon were carried out at ~30 K, 100 K or RT, whereas the implantations into germanium were performed at ~30 K. The absorbance spectra were recorded with a resolution of $\sim 0.5 \text{ cm}^{-1}$, except for the uniaxial stress measurements on Ge:H, which were carried out with a resolution of $\sim 0.8 \text{ cm}^{-1}$.

Also the infrared absorption measurements were performed analogous to the measurements described in chapter VI and VII. The measurements associated with the annealing and isotope substitution studies were performed at $\sim 80 \text{ K}$ ($9 \pm 1 \text{ K}$) in silicon (germanium), whereas the uniaxial stress measurements were carried out at ~ 4 or $\sim 80 \text{ K}$ (80 K).

C. Results

1. The infrared absorption spectra

The implantation of protons into silicon gives rise to about 20 sharp absorption lines in the range $1800 - 2250 \text{ cm}^{-1}$, as shown in Fig. VIII.2. When deuterons are implanted, the lines shift down in frequency by a factor $\sim\sqrt{2}$, which establishes that the absorption lines reflect the excitations of hydrogen-related local vibrational modes. In agreement with the assignments made in the previous chapters, we ascribe these lines to Si-H stretch modes. In addition, about 10 sharp absorption lines are observed in the range $700 - 850 \text{ cm}^{-1}$ in Si:H, and we assign these lines to Si-H bend modes. No counterparts of these lines are observed in the deuterium-implanted samples, presumably because their frequencies are below the detection limit of $\sim 600 \text{ cm}^{-1}$ with our setup. Of particular interest in this work are the Si-H modes at $743.1, 748.0, 1986.5,$ and 1989.4 cm^{-1} , which are shown in the insets of Fig. VIII.2. In the Si:D sample, the frequencies of the two similar stretch modes are 1446.1 and 1448.2 cm^{-1} .

In germanium implanted with protons, similar series of absorption lines are observed in the ranges $650 - 800 \text{ cm}^{-1}$ and $1750 - 2100 \text{ cm}^{-1}$ (see Fig. VIII.2). Again, the lines in the high-frequency range are observed to shift down in frequency by a factor $\sim\sqrt{2}$ when deuterons are substituted for protons. We assign the lines in the low-frequency range to Ge-H bend modes and those in the high-frequency range to Ge-H stretch modes. The deuterium counterparts of the lines in the low-frequency range are inaccessible with our experimental setup as in the silicon case.

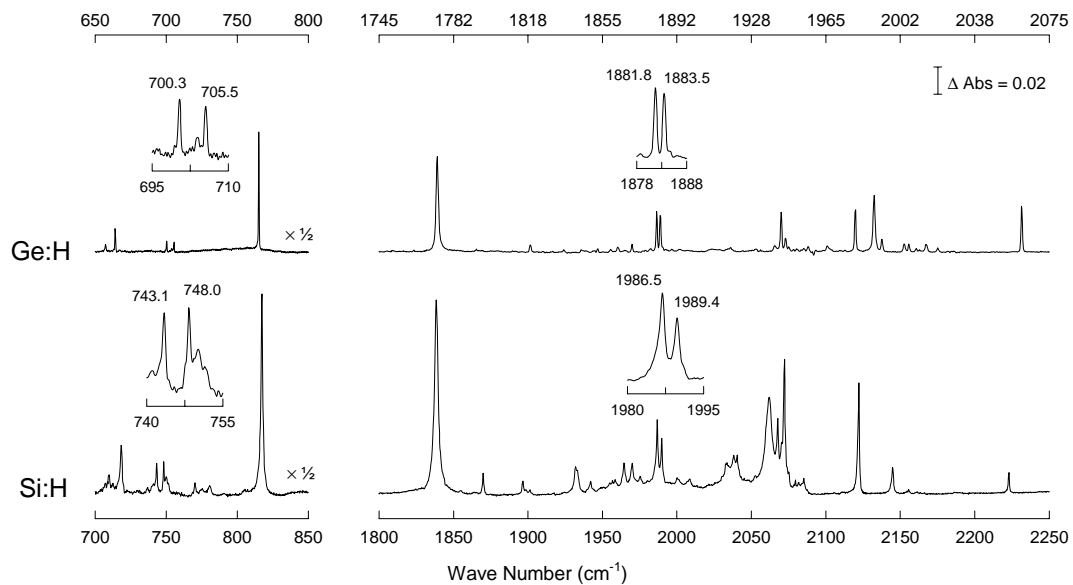


Fig. VIII.2. Absorbance spectra of Si:H (bottom) and Ge:H (top) measured at 9 K after room temperature annealing. The insets show the lines of particular interest to this work.

Located approximately in the middle of the stretch-mode range of Ge:H is a doublet of lines at 1881.8 and 1883.5 cm^{-1} , which shift down to 1357.6 and 1359.0 cm^{-1} in Ge:D. Another doublet of lines at 700.3 and 705.5 cm^{-1} is observed in the bend-mode range. Within 0.3%, the frequencies of the four Ge-H modes scale with the four Si-H modes specified above. The average frequency ratio between the similar Ge-H and Si-H modes is 0.945, which is within the range of ratios 0.896 to 0.965 obtained for similar modes in germane (GeH_4) and silane (SiH_4) [16]. This strongly suggests that the four Si-H and Ge-H modes originate from defects with essentially the same structures in the two materials.

2. Isochronal annealing

An isochronal annealing sequence was performed in which the samples were annealed for 30 min. at each temperature, starting at room temperature and going up to ~ 800 K in steps of ~ 20 K. The absorbance spectra were measured after each step. The dependencies on the annealing temperature of the four Si-H and Ge-H lines are shown in Fig. VIII.3. The four lines within each set always appear with the same relative intensities, independent of the annealing temperature and of the implanted dose. This strongly suggests that the four lines originate from the same defect. All other lines in Fig. VIII.2 have different annealing behaviours and do, therefore, not originate from this defect. The set of four lines disappear together at ~ 480 K in silicon and at ~ 465 K in germanium. This difference in annealing temperature of the defect in silicon and germanium is comparable to that of the H_2^* defect in the two materials (see chapter V). This suggests that the four Si-H and Ge-H modes originate from identical defects in the two materials.

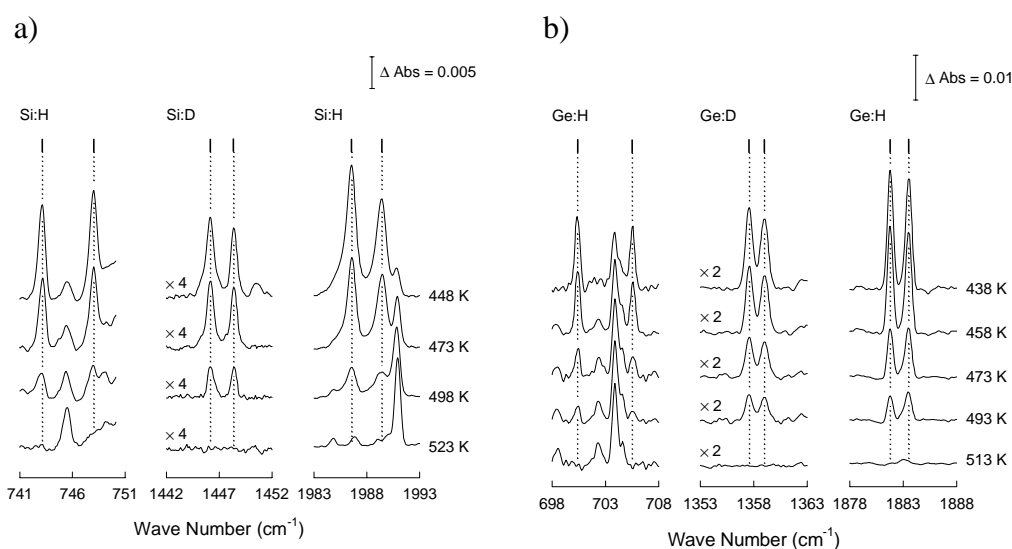


Fig. VIII.3. Isochronal annealing behaviours of the absorption lines at a) 743.1, 748.0, 1986.5, and 1989.4 cm^{-1} in Si:H, and at 1446.1 and 1448.2 cm^{-1} in Si:D, and b) at 700.3, 705.5, 1881.8, and 1883.5 cm^{-1} in Ge:H, and at 1357.6 and 1359.0 cm^{-1} in Ge:D.

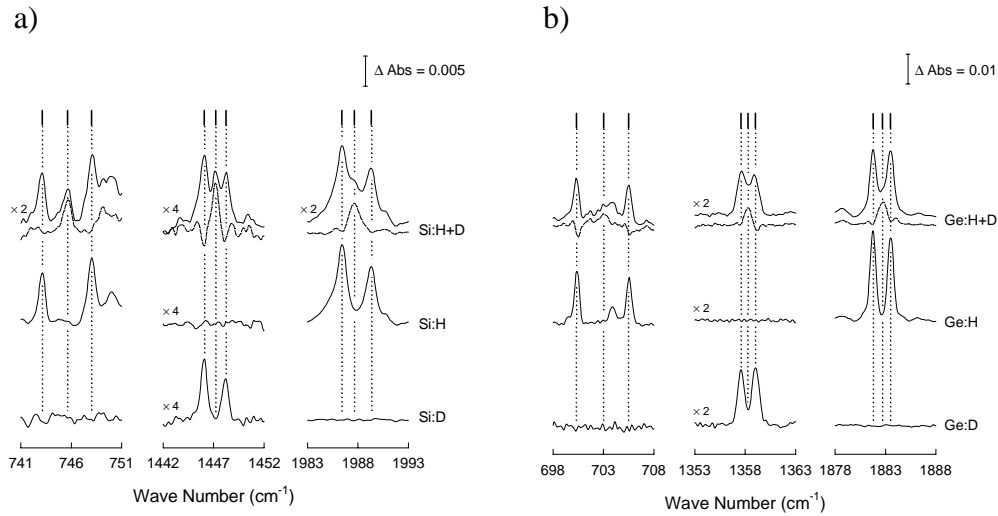


Fig. VIII.4. The result of isotope substitution on the Si-H lines at a) 743.1, 748.0, 1986.5, and 1989.4 cm^{-1} , and the Si-D lines at 1446.1 and 1448.2 cm^{-1} , and on the Ge-H lines at b) 700.3, 705.5, 1881.8, and 1883.5 cm^{-1} , and the Ge-D lines at 1357.6 and 1359.0 cm^{-1} . The dashed lines in the upper part of the figure are the Si:H+D (Ge:H+D) spectrum subtracted by the Si:H (Ge:H) or Si:D (Ge:D) spectrum.

3. Isotope substitution

Absorbance spectra measured on silicon and germanium samples coimplanted with protons and deuterons are shown in the upper part of Fig. VIII.4. Apart from the lines observed in samples implanted with a single isotope, three additional lines are observed at 745.7, 1447.3, and 1987.8 cm^{-1} in silicon and at ~ 703 , 1358.4, and 1882.8 cm^{-1} in germanium. The additional lines have the same annealing behaviour as the six lines in the single-isotope samples of each material. Therefore, the additional lines are ascribed to isotopically mixed configurations of the same defect. The observation of only two additional stretch-mode lines, of which one involves hydrogen and the other involves deuterium, indicates that the defect contains two equivalent hydrogen atoms. Also the observation of a single additional line in the Si-H bend-mode range is consistent with this. As can be seen from Fig. VIII.4.b, the additional line at ~ 703 cm^{-1} in the Ge-H bend-mode range is not resolved convincingly. The intensities of the isotopically mixed lines are generally weak in our germanium samples, and the 703- cm^{-1} line overlaps with a nearby unrelated line.

4. Uniaxial stress

Both the 1881.8- and 1883.5- cm^{-1} lines in Ge:H split into three components when uniaxial stress is applied along the [100] axis, as shown in Fig. VIII.5. This implies that these absorption lines either correspond to one-dimensional modes of a defect with triclinic, monoclinic-II or orthorhombic-II symmetry or to a two-dimensional mode of a centre with tetragonal symmetry

(see Table II.3). The presence of two equivalent Ge-H bonds is only compatible with tetragonal and orthorhombic-II symmetries if the two bonds are aligned with the same $\langle 100 \rangle$ axis. This, however, would imply that only one of the two stretch modes should be infrared active, in conflict with the observation of two lines of almost equal intensity. The presence of two equivalent Ge-H bonds also suggests that the point group of the defect possesses at least one symmetry element in addition to the identity operation. Consequently, only monoclinic-II symmetry appears to be in accordance with both the observed splitting under $[100]$ stress and the presence of two equivalent Ge-H bonds. Of course, the stress-patterns of the 1881.8- and 1883.5- cm^{-1} lines for $[111]$ and $[110]$ stresses should also be consistent with monoclinic-II symmetry. However, at this point we postpone further discussion of the Ge-H stretch data to Sec. VIII.E.1, where a detailed analysis is presented. We were unable to study the uniaxial stress responses of the 700.3- and 705.5- cm^{-1} lines as they lie in the frequency range cut off by the BaF_2 windows of the cryostat.

The Si-H lines at 743.1, 748.0, 1986.5, and 1989.4 cm^{-1} are less sensitive to uniaxial stress than the Ge-H lines discussed above. The splitting into three components for $[100]$ stress could not be resolved at 80 K. Therefore, the uniaxial stress-response for $[100]$ stress was measured also at liquid helium temperature where the absorption lines are narrower. The results are shown in Fig. VIII.6. It is evident that the 748- cm^{-1} line splits into three components, indicating the monoclinic-II symmetry also in silicon. For the 743.1-, 1986.5-, and 1989.4- cm^{-1} lines only two components could be resolved. Further discussion of the Si:H data is also postponed to Sec. VIII.E.2.

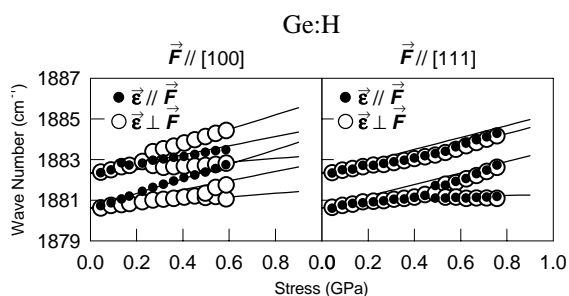


Fig. VIII.5. The stress-response of the 1881.8- and 1883.5- cm^{-1} lines in Ge:H for uniaxial stress along $[100]$ and $[111]$ measured at 80 K. The solid (open) symbols correspond to the infrared light polarised parallel (perpendicular) to the applied stress. The solid lines are obtained from the second-order analysis described in Sec. VIII.E.1 with the parameters presented in Table VIII.3

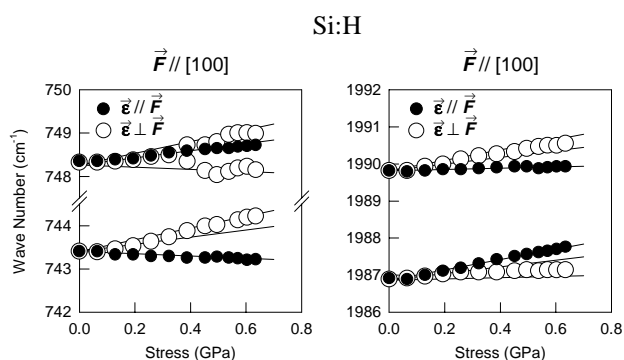


Fig. VIII.6. The stress-response of the 743.1-, 748.0-, 1986.5-, and 1989.4- cm^{-1} lines in Si:H for $[100]$ stress measured at ~ 4 K. The solid (open) symbols correspond to the infrared light polarised parallel (perpendicular) to the applied stress. The solid lines represent the best first-order fit to the data as described in Sec. VIII.E.2.

D. The stress-pattern of IH_2

In this section, the uniaxial stress-pattern is derived for the local vibrational modes of a monoclinic-II defect with two weakly coupled Si-H or Ge-H bonds. It is shown that the piezo-spectroscopic parameters in Table II.3 are equal for the modes that correspond to the symmetric and asymmetric combinations of equivalent displacement coordinates of the two bonds. Usually, the theoretical stress-pattern is based on first-order perturbation theory, which requires that the stress-induced frequency shifts be small compared to the separation of the modes. This requirement is not fulfilled for the modes discussed in this work and, therefore, the theory is extended to include second-order effects.

1. Basic model

The experimental results presented in Sec. VIII.C indicate that the defect contains two equivalent Si-H or Ge-H bonds and has monoclinic-II symmetry. Thus, the two bonds transform into one another by a 180° rotation about a $\langle 100 \rangle$ axis. A simple model containing such two bonds is shown in Fig. VIII.7. The local vibrational modes of hydrogen in silicon and germanium are effectively decoupled from the collective vibrations of the host lattice. Consequently, the local modes of our defect may be described by the coupled oscillations of two individual Si-H or Ge-H bonds. Each bond has three vibrational degrees of freedom, corresponding to a bond-stretch and two perpendicular bond-bend vibrations. Let the displacement coordinate that describes the stretching of the i th bond be denoted r_i and those describing the angular vibrations of the bond be denoted α_i and β_i (see Fig. VIII.7). In principle, the local mode frequencies may be determined from the eigenvalues of the Hamiltonian:

$$\hat{H} = \hat{T}_{r_1} + \hat{T}_{\alpha_1} + \hat{T}_{\beta_1} + \hat{T}_{r_2} + \hat{T}_{\alpha_2} + \hat{T}_{\beta_2} + \hat{V}(r_1, \alpha_1, \beta_1, r_2, \alpha_2, \beta_2), \quad (\text{VIII.1})$$

where \hat{T}_{ξ_i} is the kinetic energy operator corresponding to the displacement coordinate ξ_i and \hat{V} is the potential energy operator for the complex. At this point, a few clarifying remarks about our choice of coordinates are appropriate. The coordinates for the i th bond are chosen so that no cross terms coupling r_i , α_i and β_i appear in the second-order Taylor expansion of \hat{V} around the point of zero displacements. In other words, r_i , α_i and β_i would be proportional to the normal

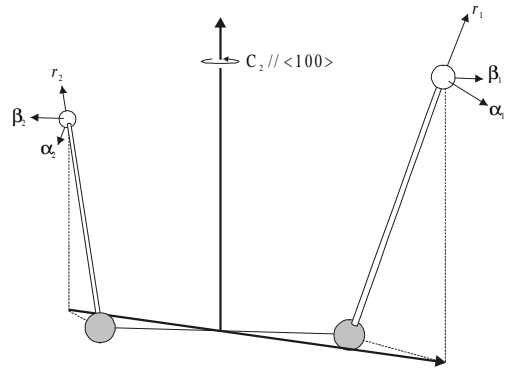


Fig. VIII.7. Illustration of the vibrational modes for a monoclinic-II centre containing two equivalent Si-H or Ge-H bonds. The shaded spheres represent silicon or germanium and the white spheres hydrogen. The displacement coordinates r_i , α_i , and β_i , $i \in \{1, 2\}$, are indicated by arrows.

coordinates of the i th bond in a situation where the displacement coordinates of the other bond were fixed at zero. With this choice, the coordinates may be divided into three sets of equivalent coordinates $\{r_1, r_2\}$, $\{\alpha_1, \alpha_2\}$ and $\{\beta_1, \beta_2\}$, which are closed under the symmetry operations of the C_2 group.

In the following, we shall neglect all terms in the potential energy \hat{V} , which couple inequivalent coordinates, i.e. coordinates from different sets. In addition, we assume that the coupling between a pair of equivalent coordinates is dominated by the quadratic term. With these assumptions, the six-dimensional problem in Eq. VIII.1 is reduced to three two-dimensional problems, each with a Hamiltonian of the type

$$\hat{H}_\xi = \hat{T}_{\xi_1} + \hat{T}_{\xi_2} + \hat{V}_\xi(\xi_1) + \hat{V}_\xi(\xi_2) + f_{12}^\xi \xi_1 \xi_2, \quad \xi \in \{r, \alpha, \beta\}. \quad (\text{VIII.2})$$

Here \hat{V}_ξ denotes a single-coordinate potential for one of the two equivalent bonds and f_{12}^ξ is the harmonic coupling constant. It may be noted that all anharmonic terms, which depend only on a single displacement coordinate ξ_i , are included in \hat{H}_ξ through \hat{V}_ξ . Such terms were in chapter V shown to give a significant contribution to the local mode frequencies of the H_2^* defect in silicon and germanium.

From each set of equivalent coordinates $\{\xi_1, \xi_2\}$, two symmetry coordinates $\xi_A = (\xi_1 + \xi_2)/\sqrt{2}$ and $\xi_B = (\xi_1 - \xi_2)/\sqrt{2}$ can be formed that transform like the symmetry species *A* and *B* of the C_2 point group. The Hamiltonian \hat{H}_ξ in Eq. VIII.2 gives rise to an *A* mode and a *B* mode with normal coordinates proportional to ξ_A and ξ_B . Thus, the two modes associated with each set of equivalent coordinates correspond to a symmetric (ξ_A) and an asymmetric (ξ_B) combination of displacement coordinates.

The couplings between the coordinates that belong to two inequivalent sets may be neglected provided that the frequency differences between modes of the different sets are much larger than the frequency shifts induced by the couplings. This condition is obviously fulfilled for stretch- and bend modes, whereas the decoupling of inequivalent bend modes is less clear. However, only two bend modes $\sim 5 \text{ cm}^{-1}$ apart are observed in both silicon and germanium. Moreover, the substitution of one of the hydrogen atoms with deuterium gives rise to one additional bend mode close to the mean frequency of the two original modes. Finally, the uniaxial stress data show that the two bend modes in silicon have different symmetry. These observations strongly suggest that the two bend modes represent the symmetric and asymmetric combination of either $\{\alpha_1, \alpha_2\}$ or $\{\beta_1, \beta_2\}$. If the observed splitting between the two modes represents a typical coupling term between angular coordinates, the coupling with other bend modes would be insignificant, unless their frequencies deviate from those of the doublet by only a few times the observed splitting. The fact that no other modes are observed within this range indicates that the assumption made above is reasonable.

The frequency splitting observed between the *A* and the *B* modes of equivalent coordinates are two or three orders of magnitude smaller than the mode frequencies. Therefore, the coupling term $f_{12}^\xi \xi_1 \xi_2$ in Eq. VIII.2 may be treated by perturbation theory. The zero-order eigenstates can be chosen to have the form $|n_1, n_2\rangle = |n_1\rangle_1 |n_2\rangle_2$, where $|n\rangle_i$ is a normalised eigenstate of the one-dimensional Hamiltonian: $\hat{H}_\xi^i = \hat{T}_{\xi_i} + \hat{V}_\xi(\xi_i)$. The quantum number n is chosen to be a non-negative integer in such a way that the energy of the state increases with increasing n . Since we are observing fundamental transitions, only the ground state ($n_1 + n_2 = 0$) and the singly-excited states ($n_1 + n_2 = 1$) are of interest. To zeroth order, the $|1,0\rangle$ and $|0,1\rangle$ states are degenerate, but the coupling will imply a splitting into an $|A\rangle$ and a $|B\rangle$ state. Therefore, we apply a basis that reflects this symmetry, i.e.,

$$|A, 0\rangle = |0, 0\rangle \quad (\text{VIII.3})$$

for the ground state, and for the singly-excited states:

$$|A, 1\rangle = \frac{1}{\sqrt{2}}(|1, 0\rangle + |0, 1\rangle) \quad \text{and} \quad |B, 1\rangle = \frac{1}{\sqrt{2}}(|1, 0\rangle - |0, 1\rangle) . \quad (\text{VIII.4})$$

2. Stress-pattern to first order

When uniaxial stress is introduced, the associated strain field changes the potential energies $\hat{V}_\xi(\xi_i)$ given in Eq. VIII.2. Since this stress-induced change is small, it is usually expanded to first order in the components of the stress tensor. For the i th bond, this leads to an additional potential energy term:

$$\Delta \hat{V}_\xi^{(i)}(\hat{\boldsymbol{\sigma}}^{(i)}) = \hbar \sum_{k,l \in \{x,y,z\}} \hat{A}_{kl}^{(i)} \sigma_{kl}^{(i)} . \quad (\text{VIII.5})$$

In this expression $\hat{A}_{kl}^{(i)}$ denotes the kl th component of the symmetric second-rank tensor $\hat{\mathbf{A}}^{(i)}$ which represents the effect of uniaxial stress on the single coordinate potential $\hat{V}_\xi(\xi_i)$ and $\sigma_{kl}^{(i)}$ is the kl th component of the stress-tensor $\hat{\boldsymbol{\sigma}}^{(i)}$. Since the two bonds are equivalent, it is convenient to introduce bond-specific coordinate systems with orthonormal bases $\{\bar{\mathbf{e}}_x^{(1)}, \bar{\mathbf{e}}_y^{(1)}, \bar{\mathbf{e}}_z^{(1)}\}$ and $\{\bar{\mathbf{e}}_x^{(2)}, \bar{\mathbf{e}}_y^{(2)}, \bar{\mathbf{e}}_z^{(2)}\}$. One of these can be chosen freely, whereas the other is obtained from the first by the C_2 rotation. When the bond-specific coordinate systems are used, the relation between the expectation values of the operators $\hat{A}_{kl}^{(1)}$ and $\hat{A}_{kl}^{(2)}$ is very simple:

$${}_1\langle n | \hat{A}_{kl}^{(1)} | n' \rangle_1 = {}_2\langle n | \hat{A}_{kl}^{(2)} | n' \rangle_2 . \quad (\text{VIII.6})$$

As a matter of convenience we choose

$$\bar{\mathbf{e}}_x^{(1)} // [100], \quad \bar{\mathbf{e}}_y^{(1)} // [010], \quad \bar{\mathbf{e}}_z^{(1)} // [001]. \quad (\text{VIII.7})$$

First, one specific defect-orientation with the two-fold axis along [001] is considered. Then, $\bar{\mathbf{e}}_x^{(1)} = -\bar{\mathbf{e}}_x^{(2)}$, $\bar{\mathbf{e}}_y^{(1)} = -\bar{\mathbf{e}}_y^{(2)}$ and $\bar{\mathbf{e}}_z^{(1)} = \bar{\mathbf{e}}_z^{(2)}$, and the relation between the stress tensor in the two bond-specific systems is

$$\hat{\boldsymbol{\sigma}}^{(2)} = \begin{pmatrix} \sigma_{xx}^{(1)} & \sigma_{xy}^{(1)} & -\sigma_{xz}^{(1)} \\ \sigma_{xy}^{(1)} & \sigma_{yy}^{(1)} & -\sigma_{yz}^{(1)} \\ -\sigma_{xz}^{(1)} & -\sigma_{yz}^{(1)} & \sigma_{zz}^{(1)} \end{pmatrix}. \quad (\text{VIII.8})$$

With Eqs. VIII.5 and VIII.8, the total stress-induced change of the Hamiltonian in Eq. VIII.2 is

$$\begin{aligned} \Delta\hat{V}_\xi^{(1)} + \Delta\hat{V}_\xi^{(2)} = & \hbar\{\hat{A}_{xx}^{(1)} + \hat{A}_{xx}^{(2)}\}\sigma_{xx} + \hbar\{\hat{A}_{yy}^{(1)} + \hat{A}_{yy}^{(2)}\}\sigma_{yy} + \hbar\{\hat{A}_{zz}^{(1)} + \hat{A}_{zz}^{(2)}\}\sigma_{zz} \\ & + 2\hbar\{\hat{A}_{xy}^{(1)} + \hat{A}_{xy}^{(2)}\}\sigma_{xy} + 2\hbar\{\hat{A}_{yz}^{(1)} - \hat{A}_{yz}^{(2)}\}\sigma_{yz} + 2\hbar\{\hat{A}_{zx}^{(1)} - \hat{A}_{zx}^{(2)}\}\sigma_{zx} . \end{aligned} \quad (\text{VIII.9})$$

With the definitions in Eq. VIII.7, the stress tensor $\hat{\mathbf{o}}^{(1)}$ is given with respect to the $\langle 100 \rangle$ axes of the diamond lattice and the bond-indices have, therefore, been dropped in Eq. VIII.9, i.e. $\hat{\mathbf{o}} \equiv \hat{\mathbf{o}}^{(1)}$. With Eqs. VIII.3, VIII.4, and VIII.9, we are able to calculate the stress-induced first-order energy shifts of the ground state $|A,0\rangle$ and the singly-excited states $|A,1\rangle$ and $|B,1\rangle$. The energy shifts for the transitions $|A,0\rangle \rightarrow |A,1\rangle$ and $|A,0\rangle \rightarrow |B,1\rangle$ are equal and given by

$$\Delta E_A^{(1)} = \Delta E_B^{(1)} = \hbar\Delta\omega^{(1)} = \hbar(\mathcal{C}\mathcal{A}_1\sigma_{zz} + \mathcal{C}\mathcal{A}_2\sigma_{yy} + \mathcal{C}\mathcal{A}_3\sigma_{xx} + 2\mathcal{C}\mathcal{A}_4\sigma_{xy}) , \quad (\text{VIII.10})$$

where the piezo-spectroscopic parameters

$$\begin{aligned} \mathcal{C}\mathcal{A}_1 = & {}_1\langle 1|\hat{A}_{zz}^{(1)}|1\rangle_{-1} - {}_1\langle 0|\hat{A}_{zz}^{(1)}|0\rangle_{-1} , & \mathcal{C}\mathcal{A}_2 = & {}_1\langle 1|\hat{A}_{yy}^{(1)}|1\rangle_{-1} - {}_1\langle 0|\hat{A}_{yy}^{(1)}|0\rangle_{-1} \\ \mathcal{C}\mathcal{A}_3 = & {}_1\langle 1|\hat{A}_{xx}^{(1)}|1\rangle_{-1} - {}_1\langle 0|\hat{A}_{xx}^{(1)}|0\rangle_{-1} , & \mathcal{C}\mathcal{A}_4 = & {}_1\langle 1|\hat{A}_{xy}^{(1)}|1\rangle_{-1} - {}_1\langle 0|\hat{A}_{xy}^{(1)}|0\rangle_{-1} \end{aligned} \quad (\text{VIII.11})$$

have been introduced. Thus, the stress splittings of the two modes are identical.

If uniaxial stress of magnitude σ is applied along the direction defined by the unit vector $\bar{\mathbf{n}}$, the components of the stress tensor are $\sigma_{ij} = \sigma \cos(\bar{\mathbf{n}} \cdot \bar{\mathbf{e}}_i^{(1)}) \cos(\bar{\mathbf{n}} \cdot \bar{\mathbf{e}}_j^{(1)})$, $i, j \in \{x, y, z\}$. For a given stress tensor $\hat{\mathbf{o}}$, the stress-induced energy shift for one particular orientation of the defect is given by Eq. VIII.10. From this particular orientation of the defect all the other defect orientations can be generated by the 24 symmetry operations \mathbf{R}_l of the T_d point group. The stress-induced energy shift for the defect orientation obtained by \mathbf{R}_l can also be calculated from Eq. VIII.10 when $\hat{\mathbf{o}}$ is replaced by

$$\hat{\mathbf{o}}_l = \mathbf{R}_l^{-1} \hat{\mathbf{o}} \mathbf{R}_l . \quad (\text{VIII.12})$$

The results for stresses along [100], [111], and [110] are identical to those obtained by Kaplyanskii [15] and are given in Table II.3. However, the present derivation shows that the piezo-spectroscopic parameters are identical for the symmetric and asymmetric modes of equivalent vibrational degrees of freedom.

The probability for the transition $|A,0\rangle \rightarrow |\Gamma,1\rangle$, where $\Gamma \in \{A, B\}$, is proportional to $|\bar{\mathbf{e}} \cdot \bar{\mathbf{d}}|^2$, where $\bar{\mathbf{e}}$ is the polarisation vector of the infrared light and $\bar{\mathbf{d}}_\Gamma = \langle A,0 | \bar{\mathbf{d}} | \Gamma,1 \rangle$ is the transition matrix element of the dipole operator $\bar{\mathbf{d}}$. Usually, the dipole operator is expanded to first order in the displacement coordinates ξ_1 and ξ_2 . Thus,

$$\bar{\mathbf{d}} = \bar{\mathbf{d}}_0 + \eta_\xi \xi_1 \bar{\mathbf{n}}_1^\xi + \eta_\xi \xi_2 \bar{\mathbf{n}}_2^\xi , \quad \xi \in \{r, \alpha, \beta\} , \quad (\text{VIII.13})$$

where $\bar{\mathbf{d}}_0$ is the permanent dipole moment, η_ξ is the effective charge, and $\bar{\mathbf{n}}_i^\xi$ is a unit vector that

defines the orientation of the induced bond-dipole corresponding to the displacement coordinate ξ_i . Using Eqs. VIII.3, VIII.4 and VIII.13, the transition matrix element is

$$\vec{\mathbf{d}}_{\Gamma} = \frac{\eta_{\xi}}{\sqrt{2}} \langle 0 | \xi_i | 1 \rangle_1 (\vec{\mathbf{n}}_1^{\xi} \pm \vec{\mathbf{n}}_2^{\xi}), \quad (\text{VIII.14})$$

where *plus* corresponds to $\Gamma=A$ and *minus* to $\Gamma=B$. Again, we first consider a particular orientation of the defect with the C_2 axis along [001]. The direction of, say, $\vec{\mathbf{n}}_1^{\xi}$ may be defined in terms of a polar angle θ and an azimuthal angle φ as shown in Fig. VIII.8. Then $\vec{\mathbf{n}}_2^{\xi}$ is related to $\vec{\mathbf{n}}_1^{\xi}$ via the C_2 rotation and it also has the polar angle θ , whereas its azimuthal angle is $180^\circ + \varphi$. Eq. VIII.14 implies that $\vec{\mathbf{d}}_A$ is parallel to the C_2 axis, and $\vec{\mathbf{d}}_B$ lies in the plane perpendicular to this axis and has the angle φ to the [100] direction. It is important to note that we can choose our coordinate axes in Fig. VIII.8 and the particular orientation of the defect in such a way that $0^\circ \leq \theta \leq 90^\circ$ and $0^\circ \leq \varphi \leq 45^\circ$.³ In the following we shall adopt this specific choice, which defines θ as the smallest angle to the C_2 axis and φ as the smallest angle to a $\langle 100 \rangle$ axis in the plane perpendicular to the C_2 axis. It must be emphasised that the values of θ and φ obtained in this way for different types of displacement coordinates, e.g. $\xi = \alpha$ and $\xi = r$, do not in general refer to the same choice of axes nor to the same particular orientation of the defect.

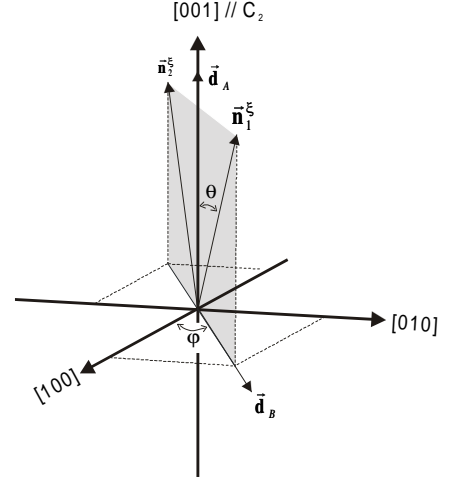


Fig. VIII.8. Definition of the polar angle θ and azimuthal angle φ that specify the directions of the unit vectors \mathbf{n}_1^{ξ} and \mathbf{n}_2^{ξ} for a specific orientation of the defect. The direction of the induced dipole moments for the A mode (\mathbf{d}_A) and the B mode (\mathbf{d}_B) are also shown.

The transition matrix elements corresponding to the other orientations of the defect are obtained by the symmetry operations \mathbf{R}_i of the T_d point group. If the defects are distributed evenly among the different orientations, the intensity of the $|A,0\rangle \rightarrow |\Gamma,1\rangle$ transition at zero stress is proportional to the sum of the transition probabilities of all the possible defect orientations:

$$I^{(\Gamma)} \propto \sum_{\mathbf{R}_i \in T_d} |\hat{\mathbf{a}} \cdot (\mathbf{R}_i \vec{\mathbf{d}}_{\Gamma})|^2, \quad \Gamma \in \{A, B\}. \quad (\text{VIII.15})$$

It may be noted that the mode intensity at zero stress $I^{(\Gamma)}$ is independent of the polarisation of the

³ We have the freedom to choose the [001] direction in Fig. VIII.8 so that $0^\circ \leq \theta \leq 90^\circ$. Moreover, the [100] and [010] direction may be chosen so that $0^\circ \leq \varphi \leq 90^\circ$. If $\varphi \in [45^\circ, 90^\circ]$, then the equivalent orientation of the defect which is generated by the reflection in the (1-10) plane would maintain the C_2 axis along [001] and a \mathbf{n}_1^{ξ} -vector with the same value of θ , but its azimuthal angle would be in the interval $[0^\circ, 45^\circ]$.

infrared light since the sum includes all symmetry operations of the T_d point group. The ratio of the A and B mode intensities at zero stress can be calculated with Eqs. VIII.14 and VIII.15, and the result depends only on the polar angle θ :

$$\left. \frac{I^{(A)}}{I^{(B)}} \right|_{\sigma=0} = \cot^2 \theta . \quad (\text{VIII.16})$$

Hence, the polar angle of the bond-dipoles may be determined from the intensities of the absorption lines at zero stress.

When uniaxial stress is applied, the intensity of an absorption line will be divided between its stress-split components. The relative intensity of a given component can be determined with Eq. VIII.15 if the sum is restricted to those symmetry operations \mathbf{R}_i , which contribute to that particular component. The relative intensities of the stress components for [100], [111] and [110] stresses with the infrared light polarised parallel and perpendicular to the applied stress are given in Table II.3. As can be seen from the table, the relative intensities of the B mode depend on the azimuthal angle ϕ of the induced bond dipole-moment. Thus, this angle may also be determined experimentally.

The first-order approach is only valid provided that the absolute value of the stress-induced coupling $\langle A,1 | \Delta \hat{V}_\xi^{(1)} + \Delta \hat{V}_\xi^{(2)} | B,1 \rangle$ is small compared to the energy splitting between $|A,1\rangle$ and $|B,1\rangle$. In the case of silicon, the observed bend modes are split by 4.9 cm^{-1} and the stretch modes by 2.9 cm^{-1} . In germanium the bend modes are split by 5.2 cm^{-1} and the stretch modes by 1.7 cm^{-1} . The maximum stress-induced frequency shifts are $\sim 1 \text{ cm}^{-1}$ in silicon and $\sim 2 \text{ cm}^{-1}$ in germanium (see Fig. VIII.5 and Fig. VIII.6) and, hence, second-order effects may be important, especially for the stretch modes in germanium.

3. Stress-pattern to second order

On the basis of the previous subsection it is straightforward to include second-order effects in the analysis of the stress response. The eigenvalue problem of the Hamiltonian, given as the sum of the zero-order Hamiltonian in Eq. VIII.2 and the stress-induced perturbation in Eq. VIII.9, is solved in the subspaces spanned by $|A,0\rangle$ for the ground state and by $|A,1\rangle$ and $|B,1\rangle$ for the singly-excited states. With this procedure⁴ we find the second-order transition frequencies $\omega_r^{(2)}$:

$$\begin{aligned} \omega_A^{(2)} &= \frac{1}{2} \omega_A^{(0)} \left(1 + \sqrt{1+x^2} \right) + \frac{1}{2} \omega_B^{(0)} \left(1 - \sqrt{1+x^2} \right) + \Delta \omega^{(1)} \\ \omega_B^{(2)} &= \frac{1}{2} \omega_B^{(0)} \left(1 + \sqrt{1+x^2} \right) + \frac{1}{2} \omega_A^{(0)} \left(1 - \sqrt{1+x^2} \right) + \Delta \omega^{(1)} \end{aligned} \quad , \quad (\text{VIII.17})$$

where $\omega_A^{(0)}$ and $\omega_B^{(0)}$ are the frequencies without stress, $\Delta \omega^{(1)}$ is the first-order energy-shifts given in Eq. VIII.10, and the coupling parameter x is given by

⁴ Note that the procedure is not a true second-order perturbation calculation.

$$x = \frac{\langle A,1 | \Delta \hat{V}_\xi^{(1)} + \Delta \hat{V}_\xi^{(2)} | B,1 \rangle}{\frac{1}{2} \hbar (\omega_A^{(0)} - \omega_B^{(0)})} = \frac{2\mathcal{B}_1 \sigma_{yz} + 2\mathcal{B}_2 \sigma_{zx}}{\frac{1}{2} (\omega_A^{(0)} - \omega_B^{(0)})} . \quad (\text{VIII.18})$$

Here, the off-diagonal piezo-spectroscopic parameters \mathcal{B}_1 and \mathcal{B}_2 are defined similarly to the parameters $\mathcal{A}_i, i \in \{1,2,3,4\}$, given in Eq. VIII.11:

$$\mathcal{B}_1 = {}_1\langle 1 | \hat{A}_{yz}^{(1)} | 1 \rangle_1 - {}_1\langle 0 | \hat{A}_{yz}^{(1)} | 0 \rangle_1 , \quad \mathcal{B}_2 = {}_1\langle 1 | \hat{A}_{zx}^{(1)} | 1 \rangle_1 - {}_1\langle 0 | \hat{A}_{zx}^{(1)} | 0 \rangle_1 . \quad (\text{VIII.19})$$

In the case of uniaxial stress in the [100] direction, all the off-diagonal stress-tensor components are zero for all orientations of the defect. According to Eq. VIII.18 this implies that x is zero and, thus, there are no second-order contributions to the transition frequency for [100] stress. For [111] and [110] stresses, however, x is generally not zero and second-order effects may become important. This reflects the fact that uniaxial stress along a $\langle 100 \rangle$ direction preserves the monoclinic-II symmetry, whereas stress in other directions reduces the symmetry of the defect to triclinic.

The transition matrix element \vec{d}_Γ given in Eq. VIII.14 is correct only in a first-order treatment. Since stress-induced coupling of the ground state to other states is neglected, the initial state of the transitions remains identical to $|A,0\rangle$. However, when $x \neq 0$ the singly-excited final state $|\Gamma,1\rangle$ will be a normalised linear combination of the $|A,1\rangle$ and $|B,1\rangle$ states:

$$|\Gamma,1\rangle = t_A |A,1\rangle + t_B |B,1\rangle , \quad (\text{VIII.20})$$

where the coefficients t_A and t_B depend on x . With this expression for $|\Gamma,1\rangle$, the transition matrix element may be calculated and we find

$$\vec{d}_\Gamma^{(2)} = \frac{\eta_\xi}{\sqrt{2}} {}_1\langle 0 | \xi_1 | 1 \rangle_1 \left\{ (t_A + t_B) \vec{n}_1^\xi + (t_A - t_B) \vec{n}_2^\xi \right\} . \quad (\text{VIII.21})$$

Now, the relative intensities of the stress-split components may be calculated as discussed in the previous subsection (see Eq. VIII.15). Obviously, the intensities of the stress-split components differ from the first-order result in Table II.3, and they depend on the magnitude as well as on the direction of the applied uniaxial stress when second-order effects are important (i.e. $x \neq 0$). Due to this complication, we are unable to give simple analytical expressions for the intensity ratios of the stress components. However, a simulation of the line profiles at the maximum stresses attained in the [100], [111], and [110] direction is presented in the next section.

E. Analysis of the uniaxial stress experiments

With the theoretical stress-pattern of a monoclinic-II centre derived in the previous section, we can perform a detailed analysis of the stress-pattern observed for the 1881.8- and 1883.5-cm⁻¹ lines in Ge:H and the 743.1-, 748.0-, 1986.5-, and 1989.4-cm⁻¹ lines in Si:H.

1. Analysis of the Ge-H lines

In Sec. VIII.C we showed that the Ge-H lines at 1881.8 and 1883.5 cm⁻¹ represent the stretch modes of a monoclinic-II defect containing two equivalent hydrogen atoms. Hence, we can use Eq. VIII.16 and the intensities of the two lines measured without stress to find $\theta = 45^\circ \pm 1^\circ$ for the Ge-H stretch modes.

As can be seen from Fig. VIII.5, the lines at 1881.8 and 1883.5 cm⁻¹ split into three components under [100] stress, and the slopes of the stress splittings for the two lines are equal within the experimental uncertainties. These observations are in accordance with the first-order stress-pattern, as expected since the coupling parameter $x = 0$ for [100] stress. The experimental and theoretical intensities of the [100]-stress components suggest that the azimuthal angle φ is close to 0°. With this angle, the first-order stress-patterns for [100] (and [111]) stresses of the lines corresponding to $|A,0\rangle \rightarrow |A,1\rangle$ and $|A,0\rangle \rightarrow |B,1\rangle$ transitions differ only by a permutation of $\mathcal{C}\mathcal{A}_1$ and $\mathcal{C}\mathcal{A}_3$. Therefore, it is not possible to ascribe a specific transition to the 1881.8- or 1883.5-cm⁻¹ line solely from the [100] (and [111]) stress-patterns. However, the observed stress-patterns for [110] stress and [001] polarisation ($\bar{\epsilon} // [001]$) are markedly different for the two lines. Only one component of the 1881.8-cm⁻¹ line is observed under these conditions, whereas the 1883.5-cm⁻¹ line is observed to split into two components of equal intensity (see Fig. VIII.9). As can be seen from Table II.3, this strongly indicates that the line at 1881.8 cm⁻¹ originates from the $|A,0\rangle \rightarrow |B,1\rangle$ transition, whereas the line at 1883.5 cm⁻¹ originates from the $|A,0\rangle \rightarrow |A,1\rangle$ transition. With this identification and $\varphi \sim 0^\circ$, the piezo-spectroscopic parameters $\mathcal{C}\mathcal{A}_1$, $\mathcal{C}\mathcal{A}_2$, and $\mathcal{C}\mathcal{A}_3$ can be determined from the [100]-stress data.

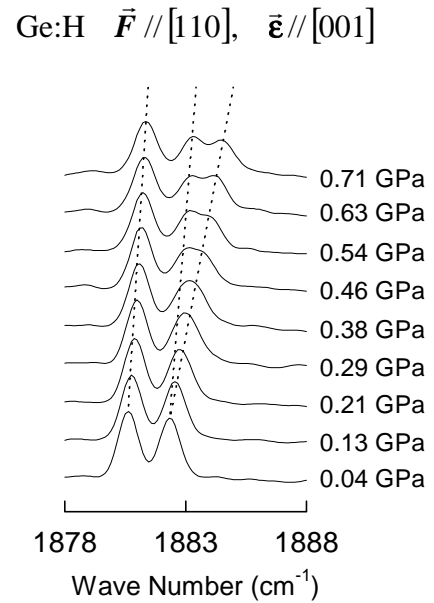


Fig. VIII.9. The stress-response of the 1881.8- and 1883.5-cm⁻¹ lines in Ge:H measured at 80 K with stress along [110] and [001] polarisation. The dotted lines indicate the stress-induced splittings.

In order to understand the observed stress-patterns for [111] and [110] stress and to obtain accurate values of φ and \mathcal{A}_4 , it is necessary to include second-order effects. For instance, it is evident from Fig. VIII.5 that the experimental stress-splittings for [111] stress are different for the 1881.8- and 1883.5-cm⁻¹ lines. The 1881.8-cm⁻¹ line splits into two components while the 1883.5-cm⁻¹ line does not split, in conflict with the first-order stress-pattern. The second-order effects are taken into account with a detailed line profile analysis of the spectra measured at maximum stresses, using the second-order theory described in Sec. VIII.D.3. At zero stress, the line shape of the Ge-H lines is nearly Gaussian. Since all the 24 different orientations of the defect are assumed to occur with equal probability, we assume that the 1881.8- and 1883.5-cm⁻¹ lines both consist of a superposition of 24 Gaussians with equal position, amplitude and width. When uniaxial stress is applied, the positions and relative amplitudes of the Gaussians are changed according to the second-order theory. The line positions at zero stress, the line widths, the polar angle θ , and the constant $\eta_{\xi} \langle 0 | \xi_1 | 1 \rangle_1$ are fixed at the values obtained from the line profiles at zero stress. The piezo-spectroscopic parameters \mathcal{A}_1 , \mathcal{A}_2 , \mathcal{A}_3 , \mathcal{A}_4 , \mathcal{B}_1 , \mathcal{B}_2 , and the azimuthal angle φ are treated as fitting parameters. In Fig. VIII.10, the line profiles observed at maximum stress are compared with those corresponding to the best fit, obtained with the parameters presented in Table VIII.3. Furthermore, the second-order line splittings for uniaxial stress along [100] and [111] that correspond to the best-fit parameters are shown as solid curves in Fig. VIII.5. It is evident that the experimental stress-patterns of the Ge-H lines at 1881.8 and 1883.5 cm⁻¹ are very well accounted for by the second-order stress-pattern of a monoclinic-II centre containing two equivalent Ge-H bonds.

Table VIII.3. The piezo-spectroscopic parameters (in cm⁻¹/GPa), the polar angles and the azimuthal angles corresponding to the best-fit curves shown in Figs. VIII.5, 6, and 10. See text for further details.

Mode	Si:H bend	Si:H stretch	Ge:H stretch
Frequency	743.1 cm ⁻¹	1986.5 cm ⁻¹	1881.8 cm ⁻¹
	748.0 cm ⁻¹	1989.4 cm ⁻¹	1883.5 cm ⁻¹
\mathcal{A}_1	-0.3 ± 0.3 ^a	0.18 ± 0.19 ^a	2.2 ± 0.2 ^b
\mathcal{A}_2	1.4 ± 0.4 ^a	0.9 ± 0.3 ^a	0.9 ± 0.2 ^b
\mathcal{A}_3	0.8 ± 0.3 ^a	1.4 ± 0.2 ^a	3.6 ± 0.2 ^b
\mathcal{A}_4	0.6 ± 0.2 ^b	0.9 ± 0.2 ^b	1.0 ± 0.1 ^b
\mathcal{B}_1			-1.4 ± 0.2 ^b
\mathcal{B}_2			1.0 ± 0.2 ^b
θ	43° ± 2°	48° ± 1°	45° ± 1°
φ	0° ± 8°		3° ± 5°

^a Measured at ~4 K

^b Measured at 80 K

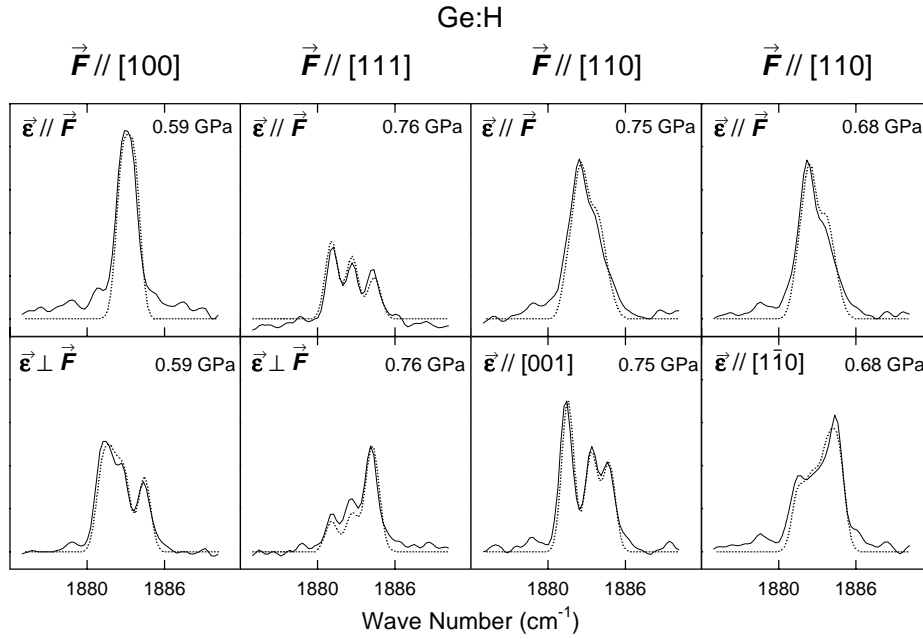


Fig. VIII.10. The profiles of the 1881.8- and 1883.5- cm^{-1} lines in Ge:H at the maximum stresses obtained. The solid curves are the measured spectra and the dotted curves represent the line profiles obtained with the best-fit parameters presented in Table VIII.3. The spectra were measured at 80 K.

2. Analysis of Si-H lines

The polar angle for the Si-H stretch modes is readily found to be $\theta = 48^\circ \pm 1^\circ$ from Eq. VIII.16 and the experimental intensities of the 1986.5 and 1989.4 cm^{-1} lines at zero stress. If we assume that the Si-H lines at 743.1 and 748.0 cm^{-1} correspond to the symmetric and asymmetric combination of two equivalent angular degrees of freedom, the polar angle $\theta = 43^\circ \pm 2^\circ$ is obtained for the two bend modes.

As mentioned in Sec. VIII.C, the Si-H lines at 743.1, 748.0, 1986.5, and 1989.4 cm^{-1} are rather insensitive to uniaxial stress and the individual stress components are not well resolved. In fact, the splitting at zero stress is at least three times larger than the experimental stress-induced shifts at maximum stress. We expect, therefore, second-order effects to be negligible for these lines and analyse the observed stress-pattern with the first-order expressions of Table II.3.

For stress along [110] and [001] polarisation, only one component is observed for the 1986.5- cm^{-1} line, whereas the line at 1989.4 cm^{-1} splits into two components of about equal intensity (see Fig. VIII.11). If we assume that the 1989.4- cm^{-1} line corresponds to the $|A,0\rangle \rightarrow |B,1\rangle$ transition, then the size of the splitting is $|\frac{1}{2}(C_{\mathcal{B}_2} - C_{\mathcal{B}_3})\sigma|$ and the azimuthal angle is $\phi \sim 45^\circ$, according to Table II.3. Then, the 1989.4- cm^{-1} line should also split into two components with about equal intensity for stress along [100] and parallel polarisation. The splitting of these two components should be $|(C_{\mathcal{B}_2} - C_{\mathcal{B}_3})\sigma|$, i.e. twice the splitting observed for [110] stress and [001] polarisation and should, therefore, easily be resolved. However, with [100]

stress no such splitting is observed for the 1989.4- cm^{-1} line and, thus, it cannot represent the $|A,0\rangle \rightarrow |B,1\rangle$ transition. On the other hand, the stress-pattern of the 1989.4- cm^{-1} line agrees with that of the $|A,0\rangle \rightarrow |A,1\rangle$ transition, if the parameters \mathcal{A}_2 and \mathcal{A}_3 are about equal. Moreover, the stress-pattern for the line at 1986.5 cm^{-1} is consistent with the $|A,0\rangle \rightarrow |B,1\rangle$ transition. Hence, we ascribe the 1986.5- and 1989.4- cm^{-1} lines to the $|A,0\rangle \rightarrow |B,1\rangle$ and $|A,0\rangle \rightarrow |A,1\rangle$ transitions, respectively. Due to the small difference between \mathcal{A}_2 and \mathcal{A}_3 , the azimuthal angle φ cannot be determined with a reasonable accuracy, but a value close to zero is consistent with the experimental data also in this case. With $\varphi = 0^\circ$, the theoretical first-order frequency shifts of Table II.3 are fitted to those observed for [100] stress. The intensity-weighted averages of the theoretical frequency shifts are used when the individual components are unresolved experimentally. The best-fit parameters \mathcal{A}_1 , \mathcal{A}_2 and \mathcal{A}_3 for the Si-H stretch modes are presented in Table VIII.3, and the solid lines in Fig. VIII.6 correspond to the theoretical frequency shifts with these parameters. The symmetry of the modes that gives rise to the lines at 743.1 and 748.0 cm^{-1} may be determined by the procedure applied just above. The 743.1 cm^{-1} line splits into two components for stress along [110] and [001] polarisation while a single component only is observed for the line at 748.0 cm^{-1} (see Fig. VIII.11). Hence, if the 743.1 cm^{-1} line represents the $|A,0\rangle \rightarrow |B,1\rangle$ transition, two components with the same intensity ratio and twice the splitting observed for [110] stress and [001] polarisation should be observed for stress along [100] and parallel polarisation. However, such a splitting is not observed (see Fig. VIII.6), and the 743.1- cm^{-1} line is assigned to the $|A,0\rangle \rightarrow |A,1\rangle$ transition. Moreover, the stress-pattern for the 748.0- cm^{-1} line is consistent with that expected for the $|A,0\rangle \rightarrow |B,1\rangle$ transition. The values of the best-fit parameters \mathcal{A}_1 , \mathcal{A}_2 , and \mathcal{A}_3 are given in Table VIII.3. The two components observed for the 748.0- cm^{-1} line for stress along [100] and parallel polarisation have almost equal intensities. From this the azimuthal angle is estimated to be $\varphi = 0^\circ \pm 8^\circ$.

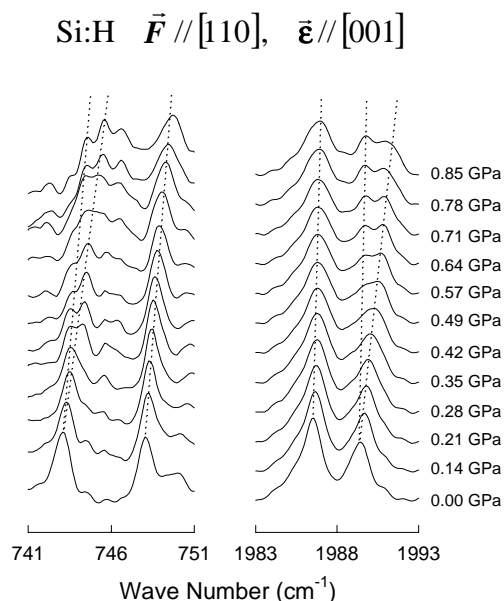


Fig. VIII.11. The stress-response of the 743.1-, 748.0-, 1986.5-, and 1989.4- cm^{-1} lines in Si:H measured at 80 K with stress along [110] and [001] polarisation. The dotted lines indicate the stress-induced splittings.

On this basis, we assign the 743.1- and 748.0-cm⁻¹ lines, respectively, to the excitations of the symmetric and asymmetric Si-H bend modes associated with equivalent angular displacement coordinates.

F. Discussion

The experiments show that the Ge-H lines at 700.3, 705.5, 1881.8, and 1883.5 cm⁻¹ represent local vibrational modes of a defect with two equivalent, weakly coupled Ge-H bonds. The response of the Ge-H lines at 1881.8 and 1883.5 cm⁻¹ to uniaxial stress is in excellent agreement with the theoretical second-order stress-pattern of the $|A,0\rangle \rightarrow |B,1\rangle$ and $|A,0\rangle \rightarrow |A,1\rangle$ transitions of a monoclinic-II centre. The polar angle of the stretch modes is found to be $\theta = 45^\circ \pm 1^\circ$ and the azimuthal angle is $\varphi = 3^\circ \pm 5^\circ$.

Likewise, the 743.1-, 748.0-, 1986.5-, and 1989.4-cm⁻¹ lines in Si:H correspond to local vibrational modes of a monoclinic-II defect that contains two equivalent and weakly coupled Si-H bonds. The ordering of the Si-H stretch modes is identical to that of the Ge-H stretch modes, i.e. the 1986.5-cm⁻¹ line corresponds to the $|A,0\rangle \rightarrow |B,1\rangle$ transition and the 1989.4-cm⁻¹ line to the $|A,0\rangle \rightarrow |A,1\rangle$ transition. The ordering of the Si-H bend modes, however, is reversed compared the stretch modes. The polar angle for the Si-H stretch modes is found to be $\theta = 48^\circ \pm 1^\circ$ and for the Si-H bend modes $\theta = 43^\circ \pm 2^\circ$. The azimuthal angle of the stretch modes cannot be determined, whereas $\varphi = 0^\circ \pm 8^\circ$ for the bend modes.

The frequencies of the four Ge-H and four Si-H modes scale very accurately with those of the germane and silane molecules. Moreover, the physical properties of the defect that gives rise to the four modes are essentially identical in germanium and in silicon. This establishes that the set of four modes originate the same defect in the two materials.

The angles θ and φ specify the direction of the unit vectors $\bar{\mathbf{n}}_1^\xi$, $\xi \in \{\alpha, \beta, r\}$, i.e. the direction of the induced dipole moment associated with a displacement of the type ξ_1 of the first bond. For stretch modes, we expect the bond-moment to be directed along the Ge-H (or Si-H) bond and, consequently, θ and φ of the stretch modes specify the direction of this bond. Hence, we can determine the smallest angle between the bond and the C_2 axis (θ) and the smallest angle between the projection of the bond onto the plane perpendicular to the C_2 axis and a $\langle 100 \rangle$ direction in this plane (φ). The values of θ and φ obtained for the Ge-H or Si-H stretch modes imply that with the C_2 axis along [001], the two Ge-H or Si-H bonds are nearly aligned with the [011] and $[0\bar{1}1]$ directions. The two Ge-H or Si-H bonds are nearly perpendicular. This suggests that the dynamical coupling of the stretch-vibrations of the two bonds is weak, and provides an intuitive explanation for the very small frequency splitting of the two stretch modes.

Moreover, we can obtain information on the nature of the Si-H bend modes at 743.1 and 748.0 cm⁻¹. If we assume that $\bar{\mathbf{n}}_1^\xi$ is parallel to the direction defined by an infinitesimal increase in the displacement coordinate ξ_1 , then $\bar{\mathbf{n}}_1^\alpha$, $\bar{\mathbf{n}}_1^\beta$ and $\bar{\mathbf{n}}_1^r$ are mutually perpendicular. However,

the values of θ and φ for the Si-H bend- and stretch modes presented in Table VIII.3 do not define perpendicular vectors. As mentioned in Sec. VIII.D, this reflects that these values do not refer to the same choice of coordinate system and/or defect orientation. If the polar angle for the Si-H stretch modes is fixed at $\theta = 48^\circ \pm 1^\circ$ and, moreover, we require that \vec{n}_1^z of the observed bend modes is perpendicular to \vec{n}_1^r , then the only solution to Eq. VIII.16 for the observed bend modes is $\theta = 137^\circ \pm 2^\circ$. We can now calculate the difference in azimuthal angle of the stretch- and bend modes to be $\Delta\varphi = 15^\circ \pm 17^\circ$, which is consistent with the values $\varphi = 0^\circ \pm 8^\circ$ for the bend modes and $\varphi \sim 0^\circ$ for the stretch modes. Thus, the bend- and stretch modes have nearly the same azimuthal angle, which implies that the bend modes are associated with the symmetric and asymmetric combinations of angular displacements almost in the plane spanned by the C_2 axis and the Si-H bond, i.e., the α coordinates defined in Fig. VIII.7.

The simplest defect that is consistent with all our findings is the IH_2 defect shown in Fig. VIII.1.d. As can be seen from the figure, this defect contains two nearly perpendicular and equivalent Si-H bonds that are almost aligned with the $[011]$ and $[0\bar{1}1]$ directions and has a C_2 axis parallel to the $[001]$ direction. On this basis, we assign the four Ge-H modes at 700.3, 705.5, 1881.8, and 1883.5 cm^{-1} and the four Si-H modes at 743.1, 748.0, 1986.5, and 1989.4 cm^{-1} to the IH_2 defect.

It may be argued that the four modes could just as well originate from a hydrogen-impurity or a hydrogen-vacancy complex. However, the concentration of impurities (apart from hydrogen) in our samples is too low to account for the strong absorption observed. Hence, hydrogen-impurity complexes can be ruled out. With respect to hydrogen-vacancy complexes, we note that the atoms surrounding a vacancy-type defect in silicon and germanium are three-fold coordinated and have a dangling bond that points in a $\langle 111 \rangle$ direction. Hydrogen may saturate this dangling bond, and the resulting Si-H or Ge-H bond will essentially be aligned with the $\langle 111 \rangle$ direction. Since this is inconsistent with the $\langle 110 \rangle$ orientation of the Si-H or Ge-H bonds, which we observe, this possibility can also be ruled out.

G. *Ab initio* calculations

In conjunction with the infrared absorption studies of the IH_2 defect in silicon and germanium, P. Leary, J. Goss, R. Jones, P. R. Briddon, S. Öberg, and S. J. Breuer, from or associated with the theory group at the University of Exeter, UK, performed *ab initio* calculations of the structure and local vibrational modes of IH_2 in silicon and germanium. In addition, the structure and the local vibrational modes of IH were calculated, together with the structure of the self-interstitial in both silicon and germanium. The theoretical work was reported together with the experimental studies in recent publication [7].

1. Theoretical method

The *ab initio* calculations were performed with the local-density-functional cluster method AIMPRO [17] on 132-134 atom clusters $X_{72}H_{60+n}$ where X is either Si or Ge and $n \in \{0,1,2\}$. One host atom and n hydrogen atoms were added to a tetrahedral hydrogen-terminated $X_{71}H_{60}$ cluster representing the perfect crystal. The self-consistent energy and the forces on the atoms were calculated and all 72 host atoms and n hydrogen atoms at the defect core were allowed to relax until the minimum energy configuration was obtained. The hydrogen atoms at the surface were fixed during this procedure. The second derivatives of the energy between the $6+n$ central atoms were calculated directly, while the derivatives between the remaining atoms were found from a Musgrave-Pople potential given in Ref. [17]. Then, the dynamical matrix of the cluster was constructed, and the local vibrational modes along with their isotope shifts calculated.

2. The self-interstitial (I)

For the isolated self-interstitial in its neutral charge state and with zero spin, a number of configurations were found to be close in energy. Here, only the two with lowest energy will be discussed. In silicon, the most stable defect was the $\langle 110 \rangle$ split-interstitial illustrated in Fig. VIII.1.a. Previous studies have also found this structure to possess the lowest energy [2-6]. To our knowledge, the self-interstitial in germanium has not previously been investigated theoretically. Also in this material the most stable configuration was found to be the $\langle 110 \rangle$ -split.

The other configuration of interest is a $\langle 100 \rangle$ -split, which consists of two atoms that share a lattice site and are split in the $\langle 100 \rangle$ direction. The point group of the unrelaxed defect is D_{2d} (tetragonal), and it was found to possess a partially occupied e (doublet) level lying around mid-gap. Hence, the structure is a candidate for a Jahn-Teller distortion, which lifts the tetragonal symmetry and splits the partially occupied e -level into singlets. The relaxation on the $[100]$ split-interstitial resulted in a large movement of one of the two core atoms along the $[011]$ direction so that the structure ended up with C_{1h} (monoclinic-I) symmetry. In silicon and germanium, this configuration had, respectively, 0.31 eV and 0.51 eV higher energy than the $\langle 110 \rangle$ -split interstitial.

3. The IH defect

The starting configurations were $\langle 100 \rangle$ and $\langle 110 \rangle$ split-interstitials with a hydrogen atom attached to one of the two equivalent core atoms. When the relaxation was carried out, the two starting configurations ended up in different configurations that both had C_{1h} (monoclinic-I) symmetry (see Fig. VIII.1.b and c). In both materials, the energy difference between the two configurations was small, with the $\langle 100 \rangle$ orientation $IH_{\langle 100 \rangle}$ being favoured by 0.24 eV in silicon over $IH_{\langle 110 \rangle}$, whereas the two configurations were degenerate in germanium. The silicon result is in disagreement with the *ab initio* calculations of Van deWalle *et al* [6], where a structure close to $IH_{\langle 110 \rangle}$ was found to be the ground state configuration. However, the $IH_{\langle 100 \rangle}$ structure is similar to that found by Deák *et al* using semi-empirical methods [8]. The calculated hydrogen-related local mode frequencies and the isotope shifts of $IH_{\langle 100 \rangle}$ and $IH_{\langle 110 \rangle}$ are given in Table VIII.4. Also presented in this table are the polar and azimuthal angles for the displacement of the Si-H or Ge-H bond for each of the modes.⁵ The displacements associated with the stretch modes deviated by less than 2° from the direction of the bond. For $IH_{\langle 110 \rangle}$ in silicon and germanium and for $IH_{\langle 100 \rangle}$ in germanium, the bend modes with the highest frequency were associated with the angular vibrations in the mirror plane of the defect, whereas the low-frequency bend modes corresponded to vibrations perpendicular to this plane. For $IH_{\langle 100 \rangle}$ in silicon, the ordering of the bend modes was reversed. So far, there have been no experimental reports of these modes. The stretch-mode frequencies in silicon at 2166.9 cm^{-1} for $IH_{\langle 100 \rangle}$ and 2190.8 cm^{-1} for $IH_{\langle 110 \rangle}$ are

Table VIII.4. The calculated local vibrational modes of $IH_{\langle 100 \rangle}$ (right) and $IH_{\langle 110 \rangle}$ (left) in silicon and germanium. The angles θ and φ specify the direction of the bond-displacement associated with the modes and the column denoted Freq. gives the frequencies of the modes in cm^{-1} . The frequencies of $ID_{\langle 100 \rangle}$ and $ID_{\langle 110 \rangle}$ are also given.

Si					Si				
Mode	$IH_{\langle 100 \rangle}$		$ID_{\langle 100 \rangle}$		Mode	$IH_{\langle 110 \rangle}$		$ID_{\langle 110 \rangle}$	
	θ	φ	Freq.	Freq.		θ	φ	Freq.	Freq.
A'	45.2°	7.33°	2166.9	1556.3	A'	36.4°	45.0°	2190.8	1574.1
A''	135.0°	0°	743.8	578.5	A'	126.4°	45.0°	882.0	649.7
A'	93.6°	93.6°	724.2	578.8	A''	90.0°	135.0°	749.0	539.3
Ge					Ge				
Mode	$IH_{\langle 100 \rangle}$		$ID_{\langle 100 \rangle}$		Mode	$IH_{\langle 110 \rangle}$		$ID_{\langle 110 \rangle}$	
	θ	φ	Freq.	Freq.		θ	φ	Freq.	Freq.
A'	45.1°	5.07°	2079.7	1478.9	A'	43.0°	45.0°	2073.7	1474.8
A'	92.5°	92.5°	734.5	521.0	A'	133.0°	45.0°	800.5	567.3
A''	135°	0°	729.9	517.8	A''	90.0°	135.0°	762.2	541.4

⁵ The two types of IH defects have monoclinic-I (C_{1h}) symmetry and do thus not possess a C_2 rotation axis. Hence, the polar and azimuthal angle can strictly speaking not be defined in the same manner as for the IH_2 defect (see Sec. VIII.D.2). Instead, the angles given in Table VIII.4 are defined with respect to a hypothetical C_2 axis

considerably higher than the 1870 cm^{-1} found previously for the $\langle 110 \rangle$ configuration by Van de Walle *et al* [6], but agrees reasonably with the 2217 cm^{-1} for the $\langle 100 \rangle$ configuration obtained by Deák *et al* [8] (see Table VIII.2).

4. The IH_2 defect

When two hydrogen atoms are added to the $\langle 100 \rangle$ and the $\langle 110 \rangle$ split-interstitials with the silicon or germanium atoms kept fixed, the minimum energy configurations have C_2 (monoclinic-II) and C_{2v} (orthorhombic-I) symmetry, respectively. When the relaxation was carried out maintaining these symmetries, then the relaxed $\langle 100 \rangle$ -structure in silicon had 2.56 eV lower energy than the relaxed $\langle 110 \rangle$ -structure. In germanium, the corresponding energy difference was 2.18 eV. When, however, the full relaxation was carried out without any symmetry constraint, then the $\langle 110 \rangle$ -defect rotated into the one derived from the $\langle 100 \rangle$ orientation. The structure of the ground state configuration of IH_2 is shown in Fig. VIII.1.d. The structure in both silicon and germanium is very similar to those given previously in silicon [6,8]. The calculated local vibrational mode frequencies of IH_2 , IHD and ID_2 are given in Table VIII.5 together with the polar and azimuthal angles of the mode displacements for one of the Si-H or Ge-H bonds. The calculated stretch-frequencies for IH_2 lie significantly below those calculated for vacancy-hydrogen defects, which in turn were about 7% higher than the experimental values (see chapter VI). This suggests that primarily the p -orbitals of the two innermost silicon and germanium atoms contribute to the bonding of hydrogen. The calculated stretch-mode frequencies are 8% too high in silicon and 9% too high in germanium compared to the observed frequencies. Such deviations are typical for the theoretical method, and may be ascribed to the overbinding caused by density-functional theory and to anharmonic effects. According to theory, the stretch modes are ordered with the A mode above the B mode in both silicon and germanium, in agreement with our observations. The calculated splittings of the two stretch modes of IH_2 (ID_2) are 1.8 (0.3) cm^{-1} in silicon and 3.4 (2.4) cm^{-1} in germanium. These agree roughly with the observed splittings of 2.9 (2.1) cm^{-1} and 1.7 (1.4) cm^{-1} in the two materials. Hence, the small splitting of the stretch modes was reproduced by the calculations. Moreover, the calculated stretch-frequencies of IHD deviate by less than 0.1 cm^{-1} from the average frequency of the pertinent two stretch modes of IH_2 and ID_2 . Hence, the calculated isotopic shifts for the stretch modes are in excellent agreement with experiment. The directions of the bond-displacements for the two stretch modes are equal and deviate by less than 2° from the directions of the bonds. In silicon, the polar angle is $\theta = 46^\circ$ and the azimuthal angle $\varphi = 10^\circ$, and in germanium $\theta = 46^\circ$ and $\varphi = 8^\circ$. These θ and φ values are in excellent agreement with the experimental results and strongly support the assignments made in the Sec. VIII.F.

directed along the vertical $\langle 100 \rangle$ axis shown in Fig. VIII.1.b and Fig. VIII.1.c.

Table VIII.5. The calculated local vibrational modes of IH_2 in silicon and germanium. The angles θ and φ specify the direction of the displacement of one of the bonds for each mode and the column denoted Freq. gives the frequencies of the modes in cm^{-1} . The frequencies of ID_2 and IHD are also given. The observed frequencies are given in parentheses.

Si					
Mode	IH_2		Freq.	ID_2 Freq.	IHD Freq.
	θ	φ			
A	45.9°	9.49°	2144.7 (1989.4)	1540.2 (1448.2)	2143.8 (1987.8)
B	46.1°	9.79°	2142.9 (1986.5)	1539.9 (1446.1)	1540.1 (1447.3)
A	129.1°	47.3°	774.7 (748.0)	590.2	771.4 (745.7)
B	127.9°	51.1°	768.1 (743.1)	582.6	727.3
B	67.7°	122.9°	736.4	564.3	589.8
A	69.8°	120.3°	717.5	555.0	579.8

Ge					
Mode	IH_2		Freq.	ID_2 Freq.	IHD Freq.
	θ	φ			
A	46.0°	8.30°	2056.7 (1883.5)	1462.5 (1359.0)	2055.1 (1882.8)
B	45.7°	8.47°	2053.3 (1881.8)	1460.1 (1357.6)	1461.3 (1358.4)
B	135.4°	15.7°	787.4 (705.5)	558.8	784.9 (~703)
A	132.0°	37.6°	784.7 (700.3)	555.7	712.4
A	74.5°	113.7°	725.0	514.7	555.9
B	86.5°	101.9°	694.6	493.1	503.7

For IH_2 , four bend modes were predicted at 717.5, 736.4, 768.1, and 774.7 cm^{-1} in silicon and at 694.6, 725.0, 784.7, and 787.4 cm^{-1} in germanium. The calculated frequencies of the hydrogen-related bend modes of the IHD defect are 727.3 and 771.4 cm^{-1} in silicon and 712.4 and 784.9 cm^{-1} in germanium. Hence, theory predicts that IHD gives rise to a bend mode between the two high-frequency (and the two low-frequency) bend modes of IH_2 . Also this is in agreement with the observations both in silicon and germanium. The Si-H bend modes at 768.1 and 774.7 cm^{-1} (717.5 and 736.4 cm^{-1}) are associated with displacements in the directions specified by the polar angle $\theta \approx 129^\circ$ and the azimuthal angle $\varphi \approx 49^\circ$ ($\theta \approx 69^\circ$ and $\varphi \approx 122^\circ$). The calculated displacement vectors for the high-frequency modes deviate substantially from those obtained experimentally ($\theta = 137^\circ \pm 2^\circ$ and $\varphi = 0^\circ \pm 8^\circ$). In addition, the calculations show that the 768.1- cm^{-1} mode is a B mode, whereas the 774.7- cm^{-1} mode is an A mode, i.e. the ordering is reversed compared to the experimental results. The explanation for these discrepancies is probably that the calculations underestimate the difference in frequency between the set of high-frequency and the set of low-frequency bend modes. Two observations support this explanation. First, only two bend modes are observed in both materials although the lower limit for detection is $\sim 600 \text{ cm}^{-1}$. This gives a lower limit on the separation of the two sets of modes at $\sim 140 \text{ cm}^{-1}$ ($\sim 100 \text{ cm}^{-1}$) in silicon (germanium), which is considerably larger than the $\sim 30 \text{ cm}^{-1}$ ($\sim 60 \text{ cm}^{-1}$) separation calculated. The calculated separation is twice as large in germanium as in silicon. If our explanation for the discrepancies is correct we will, therefore, expect that the calculated normal modes of IH_2 in germanium are in better agreement with the observations. It should be

stressed that this argument relies heavily on the fact that the calculated structures of the IH_2 defect in silicon and germanium are almost identical. The ordering of the calculated bend modes of IH_2 in germanium is different than that of IH_2 in silicon (see Table VIII.5) and in total agreement with the observations for the Si-H bend modes. Moreover, the calculated polar and azimuthal angles of the bond-displacements for the two high-frequency bend modes in germanium are qualitatively consistent with those observed. These considerations support our explanation of the discrepancies.

H. Conclusion

The infrared absorption lines at 743.1, 748.0, 1986.5, and 1989.4 cm^{-1} in Si:H and at 700.3, 705.5, 1881.8, and 1883.5 cm^{-1} in Ge:H originate from a defect containing two equivalent and weakly coupled Si-H or Ge-H bonds. The symmetry of the defect is monoclinic-II corresponding to a C_2 point group. The two Si-H or Ge-H bonds are almost perpendicular and their directions deviate only by a few degrees from $\langle 110 \rangle$. The structure of IH_2 in silicon and germanium calculated by *ab initio* theory is in excellent agreement with the information deduced experimentally, confirming the identity of the defects as the fully hydrogenated self-interstitial. Moreover, the small frequency splittings between the two stretch- and the two bend modes are reproduced by the theoretical calculations together with the isotopic shifts. The calculated frequencies deviate by 8-9% from those observed, which is typical for the method. Based on these findings, we conclude that the Si-H modes at 743.1, 748.0, 1986.5, and 1989.4 cm^{-1} and the Ge-H modes at 700.3, 705.5, 1881.8, and 1883.5 cm^{-1} originate from the IH_2 defect.

I. References

- [1] G. D. Watkins, in *Materials Science and Technology* Vol 4, edited by W. Schröter (VCH, Weinheim, 1991).
- [2] Y. Bar-Yam and J. D. Joannopoulos, *Phys. Rev. Lett.*, **52**, 1129 (1984).
- [3] R. Car, P. J. Kelly, A. Oshiyama and S. T. Pantelides, *Phys. Rev. Lett.*, **54**, 360 (1985).
- [4] P. E. Blöchl, E. Smargiassi, R. Car, D. B. Laks, W. Andreoni and S. T. Pantelides, *Phys. Rev. Lett.*, **70**, 2435 (1993).
- [5] D. J. Chadi, *Phys. Rev. B*, **46**, 9400 (1992).
- [6] C. G. Van de Walle and J. Neugebauer, *Phys. Rev. B*, **52**, R14320 (1995).
- [7] M. Budde, B. Bech Nielsen, P. Leary, J. Goss, R. Jones, P. R. Briddon, S. Öberg, and S. J. Breuer, *Phys. Rev. B*, **57**, 4397 (1998).
- [8] P. Deák, M. Heinrich, L. C. Snyder and J. W. Corbett, *Mater. Sci. Eng.* **B4**, 57 (1989).
- [9] P. Deák, L. C. Snyder, M. Heinrich, C. R. Ortiz and J. W. Corbett, *Physica B*, **170**, 253 (1991).
- [10] C. G. Van de Walle, *Phys. Rev. B*, **49**, 4579 (1994).

- [11] H. J. Stein, *J. Electronic Mat.*, **4**, 159 (1975).
- [12] T. S. Shi, G. R. Bai, M. W. Qi, and J. K. Zhou, in "Defects in Semiconductors", edited by H. J. von Bardeleben, *Materials Science Forum Vol. 10-12* (Trans Tech, Aedermannsdorf, 1986), 597 (1986).
- [13] L. M. Xie, M. W. Qi and J. M. Chen, *J.Phys.: Condens. Matter*, **3**, 8519 (1991).
- [14] Y. C. Du, Y. F. Chang, X. T. Meng, and H. Y. Sheng, *Sci. Sin. A*, **30**, 176 (1987) (in chinese).
- [15] A. A. Kaplyanskii, *Opt. Spectrosk.* **16**, 557 (1964) [*Opt. Spectrosk. (USSR)* **16**, 1031 (1964)].
- [16] *American Institute of Physics Handbook*, 3rd ed. edited by D. W. E. Gray (McGraw-Hill, New York, 1972), p. 7-189.
- [17] R. Jones, *Phil. Trans. Roy. Soc. London Ser. A*, **341**, 351 (1992).

IX. Summary

The present thesis has described experimental studies of hydrogen-related point defects in silicon and germanium single-crystals implanted with protons and/or deuterons. The infrared absorption of the samples was measured with an FTIR spectrometer at cryogenic temperatures. The thermal stability and correlation of the absorption lines was studied by isochronal annealing. Isotope substitution was used to assign the lines to hydrogen-related local vibrational modes, and to study the number of hydrogen atoms contained in the defects. Finally, uniaxial stress measurements were performed in order to determine the symmetry of the defects and the degeneracy of the final state associated with the absorption lines. The experimental information on the defects was compared with the atomic structure, vibrational modes, and binding energies predicted by theory, which allowed some of the infrared absorption lines to be assigned to specific defects.

In chapter IV it was shown that implantation of protons into silicon at ~ 20 K gives rise to a very intense absorption line at 1998 cm^{-1} , which is identical to the 1990-cm^{-1} line observed by Stein at ~ 80 K. The annealing behaviour of the 1998-cm^{-1} line and absorption measurements with and without illumination with band-gap light showed that the line originates from hydrogen at the bond-centre site in the positive charge state (H_{BC}^+). No other absorption lines were observed in the Si-H stretch or bend regions, suggesting that essentially all the protons implanted into silicon at ~ 20 K form H_{BC}^+ centres. The 1998-cm^{-1} line anneals at two distinct stages. At the first stage at ~ 100 K, the intensity of the line decreases by $\sim 20\%$, and the 2038-cm^{-1} line of *VH* appears. This stage is ascribed to trapping of monovacancies by H_{BC}^+ . The second stage occurs at ~ 200 K in the dark, at which the 1998-cm^{-1} line disappears. This annealing stage is attributed to the on-set of H_{BC}^+ migration.

Chapter V described the observation of the H_2^* defect in germanium implanted with protons at ~ 30 K. After annealing at room temperature, a quartet of lines originating from the same centre was observed at 765 , 1499 , 1774 , and 1989 cm^{-1} (see Fig. IX.1). The centre has trigonal symmetry and contains two inequivalent hydrogen atoms bonded to germanium. The vibrational characteristics of the centre are, apart from a downshift in vibrational frequency, very similar to those of the H_2^* defect in silicon identified by Holbeck *et al.* Therefore, the four lines were assigned to the H_2^* defect in germanium. The stretch frequencies were interpreted in terms of a simple model consisting of two coupled one-dimensional Morse-potential oscillators. The assignment of the 765 -, 1499 -, 1774 -, and 1989-cm^{-1} lines to the H_2^* defect in germanium was supported by *ab initio* theoretical calculations.

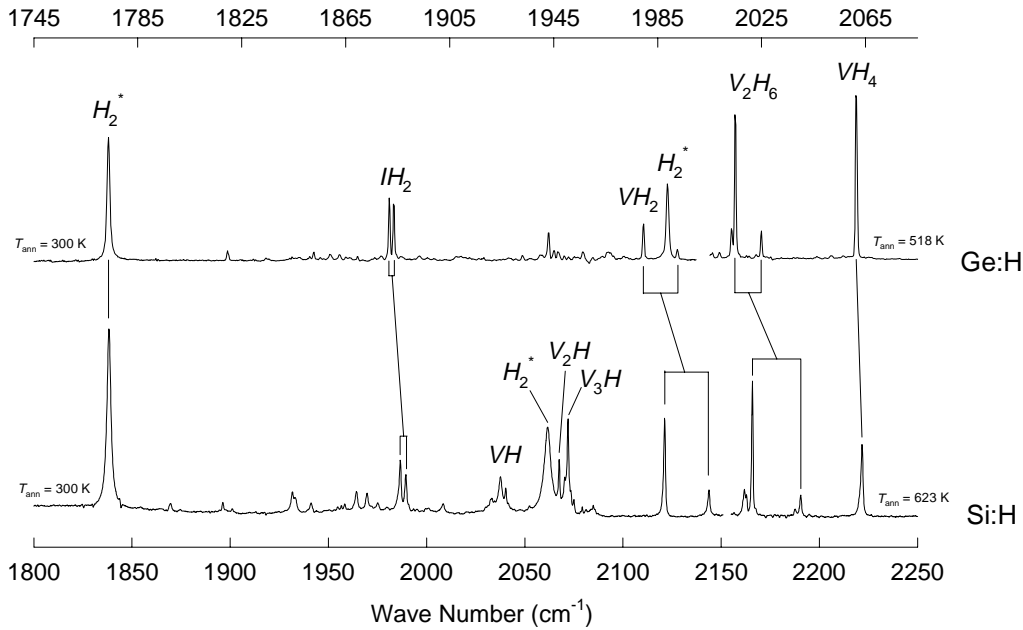


Fig. IX.1. Assignments of infrared absorption lines to hydrogen-related defects in proton implanted silicon (bottom) and germanium (top).

Chapter VI was concerned with infrared absorption studies of vacancy-hydrogen complexes in silicon. Implantation of protons into silicon at ~ 100 K followed by annealing at room temperature gives rise to a number of absorption lines in the Si-H stretch region, as shown in Fig. IX.1. The lines at 2121 and 2145 cm^{-1} originate from B_1 and A_1 modes of a centre with orthorhombic-I symmetry that contains two equivalent hydrogen atoms. The observed symmetry of the centre, the ordering of the vibrational modes, the isotopic shifts, and the location of the modes between those of VH and VH_4 are consistent with theoretical predictions for VH_2 in silicon. Hence, the 2121 - and 2145 - cm^{-1} lines were assigned to this complex. The annealing of the 2121 - and 2145 - cm^{-1} lines was ascribed to the capture of hydrogen by VH_2 , which converts the defect into the hydrogen-saturated vacancy VH_4 . Another pair of lines appears at 2166 and 2191 cm^{-1} after annealing at ~ 560 K. The lines originate from an E and an A Si-H stretch mode of a trigonal centre, which contains at least three hydrogen atoms. The ordering of the modes, and the theoretical prediction that interstitial SiH_3 does not correspond to a low-energy configuration, strongly suggests that the 2166 - and 2191 - cm^{-1} lines originate from VH_3 or V_2H_6 . Because of the correlated annealing of VH_3 observed by EPR and the absorption lines at 2155 and 2185 cm^{-1} , as discussed in chapter VI, the 2166 - and 2191 - cm^{-1} lines are assigned to V_2H_6 in silicon. This assignment is also consistent with that annealing at elevated temperatures results in the formation of hydrogen-saturated defects, as suggested by the apparent conversion of VH_2 into VH_4 at ~ 480 K.

Chapter VII extended the infrared absorption studies of vacancy-hydrogen complexes to proton-implanted germanium. Two pairs of absorption lines were observed at {1979.5, 1992.6} and {2014.9, 2024.8} cm^{-1} which, apart from a downshift in vibrational frequency, have vibrational characteristics essentially identical to those of the lines at {2121, 2145} and {2166, 2191} cm^{-1} in Si:H. The lines at 1979.5 and 1992.6 cm^{-1} were therefore assigned to VH_2 , and the 2014.9- and 2024.8- cm^{-1} lines to V_2H_6 in Ge:H. In addition, an absorption line at 2061.5 cm^{-1} was studied in detail. The properties of the 2061.5- cm^{-1} line are very similar to those of the 2223- cm^{-1} line in Si:H previously assigned to VH_4 . For example, both lines have the highest stretch frequency in the spectra, they both originate from a T mode of a cubic centre, and the isotopic shifts and annealing behaviour of the two lines are qualitatively very similar. Based on these similarities, the 2161.5- cm^{-1} line was assigned to VH_4 in germanium.

In the last experimental chapter (chapter VIII), absorption lines at 743.1, 748.0, 1986.5, and 1989.4 cm^{-1} in Si:H and 700.3, 705.5, 1881.8, and 1883.5 cm^{-1} in Ge:H were assigned to the hydrogen-saturated self-interstitial IH_2 in silicon and germanium. The four lines in each material originate from the same defect, which contains two equivalent hydrogen atoms. Moreover, the scaling of vibrational frequencies and the similar annealing behaviour of the lines in Si:H and Ge:H strongly suggests that the two quartets of lines originate from the same defect in silicon and germanium. The stress-pattern of the 1881.8- and 1883.5- cm^{-1} lines in Ge:H were consistent with those expected theoretically for B and A modes of a centre with monoclinic-II symmetry, provided that mixing of the first-excited states induced by the uniaxial stress was taken into account. The relative intensities of the lines observed with and without uniaxial stress were interpreted in terms of a bond-dipole model. Within this model, the Ge-H bonds were found to be nearly parallel to $\langle 110 \rangle$ directions. The 743.1-, 748.0-, 1986.5-, and 1989.4- cm^{-1} lines in Si:H are rather insensitive to uniaxial stress. The observed stress-patterns are, however, fully consistent with those expected for a centre with monoclinic-II symmetry with Si-H bonds directed along $\langle 110 \rangle$ directions. The experimental structural information on the lines at 743.1, 748.0, 1986.5, and 1989.4 cm^{-1} in Si:H and 700.3, 705.5, 1881.8, and 1883.5 cm^{-1} in Ge:H is in excellent agreement with the predictions made by theory for the hydrogen-saturated self-interstitial and, consequently, the quartet of lines in each material was assigned to this defect.

Table IX.I. Assignments of infrared absorption lines in proton-implanted silicon and germanium to hydrogen-related defects. The rows denoted “XH₄” give the vibrational frequencies of molecular silane and germane.

Centre	Symmetry	Mode	Si		Ge		$\omega_{\text{Si}}/\omega_{\text{Ge}}$	$T_{\text{Si}}/T_{\text{Ge}}$
			ω (cm ⁻¹)	T_{ann} (K)	ω (cm ⁻¹)	T_{ann} (K)		
H_{BC}^+			1998	190				
H_2^*	trigonal	<i>E</i>	817 ^a		765		1.068	
		<i>A</i>	1599 ^{a,b}	435	1499 ^b	420	1.067	1.04
		<i>A</i>	1838 ^a		1774		1.036	
		<i>A</i>	2062 ^a		1989		1.037	
VH_2	orthorhombic-I	<i>B</i> ₁	2121		485		1979.5	
		<i>A</i> ₁	2145	1992.6		1.077		
VH_4	cubic	<i>T</i>	2223 ^a	775	2061.5	590	1.078	1.31
V_2H_6	trigonal	<i>E</i>	2166	800	2014.9	620	1.075	1.29
		<i>A</i>	2191		2024.8		1.082	
IH_2	monoclinic-II	<i>A</i>	743.1	485	700.3	465	1.061	1.04
		<i>B</i>	748.0		705.5		1.060	
		<i>B</i>	1986.5		1881.8		1.056	
		<i>A</i>	1989.4		1883.5		1.056	
XH ₄	<i>T_d</i>	<i>A</i> ₁	2191		2114		1.036	
		<i>T</i> ₂	2187		2106		1.039	
		<i>E</i>	975		931		1.047	
		<i>T</i> ₂	914		819		1.116	

^a Not assigned in the present work.

^b Second-harmonic transition.

In 1994 when this PhD project initiated, the origin of all the absorption lines in the Si-H stretch region shown in Fig. IX.1 was uncertain, except the 1838-, 2062-, and 2223-cm⁻¹ lines ascribed to H_2^* and VH_4 . In contrast, all the prominent absorption lines have now been identified, and the understanding of hydrogen-related defects in silicon has increased accordingly. The large spread in Si-H stretch frequencies shows that the local modes are very sensitive to the bonding configuration of the defects. Based on the assignments indicated in Fig. IX.1, the hydrogen-related complexes can be divided into three groups. The lines in the range 2000 – 2100 cm⁻¹ (except the 2062-cm⁻¹ line from H_2^*) originate from defects containing a single hydrogen atom bonded to a dangling bond in a vacancy-type defect. The lines located above 2100 cm⁻¹ are ascribed to vacancy-hydrogen complexes containing more than one Si-H bond in the same vacancy, and the high stretch frequency is attributed to the repulsion between the Si-H bonds. Finally, the calculated structures of the H_2^* and IH_2 defects indicate that the absorption lines located below 2000 cm⁻¹ originate from Si-H bonds with the silicon atom located close to the plane spanned by its three nearest neighbour silicon atoms. The low stretch frequencies can therefore be explained by hydrogen being bonded to a silicon orbital with *p* rather than *sp*³

character. The experimental and theoretical results indicate that the stretch frequency decreases whereas the bend frequencies increase with increasing p character of the silicon orbital.

The assignments of the absorption lines to specific defects and the studies of the annealing behaviour of the lines reported in the present thesis or by others, provide a qualitative understanding of the thermal development of hydrogen-related defects in proton-implanted silicon. Implantation of protons into silicon at ~ 20 K results in the formation of H_{BC}^+ centres and intrinsic defects such as monovacancies and self-interstitials. Upon annealing at ~ 100 K, the monovacancies become mobile, which causes them to 1) get trapped at another vacancy or vacancy-cluster, 2) recombine with a self-interstitial, or 3) get trapped at a H_{BC}^+ centre, which leads to the formation of the VH complex. As discussed in chapter IV, approximately 20% of the H_{BC}^+ centres disappear at this stage. At ~ 200 K the H_{BC}^+ centres become mobile and are trapped at e.g. vacancy-clusters, self-interstitials, or VH defects, which leads to the formation of IH_2 , VH , V_2H , V_3H , VH_2 , VH_3 , and VH_4 complexes. In addition, some of the mobile hydrogen atoms trap each other and form H_2^* defects. The formation of this variety of defects is the reason for the complicated absorption spectrum observed after room temperature annealing. Annealing at ~ 500 K causes the H_2^* and IH_2 defects to disappear, presumably due to thermally induced dissociation. The hydrogen released by this process gets trapped by vacancy-hydrogen complexes, which results in the formation of the hydrogen-saturated defects VH_4 and V_2H_6 . At ~ 800 K, the VH_4 and V_2H_6 complexes dissociate and the hydrogen diffuses out of the sample.

The motivation for extending the studies of hydrogen-related defects to proton-implanted germanium was to clarify whether hydrogen forms the same type of point defects in germanium as in silicon. The infrared absorption studies described in this thesis show that the H_2^* , VH_2 , VH_4 , V_2H_6 , and IH_2 defects are formed in proton-implanted germanium in similar numbers as in silicon. Moreover, the Ge:H spectrum is qualitatively very similar to the Si:H spectrum (see Fig. IX.1), which suggests that the defects have similar structures in the two materials. Quantitatively, the vibrational frequencies are 4 – 8% higher in silicon than in germanium, which is close to the 4% difference in frequency of the stretch modes of silane and germane. As shown in Table IX.I, the annealing temperatures of the defects are 4 - 30% lower in germanium than in silicon. This is qualitatively consistent with the Ge-H bond being $\sim 20\%$ weaker than the Si-H bond. In summary, the experimental studies described in the present thesis establish that the same defects are formed above room temperature in proton-implanted silicon and germanium, and that the differences in vibrational frequencies and thermal stability essentially may be ascribed to the difference in strength of the Si-H and Ge-H bonds.

X. Danish summary

Denne afhandling omhandler brint-relaterede punktdefekter i enkelt-krystallinsk silicium og germanium studeret med infrarød absorptionspektroskopi. Det eksperimentelle arbejde blev udført ved Institut for Fysik og Astronomi, Århus Universitet, i perioden fra august 1994 til juni 1998. Inkluderet i Ph.D. forløbet var et fem måneders ophold ved Oak Ridge National Laboratory, Tennessee, USA, fra september 1997 til og med januar 1998. De experimentelle resultaterne opnået under dette ophold er ikke inkluderet i denne afhandling. Ph.D. projektet var finansieret af et stipendium fra ACAP (Aarhus Center for Atomfysik), som er et grundforskningscenter ved Institut for Fysik og Astronomi, Århus Universitet, oprettet af Danmarks Grundforskningsfond.

Formålet med projektet er at identificere brint-relaterede punktdefekter i silicium og germanium samt at studere mikrostrukturen af disse defekter. Defekterne blev studeret med infrarød absorptionspektroskopi i kombination med udglødning, isotopsubstitution og uniaksialt stress.

Infrarød absorptionspektroskopi måler absorptionen af infrarødt lys forårsaget af lysets passage gennem en given prøve. Brint-relaterede punktdefekter giver anledning til vibrationelle tilstande, der svarer til kollektive vibrationer af brintatomerne og de nærmeste skaller af omkringliggende gitteratomer. Vibrationstilstandenes frekvenser er stærkt afhængige af måden, hvorpå brinten er bundet til gitteratomerne, og derfor af defekternes mikrostruktur. Tilstedeværelsen af brint-relaterede defekter giver sig til udtryk ved forekomsten af skarpe absorptionslinier i den infrarøde del af prøvens absorptionspektrum, som skyldes excitationer fra defekternes grundtilstand til de første-exciterede vibrationelle tilstande. Antallet af absorptionslinier hidrørende fra samme defekt er bestemt af antallet af brintatomer indeholdt i defekten og defektens symmetri, og det er derfor vigtigt at bestemme hvilke absorptionslinier, der stammer fra samme defekt. Dette kan f.eks. gøres ved at måle effekten af opvarmning (udglødning) af prøven på intensiteten af absorptionslinierne. Et mindstekriterium for at tilskrive absorptionslinier til samme defekt er, at intensitetsforholdene af de pågældende linier er uafhængige af udglødningstemperaturen. Vibrationsfrekvensen hørende til en lokal vibrationstilstand er tilnærmelsesvis omvendt proportional med kvadratroden af massen af brintisotopen involveret i vibrationen. Vibrationsfrekvensen vil derfor mindskes med en faktor $\sim\sqrt{2}$, hvis brinten substitueres med deuterium. Et sådant isotopskift er karakteristisk for en brint-relateret vibrationstilstand og bruges til entydigt at tilordne absorptionslinier til sådanne tilstande. Hvis både brint og deuterium forefindes i krystallen, er der mulighed for at danne defekter, der indeholder begge isotoper. Pga. den store forskel i

vibrationsfrekvens for brint og deuterium er den vibrationelle kobling mellem båndene i en defekt, der indeholder både brint og deuterium, markant forskellig fra koblingen i defekter, der udelukkende indeholder brint eller deuterium. Defekter bestående af en blanding af isotoper vil derfor give anledning til et antal nye linier i prøver indeholdende begge isotoper. Antallet af nye linier giver information om antallet af brintatomer indeholdt i defekten, og om brintatomerne er ækvivalente. Symmetrien af punktdefekten og slutttilstanden associeret med en given absorptionslinie kan bestemmes ved at måle det infrarøde absorptionspektrum med uniaksialt stress (spænding) pålagt parallelt med krystallens [100], [111] og [110] retninger. Det pålagte stress deformerer krystallen, og bevirker dermed, at alle orienteringer af en given defekt ikke længere er ækvivalente. Endvidere kan det pålagte stress reducere defektens symmetri, hvilket kan mindske eller ophæve en eventuel udartning af de vibrationelle tilstande. I praksis kan det pålagte stress inducere et frekvensskift og en opsplitning af absorptionslinierne. Opsplitningsmønstret af en absorptionslinie for stress langs [100], [111] og [110] retninger, og målt med det infrarøde lys polariseret parallelt med eller vinkelret på stress-retningen, er karakteristisk for defektens symmetri (det krystallografiske system) og symmetrien af den vibrationelle slutttilstand.

I denne afhandling har infrarød spektroskopi i kombination med udglødning, isotopsubstitution og uniaksialt stress været brugt til at bestemme antallet af brintatomer indeholdt i defekten samt symmetrien af defekten og den vibrationelle slutttilstand. Frekvensen af de observerede absorptionslinier giver information om måden hvorpå brinten er bundet til gitteret, og frekvensforskellen mellem linier hørende til samme defekt er ofte udtryk for styrken af den vibrationelle kobling mellem forskellige bånd. På trods af at de mikrostrukturelle informationer, der kan udledes fra absorptionsmålinger, kan være forholdsvis detaljerede, tillader de sjældent en entydig identifikation af den pågældende defekt. Tilordningen af et sæt absorptions linier til en specifik defekt er derfor typisk baseret på en sammenligning af de eksperimentelle resultater med resultatet af detaljerede teoretiske beregninger af totalenergien, symmetrien og den atomare konfiguration for forskellige defekter samt eventuelt frekvenser og isotopskift for defekternes lokale vibrationstilstande. Entydige tilordninger af absorptionslinier kan også opnås ved at sammenholde de eksperimentelle resultater med informationen opnået med komplementære eksperimentelle teknikker såsom EPR (Elektron Paramagnetisk Resonans).

Prøverne studeret i denne afhandling bestod af enkelt-krystallinsk silicium eller germanium implanteret med protoner og/eller deutroner ved temperaturer i intervallet 20 - 300 K. Hver af prøverne blev implanteret ved 50 - 100 forskellige ion-energier, hvilket resulterede i en homogen brint og/eller deuterium koncentration på ~ 0.0002 at. % eller ~ 0.02 at. %, der strakte sig over en dybde på $\sim 500 \mu\text{m}$ eller $\sim 50 \mu\text{m}$. Implantation ved en række forskellige energier gør det muligt at kombinere relativt store implantationsdoser med relativt lave koncentrationer af brint og implantationsskabte defekter.

Det første eksperimentelle kapitel (kapitel IV) omhandlede studier af silicium implanteret med protoner og/eller deutroner ved ~ 20 K. Lokalkoncentrationen af brint og/eller deuterium var ~ 0.0002 at. % i disse prøver. Efter implantationen blev det infrarøde absorptionsspektrum målt ved ~ 9 K, uden at prøven havde været opvarmet mellem implantationen og absorptionsmålingen. Absorptionsspektret af den proton-implanterede prøve bestod af en meget intens absorptionslinie ved 1998 cm^{-1} . Udglødningsopførslen af linien i mørke og under belysning med båndgabslys viste entydigt, at den stammer fra den positive ladningstilstand af brint lokaliseret på midten af et bånd mellem to silicium atomer (H_{BC}^+). 1998-cm^{-1} linien er den eneste absorptionslinie i spektret efter implantation ved ~ 20 K, hvilket indikerer at praktisk talt alle protoner implanteret ved denne temperatur danner H_{BC}^+ defekter. 1998-cm^{-1} linien reduceres i intensitet med $\sim 20\%$ ved opvarmning til ~ 100 K, og forsvinder helt ved ~ 200 K. Den første intensitetsreduktion tilskrives at en del af H_{BC}^+ defekterne indfanger en monovakance, og omdannes til et vakance-brint kompleks (VH). Det andet udglødningstrin ved ~ 200 K tilskrives at H_{BC}^+ defekterne begynder at diffundere, hvorefter de bindes til eksempelvis et underkoordineret siliciumatom i en vakance-type defekt. Opvarmning af prøven til over 200 K resulterer i et kompliceret absorptionsspektrum, som består af 10 - 20 absorptionslinier i frekvensområdet $1800 - 2250 \text{ cm}^{-1}$ samt en række linier i området $600 - 850 \text{ cm}^{-1}$. De førstnævnte linier stammer fra excitationer af Si-H strækningsvibrationer af forskellige brint-relaterede defekter, mens de lavfrekvente linier tilskrives Si-H bøjningsvibrationer.

I kapitel VI og VIII blev et udvalg af absorptionslinierne, der observeres efter opvarmning til stuetemperatur, studeret i detalje og tilskrevet specifikke brint-relaterede defekter. Til disse studier blev prøver med brint eller deuterium koncentrationer på ~ 0.02 at. % benyttet. De eksperimentelle studier viste at linierne ved 2121 og 2145 cm^{-1} hidrører fra den samme defekt, som indeholder to brintatomer og har ortorombisk-I symmetri. Baseret på en meget god overensstemmelse mellem de eksperimentelle resultater og teoretiske forudsigelser blev de to linier tilskrevet to brintatomer bundet i en monovakance (VH_2). Tilsvarende viste absorptionsmålingerne at linierne ved 743.1 , 748.0 , 1986.5 og 1989.4 cm^{-1} tilhører den samme defekt, som

har monoklin-II symmetri. Linierne blev tilskrevet IH_2 defekten, som består af to silicium atomer, der deler en substitutionel gitterposition, mættet med to brintatomer. Opvarmning af prøven til ~ 500 K resulterer i en markant ændring af det infrarøde absorptionsspektrum, hvilket viser at en refordeling af brinten finder sted. F.eks. forsvinder de to ovennævnte sæt af linier ved denne temperatur, og linier ved 2166 og 2223 cm^{-1} tiltager kraftigt i intensitet. Der har i en årrække været enighed om at 2223-cm^{-1} linien stammer fra den brint-mættede monovakance VH_4 , hvorimod 2166-cm^{-1} linien ikke entydigt er blevet tilskrevet en specifik defekt. I kapitel VI af denne afhandling blev det vist at 2166-cm^{-1} linien stammer fra samme defekt som en linie ved 2191 cm^{-1} , samt at denne defekt indeholder mindst tre brintatomer og har trigonal symmetri. De to linier blev tilskrevet den brint-mættede divakance V_2H_6 .

Tilordningerne af absorptionslinier til brint-relaterede defekter i proton-implanteret silicium og studier af udglødningsopførslen af disse linier, udført i forbindelse med dette Ph.D. projekt og af andre forskere, giver et kvalitativt billede af den termiske udvikling af brint-relaterede defekter i proton-implanteret silicium. Implantation af protoner ind i silicium ved ~ 20 K resulterer i dannelsen af brint lokaliseret på bånd-center positioner i gitteret samt vakancer og interstitielle siliciumatomer. Ved opvarmning til ~ 100 K bliver monovakancerne (V) mobile, hvorefter de 1) møder hinanden og danner divakancer (V_2) eller vakance-klynger, 2) møder et interstitielt siliciumatom (I) og dermed rekombinerer, eller 3) møder et brintatom og danner VH komplekset. Dette udglødningstrin reducerer antallet af brintatomer på bånd-center positioner med $\sim 20\%$. Ved ~ 200 K bliver brintatomerne mobile, hvorefter de bliver fanget af implantationsskabte vakancer-klynger og interstitielle siliciumatomer, hvilket eksempelvis fører til dannelse af IH_2 , VH , V_2H , V_3H , VH_2 , VH_3 og VH_4 komplekser. Tilmed vil nogle af brintatomerne fange hinanden og danne H_2^* . Dannelsen af dette væld af forskellige defekter er årsagen til det komplicerede absorptionsspektrum af proton-implanteret silicium ved stuetemperatur. Opvarmning til ~ 500 K bevirker at H_2^* og IH_2 forsvinder, sandsynligvis pga. dissociation. Dette frigiver brint, som bliver fanget af de umættede vakance-brint komplekser, og omdanner disse til VH_4 og V_2H_6 . Omkring ~ 800 K dissocierer VH_4 og V_2H_6 komplekserne, og brinten diffunderer ud af krystallen.

Denne afhandling har endvidere beskrevet infrarød absorptionsstudier af proton-implanteret germanium. Formålet med disse studier var at undersøge om brint danner de samme typer defekter i germanium som i silicium. Absorptionsspektret af proton-implanteret germanium er kvalitativt meget lig spektret for en tilsvarende silicium prøve. I kapitel V, VII og VIII blev det vist at H_2^* , IH_2 , VH_2 , VH_4 og V_2H_6 defekterne dannes i proton-implanteret germanium i omtrent samme antal som i silicium, samt at strukturen af defekterne er meget ens i de to materialer. De observerede

vibrationsfrekvenser for defekterne er 4 - 8% lavere i germanium end for tilsvarende defekter i silicium, og temperaturen hvorved defekterne forsvinder er 4 - 30% lavere. Disse forskelle kan primært tilskrives forskellen i styrken af Ge-H og Si-H båndet.

XI. Acknowledgements

I would like to extend my gratitude to the people who made the completion of this work possible. First of all, I would like to thank my supervisor Brian Bech Nielsen for innumerable inspiring discussions and for his guidance and support. Knud Bonde Nielsen is thanked for his assistance with the Tandem accelerator and for his interest in my projects. I would also like to thank Pia Bomholt for carefully preparing the samples that I used and crushed.

Bob Jones, Paul Leary, Jonathan Goss, and James Coomer from the theory group at the University of Exeter are gratefully acknowledged for their continuing interest in my projects and for sharing results prior to publication.

I am indebted to my friend Kasper O. Schweitz for proof-reading the manuscript and for his tireless support during the hard times of the writing process – thank you for pulling me through!

Finally, I would like to extend my deepest gratitude to my wife Dorthe for her endless patience and support.